NASA TECHNICAL MEMORANDUM

NASA TM X-64723

February 1973

(NASA-TM-X-64723) RESEARCH ACHIEVEMENTS REVIEW. VOLUME 4, REPORT NO. 7: PROCESS ENGINEERING RESEARCH AT MSFC (NASA) 143 p HC $9.25 CSCL 05A

N73-22915 THRU N73-22925 Unclas G3/34 68821

NASA TM X-64723

PROCESS ENGINEERING RESEARCH AT MSFC

RESEARCH ACHIEVEMENTS REVIEW

VOLUME IV REPORT NO. 7

SCIENCE AND ENGINEERING DIRECTORATE
GEORGE C. MARSHALL SPACE FLIGHT CENTER
MARSHALL SPACE FLIGHT CENTER, ALABAMA

1. Report No. NASA TM X-64723	2. Government Accession No.	3. Recipient's Catalog No.
4. Title and Subtitle RESEARCH ACHIEVEMENTS REVIEW, VOL. IV, REPORT NO. 7 Process Engineering Research at MSFC		5. Report Date February, 1973
		6. Performing Organization Code
7. Author(s) Ralph Herndon, Edwin L. Brown, L. C. Jackson, R. V. Hoppes, John R. Rasquin, I. C. Yates, Vaughn H. Yost, James L. Splawn, Hubert E. Smith, and Herman T. Blaise		8. Performing Organization Report No.
9. Performing Organization Name and Address George C. Marshall Space Flight Center Marshall Space Flight Center, Alabama 35812		10. Work Unit No.
		11. Contract or Grant No.
		13. Type of Report and Period Covered Technical Memorandum
12. Sponsoring Agency Name and Address National Aeronautics and Space Administration Washington, D.C. 20546		14. Sponsoring Agency Code

15. Supplementary Notes

Prepared by Process Engineering Laboratory, Science and Engineering

16. Abstract

The demands on process engineering technology are becoming more critical and challenging as this nation's space program moves from the "one shot" launch vehicle concept to the multilaunch capability. A long duration Skylab, the Space Shuttle and the permanent Space Station or Space Base will require efficient and economic reuse of launch vehicles. This reuse requirement and long life orbiting systems expose new research areas. Material processing on earth and in space, advanced manufacturing technology, zero gravity simulation, life support hardware, and remote material handling systems are discussed in the 10 papers of this review, describing applicable achievements and future plans for process engineering research.

1. Flat Conductor Cable (FCC) satisfies the stringent demands set down for today's complex, electrical interconnection systems in space vehicles. Past and present applications of FCC are described.

2. Fiber-composites technology assessment and development efforts and the application of such technology to the structural hardware of the Space Shuttle are reviewed and discussed.

3. Galvanic forming techniques for producing small experimental blast nozzles for wind tunnel use, metallic shielding for cable-shape transformation joints, slit masks used in making thin-film hybrid microcircuits, and other such small items for space vehicle hardware applications are described.

4. Electron-beam welding systems of three major types are reviewed.

Continued

17. Key Words (Suggested by Author(s))		18. Distribution Statement
composite structures	Flat Conductor Cable	Unclassified — Unlimited
galvanic forming	neutral buoyancy space simulation	John T. Hoffman S&E-R
electron beam welding	EKG isolator and cardiotachometer	
quartz gyro	free-flying teleoperator	
composite casting, zero-g		

19. Security Classif. (of this report)	20. Security Classif. (of this page)	21. No. of Pages	22. Price
Unclassified	Unclassified	149	NTIS $3.25

MSFC - Form 3292-1 (Rev December 1972)

For sale by National Technical Information Service, Springfield, Virginia 22151

5. Quartz gyroscopes for the general relativity satellite are being built by unusual and precise techniques. The techniques presented herein permit manufacture and measurement of the gyroscope rotor and housing to a configuration not heretofore produced.

6. Composite-casting demonstration results from the Apollo 14 flight are covered.

7. Zero gravity for manufacturing-in-space process studies has been obtainable for the past 2 years only from two techniques. One technique is the drop tower; the other is a KC-135 aircraft, flying a free-fall trajectory. The advantages and disadvantages of these techniques, and the results obtained from each in the process studies are described.

8. The MSFC Neutral Buoyancy Simulator, used to duplicate the weightlessness condition experienced by astronauts, is described.

9. An electrocardiogram (EKG) isolator system and a compact, digital-unit cardiotachometer system are described.

10. Free-flying teleoperator (remote maneuvering units) development testing and demonstration effort over a 5-year period are presented. Several potential applications of simulators for development of manipulator systems and subsystems are evaluated.

PREFACE

The Research Achievements Reviews document research accomplished by the laboratories of Marshall Space Flight Center. Each review covers one or two fields of research and attempts to present the results in a form readily usable by specialists, system engineers, and program managers.

Reviews of this fourth series are designated Volume IV and will span the period from May 1970 through May 1972.

In accordance with NASA policy the International System of Units (SI Units), as defined in NASA SP-7012, is used in this publication.

The papers in this report were presented September 30, 1971.

William G. Johnson
Director
Research Planning Office

CONTENTS. . .

FLAT CONDUCTOR CABLE DEVELOPMENT

LIST OF TABLES

LIST OF ILLUSTRATIONS

COMPOSITE STRUCTURES

By Edwin L. Brown

CONTENTS (Continued)...

LIST OF TABLES

LIST OF ILLUSTRATIONS

GALVANIC FORMING

By L. C. Jackson

CONTENTS (Continued)...

LIST OF ILLUSTRATIONS

VERSATILITY IN ELECTRON BEAM WELDING – A RATIONAL APPROACH

By R. V. Hoppes

LIST OF ILLUSTRATIONS

CONTENTS (Continued)...

QUARTZ GYRO MANUFACTURING AND MEASURING

By John R. Rasquin

LIST OF ILLUSTRATIONS

CONTENTS (Continued). . .

APOLLO 14 COMPOSITE CASTING DEMONSTRATION

By I. C. Yates

LIST OF TABLES

LIST OF ILLUSTRATIONS

CONTENTS (Continued)...

EXPERIMENTAL STUDIES OF MANUFACTURING PROCESSES PERFORMED IN ZERO-G

By Vaughn H. Yost

CONTENTS (Continued)...

LIST OF TABLES

LIST OF ILLUSTRATIONS

CONTENTS (Continued)...

CONTENTS (Continued)...

NEUTRAL BUOYANCY SPACE SIMULATION

By James L. Splawn

LIST OF ILLUSTRATIONS

THE EKG ISOLATOR AND CARDIOTACHOMETER SYSTEM

By Hubert E. Smith

CONTENTS (Continued). . .

LIST OF ILLUSTRATIONS

FREE FLYING TELEOPERATOR

By Herman T. Blaise

LIST OF ILLUSTRATIONS

CONTENTS (Concluded)...

N73-22916

FLAT CONDUCTOR CABLE DEVELOPMENT

By

Ralph Herndon

This paper discusses the Flat Conductor Cable (FCC) development capability presently available at Marshall Space Flight Center's (MSFC) Process Engineering Laboratory for use in space applications. This discussion includes a short history of FCC, a brief examination of the makeup of a typical FCC system, some of the advantages and disadvantages of an FCC system, and some of the past, present, and proposed FCC applications.

The first modern FCC was manufactured approximately 14 years ago by printing and etching using printed circuit methods. Shortly thereafter, FCC's were manufactured in collator type machines. The Tape Cable Corporation and IRC offered the first commercial FCC's. To date, there are at least 30 major manufacturers producing FCC and associated hardware. Many companies, especially aircraft companies, have their own FCC program. Most of these were begun during the past 5 years. The last 2 years have seen tremendous progress in FCC and associated hardware development.

The MSFC FCC program was begun some 14 years ago under the direction of Mr. Wilhelm Angele. The first prototype cables were essentially flexible printed circuits that demonstrated the desirable characteristics of FCC; i.e., time savings in assembly, ease of inspection, and elimination of wiring errors.

A present FCC system is composed of an FCC, plugs and receptacles, circuit change devices, fasteners, support brackets, and transitions for interconnecting FCC to round wires. The basic principle on which the MSFC system is designed is the use of the flat conductors of the cable as a connector contact, which allows a minimum of electrical joints in a connective system.

The standard FCC of MSFC is composed of rolled or slitted flat conductors laminated between two thin films of an insulating material, such as a polyester (Mylar), and bonded with a suitable adhesive, such as polyester or urethane. Figure 1 shows typical rolls of FCC. High temperature FCC has rolled or slitted copper, flat conductors laminated between two layers of a polyimide insulating material (such as Kapton); the layers are bonded with fluorocarbon propropylene (FEP) "Teflon" which serves as additional insulation as well as an adhesive. High density FCC is fabricated by bonding an insulating polyimide material (such as Kapton) to sheet copper stock into which the conductor core configuration is chemically etched. The etched conductor is covered with a layer of FEP Teflon and an additional layer of insulating film material. The power cable is similar to standard FCC except that the conductors are fewer and considerably larger; for example, 2.50×10^{-2} by 11.40×10^{-1} cm (10 by 450 mil). The conductors for each of these types of flat conductor cables may be made of any electrical conductor material, but copper of the rectangular type that conforms to specification MIL-C-55543 is generally used. Another method for manufacturing cable is to weave cables using commercial weaving practices to apply the insulation thread in order to space and securely hold the rectangular, solid conductor in place. The various methods of fabricating FCC are:

1. Printing-etching
2. Vacuum deposition
3. Extrusion
4. Weaving
5. Tower coating-laminating
6. Laminating-collating
7. Combination of the above

It is frequently necessary to use shielded flat conductor cable. FCC is shielded by placing a foil strip on either one or both sides of the flat conductor cable. The shielding may be a material of high electrical conductivity, ferromagnetic metal of high permeability, or both.

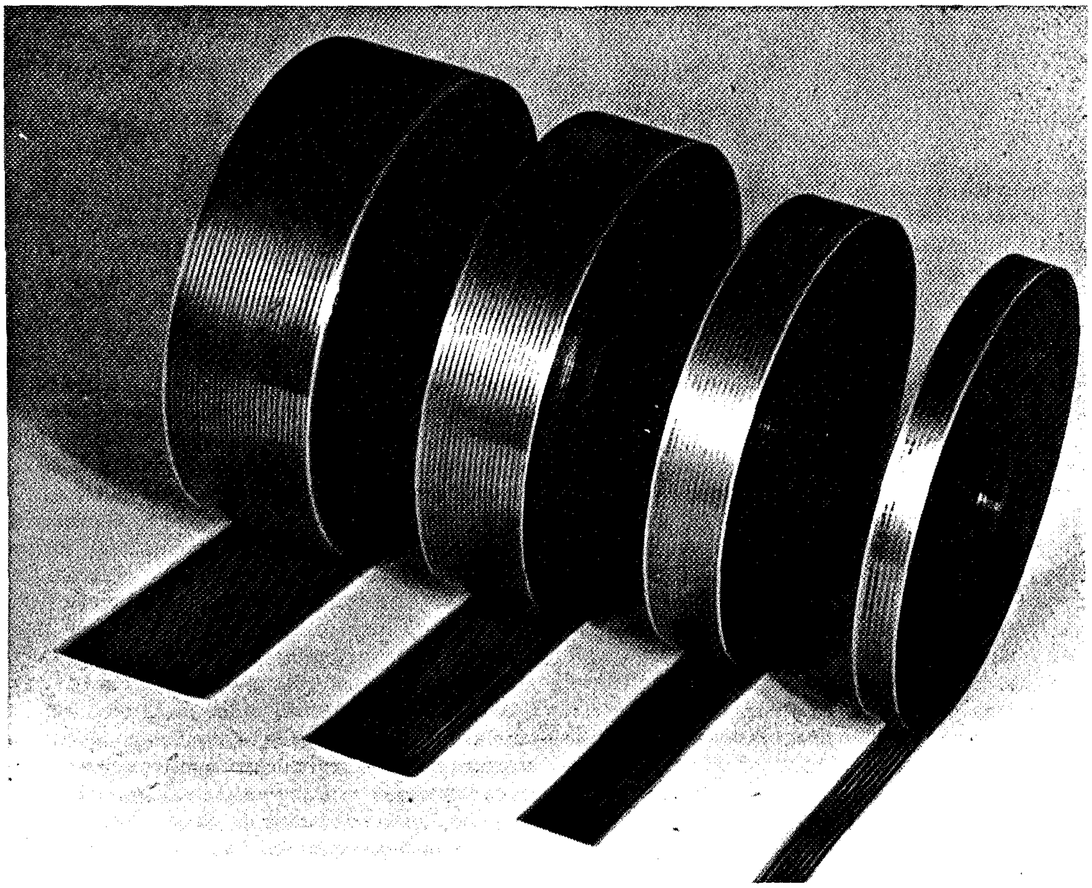

Figure 1. Typical rolls of FCC.

The connectors referred to in this system consist of a rectangular shaped receptacle and matching plug(s). The plugs when assembled become an integral part of the cable and mate with the female portion (receptacle) of the connector. Figures 2 and 3 show cross sections of a receptacle and plug, respectively.

Two types of flat cable connector plugs are used. The first is a molded-on type and the second is assembled from premolded parts. These two types of plugs have two common features; they serve as the male contact for the connector and they have integral polarity keys to prevent reversed insertion.

The FCC receptacles are designed for reliability, simplicity, and light weight. Contact springs for these receptacles are contained in an insert made from high grade dielectric material, such as diallyl phthalate for low temperature (100°C) applications and Fiberite epoxy material for high temperature (200°C) applications. These inserts are sealed around the contact springs to prevent moisture penetration and are placed in an aluminum housing for environmental protection. A gasket serves as a seal between the receptacle housing (shell) and the black box or bulkhead.

Two types and configurations of receptacles have been developed and manufactured. The first type, plug-to-plug, is for receiving a flat conductor cable or a printed circuit board on the secondary side. The second type of receptacle, solder-well, has solder lugs for attaching round wires. Figure 4 shows the types of receptacles that are typical of FCC connectors. These receptacles, varying in size from 2.50 to 7.60 cm (1 to 3 in.), can be used for all types of FCC cables including power cables (cables with wide conductors) without modification. Only bus bars joining the

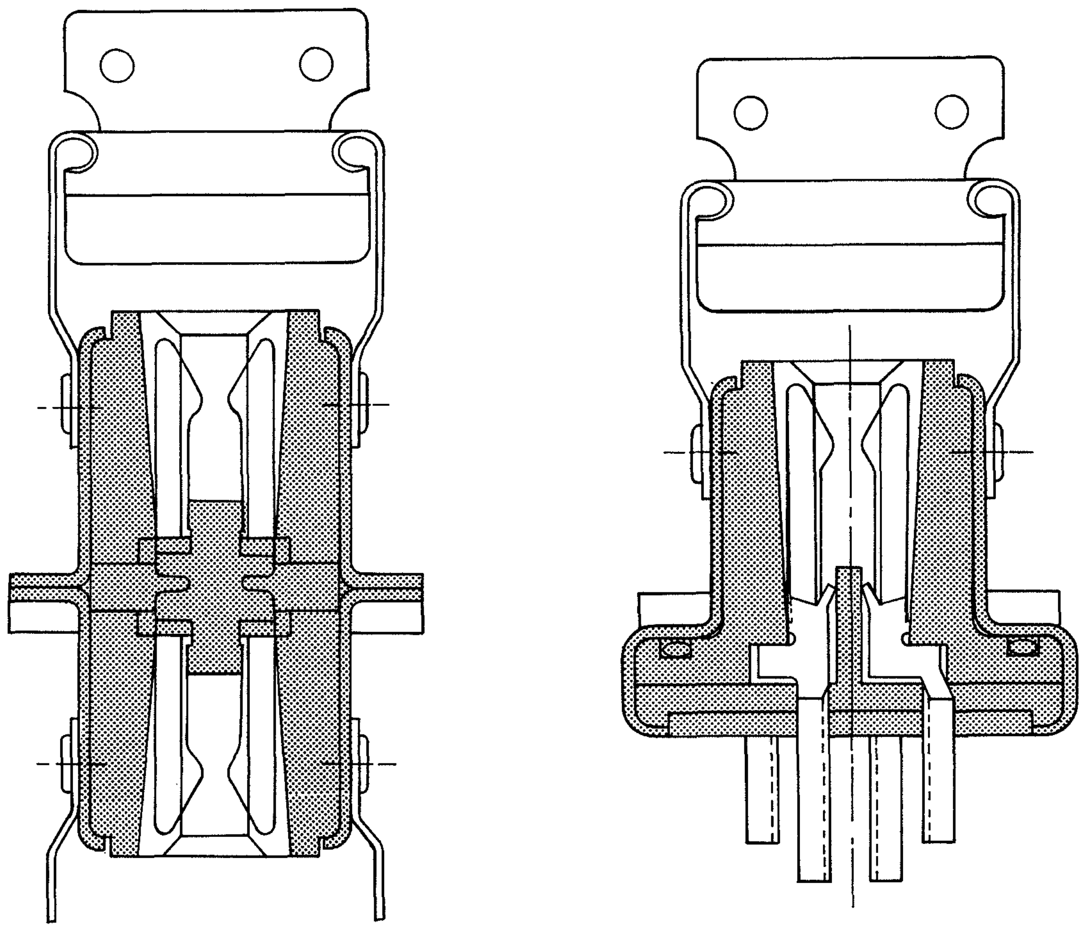

PLUG-PLUG TYPE

PLUG-SOLDER TYPE

Figure 2. Cross sections of FCC receptacles.

solder lugs in the rear of the receptacle need to be added to parallel the contacts for use with power conductors. Specification MIL-C-55544 is used for testing and qualifying these receptacles.

In addition to the basic cable system described above, associated hardware such as cable holddown clamps, pin-function change equipment, and transition pieces for changing from FCC to round wire is available. Space does not permit an elaboration on the types and design characteristics of each item of associated hardware. Figure 5 shows a typical system of FCC as used in the Saturn S-IVB aft skirt study by Douglas Aircraft Corporation.

A number of applications exist illustrating the versatility and advantages that may be achieved using an FCC system. Some of these applications are discussed in the following paragraphs.

- Pegasus Meteoroid-Detection Satellite

The highly successful Pegasus meteoroid-detection satellite (Fig. 6) built by Fairchild-Hiller Corporation, used FCC in two major areas. FCC was the interconnection medium for the deployable detector panel wings, transmitting meteoroid penetration data from the aluminum panels to the instrumentation cannister of the spacecraft.

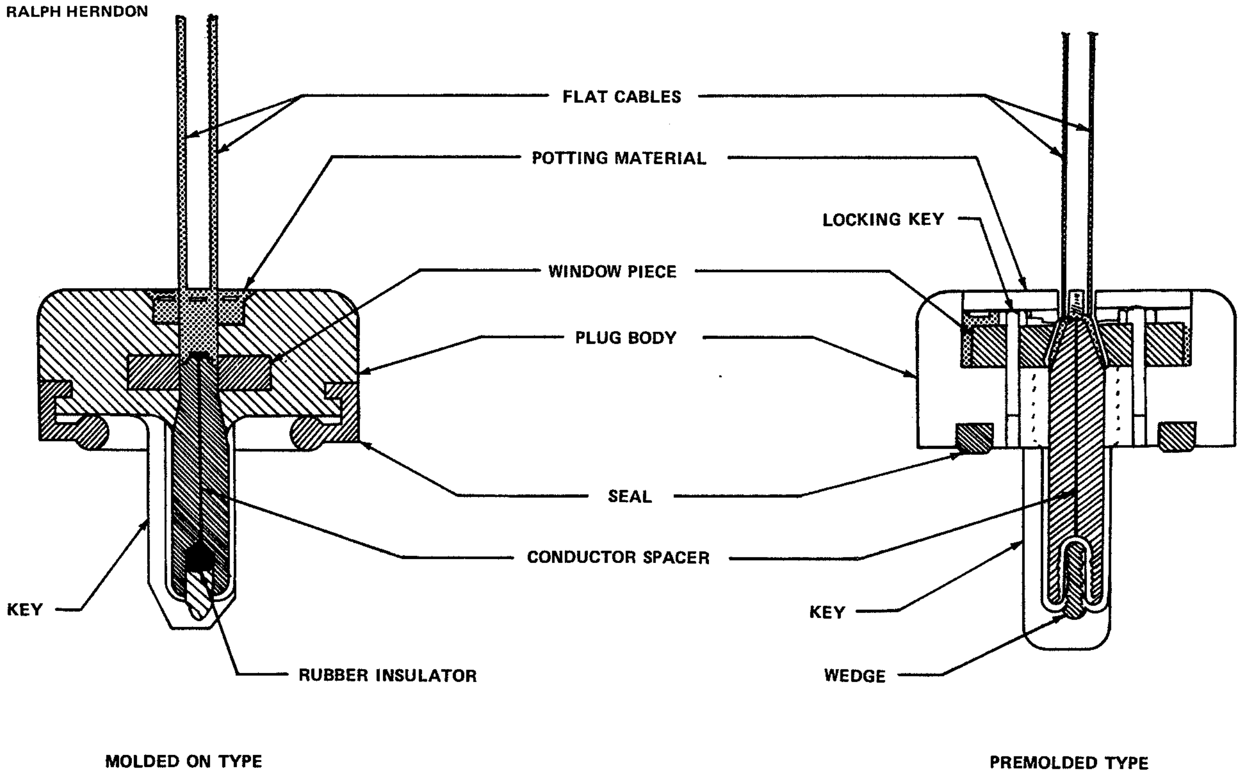

Figure 3. Cross sections of FCC plugs.

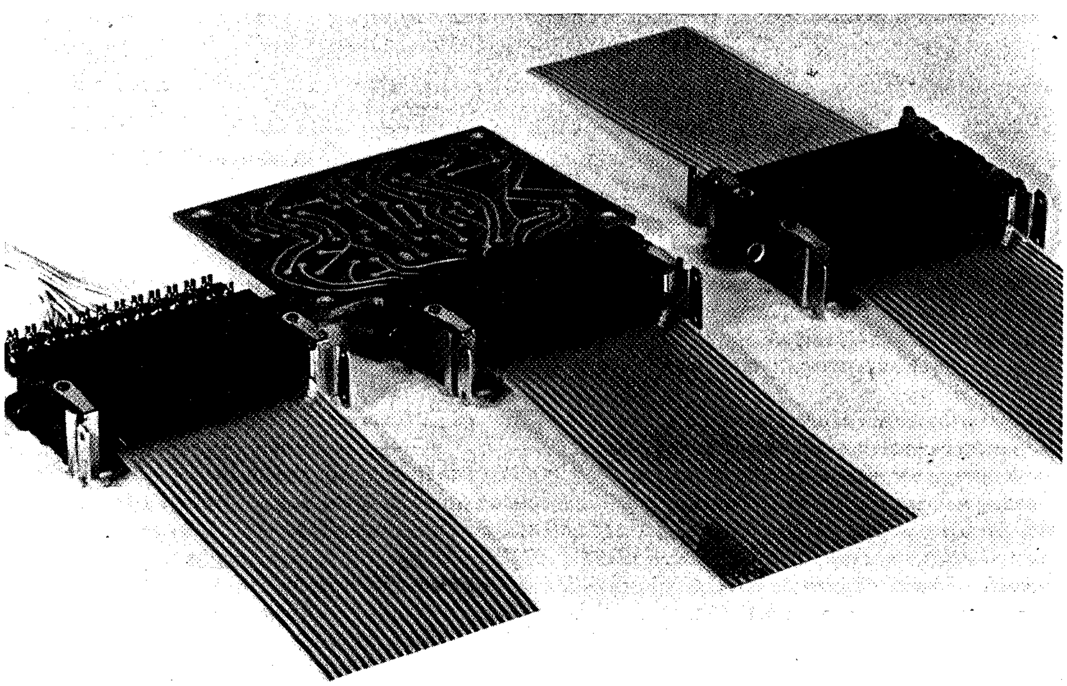

Figure 4. Three types of typical FCC receptacles.

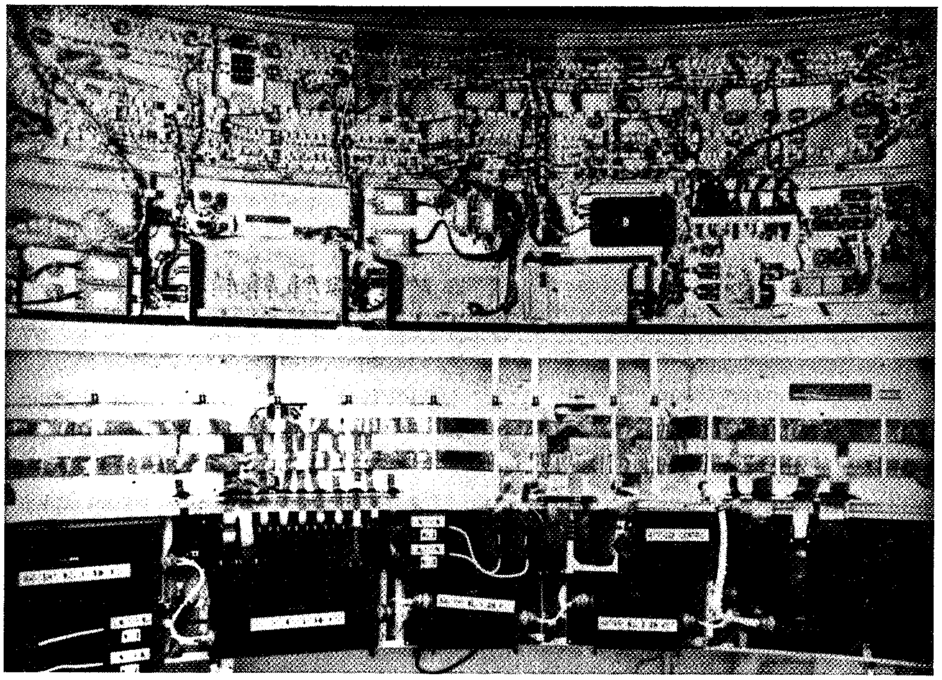

Figure 5. Typical system of FCC used in the Saturn S-IVB aft skirt.

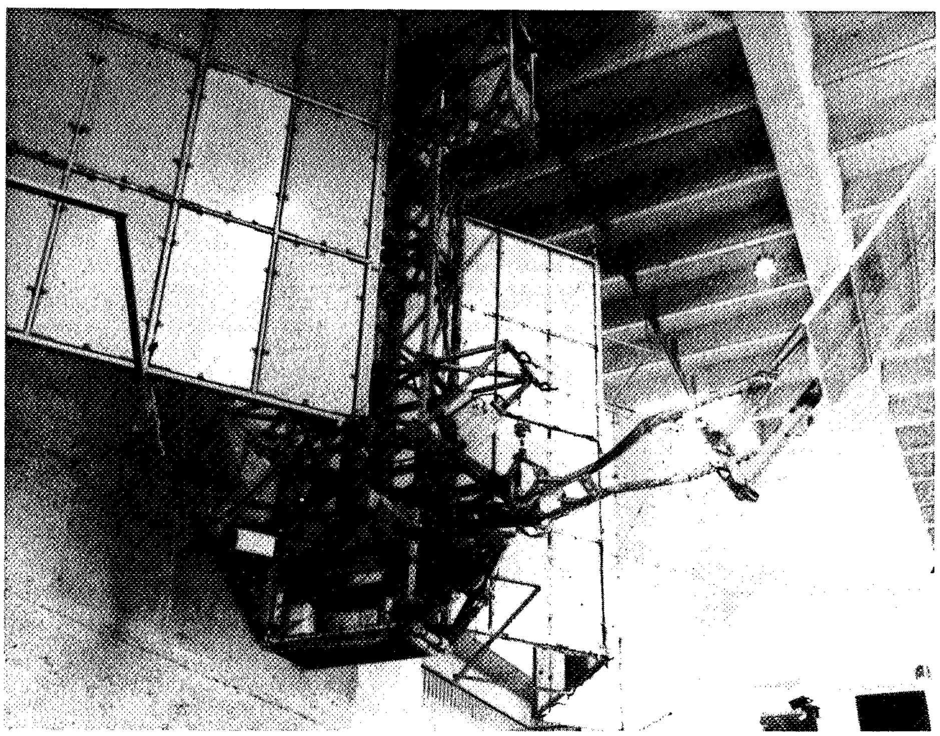

Figure 6. Pegasus meteoroid-detection satellite.

Also, FCC was the link between the cannister and the forward altitude control sensors, as well as the temperature sensors located in the forward solar array.

- Apollo Lunar Surface Experiment Package (ALSEP)

In the original ALSEP system (Fig. 7), Bendix used FCC to connect lunar experimental packages to a central data package. As a later development, the magnetic experiment package was fabricated as a separate portable unit in which FCC linked the sensor head with the remainder of the unit. The ALSEP system consists of instruments designed to provide lunar data in the areas of geophysics, solar wind, atmosphere, and magnetic fields. Portions of this system were left on the moon during the Apollo 12, 14, and 15 missions. Improved versions are planned for missions 16 and 17.

FCC was selected as the interconnecting cable because of the resulting weight reduction from 4.5 kg (10 lb) for conventional wiring to 1.1 kg (2.4 lb) for FCC and the resulting ease in storing and extending the lunar packages up to 18.3 m (60 ft) from the central data package.

- Hughes Lunar Surveyor Landing Craft

FCC constructed for specific electrical characteristic requirements was used to interconnect the electronics and the sensor of the alpha-scattering unit used to analyze the lunar soil. This cable contained 1.00×10^{-2} by 10.20×10^{-2} cm (4 by 40 mil) flat conductors for the temperature sensor and heater, special configuration 0.76×10^{-2} by 2.50×10^{-2} cm (3 by 10 mil) conductors for alpha and proton gates, and 0.76×10^{-2} by 6.40×10^{-2} cm (3 by 25 mil) conductors for proton sensors. Sprayed-on silver paint was used for the shield, and contact was made directly to grounded connectors through prepunched holes in the insulation.

- Apollo Telescope Mount (ATM)

FCC will be used for transferring electrical signals across two interfaces in the torque-sensitive gimbal system of the ATM's 705 unit (caging and gimbal assembly). The ATM, part of the Skylab operation, is being designed and built by NASA-MSFC.

The major reasons for selecting FCC rather than round wire are its reduced weight and volume,

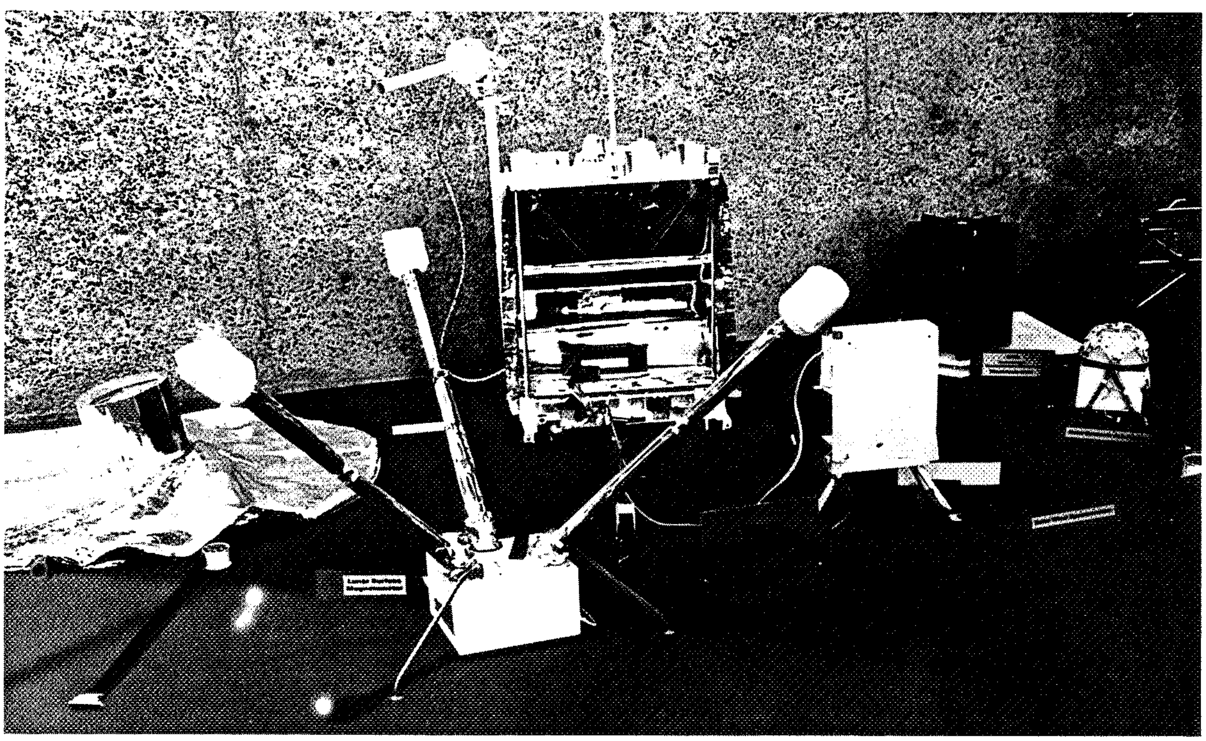

Figure 7. ALSEP system showing the use of FCC.

lower torque requirements, higher density, and greater flexibility. Using FCC, torque reductions of up to 90 percent can be achieved, a critical requirement for proper functioning of the torque-sensitive gimbal system. Because of its high density, FCC can be fitted into the limited space in the cable arch that feeds electrical cable from the roll adaptor to the roll ring of the gimbal system. Redesign of the arch to permit use of the bulkier round wire cable would have necessitated a major revision to the 705 unit. Another desirable feature of FCC is its extreme flexibility, which permits radial motion of ± 120 deg in the roll adaptor with much less power.

Two types of FCC will be used. The 6.4-cm (2.5-in.) signal cable is Kapton-insulated and contains thirty-two 0.76×10^{-2} by 12.7×10^{-2} cm (3 by 50 mil) conductors on 19.0×10^{-2} cm (75 mil) centers. The 6.4-cm (2.5-in.) power cable is also Kapton-insulated and contains eight 0.76×10^{-2} by 62.5×10^{-2} cm (3 by 250 mil) conductors on 76.2×10^{-2} cm (300 mil) centers. About 180 layers of cable and shield will carry a total of 2500 conductors across the two gimbal interfaces to the experiment-containing cannister.

- Lunar Portable Magnetometer (LPM)

The Lunar Portable Magnetometer, part of the ALSEP system, was designed for the purpose of obtaining magnetic field measurements at various locations in the vicinity of the Apollo touchdown point on the moon. Approximately 15.2 m (50 ft) of FCC connects the sensor head (mounted on a tripod) with the electronics and data display assembly. This cable is wound on a spool and can be reeled up when the instrument is not in use (Fig. 8). The LPM was used on the Apollo 14 mission and has been proposed for use on Apollo 16. Figure 9 shows the LPM on the surface of the moon.

Because the magnetometer assembly was intended to be a portable unit, weight and space considerations were of major importance in the selection of FCC over round wire. The flat cable used is Kapton-insulated, 6.4 cm (2.5 in.) wide, and contains thirty-two 0.76×10^{-2} by 12.7×10^{-2} cm (3 by 50 mil) conductors. One end is terminated to an MSFC-type plug and mated with an MSFC receptacle mounted to the electronics box. The opposite end of the FCC is terminated in an MSFC-type transition to 22-AWG round wires which become

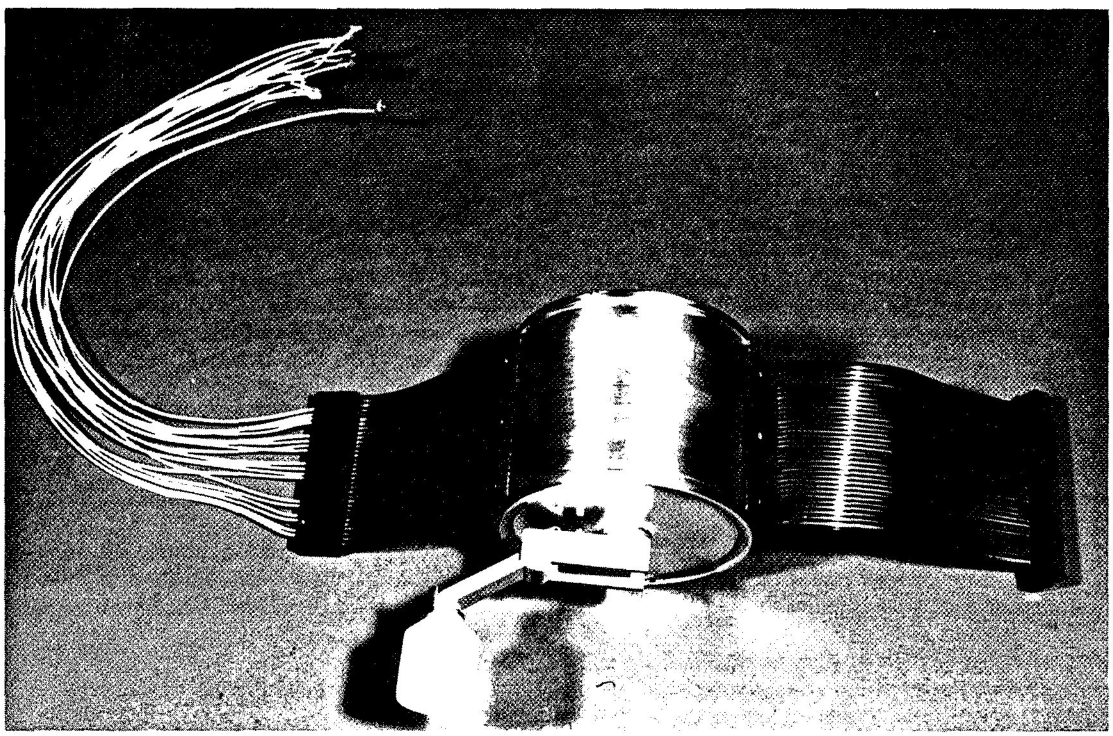

Figure 8. Spool-wound FCC used in the LPM.

Figure 9. LPM on the surface of the moon.

an integral part of the sensor head assembly. The total weight of the cable assembly, connectors, and reel assembly is 1.1 kg (2.5 lb).

- Saturn 201 Instrumentation Unit

An FCC system was used to interconnect one measuring rack with its associated equipment in the successful Saturn 201 instrumentation unit. The instrumentation unit is 6.6 m (21.5 ft) in diameter by 0.9 m (3 ft) long. It generates command signals for the Saturn stages and contains power, instrumentation, guidance, and control circuitry.

The Mylar-insulated FCC used contains 1.0×10^{-2} by 10.2×10^{-2} cm (4 by 40 mil) conductors on 19.0×10^{-2} cm (75 mil) center-to-center spacing. The FCC is terminated in NASA-MSFC direct-contact connectors and in existing round wire connectors.

- Electronic Drawer Reels for Saturn V Ground Support Equipment

FCC interconnect reels were used to facilitate drawer action on the rack-mounted ground support equipment for the Saturn V optical tracking system. The reels allowed drawers to be pulled out and tilted 90 deg up or down while the equipment remained in full operation. Two FCC reels were used for each drawer, with 16 cables per reel. Mylar was used for insulating the 2.50-cm (1-in.) wide cables, and copper shielding was placed between strips where necessary.

- KC-135 Experiment Platform

FCC was used for power distribution and signal transmission in an experiment platform for zero-g testing of the M-512 facility. The M-512 facility, developed by NASA-MSFC, will provide the capability for conducting manufacturing engineering experiments in the Saturn I orbital workshop.

Other applications illustrating the versatility and advantages of an FCC system include the following:

1. Ships Inertial Navigation Systems (SINS)

2. Naval Shipboard Equipment, Librascope — 5.0-cm (2-in.) Mylar insulated FCC was used as the total interconnecting medium in a Naval shipboard electronics equipment design.

3. MK48 Torpedo Fire Control System

4. Research Space Vehicle Program — Digital Sensors Corporation (now a part of Ansley West

Corporation) used FCC in a program distributor unit for a research space vehicle program.

5. Minuteman II Gyro

6. Upstage Guidance Command Unit

7. Spartan Warhead — McDonnell-Douglas Corporation used FCC assemblies on the Spartan vehicle to transmit control and instrumentation signals through the warhead section. Other applications that could be mentioned will soon be covered in a report being prepared by MSFC.

Two proposed FCC applications are discussed in the following.

- Boeing 747 Aircraft

The Boeing Company designed an FCC configuration to meet the requirements of a 61.0-m (200-ft) long, 90 kV-A, three-phase, auxiliary power unit (APU) feeder system used in the 747 commercial transport airplane. FCC was evaluated as part of a continuing effort to achieve greater weight reduction in airplane design. Results of laboratory temperature rise and impedance tests indicated that FCC, with 77 percent of the conductor cross-sectional area of installed round wire, could fulfill the electrical requirements of the 747 APU. (See Figure 10 and Table 1 for further details.)

- Solar Array

NASA-MSFC has accomplished the initial design of the solar array for the Saturn I Orbital Workshop using the low profile and small bend radius characteristics of FCC for power and instrumentation interconnection between the solar cables and power boxes. Figure 11 shows one-third of the wing beam fairing with 3 of the 10 foldout wing panels attached.

Other areas of application of FCC are being studied and placed into practice at the present time. The New York State Urban Housing Development Corporation (state operated) is proposing the use of FCC in low voltage house wiring applications. Through the use of adhesives, FCC could be fastened to prefabricated walls and covered with a special paint that has been developed. This method saves fabrication time and cost. At present the use of FCC for low voltage wall switches and intercom systems, alarm systems, power panels, etc., are being studied for use in 43 000 units per year. High voltage FCC lines are being studied for use in base boards and around door casings.

Some of the advantages of using FCC are as follows.

1. There is a weight savings of up to 70 percent by the collective strength of conductors and by electrically and mechanically stronger installation.

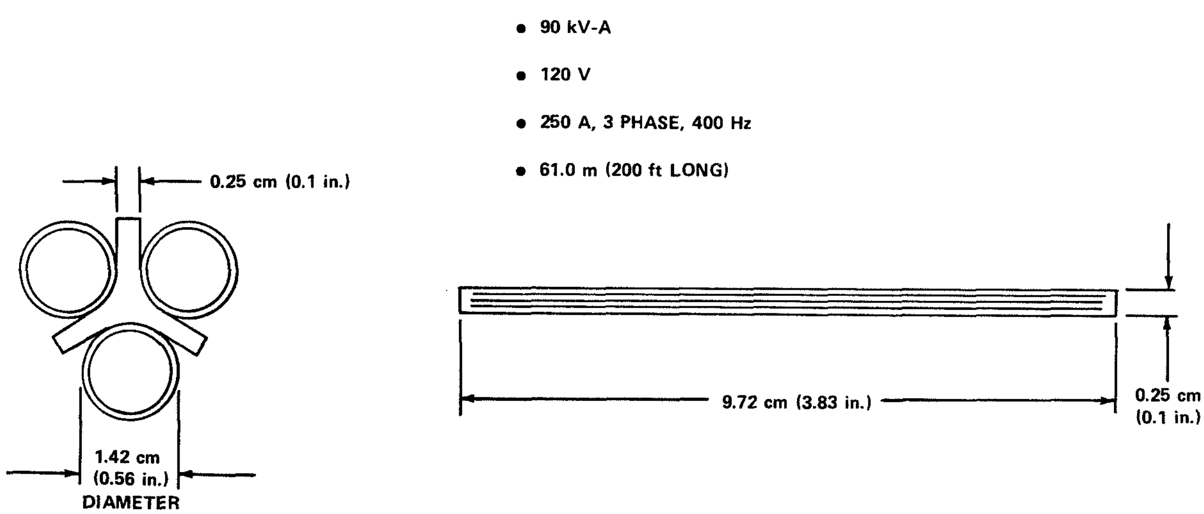

Figure 10. Diagram of FCC power cable for Boeing 747.

TABLE 1. WEIGHT SAVINGS EXAMPLE

Boeing 747 Power Feeder Cable		
61.0 m (200 ft) Long 400 Hz	90 kV-A 120 V	3-Phase 250 A
Round Conductor	Flat Conductor	
AWG 2/0 Aluminum 0.670 cm² (0.104 in.²)	0.060 by 8.40 cm (0.025 by 3.32 in.) Aluminum 0.540 cm² (0.083 in.²), cos $\phi \sim 1$	

	Round Copper	Round Aluminum	Flat Aluminum
Weight	100	46	36
Savings (percent)		54	64

2. There is a typical space savings of 80 percent due to the flatness of FCC.

3. There is a typical cost savings of 80 percent.

4. There is a time savings of up to 80 percent resulting from FCC geometry and tooling for termination, testing, and installation.

5. FCC is simpler to support.

6. FCC has controlled electrical characteristics.

7. FCC has repeatability from unit to unit.

8. FCC has an electric load capacity up to 50 percent higher even in vacuum because of larger surface area and less insulation volume (Fig. 12).

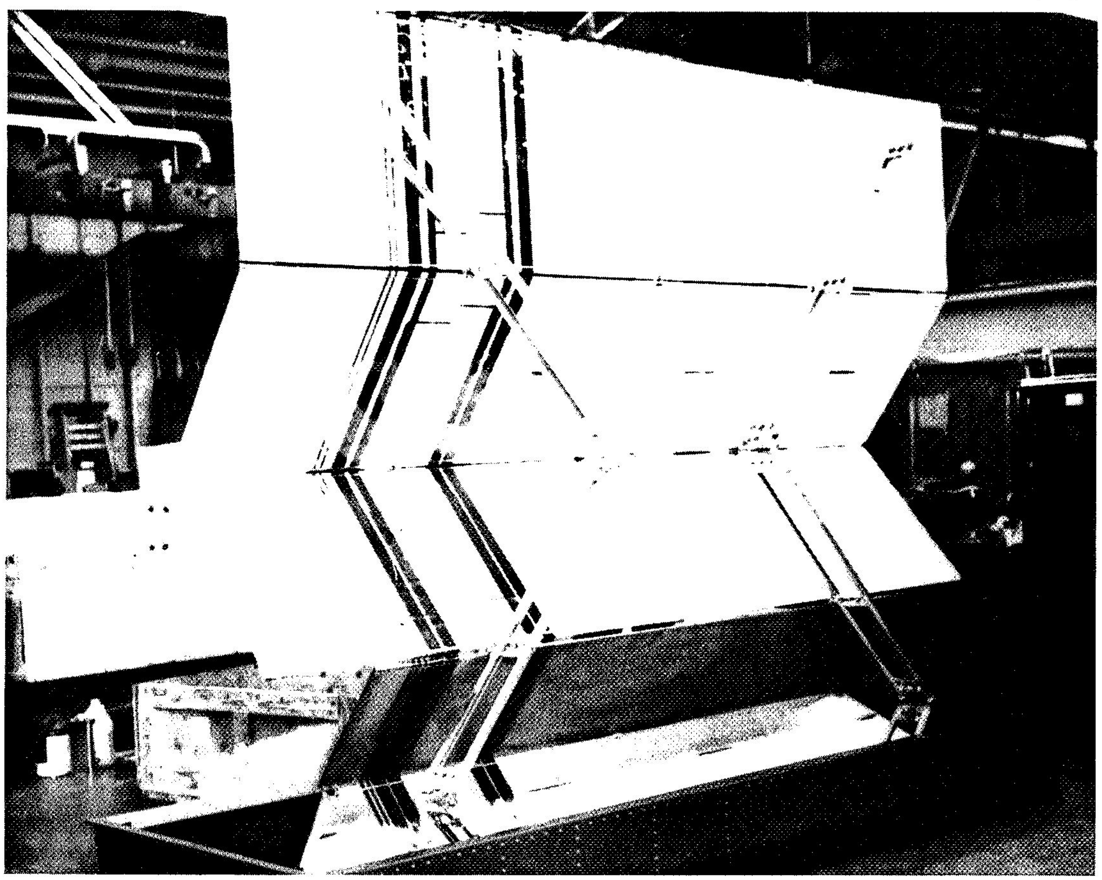

Figure 11. Portion of the wing beam fairing of the solar array for the Saturn I Orbital Workshop.

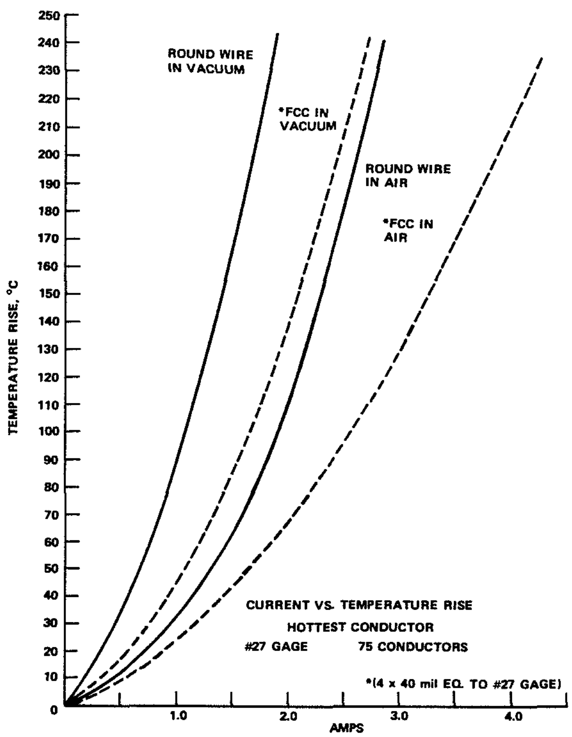

Figure 12. Current versus temperature rise of FCC and round copper wire in air and in vacuum.

9. FCC has a much greater resistance to bending damage.

10. Termination by layer instead of by conductor reduces assembly cost and increases reliability; much less identification is required for individual conductors.

11. FCC eliminates many round wire shielding requirements by controlled location of all conductors.

12. There is greater system flexibility with the use of distributors.

Some of the major FCC disadvantages are as follows:

1. FCC is a new system with fewer developed hardware items, less experience, and less design knowledge available.

2. New engineering, manufacturing, and quality control technology development are required for FCC.

3. FCC requires the use of distributors for more complicated systems.

4. FCC is more difficult to bend in three planes simultaneously without coiling the FCC.

5. Limited tooling is available for use in fabricating FCC systems.

6. Prices for FCC and associated systems hardware is high because of limited production quantities.

Although this discussion has only scratched the surface in considering the uses of FCC, the potential can be seen. Problem areas that seemed insurmountable a few years ago are small today. An FCC mil specification for the Army, Navy, and Air Force has been generated, a much wider variety of termination hardware has been developed, and a more comprehensive use of FCC has been made. These are some of the problems that have been overcome. The future use of FCC in aerospace programs is bright because of the weight, volume, and cost savings that are obtainable.

N73-22917

Preceding page blank

COMPOSITE STRUCTURES

By

Edwin L. Brown

ABSTRACT

A review of the research and development efforts required to assess and develop the technology for application of fiber composites to Space Shuttle structural hardware is presented. This paper covers, in general, the Marshall Space Flight Center (MSFC) research programs in boron-aluminum.

INTRODUCTION

Studies conducted on the Space Shuttle and its missions have resulted in the conclusion that advanced, lightweight, high strength structural materials must be utilized to maximize orbital payload capability. In addition to the payload requirement, the center of gravity is critical because of the number of engines required to meet the objectives of Shuttle missions. Based on these and other factors, it was determined that an extensive effort must be made to reduce structural weight.

The first studies conducted on weight reduction for the Shuttle indicated several areas where boron-epoxy, boron-polyimide, boron-aluminum, and graphite material could be utilized to attain average weight reductions of 30 percent per component. Some studies indicated a net weight reduction of 5 to 9 percent in the structure (Tables 1 and 2).

In view of these facts, MSFC has initiated a program to establish the necessary technology for assessing and applying composite materials for Shuttle structural applications. The potential savings has been evaluated to ascertain the maximum weight advantage with the minimum developmental risk. Boron-epoxy material represents the minimum developmental risk and is the composite that is most nearly state-of-the-art. The 181 kg (400 lb) saved by employing a boron-epoxy thrust structure represents only a limited developmental risk.

BORON-ALUMINUM

Of all of the composites considered for the Shuttle, the most emphasis has been placed on boron-aluminum because of its apparent advantages for thrust structure applications and application to other elevated temperature areas. Yet, the state of development of boron-aluminum is not as advanced as the epoxy matrix composites. Very rapid advances have been made in epoxy matrix composites

TABLE 1. POTENTIAL WEIGHT SAVINGS — SPACE SHUTTLE ORBITER

Component	Present, kg (lb)	Composites, kg (lb)	Weight Savings, kg (lb)	Savings (%)
Engine Thrust Structure	726 (1 600)	544 (1 200)	181 (400)	25
Longerons	454 (1 000)	272 (600)	181 (400)	40
Fuselage Skin-Stringers	4 854 (10 700)	3 629 (8 000)	1 225 (2 700)	25
Frames and Wing Carry-Through	4 536 (10 000)	3 629 (8 000)	907 (2 000)	20
Vertical Tail	1 724 (3 800)	1 225 (2 700)	499 (1 100)	29
Wing	8 119 (17 900)	6 305 (13 900)	1 814 (4 000)	22
Horizontal Tail	2 177 (4 800)	1 678 (3 700)	499 (1 100)	23
Elevator	499 (1 100)	363 (800)	136 (300)	27
TPS Heat Shields	7 076 (15 600)	5 126 (11 300)	1 950 (4 300)	28
TPS Standoff Columns	499 (1 100)	318 (700)	181 (400)	36
Total	30 664 (67 600)	23 089 (50 900)	7 7573 16 700)	25

PRECEDING PAGE BLANK NOT FILMED

TABLE 2. POTENTIAL WEIGHT SAVINGS PER MATERIAL — SPACE SHUTTLE ORBITER

Composite Materials	Component	Component Weight Saving, kg (lb)	Total Material Weight Saving, kg (lb)
Boron-Epoxy	Engine Thrust Structure	181 (400)	181 (400)
Boron-Aluminum	Longerons	181 (400)	2 812 (6 200)
	Fuselage Skin Stringer	1 225 (2 700)	
	Frames and Wing Carry-Through	907 (2 000)	
	Vertical Tail	499 (1 100)	
Boron-Titanium	Wing	1 814 (4 000)	2 540 (5 600)
	Horizontal Tail	499 (1 100)	
	TPS Heat Shields (Side)	227 (500)	
Refractory Wire Super Alloy	Elevator	136 (300)	2 041 (4 500)
	TPS Heat Shields (Bottom)	1 724 (3 800)	
	TPS Standoff Columns	181 (400)	

within the past several months and there are now a considerable number of producers, although each producer prepares his composite in a different and often proprietary process. Some techniques limit the shape of the product, while other techniques are suitable for producing a wide variety of shapes. Prices for these materials vary from \$113/kg (\$250/lb) to \$635/kg (\$1400/lb) based on bulk purchases, but are considerably higher for small quantity purchases.

Most of the boron-aluminum manufactured to date is based on 10.2×10^{-3} cm (4.0 mil) boron fibers and an 1100 aluminum matrix. More recently, to gain transverse strength in the parts, emphasis has shifted to the 14.2×10^{-2} cm (5.6 mil) fiber and alloy matrices such as 6061, which is heat treatable.

The current forecast on the availability of boron-aluminum for use in Shuttle hardware shows that the material will be available in sufficient quantities, but there are some deficiencies that may hinder its use. The cost of boron-aluminum is still too high, and cost-effective studies may rule out its use, whereas otherwise it would be an ideal material. Joining methods are not yet well established for high efficiency joints, and structural tests on fabricated components are very limited. The tests that have been made clearly demonstrate that extreme care must be taken to distribute loads uniformly and in the right direction, since most of the material is used in anisotropic forms with an extremely high ratio between transverse and longitudinal properties. As with other composites, cross-plying can be used in this material, but it is not feasible in many of the shapes being considered.

A weight savings of 181 kg (400 lb) by using a boron-epoxy thrust structure and a savings of 1134 kg (2500 lb) by using boron-aluminum stringers results in a total weight savings of 1315 kg (2900 lb). This is approximately 17 percent of the total potential of 7575 kg (16 700 lb) and is considered an achievable goal. Table 3 and Figure 1 illustrate areas where this weight savings would occur.

BORON-ALUMINUM COMPONENT

In the case of boron-aluminum composites, it was felt that substantial development was required and that this development needed to commence immediately. It was also decided that the quickest way to encounter the problems that would exist in building reliable flight hardware was to build a reasonably large component in the manufacturing area. It was felt that enough of the basic problems had been solved in the laboratory to enable manufacturing to begin.

TABLE 3. COMPOSITES POTENTIAL WEIGHT SAVINGS

Application	Baseline Weight, kg (lb)	Weight Savings with Composites, kg (lb)
Thrust Structure Utilize Boron-Epoxy Over Titanium Thrust Tubes	744 (1 640)	184 (406)
Payload Door Utilize Boron-Aluminum Stiffeners	905 (1 995)	59 (130)
Intermediate Fuselage Frames Utilize Boron-Aluminum Frame Caps	1 851 (4 080)	186 (410)
Shear Panels Utilize Boron-Aluminum Stiffeners	1 452 (3 200)	170 (374)
Wing Skin Stiffeners Utilize Boron-Aluminum Stiffeners	2 116 (4 664)	529 (1 166)
Major Fuselage Frames (Wing Attach, Interconnect Tail Support Frames, etc.) Utilize Boron-Aluminum Frame Caps	3 164 (6 980)	194 (428)
Total	10 232 (22 559)	1 322 (2 914)

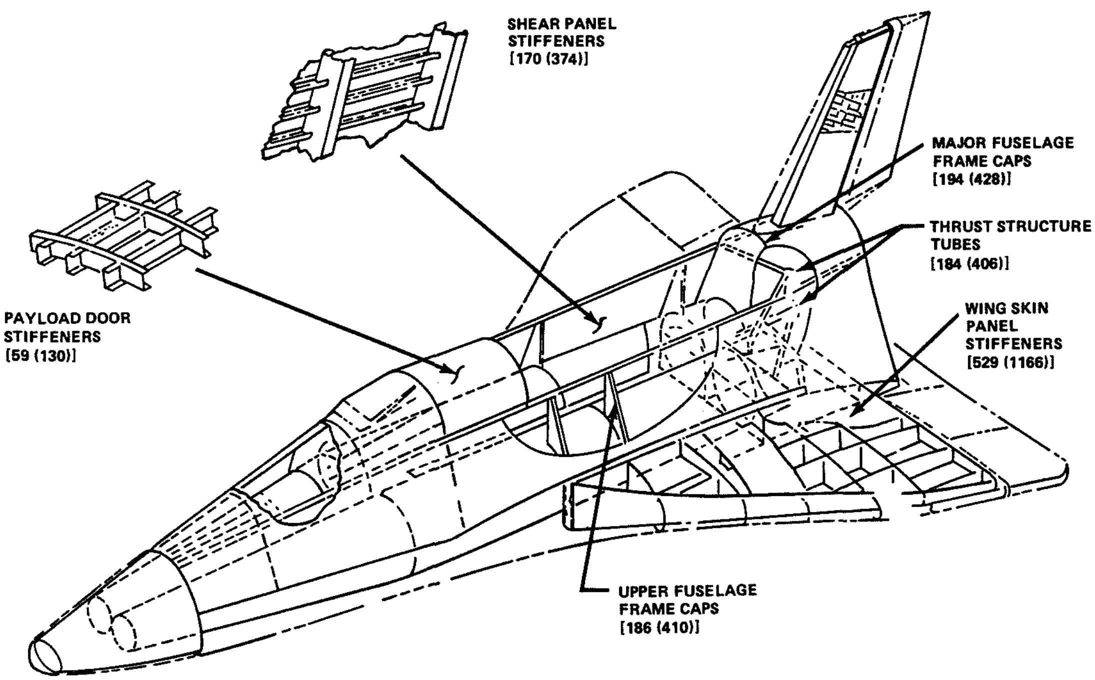

Figure 1. Applications of composite materials for Shuttle Orbiter.

A 10.2 by 12.7 cm (4 by 5 ft) skin stringer component, representative of Shuttle fuselage skin, was selected to be manufactured. This component was of reasonable size and complexity. Thus, a contract was established with McDonnell Douglas Corporation and the program was funded jointly by McDonnell Douglas and NASA, with the larger portion of the funding being borne by McDonnell Douglas.

The schedule for the six tasks in this program is shown in Table 4. Tasks I and II were devoted to developing the process and fabrication techniques in the manufacturing area. Task III consisted of a limited number of element tests to verify the success of processing and fabrication techniques, and to obtain data for the design and analysis of the skin stringer panel. The panel was designed and analyzed during task IV, fabricated during task V, and tested during task VI.

TEST RESULTS

The completed panel is shown in Figure 2. It consists of eleven 24-ply boron-aluminum zee stringers and an 8-ply boron-aluminum ± 45-deg laminate skin. The stringer spacing is 10.85 cm (4.27 in.). Three titanium channel frames are attached to I-beams for testing. Figures 3 and 4 show the panel loading and test setup.

After preliminary compression and shear loadings at room temperature, the panel was tested at 260°C (500°F). It had reached 50-percent compression load and 40-percent shear load when initial failure occurred. The initial failure is believed to have been a local shear failure at the end of a steel filler, which was added to make the panel compatible with the test fixture. The location of this steel filler is shown in Figure 5. A portion of the applied compression load is carried by the steel filler because of compatible strains. Since this filler does not extend to the ends of the panel, the load is introduced into the filler as a high local shear flow. When this is added to the shear flow induced by the applied shear load (Fig. 6), total shear flow in the corner exceeds the allowable shear flow.

The initial failure resulted in an additional compressive load in the adjacent stringer and initiated its failure. When it failed, the next stringer was overloaded and failed, and so on.

TABLE 4. BORON-ALUMINUM STRUCTURE PROGRAM SCHEDULE

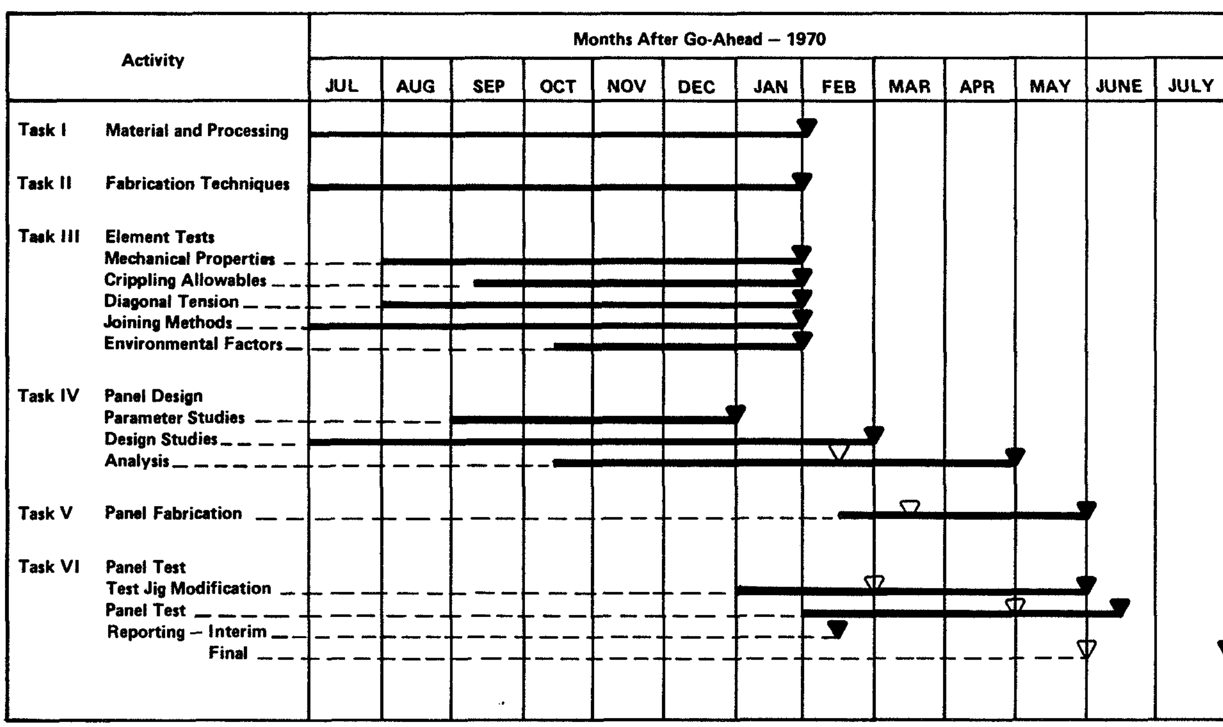

Figure 2. Test panel.

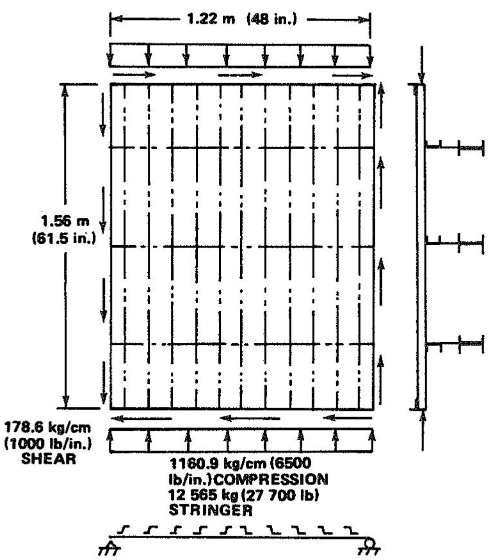

Figure 3. Panel test loading.

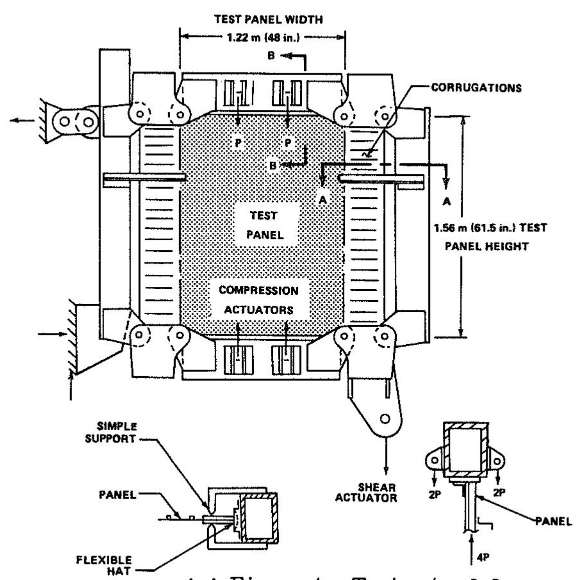

Figure 4. Test setup.

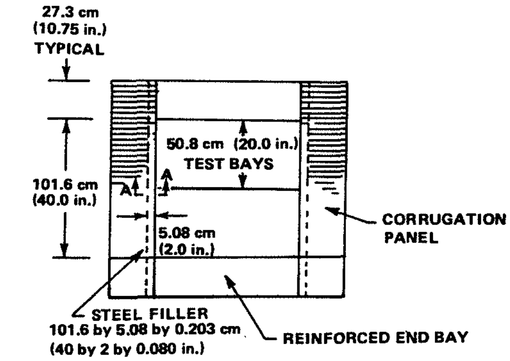

Figure 5. Location of steel filler.

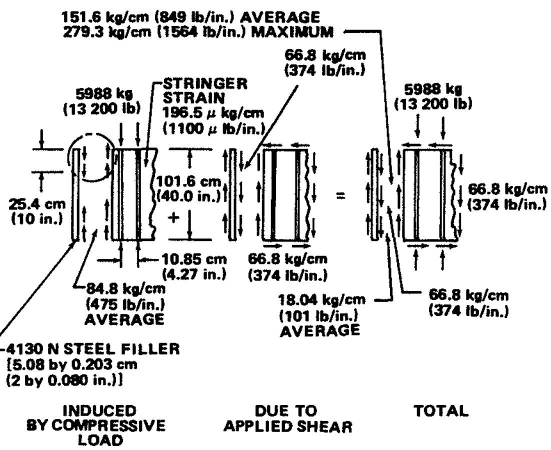

Figure 6. Shear flow at edge of panel.

The additional compressive load in the stringers, however, should not have been sufficient to have caused a failure. Upon investigation, it was determined that there was lateral bending and deflection in the free flange of the stringer. This deflection is resisted by the skin, which results in an induced secondary load in the transverse direction. This transverse stress occurs in the corner of the attached flange, as shown in Figure 7, and exceeds the allowable stress. All failed stringers had a failure in this corner.

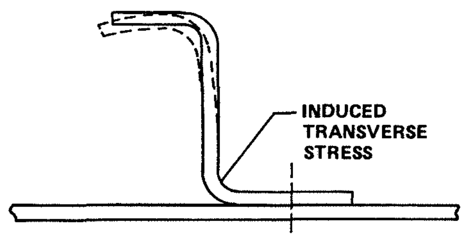

Figure 7. Stringer deflection.

CONCLUSIONS

From these failures we learned the importance of (1) fully understanding what takes place in the composite structure and (2) designing to maximize the advantages of the composite and minimize the limitations.

A steel filler added to a typical aluminum or titanium test panel would probably not have caused a failure because of the forgiving nature of these materials. A boron-aluminum panel, however, with its low elongation, is not capable of much redistribution before failure results. The transverse properties of boron-aluminum need improving. However, since these properties will always be low compared with the longitudinal properties, the design must take this into consideration. Symmetrical stringer designs will minimize lateral deflections and resulting induced loads in the transverse direction.

In conclusion, MSFC has approximately 20 major programs directed toward application of composites for the Shuttle structure, 8 of which are boron-aluminum. No one composite will fill all of the requirements. There is a wide variety of other composites that will probably find structural applications in the Shuttle, including many combinations of fiberglass, phenolic honeycomb, aluminum, epoxy, beryllium, etc. For the most part, these are considered state-of-the-art materials, and many forms of adhesively bonded composites are commercially available. With the weight savings principles to be emphasized in the Shuttle, it is likely that composites of this type will play a very important role.

N73-22918

GALVANIC FORMING

By

L. C. Jackson

ABSTRACT

Complex hardware configurations consisting of items such as small experimental blast nozzles for wind tunnel use, metallic shielding for cable-shape transformation joints, and slit masks utilized in production of thin-film hybrid microcircuits by vacuum evaporation have been produced by galvanic forming techniques.

The techniques developed for fabrication, the availability of new processes that exhibit unusual properties or combinations of properties, and the combination of other processes with galvanic forming to produce unusual results are presented herein.

INTRODUCTION

Galvanic forming, more commonly known as electroforming, may be defined as follows: The formation of items by electrodeposition of metals, alloys, or polymers where the article produced may consist of the item alone (the conductive base being removed) or the item in conjunction with the conductive base; the term galvanic forming is synonomous with electroforming. The practice of the art of electroforming has been utilized for over 50 years in the production of products that have a direct bearing on our everyday lives. Perhaps the most widely used commercial electroforming technique in use today is in the manufacturing of stamping dies used to produce the millions of phonograph records sold daily. The fact that electroforming will reproduce any surface with exact fidelity makes the production of items such as phonograph records possible.

Development work at Marshall Space Flight Center (MSFC) has resulted in articles with even greater dimensional accuracy being produced when the electroforming art was combined with scientific principles, sound engineering judgment, and developed techniques. The first, and perhaps the most unusual, item electroformed at MSFC was a small experimental blast nozzle for use by wind tunnel personnel. The basic schematic for electroforming any article is shown in Figure 1 and Figure 2 depicts the design information for electroforming wind tunnel blast nozzles. Note particularly the requirements for the static tubes in the skirt area and the small diameter throat size.

Basically, the procedure utilized to fabricate the wind tunnel blast nozzle by electroforming was to machine an interior mandrel from aluminum to the required interior tolerances and surface finish, heavy electroform over the aluminum to the design thickness, and selectively etch away the aluminum mandrel leaving the finished part. Personnel having precision machining experience with beryllium on such items as gyroscope hardware were chosen to perform the machining of the mandrels. Difficulty arose immediately when it was discovered that the nozzles with designed throats that were small in diameter did not have sufficient mechanical strength to overcome the torque created by the ball bearing tailstock that exists in conventional lathe equipment. This problem resulted in the mandrel being twisted in the small throat area, and the work had to be discontinued. The problem was solved by fabrication of an air-bearing tailstock center that proved to be virtually friction free and performed exceptionally well. This was the first known application of the air-bearing principle to conventional machining operations.

The selection of material for electroforming was predicated upon the following requirements:

1. Low stress level in the deposit.
2. Physical strength of the deposit.
3. Weldable material (for subsequent fabrication).
4. Ductility of the deposit.
5. Availability of a solution.
6. Solderable (a later requirement).

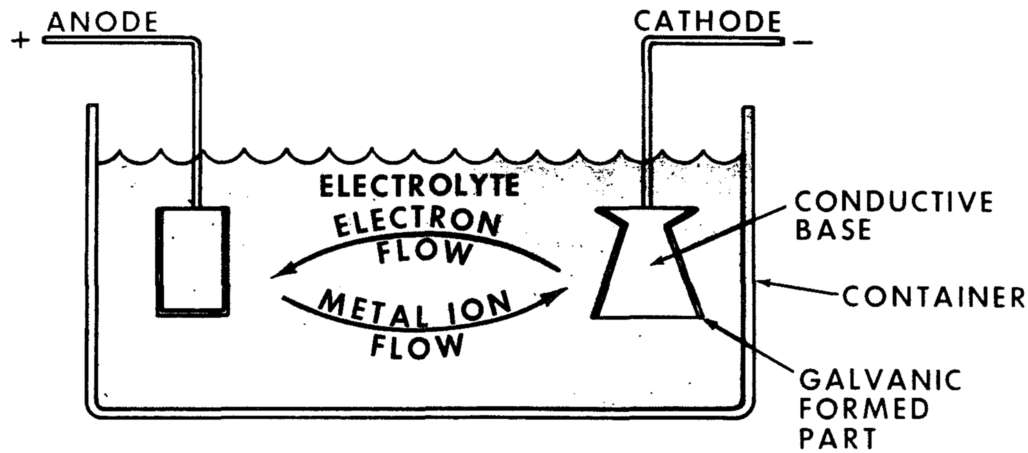

Figure 1. Basic schematic for electroforming.

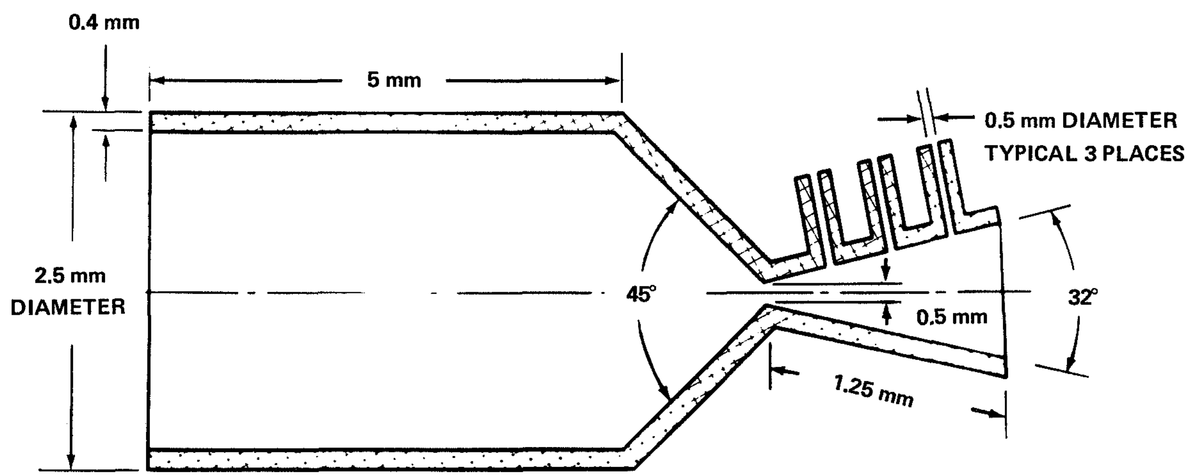

- FABRICATED BY ELECTROFORMING
- MATERIAL-NICKEL (LOW STRESS)
- INTERIOR SURFACE ROUGHNESS 5.08 μcm (2 μin.)

Figure 2. Design information for wind tunnel blast nozzle.

ELECTROFORMING PROCESS

Electroplating The Mandrel

The system selected for electroplating the mandrel that fulfilled all the requirements was a sulfamate-type nickel electroforming bath. The parameter of low stress level was of greatest importance since the electroform that is deposited with highly stressed material is subject to dimensional changes and warpage when the mandrel is removed, thus rendering the item useless. Tests were conducted to determine operating parameters that would produce deposits in the required thickness range with very low tensile or compressive stresses. The parameters of solution temperature and plating current density are the factors that control stress. These factors were investigated by plating one side of an aluminum strip to the design thickness, dissolving away the supporting aluminum, and observing the curling reaction of the unsupported electroplate. Curling or moving the strip away from the original backing indicated tensile stress, while compressive stress was indicated by the reverse action. Ideal zero or near zero stresses were obtained at a solution temperature of 55°C and a current density of 4.2 A/dm^2. It was under these conditions that electroplating the mandrel was performed. It was recognized from experience that in order for the wall thickness to be uniform around the mandrel, the mandrel would have to be slowly rotated since it was impractical to build a circular anode with a perfectly centered electroform. This was accomplished with mandrel rotation about the axis at 12 rpm. A second consideration with regard to thickness uniformity was the anode shape necessary to give proper primary current distribution to the full length of the mandrel. The best shape was determined from experience in electroplating, and by trial of three different shapes of anodes followed by cross-sectioning of samples and measurement of thicknesses.

Hydrogen Bubbles

Once the parameters for operating were determined it was necessary to provide a method for removing formed hydrogen bubbles from the nickel surface and to ensure that the solution contained no foreign particles that would be detrimental to the deposit. Hydrogen bubbles produced in the course of electrodeposition had to be removed to prevent the surface of the electroform from pitting and thus destroying the physical properties as well as the cosmetic appearance.

A discharge velocity of 100 cm/sec through a multiple opening sparger tube located 7 to 9 cm from the sample surface was sufficient to mechanically scrub the hydrogen bubbles from the surface and simultaneously surround the electroform with a cleaned solution that had been filtered through a 10-μm filter immediately prior to impingement of the solution on the work surface.

The area of the surface to be electroformed was calculated mathematically, both for starting the electroform and completion since the area varied with electroform size change. This calculation was required to obtain the correct current density that would give optimum low stress conditions.

Nozzle Throat

The first full thickness electroform was returned to machining for adjustment of length (both nozzle skirt and entry chamber) by cutoff machining. At this point another problem arose when the metal deposited in the V-groove of the nozzle throat was of insufficient strength to withstand the machining stresses even with the air-bearing tailstock. This difficulty was partially a result of the somewhat lower current density and resulting thin electroform in the throat area, but the largest contributing factor was the metallurgical structure of the deposit in the groove or throat area. As expected the electroform developed a natural, folded, parting-line type structure in the columnar deposit normal to the surface around the throat area. This problem was solved before the continuation of electroforming by applying a nickel coating of approximately 0.1 mm to the mandrel; removing the mandrel from the bath; wrapping the throat area with soft solid copper wire (0.3 mm in diameter) until the groove area contained no sharp interior corners; applying a strong stainless steel type solder that bonded the wires to each other and to the electroform; mechanically smoothing down the surface of the high strength solder area; and recleaning and deoxidizing the nickel, solder, and exposed copper wires until the desired thickness calculated in accordance with Faraday's law was obtained. A total tank time of 7.5 hours per electroform was required.

After completion of electroforming, a machining operation to fix the length of the skirt (measured

from the throat area) and entry chamber was performed. These dimensions were calculated from the unplated and masked-off entry chamber end of the mandrel prior to electroforming.

After completion of the cutoff machining operations, a portion of the mandrel core was removed by machining in order to reduce etching time and the amount of material to be etched away in the next operation.

Etching

Etching to remove the aluminum mandrel was accomplished in a 25-percent volume of hydrochloric acid beginning at ambient temperature. This etchant was chosen because of its speed, which is greatly accelerated by exothermic reaction, in removing aluminum. The etchant is ideally suited for this purpose since the essentially pure nickel electroform is not affected by the etchant.

The final operation before delivery to the customer was to mechanically polish away etching residues with 10 000 grit cloth to expose the pure bright nickel surfaces.

BLAST NOZZLES PRODUCED

The techniques presented were used to produce 24 experimental blast nozzles with throat diameters varying from 0.5 mm to 1.25 mm. In addition, one nozzle was produced that incorporated three 0.5-mm diameter static tubes in the skirt area. The nozzle with three static tubes was fabricated in the same manner as the other nozzles except that three pieces of 0.5-mm diameter aluminum wire were attached to the mandrel portion of the skirt by drilling holes of the same diameter in the mandrel normal to the surface and inserting the wires. Electroforming, wire wrapping, soldering, and further electroforming followed. A savings of $9000 on this single order of nozzles was realized by using the electroforming technique and MSFC developments instead of fabricating using machining techniques alone.

Another item that has been produced successfully by electroforming is a copper shield for use in a cable transformation joint. Details of this item are shown in Figure 3. A total of 100 of these shields with 4-mm thick copper walls was required. Because of the physical size and shape of the shield and the quantity requirement, it was impractical, if not

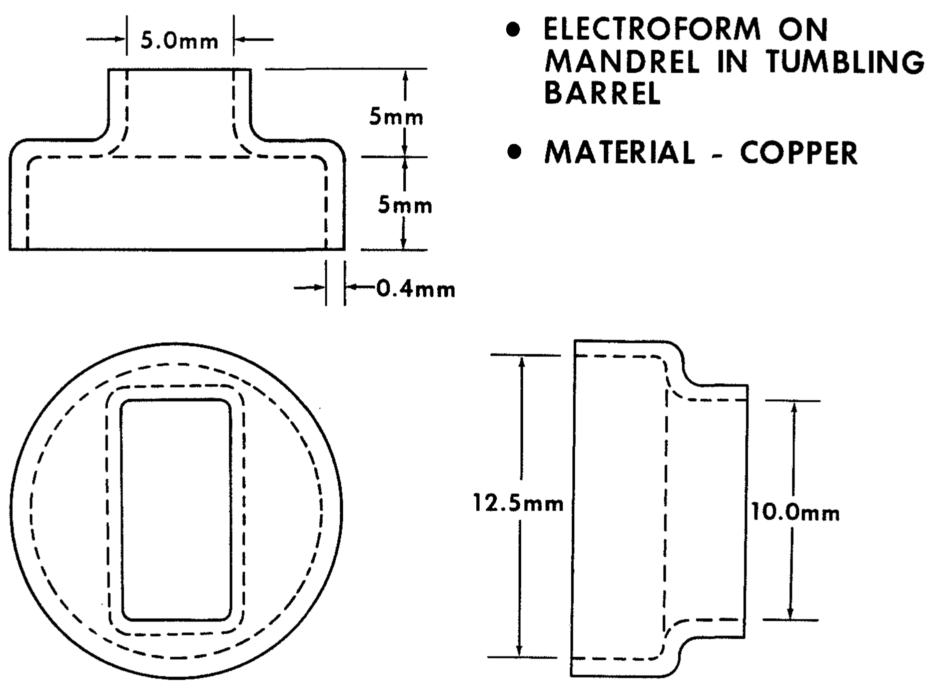

Figure 3. Cable transformation shield.

impossible, to design conforming anodes for the electroforming operation and to rotate the part as was done previously. This problem was solved by applying a thin (0.01 mm) strike coating of copper to the aluminum mandrel and using rack electroplating techniques. After the electroplated aluminum parts were removed from the rack, the thin copper-coated aluminum parts were transferred to a horizontal electroplating barrel, cleaned and deoxidized, and transferred to the selected copper plating bath for buildup to the desired 4-mm wall thickness. The theoretical thickness was calculated using Faraday's law. Ends were machined off before dissolving the mandrel material.

The technique of barrel electroforming is considered a new development since no mention of the technique has ever appeared in trade literature. The concept of continuously rotating and moving the electroform in a random manner to eliminate the primary electrical field effect, which is the primary factor in producing uneven thickness buildup, is the principle upon which this technique is based. An added advantage of barrel electroforming is the mechanical movement and scrubbing that removes the ever-present hydrogen bubbles on the work surface.

EVAPORATION MASKS

The utilization of electroforming and graphic arts techniques for fabricating accurate metallic masks used in the production of hybrid microelectronic thin-film circuits has been accomplished. Details of some of the more pertinent dimensions of a thin-film hybrid microcircuit evaporation mask are shown in Figure 4. Note particularly the 0.1-mm fine lines, which are used for depositing thin-film resistors, and the required tolerance of ± 0.005 mm. This tolerance is one of the parameters for determining resistance value of a given line in the hybrid circuit, and it must be held within the stated tolerances to give the various resistors the designed value and tolerance.

The type of evaporation masks manufactured by the electroforming technique are called bimetallic masks because of the use of a second metal to give mechanical strength to the thin electroform. Figure 5, which is self-explanatory, shows an enlarged cross-sectional view of a bimetallic mask during various stages of manufacturing. To produce bimetallic masks, techniques had to be developed for achieving ultimate thickness in the liquid-applied photosensitive resist and a base material that was compatible with the electroformed metal and capable of being selectively removed without damage to the electroform had to be selected.

The technique used for achieving a thick film of photosensitive resist consisted of alternate spray coating and drying to obtain films of various thicknesses. It was found that the maximum usable resist film thickness obtainable was approximately 0.002 mm. Thicknesses of photosensitive resist greater than 0.002 mm tended to distort and slide off the copper surface during the developing process; therefore, thicker film could not be used. Thicknesses of photosensitive resist less than 0.002 mm reduced the electroform thickness and made the mask even more fragile.

NEW FIELDS IN ELECTROFORMING

A sheet film photosensitive resist will be available soon as an MSFC capability. This new material is capable of producing photosensitive resist images up to approximately 0.25 mm thick, which opens new fields in electroforming. Using this new material, thin details can be produced directly from a line drawing by the photoelectroforming process.

To date, work at MSFC has consisted of the use of chemically dissolvable mandrels only. Electroforming is not limited in this respect because mandrel materials, such as aluminum, may be classified as expendable. Other expendable mandrel materials include low melting alloys that do not alloy with the electroform; plastics from which the deposit can be peeled or the plastic removed by thermal, chemical, and/or vacuum techniques; and even wood which can be burned away. Bags, shoes, and cases fabricated from a man-made material embossed by an electroform whose master mandrel was an alligator or reptile skin are commercially available. Resuable mandrels usually consist of metals that have hard-to-remove oxides on the surface. Such metals include stainless steels, nickel, or other high nickel alloys. In this instance the oxide barrier layer prevents the electroform from adhering tightly. Many of these type mandrels are collapsible and consist of two or more parts for easy removal.

Electroforming techniques are presently being used in the formation of large rocket engine thrust chamber liners.

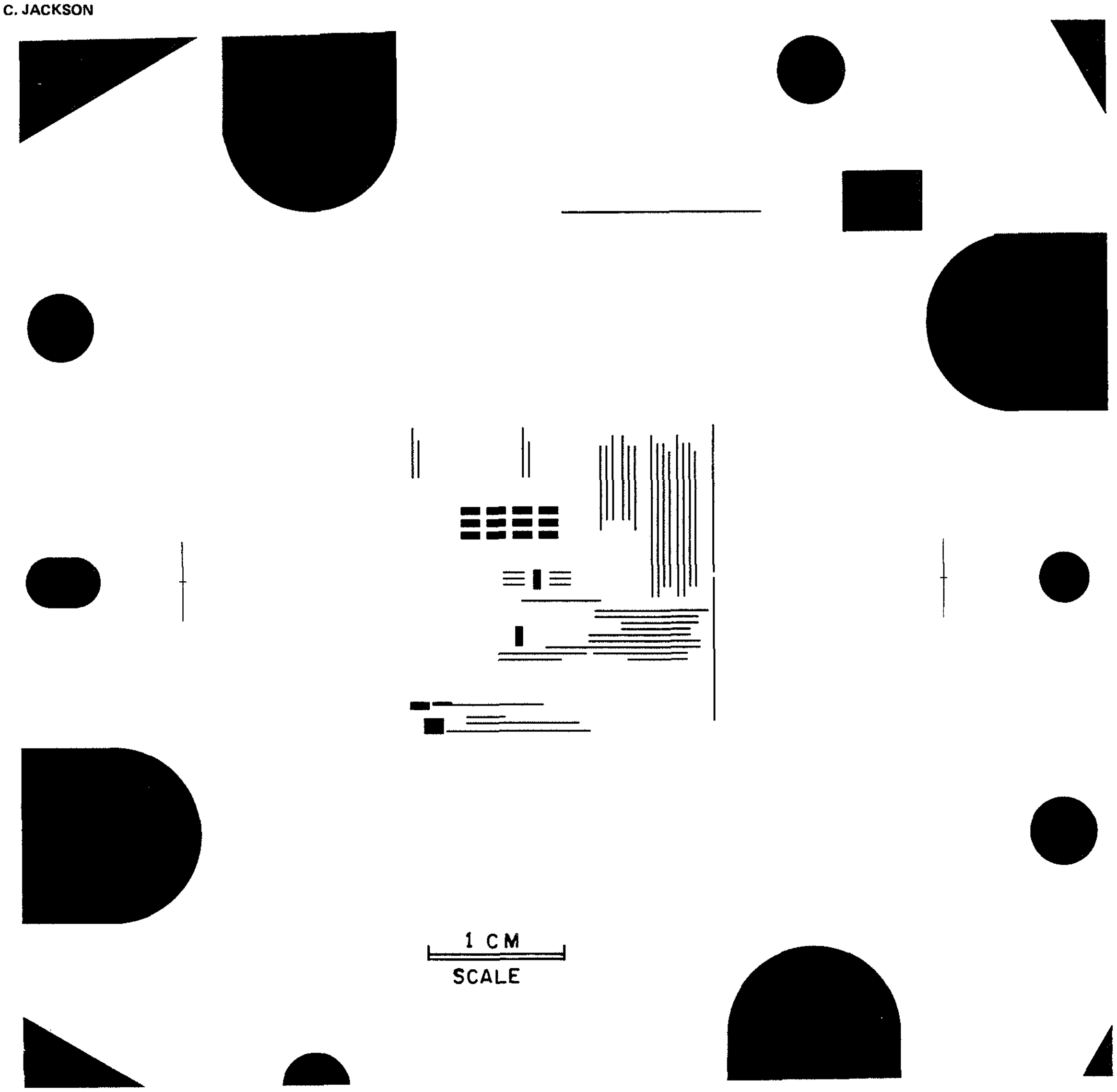

Figure 4. Hybrid microcircuit evaporation mask.

CONCLUSION

A wide variety of materials is presently available to the designer for the fabrication of electroformed articles. Included in these materials are deposits that exhibit high tensile strength, high modulus of elasticity, and high elongation before rupture. In addition, electroformable metals and alloys are available that exhibit low melting points, pleasing cosmetic appearance, high heat resistance, magnetic properties for memory uses, and many other physical attributes. Added to this is the capability of reinforcement with such materials as boron or glass fiber, particle inclusion doping capability with such materials as diamond or boron, and the ability to form composites with post-thermally-diffused coatings of various electroformed metal layers.

By utilization of the electroforming art and the application of sound scientific principles using the latest available materials and process technologies, the designer has available a precision tool for fabrication of complex designed details with the most desirable properties.

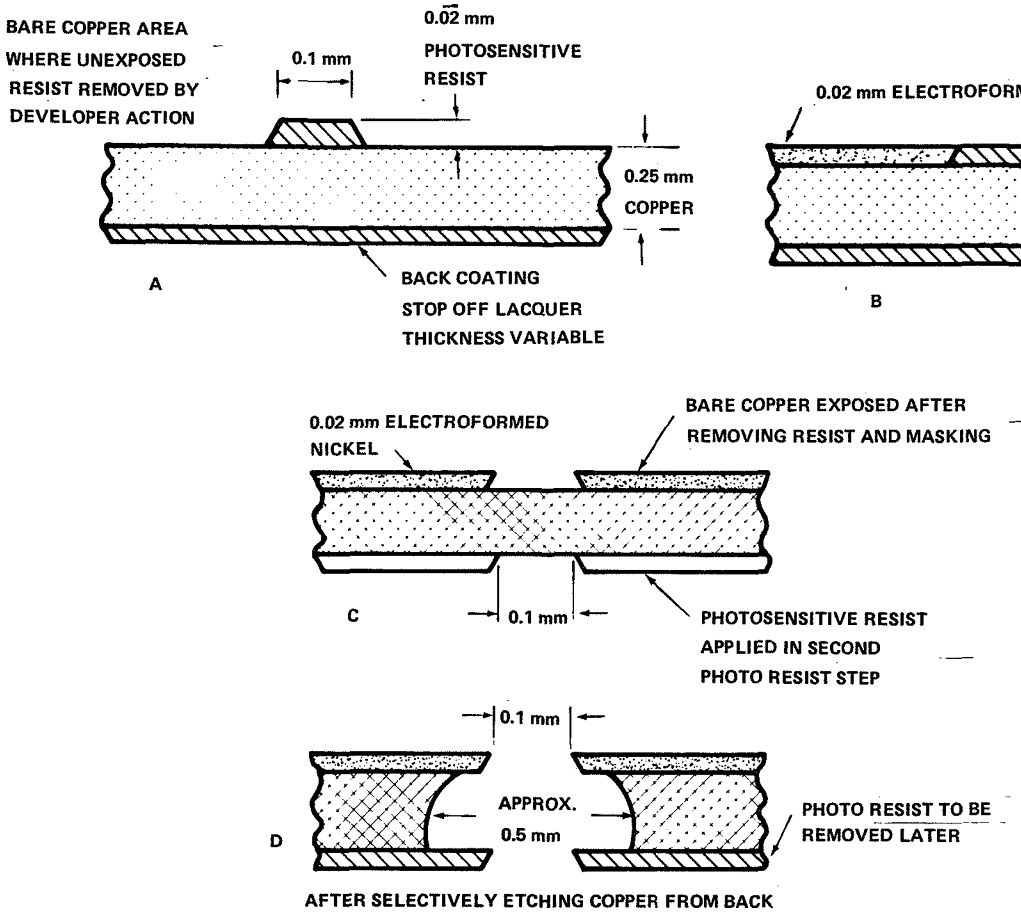

Figure 5. Bimetallic hybrid circuit evaporation mask.

N73-22919

Preceding page blank

VERSATILITY IN ELECTRON BEAM WELDING—A RATIONAL APPROACH

By

R. V. Hoppes

ABSTRACT

Electron beam welding is a low energy process that causes the least reorganization of material. Its use is limited by the vacuum chamber requirement. Three steps have been taken to increase electron beam versatility: (1) a split chamber; (2) a local moving chamber; and (3) a nonvacuum system.

In space, electron beam welding will be highly versatile and will constitute the first metals-joining experiment outside the earth's atmosphere and gravity.

INTRODUCTION

One of the most challenging and exciting material-joining processes is the electron beam (EB) system. It is challenging in the sense that many limitations must be overcome or minimized before the process is as practical and versatile as the more common modes, such as the tungsten inert gas (TIG) process. It is exciting in the sense that electron beam welds most nearly approach the structure and strength of the surrounding sound parent material. Although most EB welding work at MSFC has involved the use of aluminum, this process shows promise of being the most versatile of all welding processes in regard to type of material and material thickness. Beginning with an account of MSFC experiences in aluminum welding, an approach to and present status of EB versatility at MSFC and a discussion of EB welding in areas outside the earth's atmosphere are presented herein.

SIGNIFICANCE OF ELECTRON BEAM WELDING

Welding requires intense heat in localized areas, which locally reorganizes the material structure. The objective of welding research is to control the degree of material reorganization. Most EB welding work at MSFC has involved the use of aluminum. The material reorganization process is as follows: (1) a change in metallurgical structure occurs; (2) there is a reduction in density or cross section; and (3) residual stresses and distortion occur. Because these areas are so interdependent, it is possible to plan a complex of studies that are also interrelated. The strength of a weld depends on its structure, density, and stress pattern.

Because heat in some span of time results in the degradation of material, it is necessary to select time-temperature relationships by which the effect of welding processes on metals can be measured. Time-temperature relationships mean the peak temperature and the time above normal temperature that adversely affect a material. Such gradients can be correlated with the responses, microstructure, porosity, and stress (Fig. 1).

Isotherms are directly related to material response and to the energy concentration, or power density, of a welding process. Of all the "practical" modes of materials joining, an electron beam is capable of the greatest concentration of energy and consequently the most localized excitation of

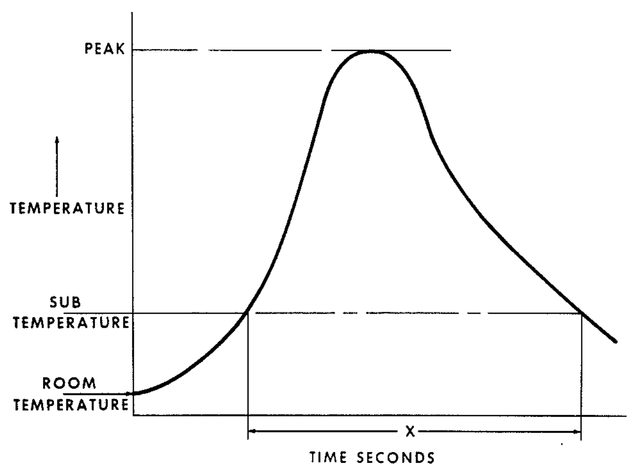

Figure 1. Time-temperature characteristics curve.

PRECEDING PAGE BLANK NOT FILMED

material. High energy concentration means narrow heat-affected zones and less material reorganization, which results in greater strength and less time for gas pores to "grow," and less metal movement and distortion. This is clearly seen in 2219 aluminum welds (Fig. 2).

Levels of energy, expressed as joules per centimeter of travel per centimeter of material thickness, or joules/cm^2 (joules/in.^{2}), result in corresponding levels of strength. Thus, 258 000 to 645 000 J/cm^2 (40 000 to 100 000 J/in.^{2}) show a plateau of 2600 × 10^5 to 2900 × 10^5 N/m^2 (37 500 to 42 000 psi) ultimate strength. As joules decrease, strength rises sharply; 64 500 J/cm^2 (10 000 J/in.^{2}) produce strengths as high as 3900 × 10^5 N/m^2 (57 000 psi). Aluminum 2219-T87 base metal has a strength of 4800 × 10^5 N/m^2 (69 000 psi). About 690 × 10^5 N/m^2 (10 000 psi) of this strength is a result of strain hardening. The unstrained condition, T-62, is listed at 4100 × 10^5 N/m^2 (59 000 psi), which was almost reached in electron beam welds of 64 500 J/cm^2 (10 000 J/in.^{2}).

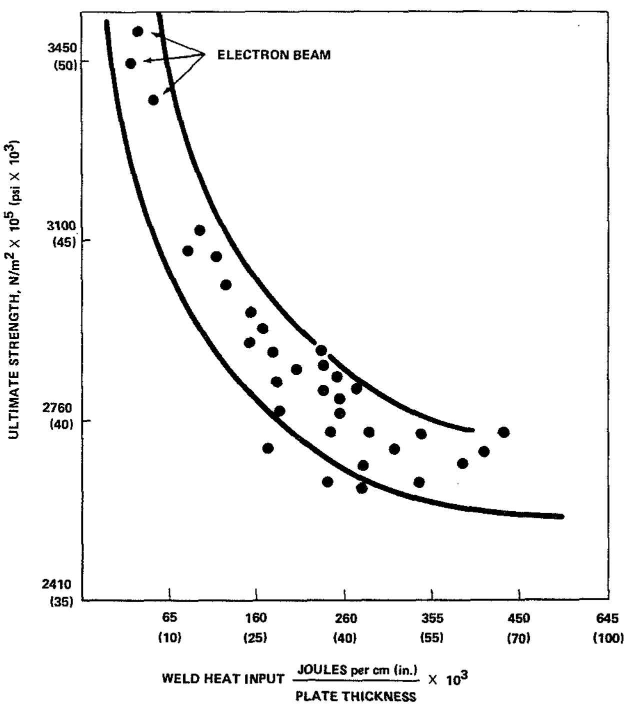

Figure 2. Relation of weld heat input to ultimate tensile strength of 2219 aluminum alloy

The effect of energy concentration is also seen metallurgically (Fig. 3). As joules decrease, there is a decrease in grain size and in copper aluminide agglomeration (Θ) at the grain boundaries. The strength versus energy curve has a steep slope from 193 500 to 64 500 J/cm^2 (30 000 to 10 000 J/in.^{2}). Perhaps this is related to a marked decrease in the excess energy over that required for activation of copper migration, but metallurgy alone may not give a complete explanation of the energy-strength relationship. Width of weld nugget, if flush, also correlates with strength. Both weld geometry and metallurgy are to a great extent determined by the amount of welding energy and, thus, indirectly by the arc power density.

In regard to porosity, the IIT Research Institute has recently completed an outstanding laboratory study of the weld defect potentials of contaminants on aluminum surfaces [1]. They conclude that the nearly zero-defect method of preweld preparation is simply metal removal. Aluminum surfaces are scraped or machined just before parts are jigged. Since many hours elapse between the start of jigging and the welding of large components, extreme care must be taken to avoid recontaminating the material. However, there is no means of measuring the quantity of recontamination, so again energy concentration comes to the rescue.

IIT Research Institute has shown in another excellent study that a long solidification time allows gas to escape from a weld puddle; a short solidification time does not allow gas pores to grow. Tests at MSFC have confirmed this work (Fig. 4). As the welding travel speed is increased (with less energy input), the porosity frequency drops and the porosity size decreases, which suggests that porosity is arrested in its formation. At some level of reduced time-temperature, porosity should be entirely stopped, or at least so finely dispersed that it would not be discernible. Just what microporosity has to do with joint performance has not been clearly defined. If the ultimate strength of aluminum welds is directly proportional to the cross-sectional area in the plane of fracture, it is conceivable that a great number of micropores would be as detrimental as a few large pores.

Distortion and metal movement during welding are directly related to material rigidity and width

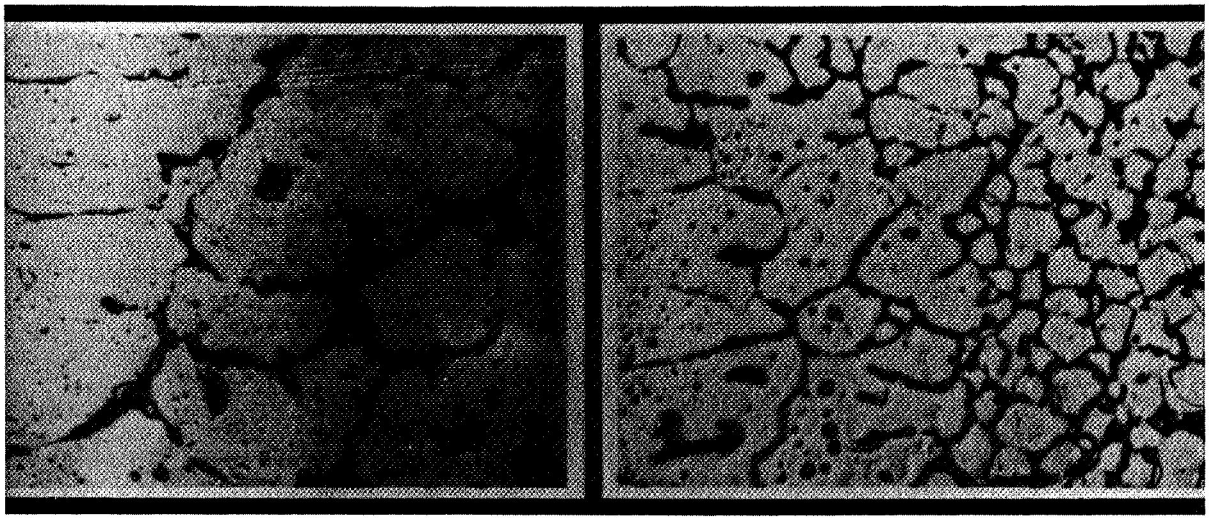

516 000 JOULES/cm^2 (80 000 JOULES/in.^{2}) 20 000 JOULES/m^2

1000 X FUSION TIME 1000 X FUSION TIME

Figure 3. Aluminum 2219 microstructure versus energy.

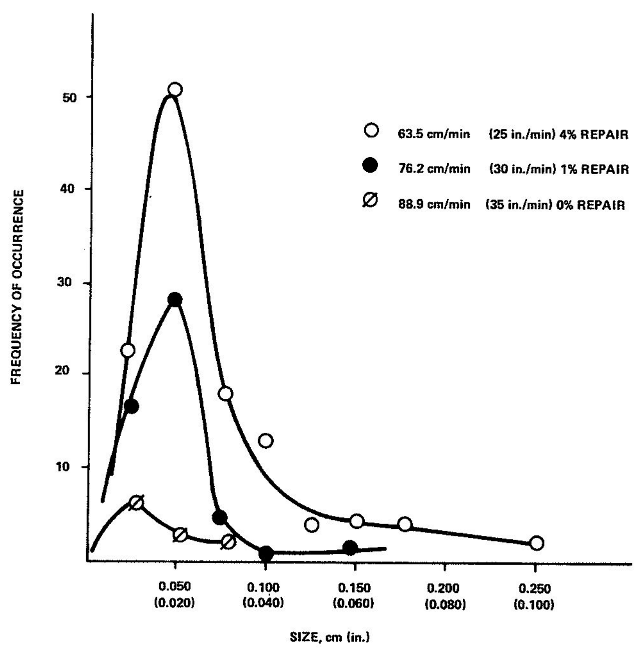

Figure 4. Frequency of occurrence of weld defects versus size.

of heat zone. Rigidity is a design factor, but the heat zone is a function of time-temperature relations. Dr. Masubuchi of Battelle Institute [2] has formulated several computer programs, one of which predicts welding isotherms when given the energy input and travel speed. A second program predicts the dynamic stress pattern while knowing the isotherms and the changing yield strength of the material. From such data, engineers can predict the critical rigidity or the critical heat zone width at which local buckling of a material may occur. Obviously, this knowledge is useful in product design and in the choice and use of joining processes.

Little analysis has been made of dynamic stress and movement of a plate during welding. The movement is quite complex and difficult to visualize from two-dimensional graphs; it is so difficult, in fact, that MSFC made an animated cartoon of the movement of a 0.64-cm (0.25-in.) thick aluminum plate while making a weld bead at about 30.5 cm/min (12 in./min). Four dial indicators on each side of the weld line at four stations were photographed at 5-sec intervals. From these measurements of metal movement toward and away from the torch, an animated cartoon was constructed. The movement was magnified so that 0.64 cm (0.25 in.) equaled 10.2 cm (4.0 in.). With this exaggeration the plate looked as if it were in agony. A single plate was used for this experiment. Surely, the movement would be more complex if two plates were being joined, particularly if the two plates were of unequal rigidity or if the isotherm was not centered on the joint. Such

movement can result in permanent misalignment of parts, complex distortion, and possible interference with gas shielding and weld geometry.

Energy concentration is important. Electron beam welded components are remarkably less distorted than parts welded by other processes (Fig. 5). Similar distortions and stress-free gas tungsten air (GTA) welds have been made at Harvey Aluminum by cryogenically spraying the panels during welding (Fig. 6). Metal adjacent to the molten puddle can expand and contract without restraint, resulting in nearly stress free panels. In some panels "peaking" and "bowing" were reduced to zero, and longitudinal residual stress was reduced from approximately 1450×10^5 N/m^2 (21 000 psi) to values as low as 760×10^4 N/m^2 (1100 psi). Stress balancing combined with energy concentration should significantly reduce metal movement, distortion, and porosity and at the same time cause less material reorganization, which results in higher strength. The most promising process to accomplish the foregoing is the EB welding process.

PROGRESS TO DATE

With present technology, parts must be in a low atmosphere if they are to be EB welded. Obviously, this limits the application of the process. A rational approach to increase the versatility of EB systems is to discard the vacuum chamber; i.e., to weld material in 1 atm. MSFC now has, after much experimentation, a nonvacuum welding system.

In 1963 a first effort to extend the use of an EB welding system was made using a "split-chamber" concept developed for MSFC by the Sciaky Bros. Co. This split chamber was a vacuum chamber reduced to a size that encompassed only the joint to be welded. As an example the 10.06-m (33-ft) diameter ring that makes the transition from a bulkhead to a cylinder in the Saturn V first stage was used. The cross section of the ring forms a Y (Fig. 7). Only short arcs of the ring segments were in a low atmosphere as may be seen from the plan view in Figure 8. One half of the chamber was stationary and the other half was moveable on a pair of precisely aligned rails and was backed away to permit placement of the workpiece or for access to the electron guns.

The critical aspect of such a system is the adequacy of the seals at the interface of the chamber halves and between the Y-ring and the chamber. Sealing between the machined mating surfaces was accomplished with neoprene rubber strips. After the chamber halves were brought into contact, four bolts, one at each corner, were tightened to produce a seal. Maintaining a seal proved to be troublesome during the Y-ring welding program. During many of the pumpdown cycles, it became evident that a leak existed somewhere in the system. Quite often further tightening of one or more of the bolts stopped the leak.

Sealing between the Y-ring and the chamber was accomplished with metal blocks, rubber strips, and either pre-formed packing or O-rings. Again small leaks were often corrected by tightening the clamping plates, however the exact location of leaks could not be determined.

Despite these problems three segments were joined into a complete ring. It may be concluded

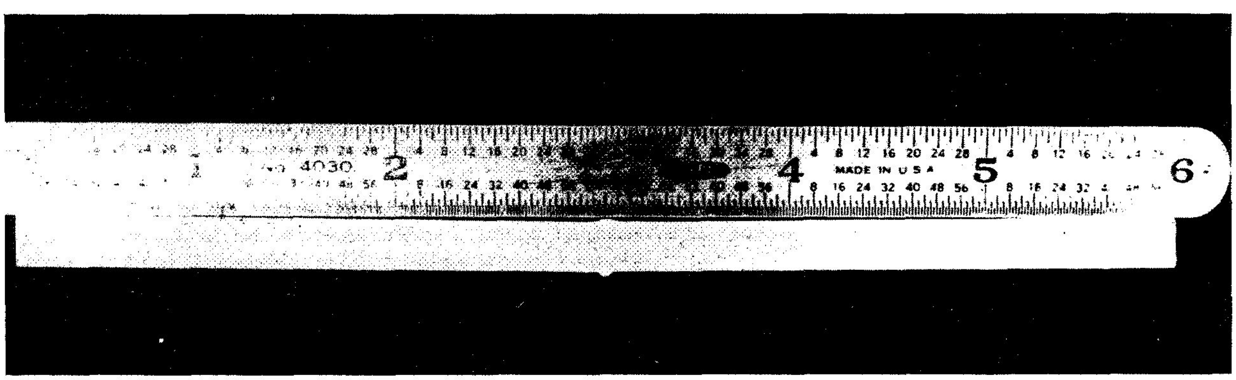

Figure 5. Electron beam weld.

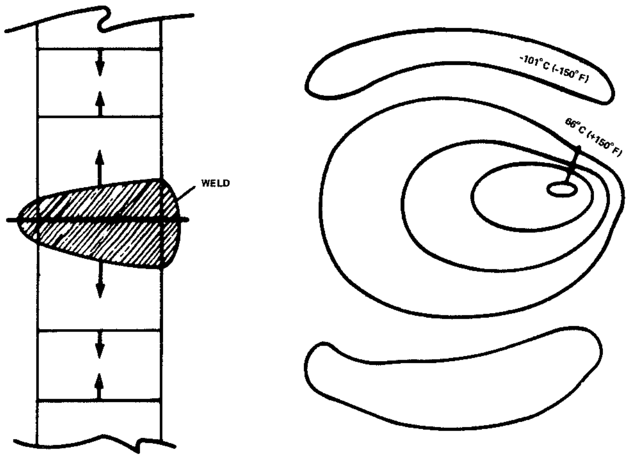

Figure 6. Stress balancing.

that these experiments demonstrated the split chamber to be a practical concept for joining large components.

The next step taken by MSFC was to sponsor development of a plasma electron beam (PEB) system with the General Electric Company at Schenectady, New York, as the contractor. PEB is a new type of electron beam source based on a cold hollow cathode gas discharge (Fig. 9). With a pressure of about 10 μm of nitrogen, for example, a body of plasma fills the cathode and an electron beam formation takes place. Beam current is controlled by varying the gas pressure and consequently the influx of positive ions. The beam is focused by a magnetic lens spaced 20.3 to 25.4 cm (8 to 10 in.) from the end of the cathode. The principle of operation is discussed in detail in the final report from the General Electric Company [3].

The PEB system offers the advantages of long cathode life and good performance under poor vacuum conditions where gaseous contaminants may be present. Parts can be welded in an atmosphere of about 75 μm. For welding structures too large to be contained in a vacuum chamber, it would seem feasible to extract the electron beam into a small chamber which moves along the weld seam maintaining a reduced pressure by means of a sliding seal. Sciaky Bros., under Air Force sponsorship, has developed such a sliding seal for their own "partial" pressure EB system. A reliable moving chamber and the relatively simple PEB system would be a significant step toward versatility. A PEB system is depicted in Figure 10. The cathode at the top of the photo is emitting an electron beam through the focusing coil into a Faraday cup.

The most recent move toward EB versatility has been a high voltage nonvacuum electron beam welding system. A newly developed model was delivered to MSFC in 1967. Powered by a 150-kV supply, the welder is of a unique compact design. The power supply and welding gun, complete with all high vacuum pumps and accessories, are assembled into a 95.26-kg (210-lb) package that can be mounted in either the down-hand or horizontal welding position (Fig. 11). It is mounted on a conventional side beam carriage. Flexible low vacuum lines permit the welding head to be traversed 1.22 m (4 ft) in a straight line. The complete unit is enclosed in a lead-shielded room. Electron emission from an indirectly heated tungsten rod is forced through differentially pumped orifices by a combination of electrostatic and electromagnetic electron optical systems. Maximum operating power is 80 mA at 150 kV. A positive

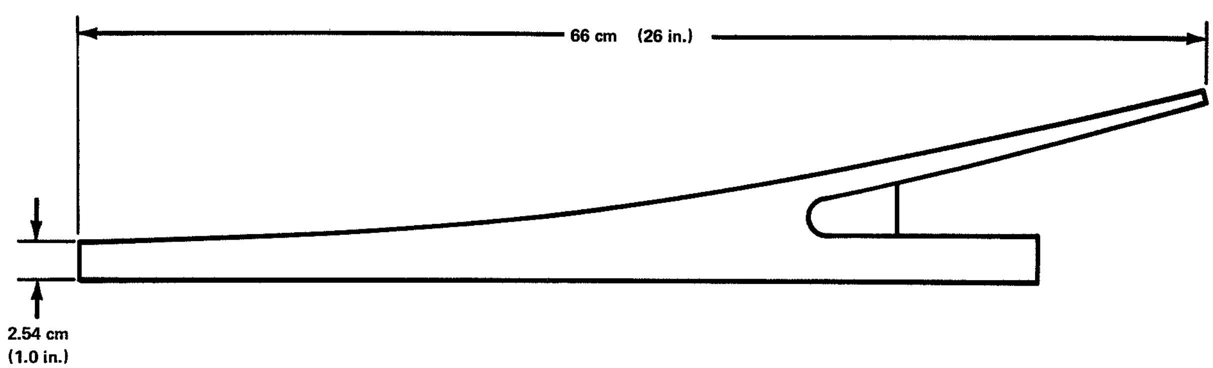

Figure 7. Saturn V 10.06-m (33-ft) diameter transition ring (Y-ring).

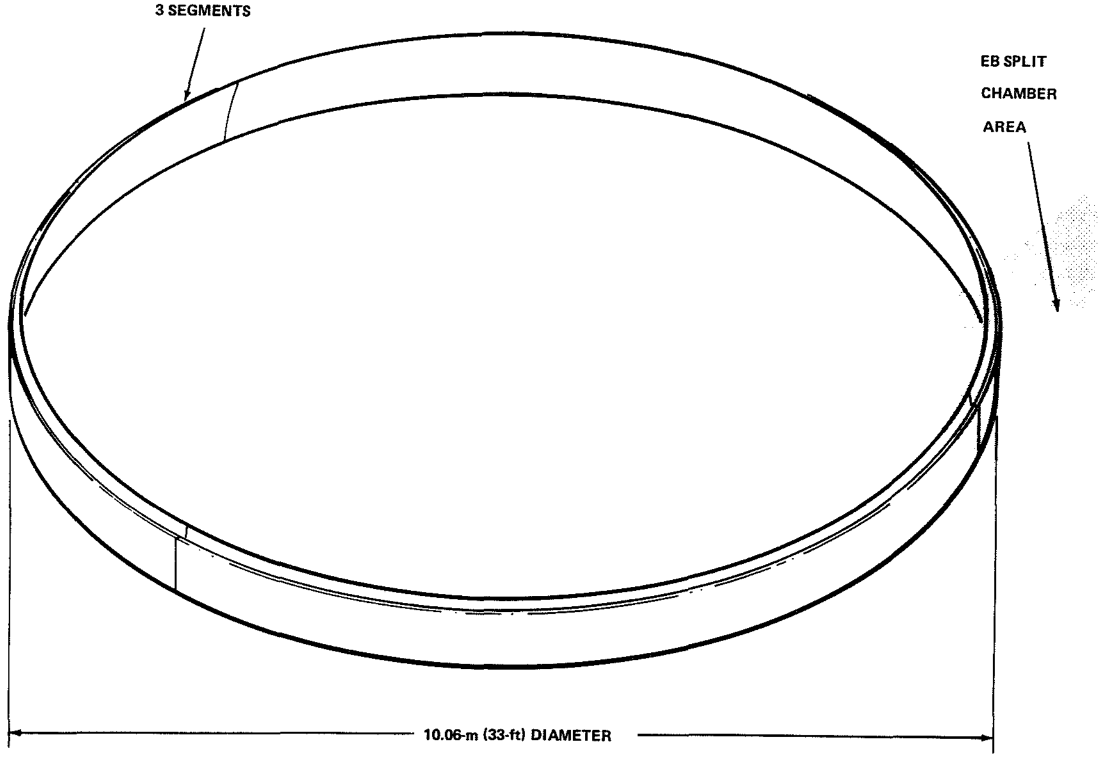

Figure 8. Transition ring welding station.

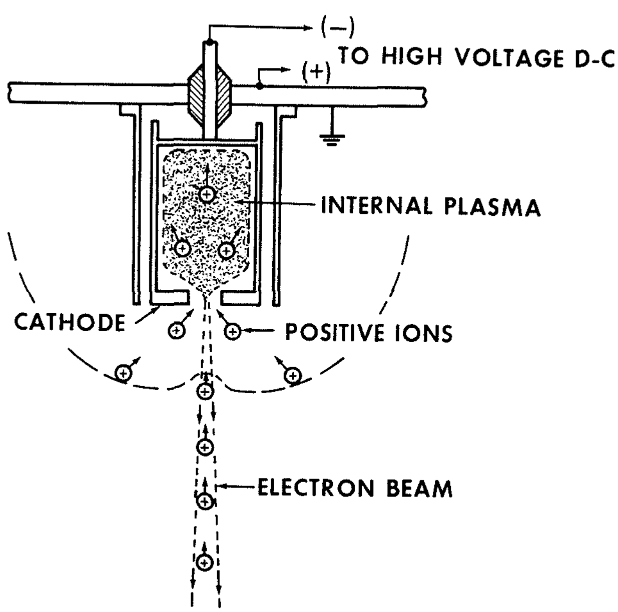

Figure 9. Beam formation in shielded PEB cathode.

pressure is applied just below the exit orifice of the gun. Welding has been performed on 0.64-cm (0.25-in.) thick aluminum and 0.318-cm (0.125-in.) and 1.27-cm (0.5-in.) thick steel.

As stated previously, if the material was welded in 1 atm, an EB system would be as applicable as the gas-arc processes. However, this poses no small challenge since the concentrated stream of electrons that makes low energy welding possible has from the onset of EB systems required a low atmospheric pressure. A low power density by a versatile EB system would only be a regression. It would be meaningful only if the welds produced were significantly superior to GTA and gas metal arc (GMA) welds. Presently, the nonvacuum system produces aluminum welds definitely inferior to hard vacuum welds, and only infrequently superior to GTA welds. Porosity is highly unpredictable. A determination has not been made as to what causes the porosity in aluminum welds; that is whether it is hydrogen or metal vapor. Welds in steel, such as 4130 sheet, more closely approximate hard vacuum welds. The nonvacuum EB system presently can be considered practical for joining small steel parts (Fig. 12).

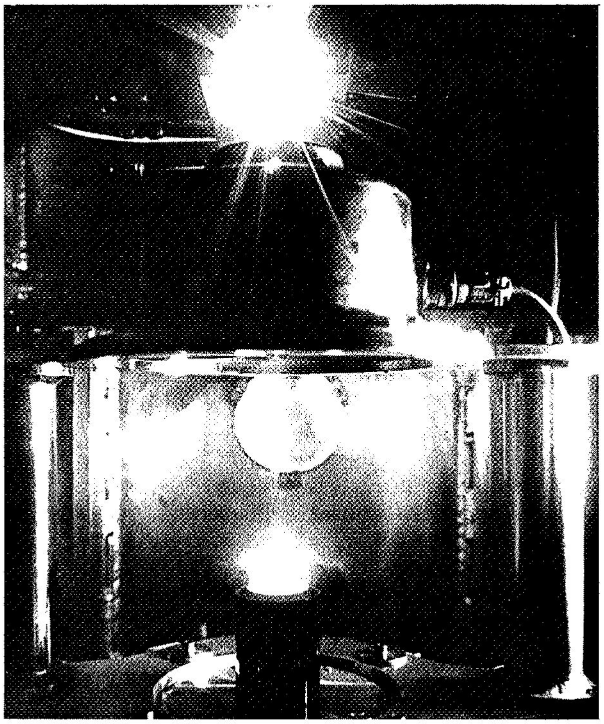

Figure 10. Plasma electron beam.

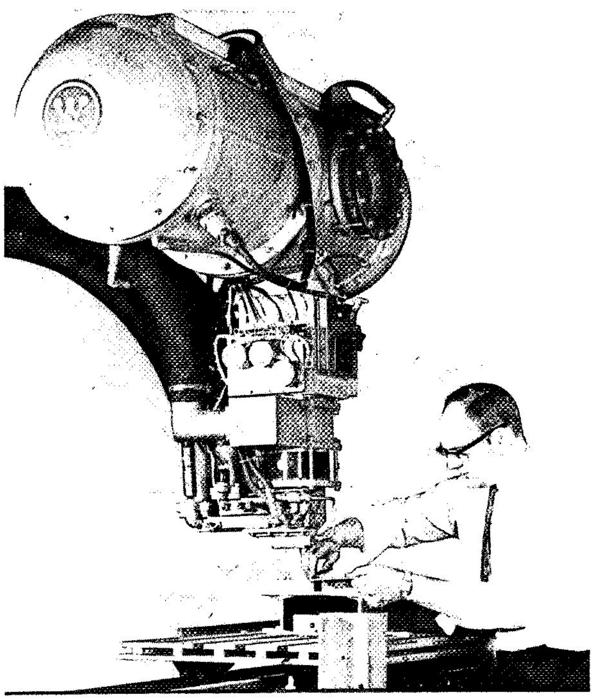

Figure 11. Nonvacuum electron beam welder.

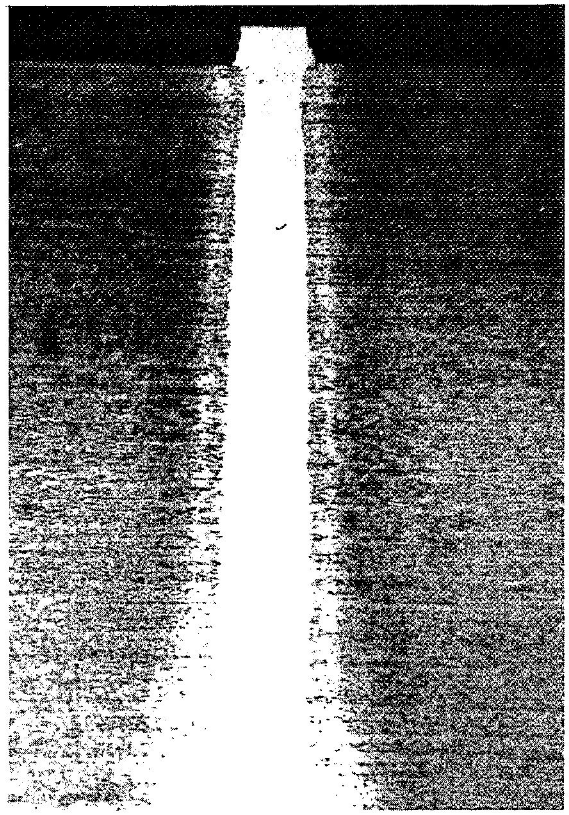

Figure 12. Nonvacuum electron beam weld.

To obtain nonvacuum EB welds in aluminum that are similar in shape to hard vacuum welds, welding must be accomplished at more than 5.08 m/min (200 in./min). Narrow welds made at any speed impose strict accuracy requirements. Transverse deviations of the beam from the center of the joint, and joint gaps of more than 0.013 cm (0.005 in.) can result in lack of fusion. The situation is greatly exaggerated when the gun is moving at 5.08 m/min (200 in./min). At this speed a seam tracking device would have to move the gun system laterally 0.013 cm (0.005 in.) in 8.46 cm (3.33 in.) of forward movement per second. Proximity of the gun to the work, less than 0.953 cm (0.375 in.), is equally critical. Even if the power density of the electron beam was increased so that much slower travel speeds could be used, that is, 1.02 m/min (40 in./min) versus 5.08 m/min (200 in./min), the accuracy of parts fitup would still be critical and seam guidance and proximity control would still be mandatory. In addition, shielding of personnel from X-rays generated by the high voltage necessitates remote monitoring of welding.

This does not imply that application of nonvacuum EB welding is and will always be impractical. However, much analysis, development, and planning are necessary before the system can be considered applicable and versatile. It should be emphasized that in a rational approach to EB welding it must be recognized and accepted that the process will have limits, just as is true with any other joining process.

Nevertheless, the economical and reliability consequences of the successful application of a nonvacuum system warrent a concentrated engineering effort. Work is presently being performed in the first of four phases of such an effort. In phase I, safety requirements, machine parameters, controls, and tooling needs are being studied. Phase II will consist of pre-process evaluation of Shuttle materials and analysis of nonvacuum welds, comparing nonvacuum welds to conventional welds. In Phase III, an automatic guidance system and facilities for a one-third scale Shuttle tank will be designed and built. The final phase will be the fabrication and nonvacuum EB joining of components.

Industry and other NASA centers have expressed interest in the application of a nonvacuum system. This is a further impetus to an early completion of the program. In particular, the system is oriented toward manufacturing the Space Shuttle.

In summary, the program goal (Fig. 13) is to increase the power density of nonvacuum to that of hard vacuum systems and yet approach the versatility of conventional modes of welding.

CONCLUSION

It appears that EB is a logical choice for welding in space, since the interesting contradiction exists that EB welding is both nonversatile and versatile; nonversatile on earth, where a "vacuum" is artificial, and most versatile in space, where an atmosphere is artificial.

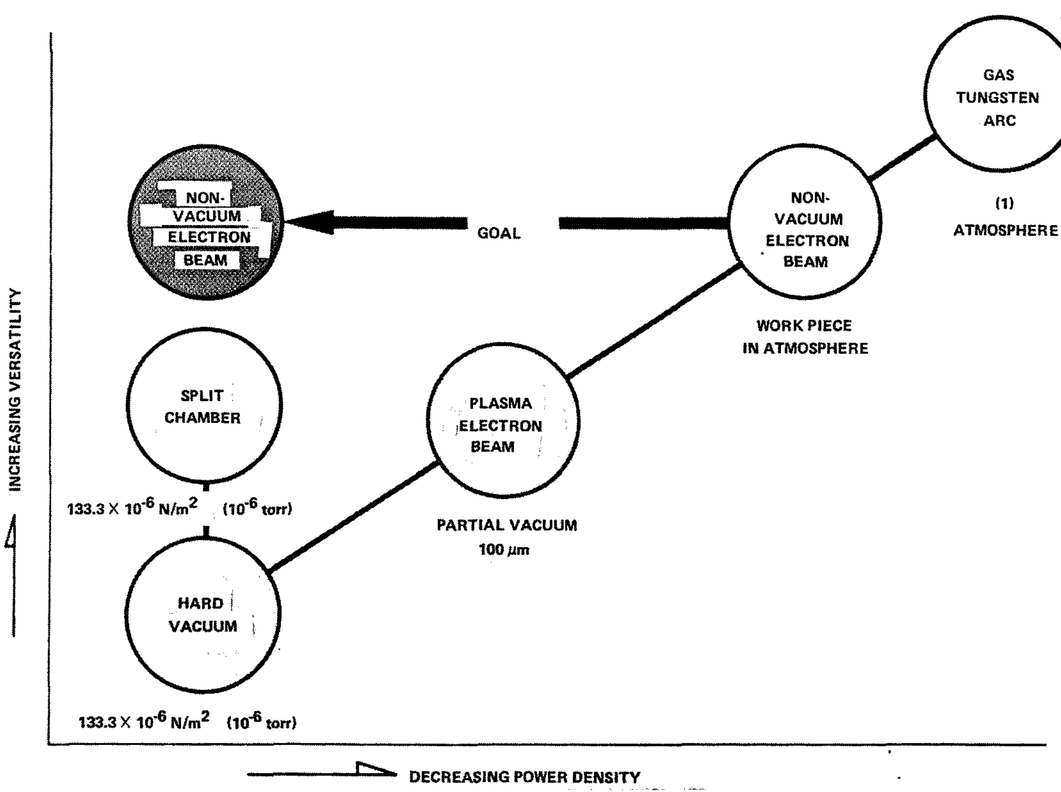

Figure 13. Versatility in electron beam welding.

MSFC has chosen EB welding for the first metals-joining experiment in space. The objective is to study behavior of molten metal at zero gravity and to seek answers to certain questions.

REFERENCES

1. Preparation and Instrumentation for Welding S-IC Components. Report No. B6065-11, IIT Research Institute, Contract NAS8-20363, Phase II, April 3, 1967.

2. Masubuchi, Koichi: Integration of NASA-Sponsored Studies on Aluminum Welding. Report No. RSIC-670, Redstone Scientific Information Center, Redstone Arsenal, Alabama, September, 1967.

3. Boring, K. L., et al.: Development of a Plasma Electron Beam Welding System. General Electric Company, Schenectady, New York, Final Report, NASA Contract NAS8-1103, March, 1968.

N73-22920

Preceding page blank

QUARTZ GYRO MANUFACTURING AND MEASURING[1]

By

John R. Rasquin[2]

ABSTRACT

The unique methods used in the manufacture of quartz gyroscopes for the General Relativity Satellite are presented herein. The General Relativity Satellite will be used to verify Einstein's general theory of relativity. If Einstein's predictions are correct, there will be two extremely small precession effects on a gyroscope in earth orbit. The precision techniques used to manufacture and measure some of the parts for the gyroscope are described.

DISCUSSION

The gyroscopes discussed herein are to be used for the verification of Einstein's general theory of relativity. A gyroscope in earth orbit will experience two precession effects. These two effects will be measured separately using two sets of gyros with their axes mutually perpendicular. The orbital motion effect will be 7 arc sec/year, and the earth rotation effect will be 0.05 arc sec/year. Since the gyro precession will be extremely small, advanced gyroscope technology much beyond the state-of-the-art is required. In fact, a gyro 10^8 times better than any presently available is required.

Figure 1[3] shows how a gyroscope that meets the requirements might look. Primarily, it consists of a niobium-coated quartz ball that spins in a spherical quartz cavity which has electrostatic support electrodes and a measuring coil deposited inside. The whole device operates at the temperature of liquid helium, and, therefore, the niobium-coated ball becomes superconducting on the surface. If the pickup coil is pulsed, it will start a circulating current around the ball. The magnetic field of the circulating current can then be picked up and the precession of the ball can be determined. The ball will be spun up by a jet of helium gas.

There are several reasons why this sort of gyro should work as specified.

1. All the parts of the gyroscope are made of essentially the same material; there are no material mismatch problems.

2. The rotating element is a sphere, which is the simplest mechanical device that can be used. The center of gravity and the geometric center are exactly the same, provided that the sphere is made of a homogeneous material.

3. There are no gimbals or bearings associated with the ball since it is supported by an electrostatic field. In zero gravity only a very weak electrostatic field is required, and this is due to gravity-gradient forces. There is no bearing because the ball is electrostatically centered.

4. There are no accelerations on the ball, not even that of gravity, because the gyro is in orbit.

---

1. This project is a cooperative effort between Stanford University and Marshall Space Flight Center. The Process Engineering Laboratory and the Space Sciences Laboratory of MSFC are developing and testing the gyros.

2. The author gratefully acknowledges the contributions made to this project by Mr. John P. Hill, S&E-PE-MW, for tool design and finishing, Mr. John R. Glaese, S&E-AERO-DO, for random motion studies, and Dr. W. H. Heybey, S&E-AERO-T (Retired), for measuring calibration.

3. Some of the figures in this paper have English units only, because the instruments illustrated use them.

PRECEDING PAGE BLANK NOT FILMED

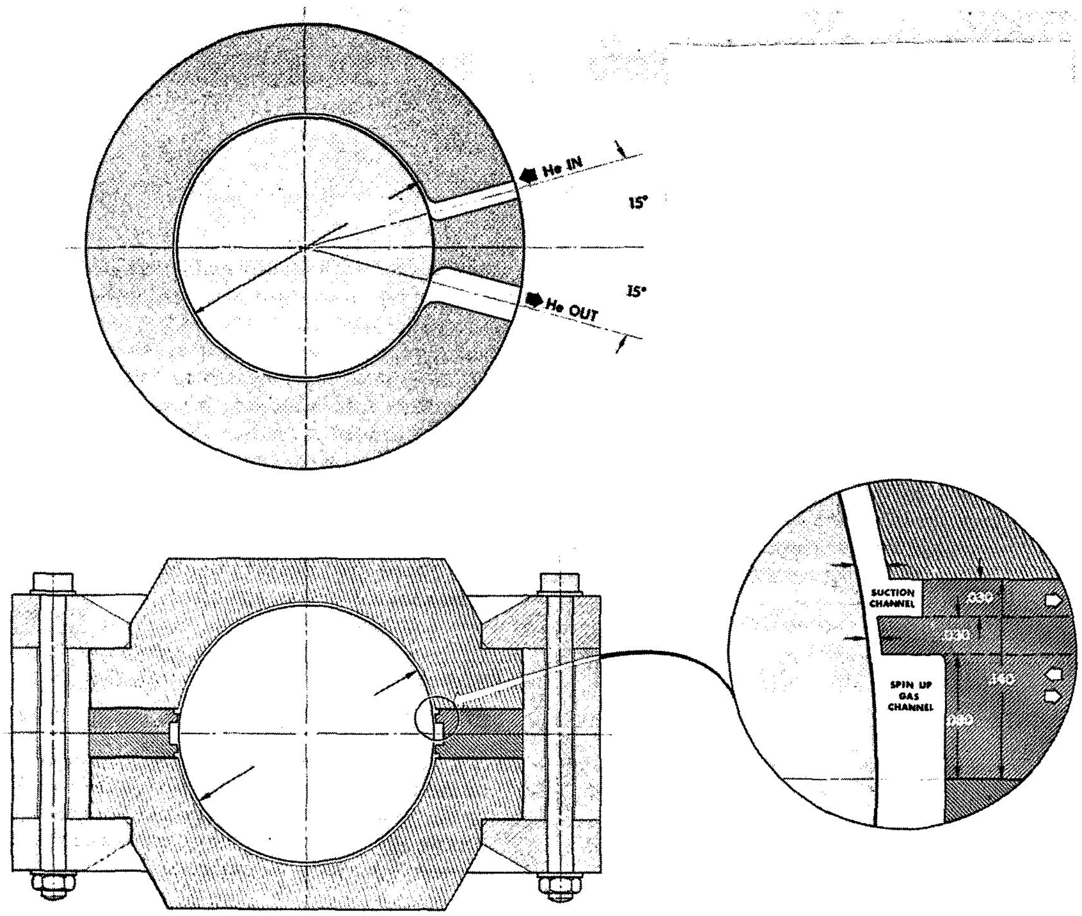

Figure 1. Cryogenic gyroscope.

5. There are no temperature changes in the material because the entire assembly runs at liquid helium temperature, approximately 4.2°K.

6. After the ball reaches operating speed, it is operating in a vacuum, so there is no aerodynamic drag.

Amorphous quartz was chosen as the material for the gyros because of its good temperature characteristics and its stability. The diameter of the ball will be 38 mm (1.5 in.) and the ball will be rounded to 2.5×10^{-6} mm (1×10^{-7} in.). Quartz with a deviation of less than 1×10^{-6} in the index of refraction across a 5.08-cm (2-in.) cube can be purchased. This material should be suitably homogeneous and should assure balance when the ball is spinning. Cubes will be purchased with all six sides polished flat so that the quality can be verified by a Schlieren optical system. Since the order of accuracy required is high, a system of measurement as well as the hardware had to be developed for this experimental apparatus; however, the method of manufacture will be discussed first.

Three boules of quartz were obtained from Corning Glass for practice material. Spheres were then rough-ground from this material to about 2-mm oversize in a Strasbaugh Universal grinding machine (Fig. 2). When a ball is ground, it is made from a cylinder that is ground first. The final grinding is done with brass laps in the machine shown in Figure 3 with 500 grit alumina. It is fine-ground in this machine to about 0.1-mm oversize and then polished. The polishing is done with the same type lap filled with lapping pitch. The laps are fixed to four sewing machine motor shafts and are loose enough so that they are free

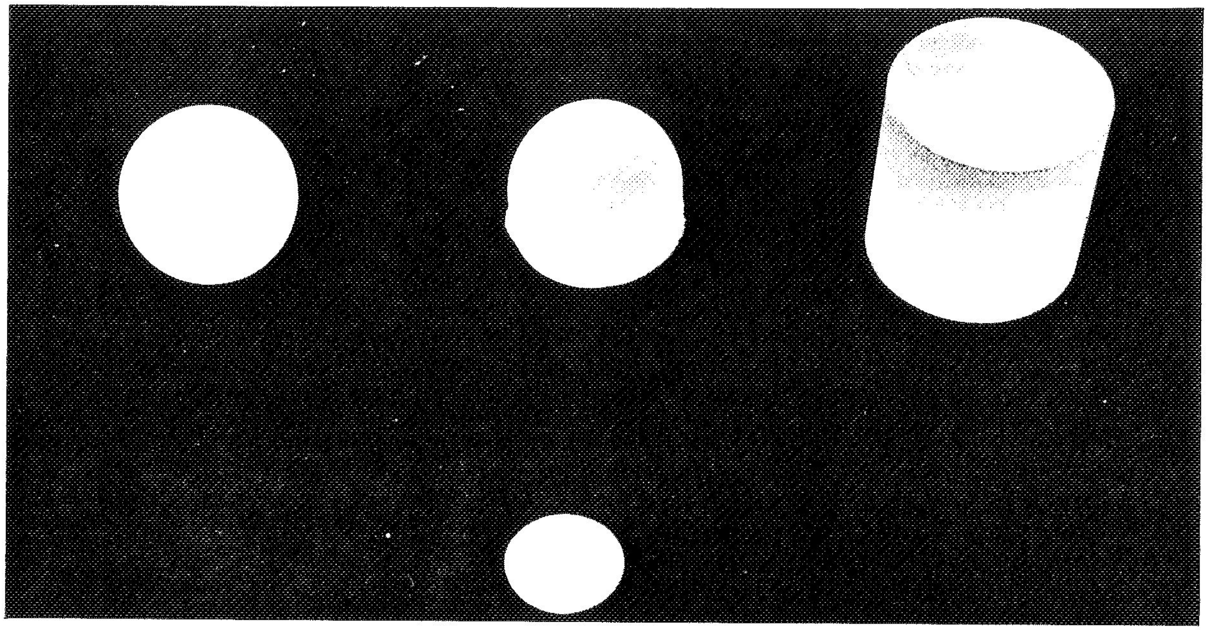

Figure 2. Stages of ball grinding.

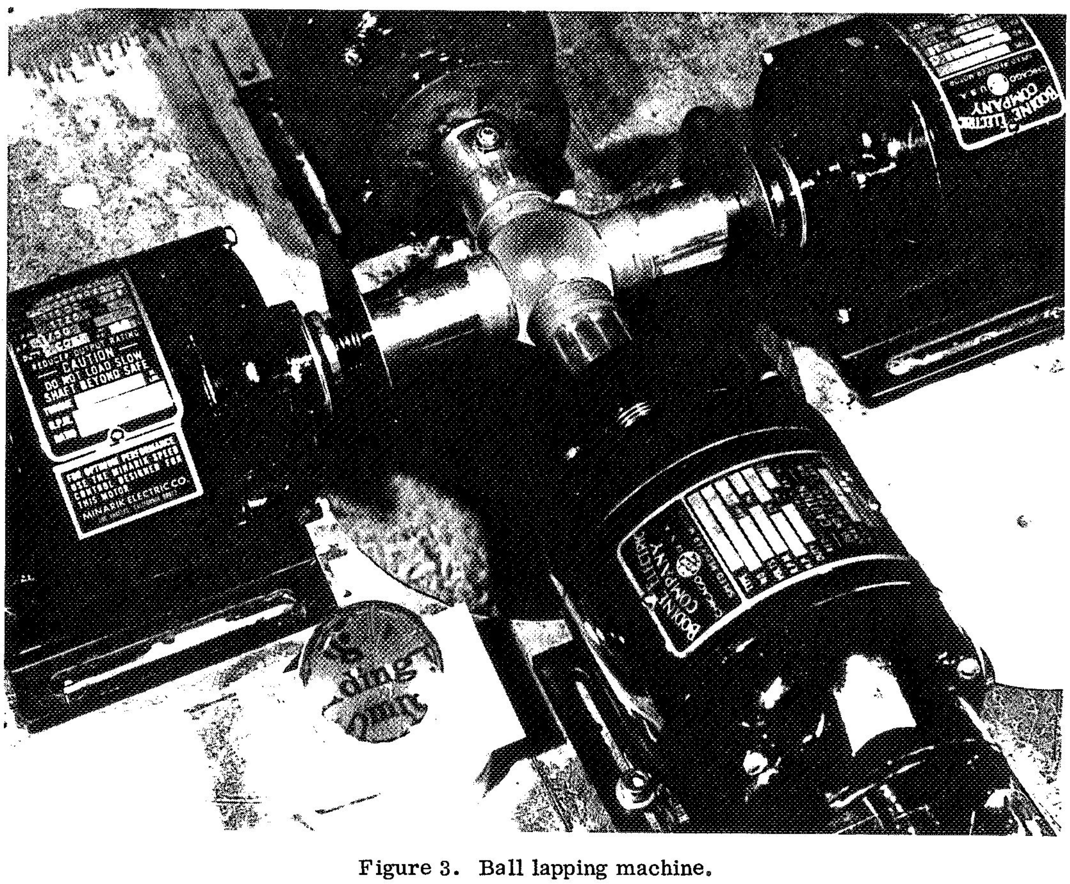

Figure 3. Ball lapping machine.

wobble slightly to compensate for minor misalignments. The laps are in the shape of a thick-walled tube on the polishing end and are about 25 mm in diameter. The diameter of the laps is not critical, but they must be small enough to avoid touching one another and large enough to run smoothly. It also helps to leave the paper in place that was used as a dam when pouring the hot pitch because the spring pressure used to force the laps against the ball is high enough to deform the laps with the passage of time. Ordinarily a ball-lapping machine uses three laps spaced 120 deg apart and positioned so as to support the ball. This does not work with a small, light ball because the ball does not weigh enough to place sufficient pressure on the laps. The ball is rough-lapped with cerium oxide and finished with barnsite.

The speed of the lap motors is controlled electronically. The motor speeds are best illustrated by Figure 4. In Figure 4, the direction upward from zero is clockwise rotation and downward from zero is counterclockwise rotation. Top motor speed is approximately 120 rpm. Speeds higher than this throw the lapping compound off the laps and the ball. A grinding cycle lasts for 2 minutes and repeats.

Ball size is measured with a light-wave micrometer (Fig. 5). Even if an optical interferometer is used, a 1/20 wavelength of blue light is about as close as one can measure with light fringes. This is approximately 25×10^{-6} mm, which is satisfactory for a size measurement but is not satisfactory for measuring roundness which is to be to 2.5×10^{-6} mm. Accordingly, some other method of measurement must be devised.

The Process Engineering Laboratory has a capacitance bridge that is capable of measurements to 1×10^{-19} F. Now, if the ball has been coated with a 1000-Å coat of metal and placed on a metal stand adjacent to an electrode, the capacitance between the ball and the electrode can be measured very accurately. This is related to distance by

$$C = E_o \frac{A}{D} ,$$

where

C = capacitance,

E_o = permittivity,

A = capacitor plate area,

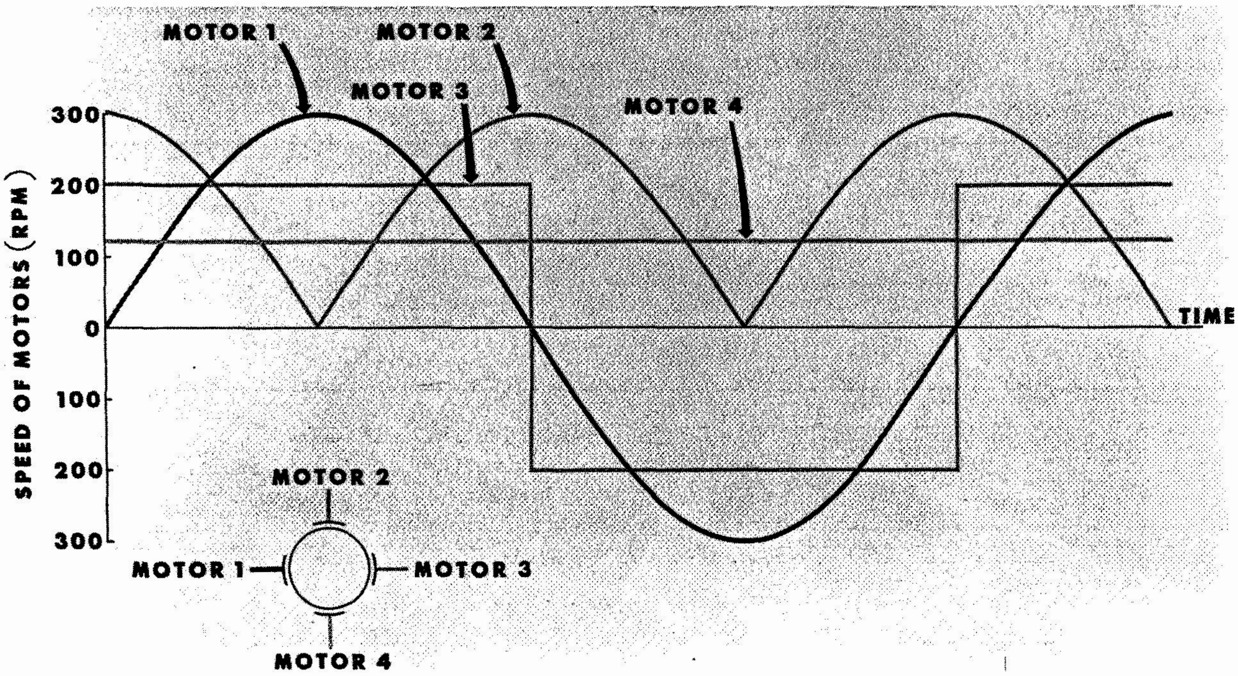

Figure 4. Speed diagram of lapping motor.

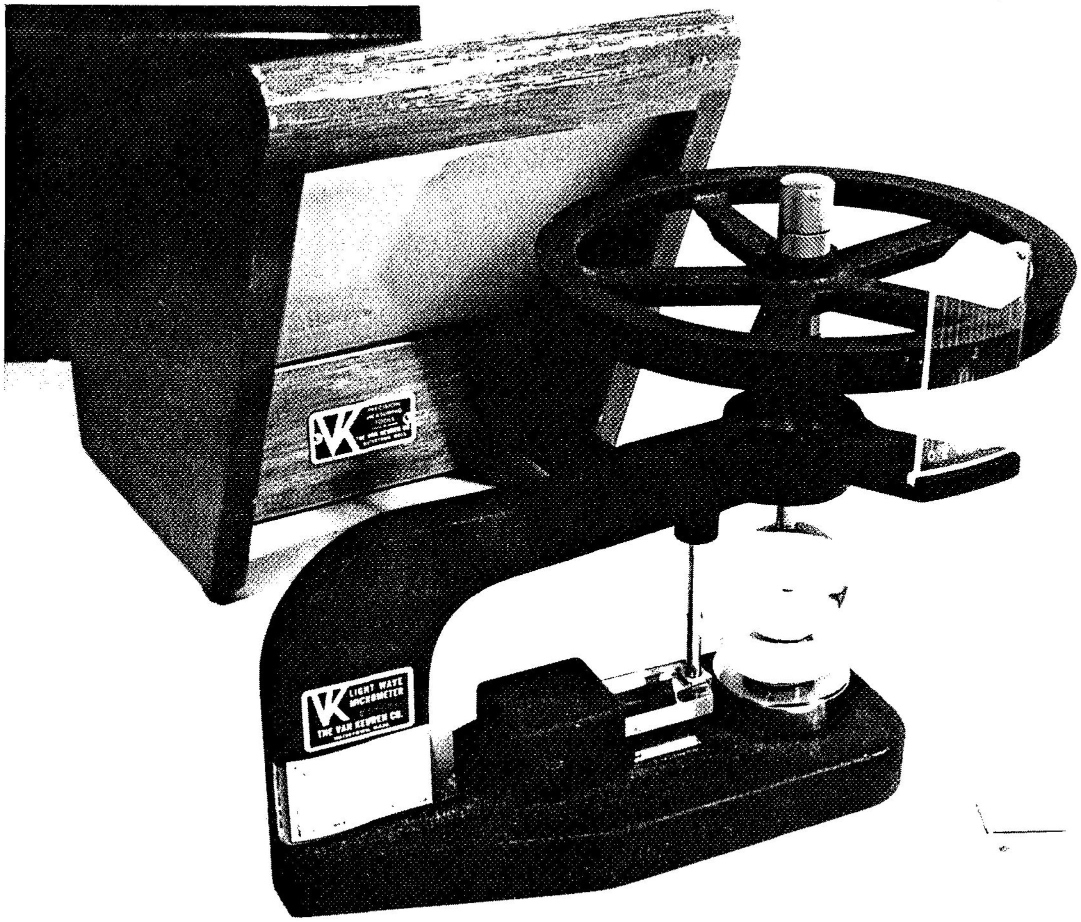

Figure 5. Light wave micrometer.

and

D = distance between plate and sphere.

A schematic of a device, which is being fabricated at this time, for measuring ball roundness is shown in Figure 6. The unit will have four electrodes instead of the two shown in the schematic and will have one electrode on top to check the position of the ball to make certain that it is in the same place each time a measurement is made. The area of the electrodes will be 1 cm^2. In use, a measurement will be taken at all four electrodes between the electrode and the ball by a connection through the ball support; then, the ball will be turned an increment and another measurement made. All measurements will be recorded as data.

The gage that contains the electrodes will deviate slightly from perfect roundness. This will show up in the data as an error that does not move as the ball is incrementally turned in the gage. Since the ball is not perfectly round, the error associated with it will move as the ball is turned. Thus, the two errors can be separated.

The measurements will be taken in a vacuum; the permittivity will be 8.85×10^{-12}, or approximately $(36 \times 10^9)^{-1}$, F/m. If it is assumed that a 1-cm^2 electrode is positioned 0.1 mm away from the coated ball, the calculated capacitance is 8.85 pF. Now, if there is a change in the distance of 2.5×10^{-6} mm (1×10^{-6} in.), a change of approximately 0.001 pF will result, which is well within the range of the capacitance bridge. It also allows small changes in the radius of the ball to be detected when the ball is rotated adjacent to the electrode.

The gyro ball is housed in a spherical quartz cavity as shown in Figure 7. In the figure a ping-pong ball was substituted for the gyro ball to show

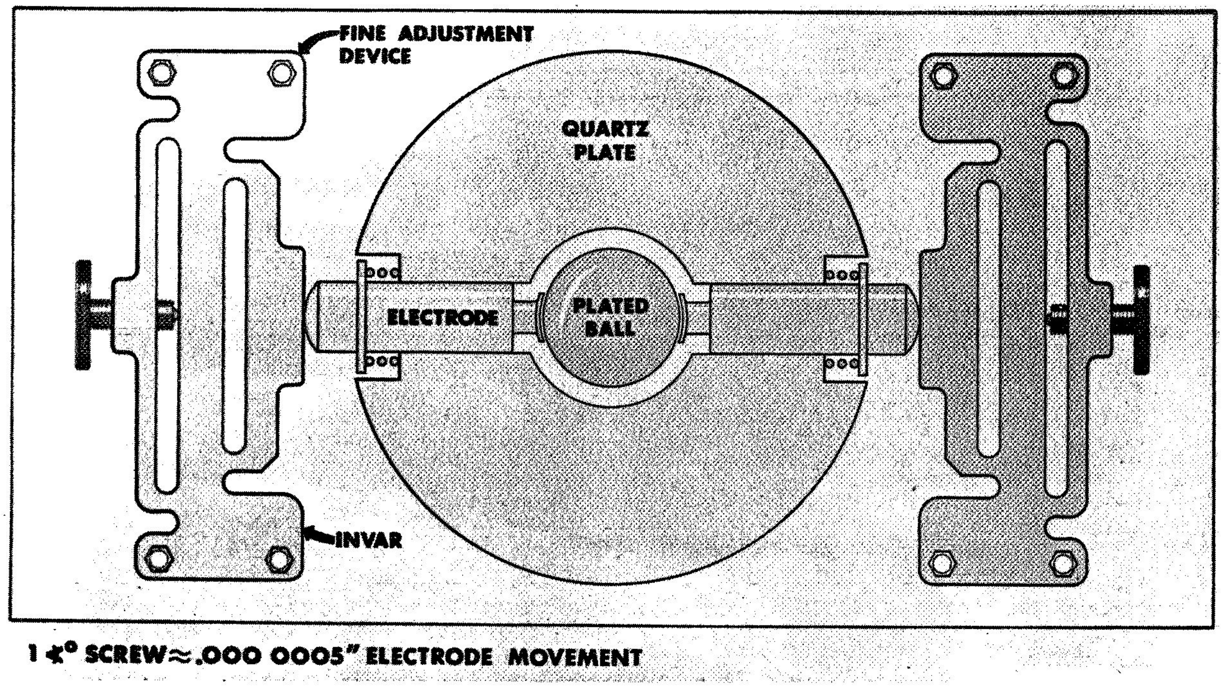

Figure 6. Instrument for measuring ball roundness.

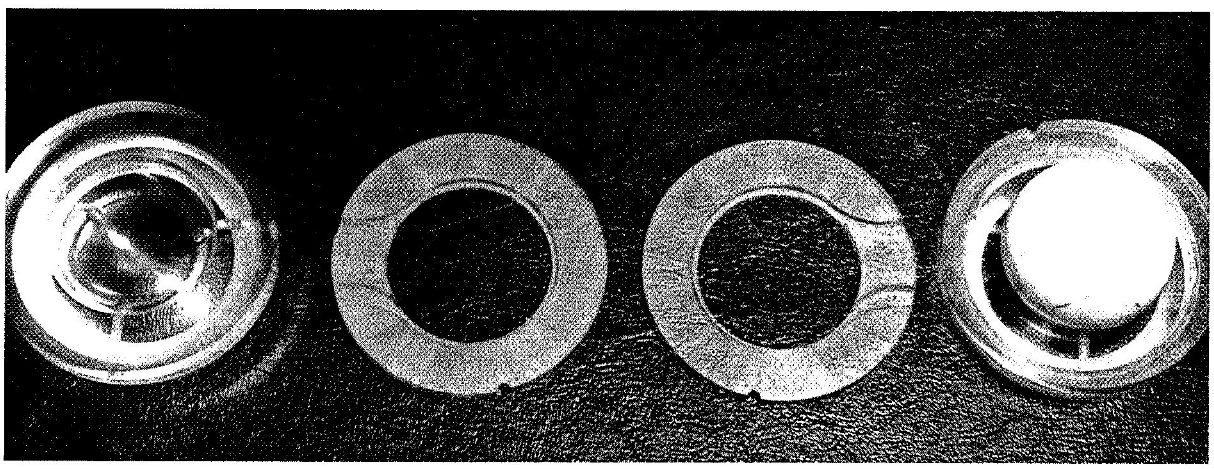

Figure 7. Quartz gyro cavities.

how the ball fits into the cavity shells. The complete cavity assembly consists of two half-shells and two rings that contain the spinup channels, exhaust, and connections to the instrumentation coil. The electrostatic support pads have not been deposited in the cavities shown in the figure.

The Process Engineering Laboratory has attempted to obtain all the necessary parts commercially, but thus far it has been impossible to obtain quartz balls with the required tolerance. The task of manufacturing the cavities is presently under contract, and hopefully the supplier will

furnish good ones. The tolerance of measurement on the cavities is such that the measurements can be made on a Tallyrond machine.

The thickness of the coating on the spheres is 1000 ± 5 Å. The thickness of the coating can be determined by color tests, but obtaining a coating that adheres well to the smooth quartz surface and applying the coating so that it is deposited uniformly is quite another problem.

The sputtering method of metal deposition was chosen, and a method of tumbling the ball during the process has been devised. Figure 8 shows the tumbling machine that was built in-house. The machine consists of two circular tracks that are inclined at an angle of 6 deg. The complete assembly is placed under a bell jar which fits over the top of a vacuum diffusion pump. The assembly cannot be tilted more because the diffusion pump would not work.

When the ball sits on the rails as shown and the rails are turned at different speeds, the ball will tumble, and if the speeds of the rails are controlled as shown in Figure 9, all areas on the ball will be exposed to the sputtering gun uniformly. The speed is again controlled electronically. An air bearing to support the ball has also been manufactured, in which argon gas is used instead of air. Since sputtering is done in an atmosphere of low pressure argon gas, this method may be superior to mechanical support if leakage can be kept low enough.

Some attempts have been made to coat the ball by electroless plating, but it has been difficult to get a catalyst to adhere to the smooth surface.

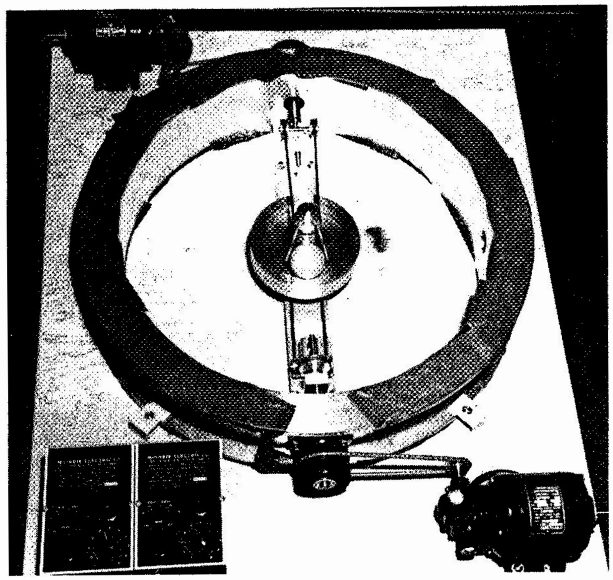

Figure 8. Ball tumbling machine.

This project consists of a series of problems that must be solved individually. Thus far, none of them seems to be insolvable, but launching of the General Relativity Satellite may be well into the future. However, even if a gyro is produced that is only 1000 times better than any gyro made to date, the project will have been worthwhile.

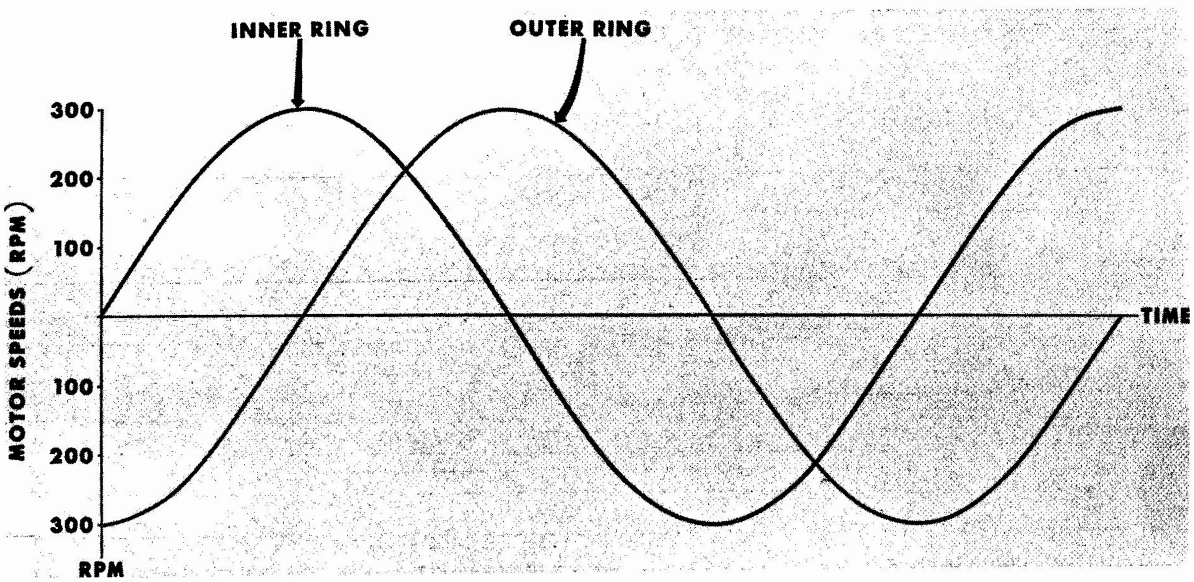

Figure 9. Motor Speed control for coating gyro balls.

N 73-22924

Preceding page blank

APOLLO 14 COMPOSITE CASTING DEMONSTRATION

By

I. C. Yates

SUMMARY

An inflight demonstration performed on Apollo 14 has shown the potential for preparing unique metal-matrix composites and mixtures of immiscible materials in a weightless environment. Gravity effects such as segregation due to density differences and disturbances due to thermal convection are eliminated. Liquid phase processes inhibited by gravity on earth may be used to manufacture unique materials in space. Three groups of composite materials samples were processed to observe the effects of melting, mixing, and solidification of materials in a weightless environment. Evaluation of the samples has shown that in this environment more homogeneous dispersions of particles, fibers, or gases may be achieved in a metal matrix and that dispersions of immiscible liquids may be maintained during solidification.

INTRODUCTION

The composite casting demonstration evolved from preliminary proposals submitted in the spring of 1970 to perform preliminary manufacturing in-space tests during the transearth coasting phase of an Apollo mission. In September of 1970 approval was given to proceed with the design and development of the demonstration and analysis to determine compatibility with Apollo 14.

The demonstration was designed and developed by the Process Engineering Laboratory, with consulting help on sample selection provided by the General Dynamics Convair Aerospace Division and Arthur D. Little, Inc. Other contributors to the sample selection were Astronautics Laboratory, Space Sciences Laboratory, and the Research Planning Office of MSFC, and Cornell Aeronautical Laboratory and TRW Systems Group. The Quality and Reliability Laboratory performed all qualification and acceptance tests with the support of Astronautics Laboratory in flammability and shock testing. All required reviews, plans, documents, and specifications were completed and approved, and the hardware was fabricated and delivered to the Kennedy Space Center by December 1970.

The purpose of the demonstration was to obtain preliminary data on the processes of melting, mixing, and solidification of metal-matrix composite materials in a weightless environment. The data were taken by postflight evaluation of samples processed in space and similar samples processed on earth. The primary objective was to evaluate the hypothesis that in a weightless environment mixtures of solids, liquids, and gases of different densities will not segregate during solidification and, consequently, unique composite materials may be formed. A secondary objective was to examine solidification phenomena in a reduced gravity environment. A group of four samples was designed especially for this objective; however, these were not processed by the astronauts because of their busy schedule during transearth coast. The data gathered from the demonstration will be used to plan further tests and to develop equipment and facilities for manufacturing in space.

DEMONSTRATION APPARATUS AND PROCEDURES

The demonstration apparatus consisted of an electrical heater, a storage box for the heater that also served as a heat sink for cooling the samples, and 18 hermetically sealed capsules containing sample materials. A beta cloth bag resembling a cartridge belt was used to store the specimens.

Procedures called for inserting each capsule into the heater as shown in Figure 1, heating for a prescribed time to melt the contents of the capsule, shaking the heater in some cases to mix the materials, and cooling by placing the heater and capsule onto the heat sink as shown in Figure 2. The right half of the aluminum storage box is a massive section with an integrally machined pin that makes

PRECEDING PAGE BLANK NOT FILMED

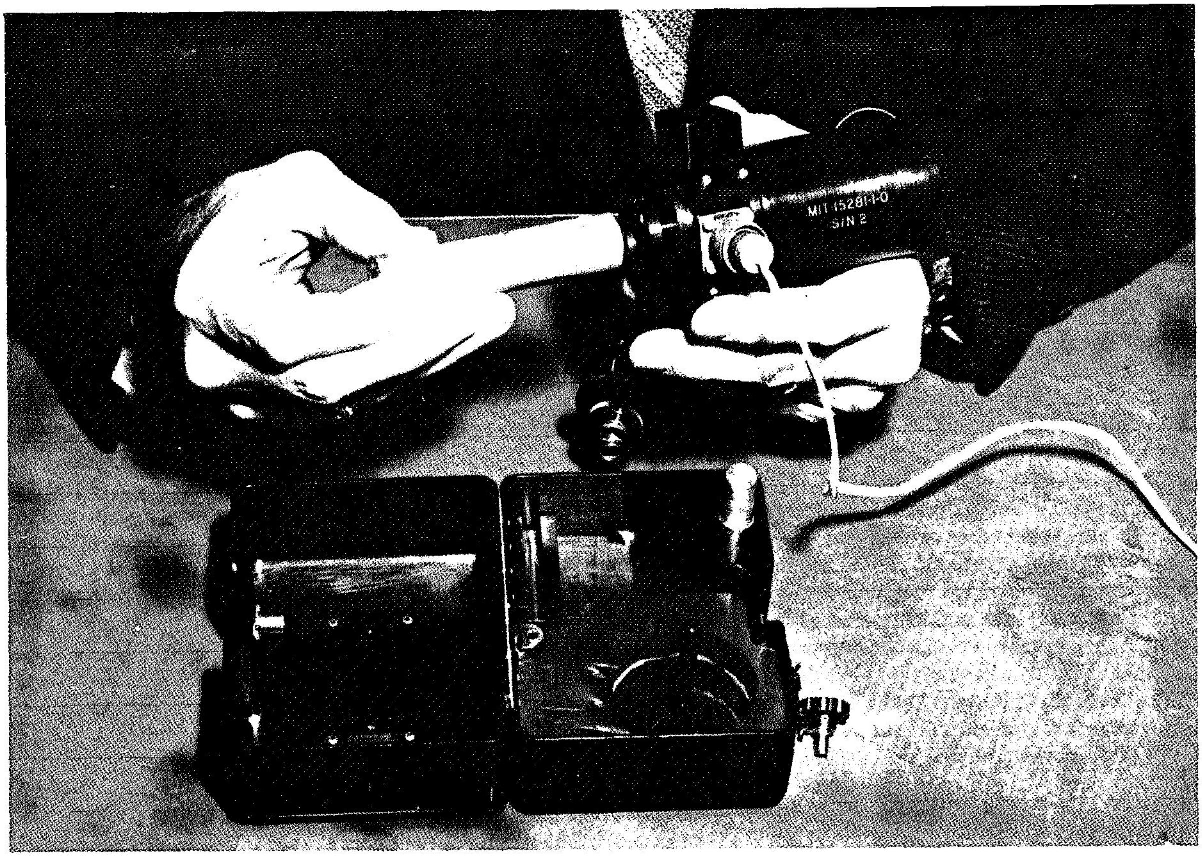

Figure 1. Composite casting heater and box with typical specimen capsule.

contact with the specimen capsule during cooling. A better view of the heat sink pin is shown in Figure 1. A bayonet type connection is made between the heater and the pin, and the spring in the upper cap holds the capsule tightly against the heat sink.

The heater operates on 27.5 Vdc from the Command Module bus using the Data Acquisition Camera power cable. Connection was made at a utility receptacle, and a switch on the panel was used to turn the heater on and off. Nominal power consumption was 34 W. A cross section of the heater, shown in Figure 3, shows the configuration with a sample capsule inside. Redundant thermal switches were used to insure that the outside surfaces of the heater did not exceed 41°C (105°F) during the heating cycle. The maximum temperature reached on the top of the capsules after 10 minutes was approximately 113°C (235°F). Cooling times of no less than 30 minutes on the heat sink reduced the temperature of the capsules to less than 38°C (100°F).

COMPOSITE MATERIALS SAMPLES

The materials selected for the demonstration were limited to low melting point materials because of safety considerations and the constraints on power consumption, weight, and size of the demonstration hardware. The basic materials used as a matrix or binder for the composites were indium bismuth eutectic alloy, which melts at 72°C, and paraffin, which melts over a range from approximately 54 to 58°C. Paraffin and sodium acetate trihydrate, which melts at 58°C, were used to demonstrate the feasibility of preparing immiscible dispersions. All the materials used met specifications for toxicity, odor, and flammability.

The composite materials samples actually processed on Apollo 14 may be grouped as follows:

1. Precompressed powder compacts containing dispersed particles.

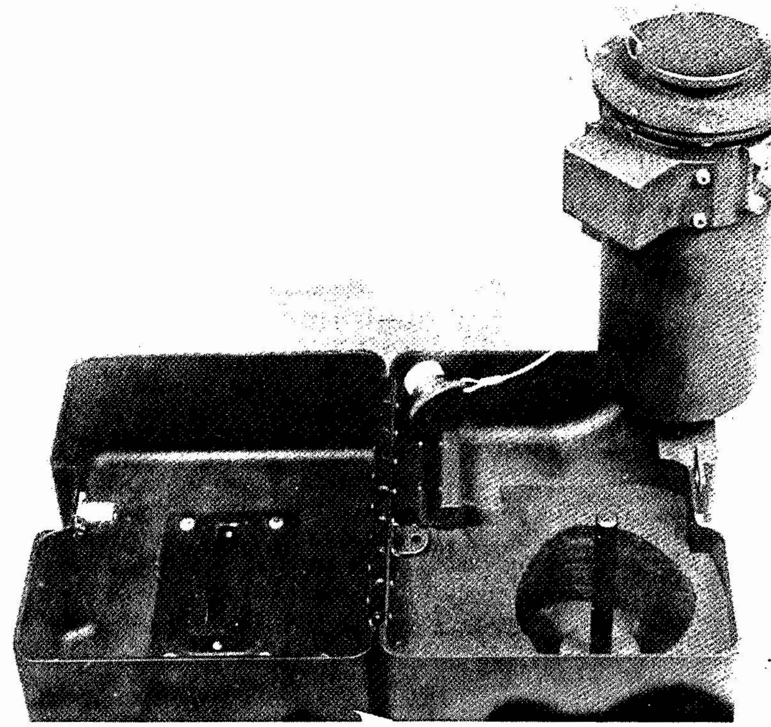

Figure 2. Composite casting heater on heat sink.

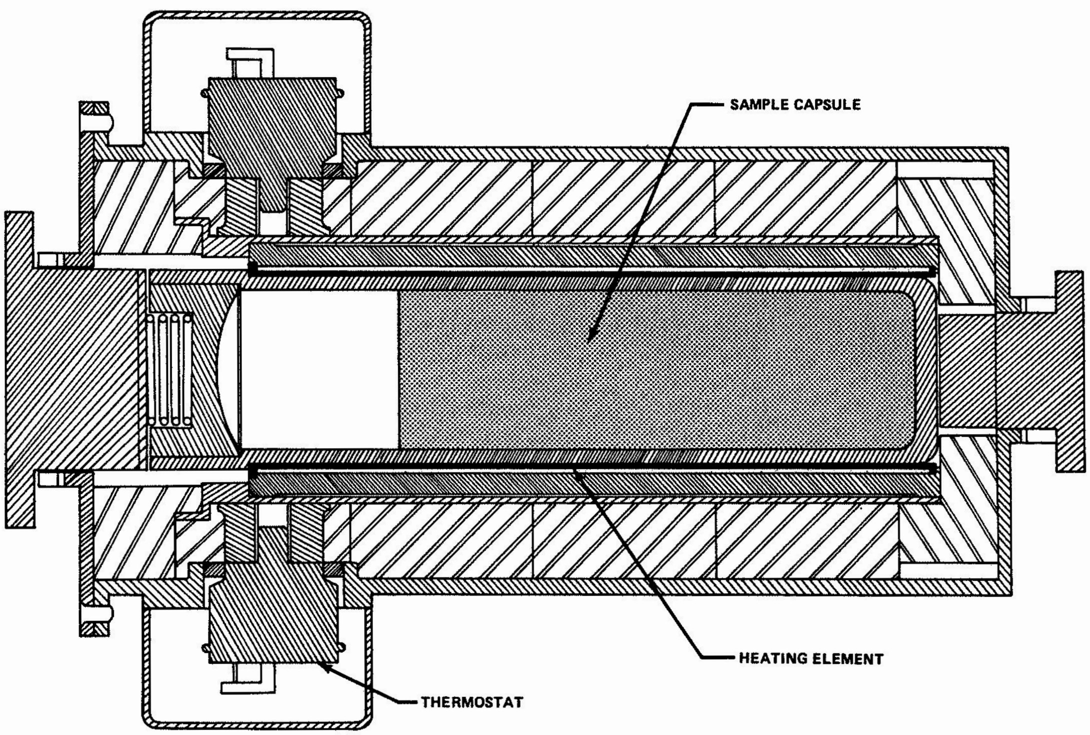

Figure 3. Cross section of heating unit with sample capsule.

2. Matrix material with fibers, particles, whiskers, and/or gas.

3. Immiscible materials dispersions.

A fourth group of specimens to study solidification phenomena was prepared and flown but none of these was processed. The composition of the 11 samples actually processed is shown in Table 1. A more detailed description of the individual specimens is included in the discussion and presentation of data which follows.

One-half of each sample, flight and ground control, was delivered to a contractor investigator, and the other half was retained at MSFC for evaluation. Contractor participation in the evaluation was as follows:

- Cornell Aeronautical Laboratory: Samples 1, 2, and 10
- Arthur D. Little, Inc.: Samples 4, 7, and 8
- General Dynamics/Convair: Samples 5 and 11
- TRW Systems: Samples 6, 9, and 12

Precompressed Powder Compacts Containing Dispersed Particles

The primary objective of this group of samples was to observe the effects on distribution of particles in a powder metal matrix that was melted and solidified in a weightless environment. The density of the nonmelting particles differs from that of the matrix.

Processing of the flight and ground control samples in this group was accomplished by placing a capsule in the heater, heating for 10 minutes to melt the indium bismuth matrix, and then cooling on the heat sink for 30 minutes. In the case of the ground control sample, the heater and sample were horizontal during the heating cycle and vertical

TABLE 1. SAMPLE COMPOSITION

Sample Group	Specimen No.	Contents by Volume	Processing
A. Precompressed Powder Compacts Containing Dispersed Particles	1 2	70% InBi Powder, 30% W 70% InBi Powder, 30% B_4C	1 Melt 2 Solidify
B. Matrix Material with Fibers, Particles, Whiskers, and/or Gas	4 5 7 8 10 11	75% InBi w/SiC, 25% Ar 75% InBi w/BeCu, 25% Void 75% InBi, 25% Ar 75% InBi w/W, 25% Void 70% InBi, 30% W 75% Paraffin w/BeCu, 25% Void	1 Melt 2 Disperse by Shaking 3 Solidify
C. Immiscible Materials Dispersions	6 9 12	50% Paraffin, 50% NaAc 40% Paraffin, 40% NaAc, 20% Ar 40% Paraffin, 40% NaAc, 20% W	1 Melt 2 Disperse by Shaking 3 Solidify

Matrix Materials

InBi — indium bismuth eutectic alloy; melting point, 72°C; density, 8.2 g/cm^3

Paraffin — melting range 54 to 58°C; density, 0.9 g/cm^3

NaAc — sodium acetate trihydrate; melting point, 58°C; density, 1.8 g/cm^3

Dispersants

W — copper-coated tungsten microspheres; density, 19.3 g/cm^3

B_4C — copper-coated boron carbide microspheres; density, 2.52 g/cm^3

SiC — copper-coated silicon carbide whiskers; density, 3.6 g/cm^3

BeCu — beryllium copper fibers; density, 8.3 g/cm^3

Ar — argon gas

during the cooling cycle. A temperature profile (Fig. 4) taken during processing of ground control specimen 1 shows that the matrix material was molten after about 6 minutes and solidified after about 20 minutes. This curve is considered typical for all samples. Care was taken to minimize accelerations while these samples were molten.

Sample 1. A mixture of 30 percent by volume of spherical copper-coated tungsten particles and 70 percent by volume of indium bismuth eutectic powder was compressed to form a powder compact with a theoretical density of 96 percent. The tungsten particles and indium bismuth eutectic powder were of the same size, -325 mesh (less than 44 μm in diameter). The compact was subsequently placed in an aluminum capsule that was hermetically sealed by electron beam welding.

The sample was designed to observe the differences in distribution of higher density particles in a lower density matrix that was melted and solidified in reduced gravity as compared to a similar sample processed on earth. The density of the tungsten particles (19.3 g/cm^3) is significantly greater than the density of indium bismuth (8.2 g/cm^3), and significant segregation of particles was expected when the matrix was melted under gravity. In the flight sample, gravity-induced segregation was not expected and a more homogeneous distribution of particles was expected, since the molten metal would tend to flow around the particles separating those in contact after the compaction process.

A detailed evaluation of the powder compact samples was performed by Cornell Aeronautical Laboratory. They compared the distribution of particles in three specimens that were identical in composition and shape but processed differently. These included:

1. Specimen 1D-A-00 — an "as-pressed" specimen not melted.

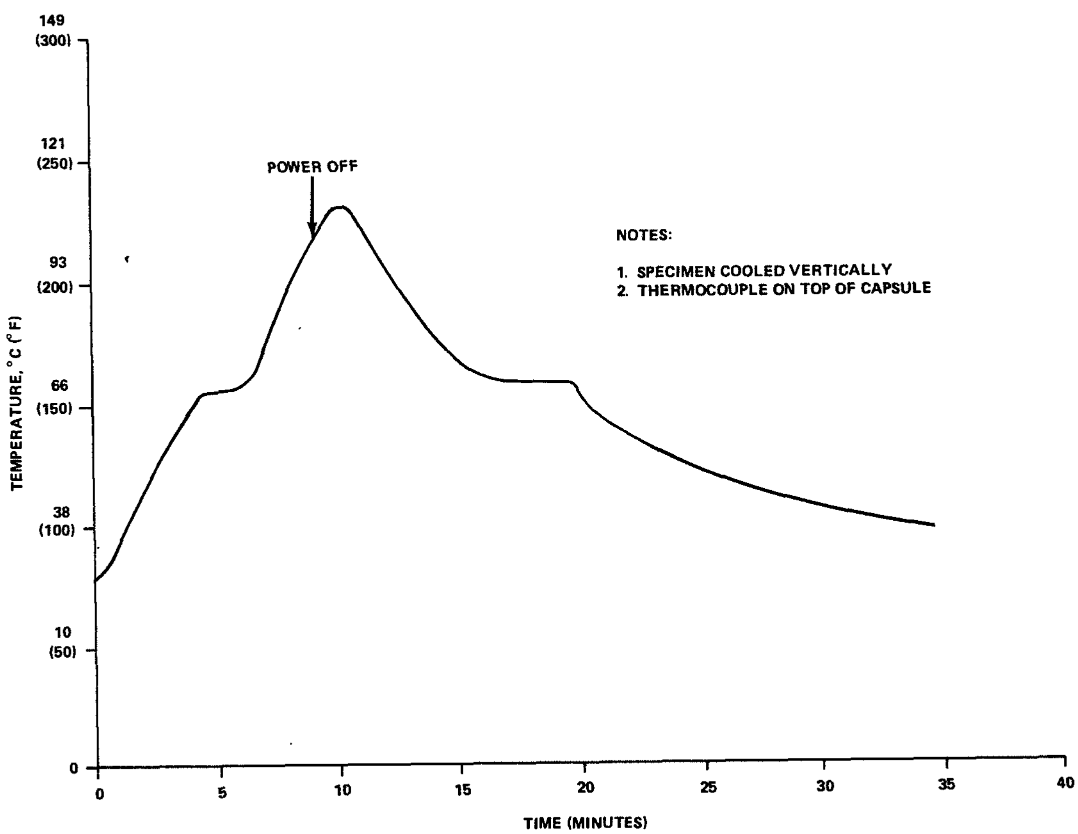

Figure 4. Heat test on specimen 1C.

2. Specimen 1C-A-00 — the control specimen melted and solidified under earth gravity.

3. Specimen 1F-A-00 — the flight specimen melted and solidified under zero gravity.

The processed samples were sectioned longitudinally and polished. Photomicrographs at 100X were made of each specimen at intervals in both the directional (axial) and cross-directional (radial) directions. The micrographs were enlarged two and one-half times for ease of counting. A point-count analysis was made to determine the distribution and volume fraction of dispersed particles. The observed results of the directional displays are shown in Figure 5. Data points taken from the cross-directional displays at the intersections with the center axis were compared with the directional displays, and generally there is good correlation between the two. A comparison of the data from the control and flight samples with the as-pressed sample indicates that a redistribution of particles occurs after melting and solidification. The distribution of the flight sample was more uniform than the control sample, indicating the advantages that may be attained by liquid phase sintering in zero gravity.

Sample 2. A mixture of 30 percent by volume of spherical copper-coated boron carbide (B_4C) particles and 70 percent by volume of indium bismuth eutectic powders was compressed to form three powder compacts with a theoretical density of 89 percent. The boron carbide particles and indium bismuth powders were of the same size, -325 mesh (less than 44 μm in diameter). In trying to press compacts to the lower theoretical density, it was impossible to obtain one of sufficient length to fill the capsule. Therefore, three compacts were used, each approximately 2.5 cm long. These were placed in an aluminum capsule and sealed by electron beam welding.

This sample was designed to observe the differences in distribution of lower density particles and gas bubbles in a higher density matrix that was melted and solidified in reduced gravity as compared to a similar sample processed on earth. The densities of the boron carbide particles (2.52 g/cm^3) and the air entrapped in the low density compact are significantly less than the density of indium bismuth (8.2 g/cm^3). Significant segregation was expected when the matrix was melted under gravity. In the flight sample, gravity-induced segregation was not

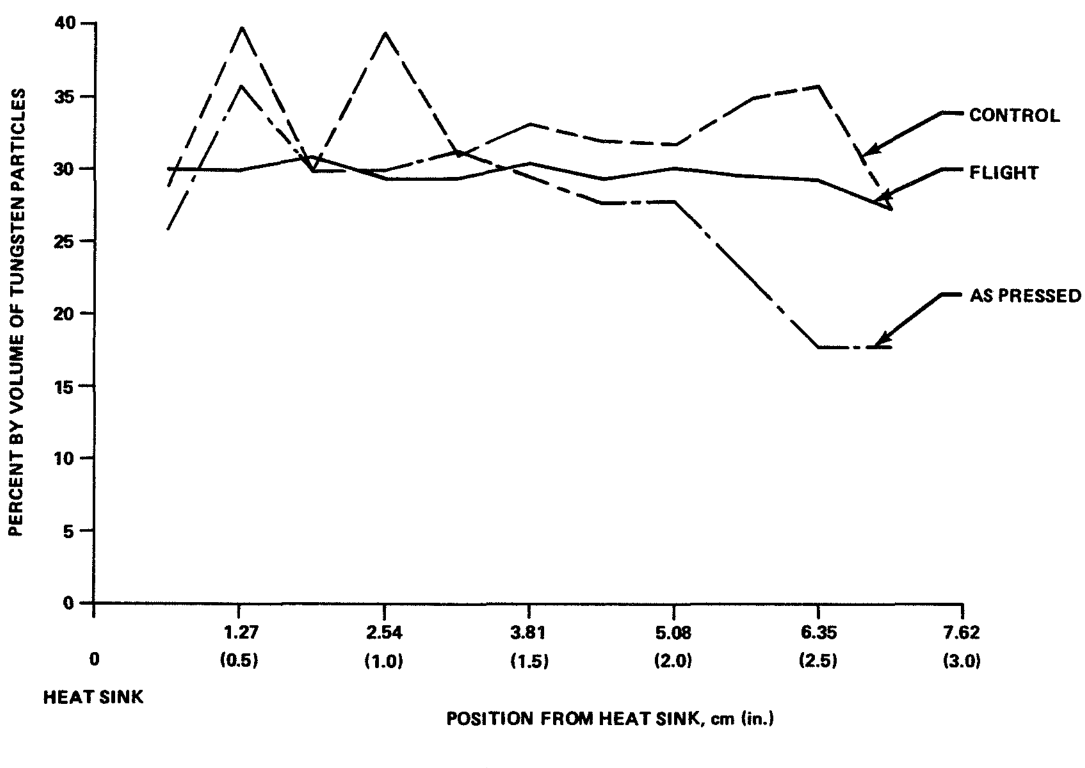

Figure 5. Directional display observed of sample 1.

expected and a more homogeneous distribution of particles was expected, since the molten metal would tend to flow around the particles separating those in contact after the compaction process.

An evaluation of these samples indicated that the powder compacts did not fully melt. Therefore, results from this sample were inconclusive.

Matrix Material with Fibers, Particles, Whiskers, and/or Gas

The primary objective of this group of samples was to demonstrate the dispersion of high and low density solid reinforcements and/or gases in a liquid phase matrix and the stability of such mixtures during solidification in a weightless environment.

Processing of the flight and ground control samples in this group was accomplished by placing the capsule in the heater, heating for 10 minutes to melt the matrix material, shaking to disperse the solids and gases in the liquid, and cooling on the heat sink for 30 minutes. The shaking procedure involved bumping each end of the heater against the heel of the hand four times to dislodge any particles trapped in the ends of the capsule; three cycles of alternately shaking the heater linearly 10 cycles and oscillating 15 cycles; and finishing by oscillating 10 cycles going from vigorous motion to very slow motion. Tests with model systems in transparent models showed this to be the best mixing procedure under the circumstances. A mechanical device would have been preferred to obtain a more vigorous, controlled mixing; however, the development and integration of such a device into the demonstration was not possible in the time available.

Evaluation of samples in this group was performed by MSFC's Process Engineering Laboratory and Astronautics Laboratory and by Arthur D. Little, Inc. on samples 4, 7, and 8 and General Dynamics, Convair Aerospace Division on samples 5 and 11.

Sample 4. Approximately 1.5 g of copper-coated silicon carbide whiskers were mixed with approximately 90 g of liquid indium bismuth eutectic, poured into a preheated aluminum capsule, and allowed to solidify. The remaining 25 percent of the capsule volume was filled with argon and the capsule was sealed. The silicon carbide whiskers (1 to 10 μm in diameter and 20 to 400 μm long) were copper-coated by an electroless plating process to promote wetting; however, it was subsequently learned that the copper-coated whiskers had oxidized prior to mixing with the metal and were essentially non-wetting.

The objective of this demonstration was to achieve a uniform distribution of whiskers and gas bubbles in a metal matrix by melting the matrix, shaking to mix the materials, and directionally solidifying in zero gravity. Areas of whisker-reinforced foam were expected in the flight sample even though the mixing techniques were inadequate to achieve a uniform dispersion. The whiskers and gas were expected to segregate from the matrix in the ground sample because of the differences in density.

The bottom fifth, dark area, of the control sample as shown in Figure 6 is fully dense with no silicon carbide whiskers or gas porosity retained. This is attributed to gravity separation of the lighter whiskers and gas bubbles. The retention of gas bubbles in the remainder of the sample is surprising because of the low viscosity of the indium bismuth alloy when molten. It appears that the whiskers have increased the apparent viscosity

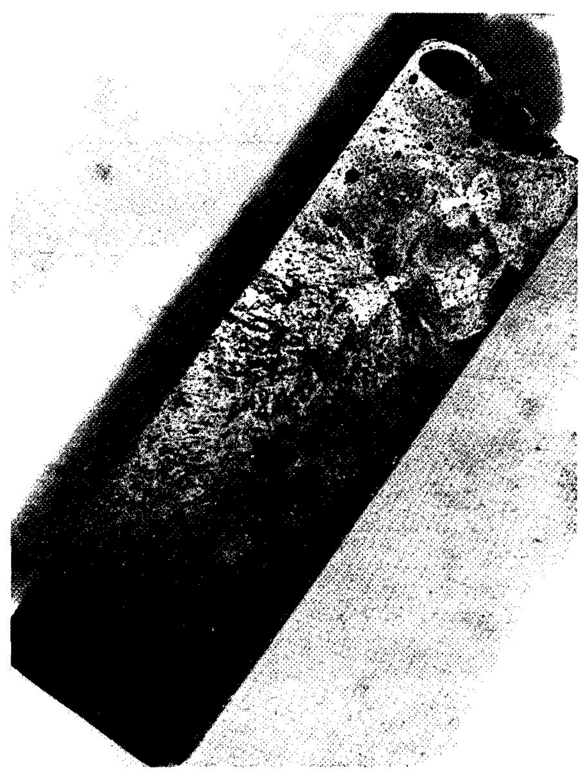

Figure 6. Macrograph of control specimen 4C-A-00.

to the point where they could not rise to the top before solidification occurred.

In contrast, the flight sample shown in Figure 7 is very uniform throughout, both in microstructure and in distribution of the gas pores. A true foam structure did not form; however, a fairly uniform dispersion of gas bubbles was maintained throughout the time required for solidification.

Sample 5. The sample was prepared by placing approximately 7 g of coated beryllium copper fibers (approximately 0.13 mm in diameter by 2.5 mm long) into a preheated aluminum capsule and then pouring in approximately 97 g of indium bismuth eutectic alloy. The mixture filled approximately 75 percent of the capsule volume. After solidification of the contents, the capsule was backfilled with argon gas and sealed by electron beam welding. Postflight evaluation of the samples determined that most of the gas had leaked from these samples during the electron beam welding operation because of failure of an O-ring seal.

The objective of this demonstration was to achieve a uniform dispersion of high strength fibers and gas bubbles in a metal matrix by melting the matrix, shaking to mix the materials, and solidifying in zero gravity. Areas of fiber-reinforced foam were expected in the flight sample if the gas had been contained in the capsule. Gravity-induced segregation was expected in the ground control even though the fibers were of approximately the same density as the matrix.

An improvement in homogeneity of fiber distribution in the flight specimens over that obtained in the ground control specimens was noted. This is most obvious in photomacrographs of the longitudinal cross sections (Fig. 8) and in a neutron radiograph of a lengthwise slice of 0.31 cm (0.125 in.) thickness (Fig. 9). The gravity-induced segregation in the ground sample is evident, even though the density of the fibers was only about 1 percent greater than that of the matrix material. The bulk of the fibers settled to the bottom; however, because of the relatively high surface area

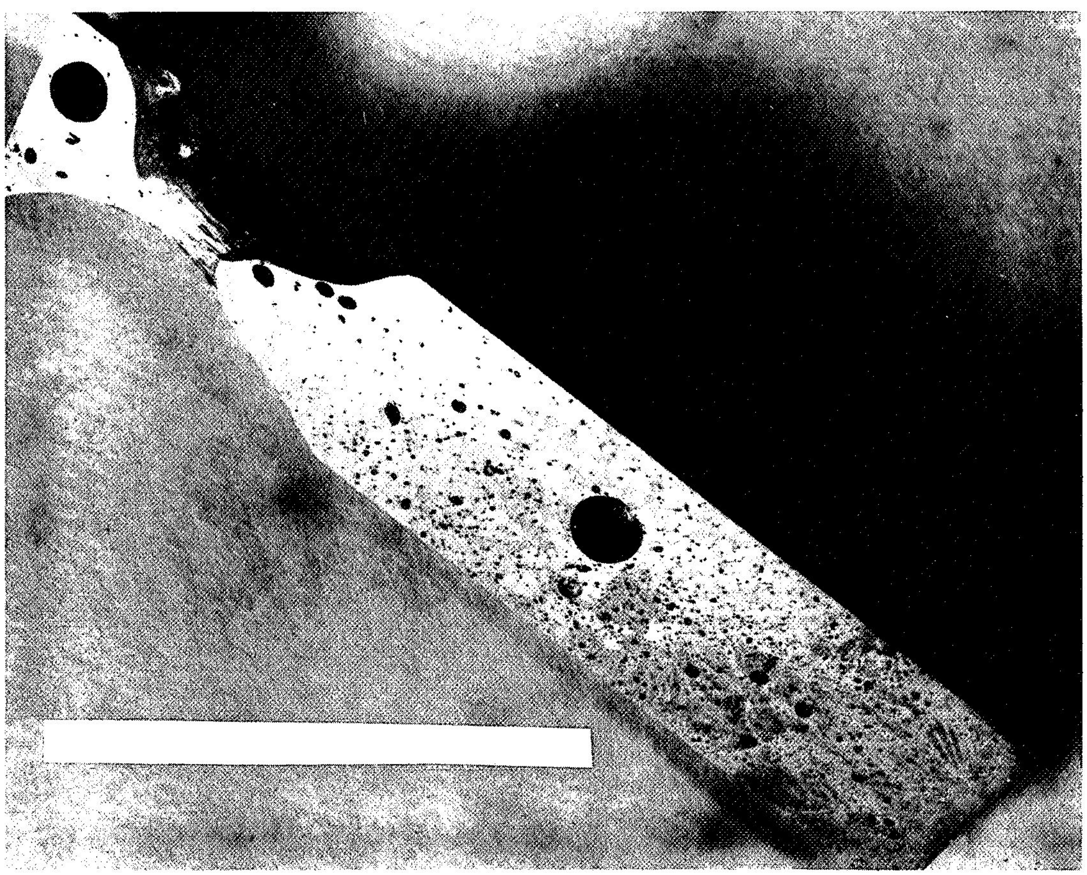

Figure 7. Macrograph of flight specimen 4F-A-00.

Figure 8. Fiber distribution, Apollo specimen 5.[1]

of the fibers and the small density difference between fiber and matrix, some fibers were trapped at the surface.

Distinct differences were observed in comparing the surface features of the ground control and flight specimens (Fig. 10). These differences can be attributed to the relative effects of gravity and surface tension in the processing environment. The liquid matrix readily assumed the shape of the container in the ground-processed sample and retained this shape upon solidification. In the flight sample, however, surface tension caused the melt to assume a hemispherical shape at the free ends (Fig. 11). Where

Figure 9. Neutron radiograph of 0.31-cm (0.125-in.) longitudinal slice (samples 5C and 5F).

fibers were present at the surface, the melt tended to retract from them which resulted in numerous depressions, exposed fibers, and a general rolling appearance. This is evident in the scanning electron microscope (SEM) pictures in Figure 11.

Sample 7. The samples consisted of 75 percent by volume indium bismuth eutectic alloy and 25 percent by volume argon gas. Approximately 100 g of molten indium bismuth eutectic alloy were poured into a preheated aluminum capsule, and a stainless steel mixing screen was preheated and inserted while the alloy was still molten. After cooling, the capsule was backfilled with argon and sealed.

The objective of this demonstration was to achieve a uniform distribution of a gas in a metal matrix by melting the matrix, shaking to mix the gas into the matrix, and solidifying in zero gravity.

1. All figures in this paper that have magnifications shown have been reduced for printing purposes.

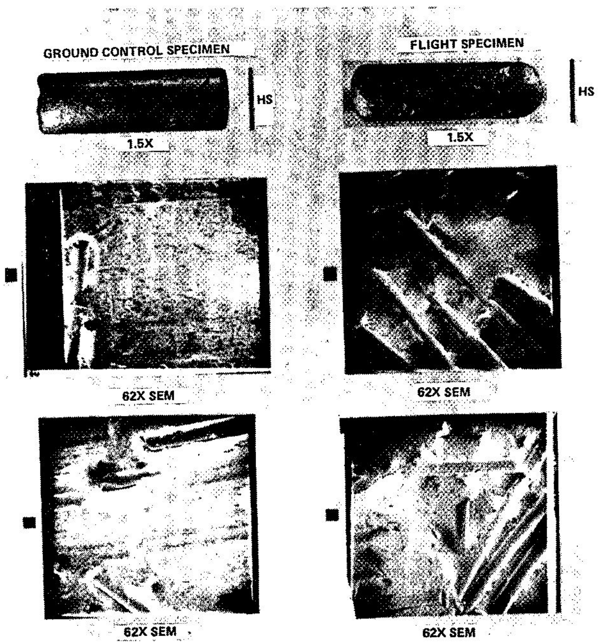

Figure 10. Surface feature comparisons.

Areas of metal containing dispersed gas bubbles were expected in the flight sample. Complete separation of the gas from the higher density metal was expected in the ground sample.

The control sample (Fig. 12) had no observable foam or gas porosity, indicating complete separation under gravitation. In contrast to the control sample, the flight sample (Fig. 13) does exhibit some retained porosity. The porosity is approximately 3 percent in the bottom half and 5 percent in the top half by volume.

In the flight sample the melt was very nearly in a free-float condition. The macrostructure reveals that contact with the container, and therefore heat extraction, occurred at only a few places. One interesting feature of the flight sample is the existence of several regions that have the appearance of rosettes or flower petals.

<u>Sample 8</u>. This sample was prepared by pouring approximately 21 g of copper-coated spherical tungsten particles (approximately 100 μm in diameter) into a preheated aluminum capsule and then adding approximately 99 g of molten indium bismuth eutectic. This filled 75 percent of the capsule. The remaining 25 percent was filled with argon gas and the capsule was sealed. Postflight examination of the specimen determined that the argon had leaked

Figure 11. Surfaces of flight sample and ground sample (samples 5F and 5C).

from the capsule during the welding operation because of failure of an O-ring seal.

The objective of this demonstration was to achieve a uniform dispersion of the dense spheres and argon gas bubbles. Areas of dispersed particles and gas bubbles were expected in the flight sample if the gas had been contained in the capsule. Gravity-induced segregation was expected in the ground control sample.

There were no tungsten spheres in the bulk of the control sample (Fig. 14). There were a few trapped in the matrix of the last material to freeze at the end opposite the heat sink. The remainder of the spheres was not incorporated into the solidified sample and was found on the external surfaces. If

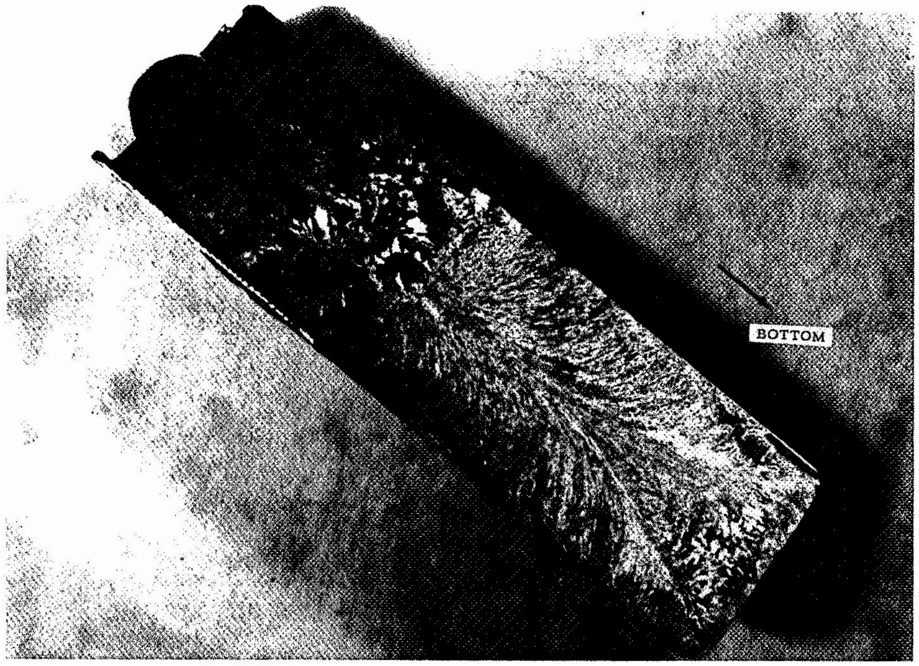

Figure 12. Macrograph of control specimen 7C-A-00.

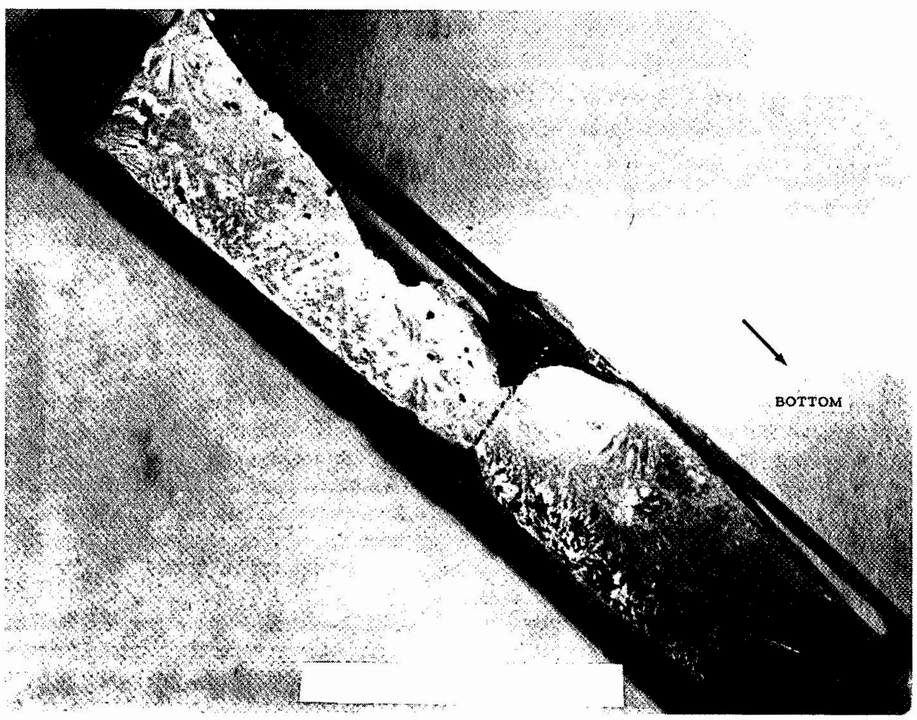

Figure 13. Macrograph of flight specimen 7F-A-00.

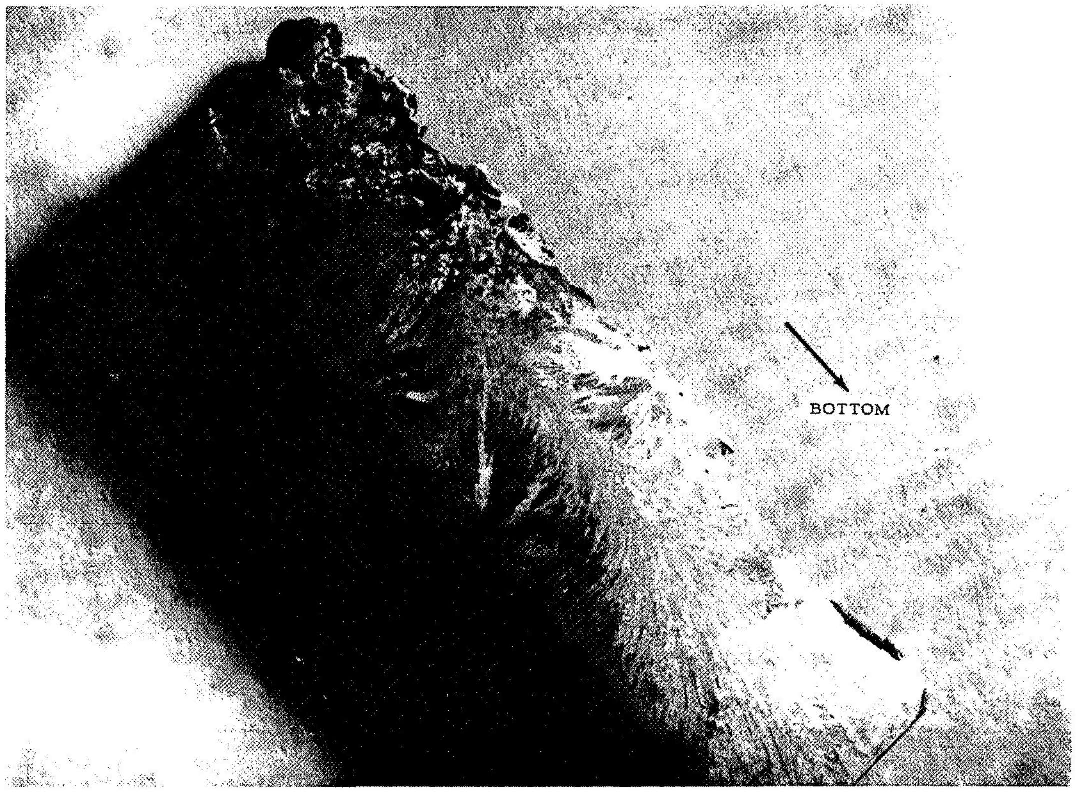

Figure 14. Macrograph of control specimen 8C-A-00.

any of the spheres were dispersed in the melt prior to solidification, they were pushed ahead by the liquid-solid interface because of their nonwetting characteristics, or they settled out under gravitation.

A considerable number of the spheres were found within the flight sample (Fig. 15), primarily in the shrinkage pores. As with flight samples 4 and 7, solidification appears to have initiated at a number of sites, so that the pore and sphere distribution are macroscopically quite uniform throughout the sample.

Sample 10. Approximately 105 g (30 percent by volume) of copper-coated spherical tungsten particles (approximately 100 μm in diameter) were placed into a preheated aluminum capsule, a tungsten mixing pellet was added, and then approximately 100 g of molten indium bismuth eutectic (70 percent by volume) were poured into the capsule. After the alloy had solidified, the capsule was sealed.

The objective of this demonstration was to achieve a uniform dispersion of the dense particles in the metal matrix. Areas of dispersed particles were expected in the flight sample. Gravity-induced segregation was expected in the ground control sample.

When the control sample was opened, large quantities of the microspheres fell out of the container, and cutting the sample in half released more of the microspheres. The copper-coated microspheres had oxidized prior to filling the capsule and were therefore not wetted by the molten indium bismuth. They aggregated and did not disperse through the specimen. The longitudinal section through the control sample (Fig. 16) shows no particles in the matrix.

The flight sample is quite different from the control sample because it was melted and shaken in space more than once because of RCS firings during the cooling cycle. The total time this sample was molten and shaken is not known; however, the repeated melting and shaking resulted in a better dispersion than was achieved in sample 8. Again,

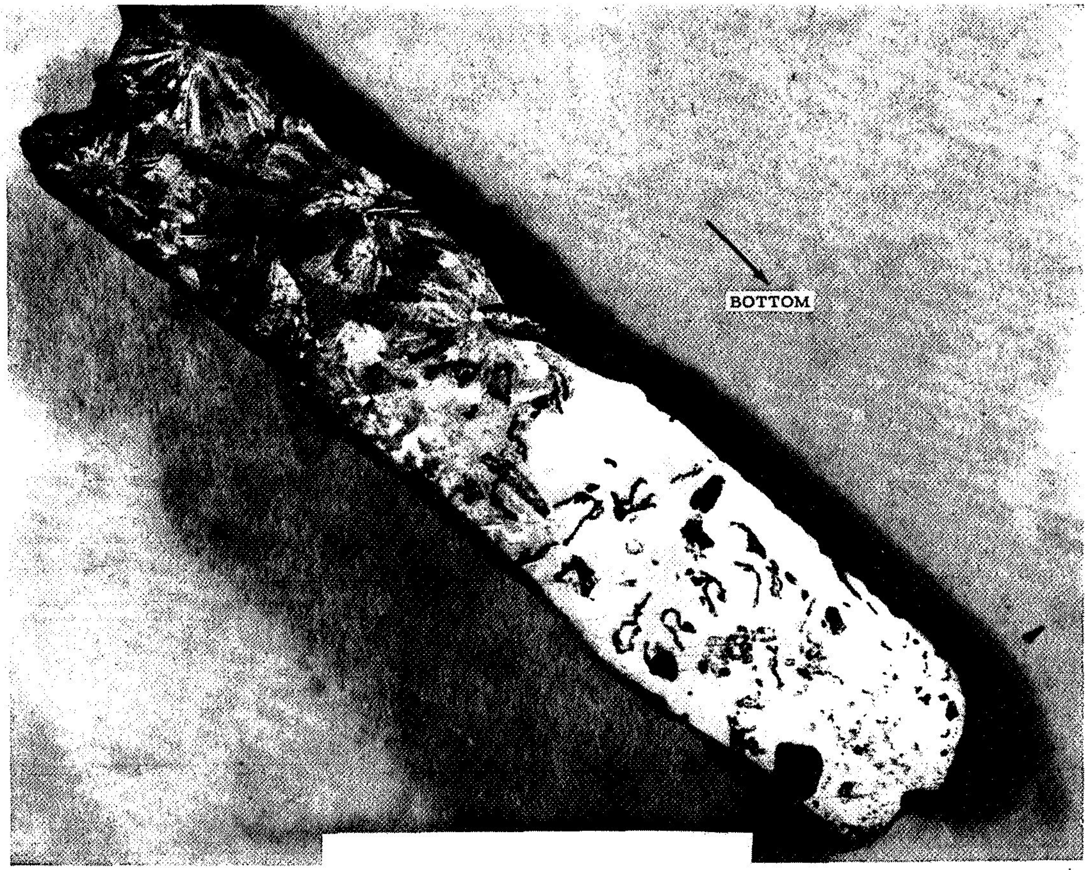

Figure 15. Macrograph of flight specimen 8F-A-00.

when this sample was opened and sectioned, a large quantity of tungsten microspheres fell out.

A comparison of the flight sample with the control sample (Figs. 16 and 17) revealed:

1. A more homogeneous distribution of microspheres in the flight sample.

2. Adhesion of the metal matrix to the microspheres throughout the exposed surface and especially in the large pockets that contained the loose non-wetting spheres.

3. Greater sphericity of the external surface of the flight sample; additionally, the pockets show more sphericity. These attributes are expected in metals processed in space.

Sample 11. Approximately 7 g of cerrobend-coated beryllium copper fibers (approximately 0.13 mm in diameter and 2.5 mm long) were placed in a preheated aluminum capsule; approximately 10 g of paraffin were then melted and poured into the capsule, filling 75 percent of the capsule volume. After the paraffin solidified, the capsule was back-filled with argon and sealed. Postflight examination of the specimens revealed that most of the argon had leaked out during the welding operation because of failure of an O-ring seal.

The objective of this demonstration was to obtain a uniform dispersion of fibers and gas in the matrix. Paraffin was chosen to provide a visual display of the dispersion. Areas of fibers and gas bubbles dispersed in the paraffin were expected in the flight sample. Gravity-induced segregation was expected in the ground control sample.

At the time of sample preparation, only coated fibers were available for flight sample 11F. Since the processing temperature was higher than the melting temperature of the coating, the coating melted during processing causing the fibers to

Figure 16. Control specimen 10C-B-00, 3X magnification.

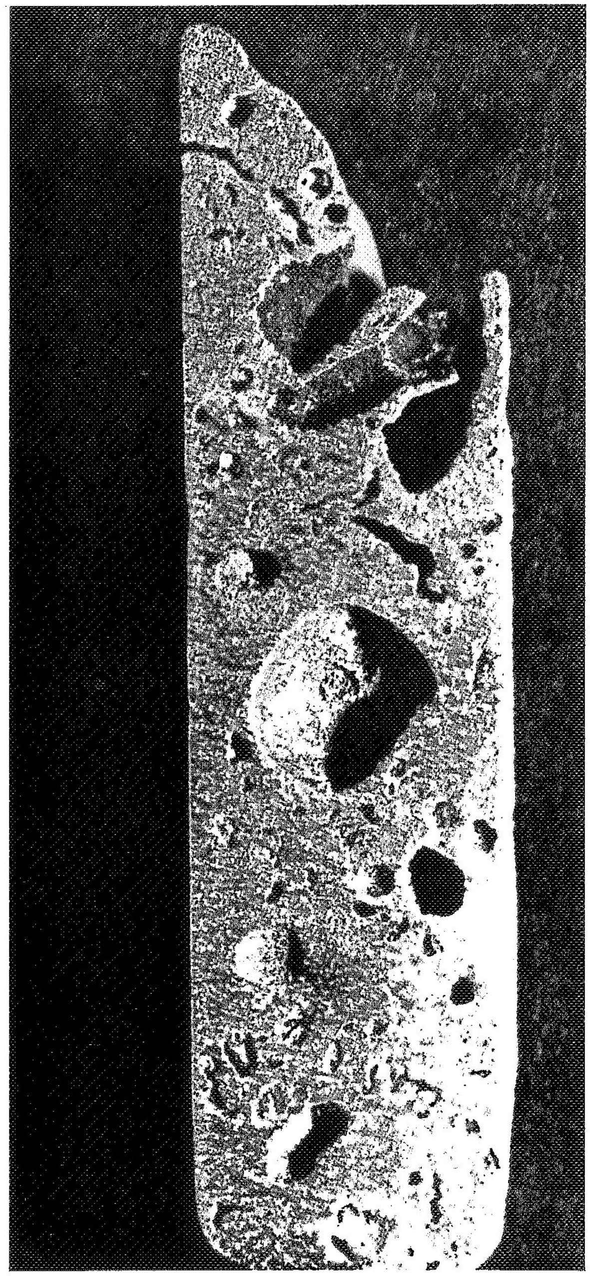

Figure 17. Flight specimen 10F-B-00, 3X magnification.

literally solder themselves into one single block of paraffin-fiber composite, while the remaining part of the sample was pure paraffin (Fig. 18). Consequently, the objectives of fiber dispersion and fiber-bubble interaction were not achieved.

As can be observed by comparing the flight sample and the ground sample (Fig. 18), a stable dispersion of gas bubbles has been achieved under zero-gravity conditions, while all bubbles in the ground sample were removed by buoyancy. A

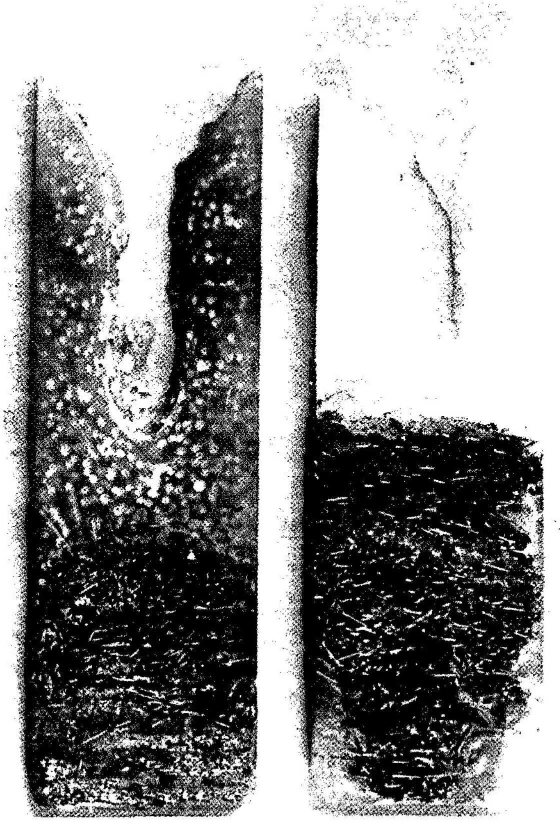

FLIGHT GROUND

Figure 18. Cross section of paraffin matrix, (samples 11F and 11C).

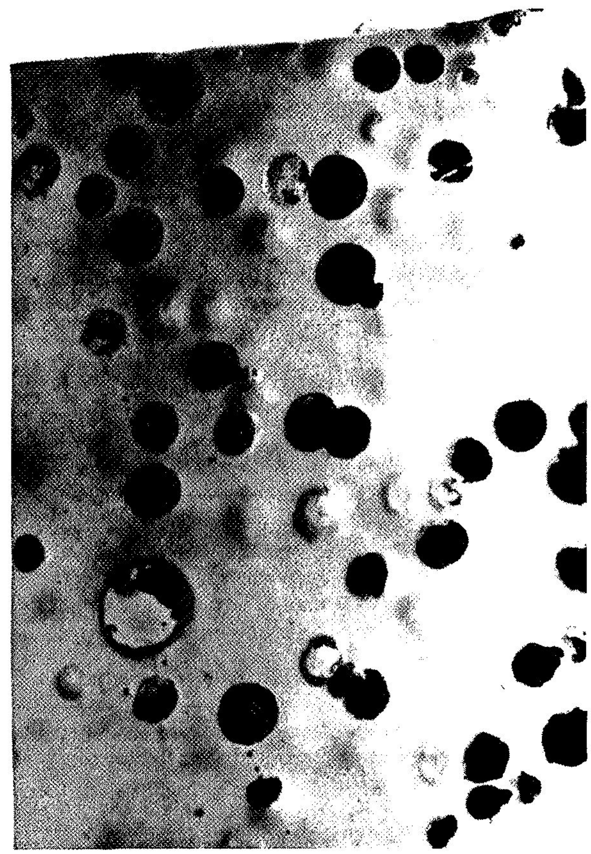

Figure 19. Closeup of gas bubbles in paraffin flight sample 11F (dark bubbles are in cut surfaces).

closeup of the bubbles is shown in Figure 19. A black coloring of the bubbles at the surface, resulting from sample cutting, was deliberately retained to distinguish them from the bubbles below the surface (light coloring). In view of the limited amount of gas present, only a low bubble density was obtained, eliminating the problems of bubble coalescence and surface stabilization.

The bubble gas may also have originated from volatiles of the paraffin. However, for the objective of this experiment, the source of the gas is immaterial.

Immiscible Materials Dispersions

The primary objective of this group of samples was to determine the effect of a low gravity environment on the dispersion of immiscible materials.

Processing of the flight and ground control samples in this group involved heating for 10 minutes to melt the immiscible materials, shaking to disperse them, and cooling for 30 minutes to solidify the sample.

Capsule Contents.

Specimen 6. 50 percent paraffin and 50 percent sodium acetate by volume; tungsten mixing pellet.

Specimen 9. 40 percent paraffin, 40 percent sodium acetate, and 20 percent argon by volume; tungsten mixing pellet.

Specimen 12. 50 percent paraffin, 40 percent sodium acetate, and 20 percent tungsten spheres by volume; tungsten mixing pellet.

Sample Composition and Preparation. Sample preparation was similar in all cases except for the addition of argon in specimen 9 and the 100-μm spherical tungsten particles in specimen 12. The procedures used are discussed in the following.

The sodium acetate trihydrate was prepared by melting at 68°C and then filtering to remove any unmelted crystals. The melted, filtered sodium acetate was then poured into a preheated capsule to the desired level and the tungsten mixing pellet was added. In specimen 12, the tungsten particles were added at this point. The melted paraffin was added to the desired level and allowed to solidify. A needle was used to puncture the paraffin to admit air and insure solidification of the sodium acetate. Sodium acetate has a tendency to supercool in the absence of air. At this point specimen 9 was backfilled with argon. The capsules were then sealed with a cap with an O-ring seal and were finally sealed by electron beam welding. Subsequent examination determined that the argon leaked out of ground control specimen 9.

Expected Observations. It was expected that there would be essentially complete segregation of the immiscible materials and the other phases in the ground samples. Zones of stabilized dispersions were expected in the flight samples.

Results. The samples in this group are extremely fragile and it was decided to allow the contract investigator, TRW Systems Group, to complete evaluation of one-half of each sample before further evaluation was attempted by MSFC or other evaluators. The results presented here are the findings of TRW.

Figure 20 is a schematic representation of the photographic documentation procedure utilized to evaluate the degree of dispersion in the specimens. The surfaces of the intact specimens were polished and then photographed at various magnifications. The specimens were then sectioned, the side of each sectioned sample closest to the heat sink end was polished, and photographs at various magnifications were taken.

Sample 6.

- Control Specimen 6C-A-00 — The paraffin, the dark material on the left in Figure 21, and sodium acetate are segregated in the control specimen with the exception that the shrinkage tube is filled with sodium acetate. This probably occurred when the

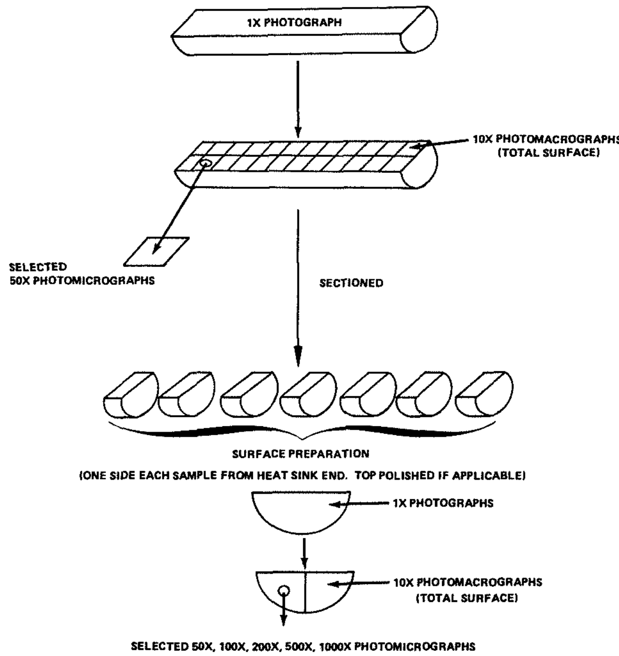

Figure 20. Schematic outline of photographic documentation procedure.

paraffin solidified, creating a partial vacuum at the top of the capsule, and aspirated the still liquid sodium acetate into the shrinkage tube.

- Flight Specimen 6F-A-00 — The sodium acetate and paraffin are partially segregated; however, there is some dispersion of sodium acetate in paraffin and paraffin in sodium acetate (Fig. 21). A thin coating of sodium acetate surrounds most of the outside of the paraffin. The sodium acetate spheres in the paraffin are reasonably uniform with the majority of the spheres being approximately 1.2 mm in diameter. The paraffin dispersions, however, are spheres with widely varying diameters.

Sample 9.

- Control Specimen 9C-A-00 — The paraffin and sodium acetate in the control sample are completely segregated (Fig. 22), with an empty shrinkage tube, unlike 6C-A-00. This is probably a result of the gas space in the capsule. The interface is almost perfectly flat, with some rounding at the sides where the capsule was in contact with the material. The sodium acetate is crystallized in a random manner, with a few large crystals in the center of the material.

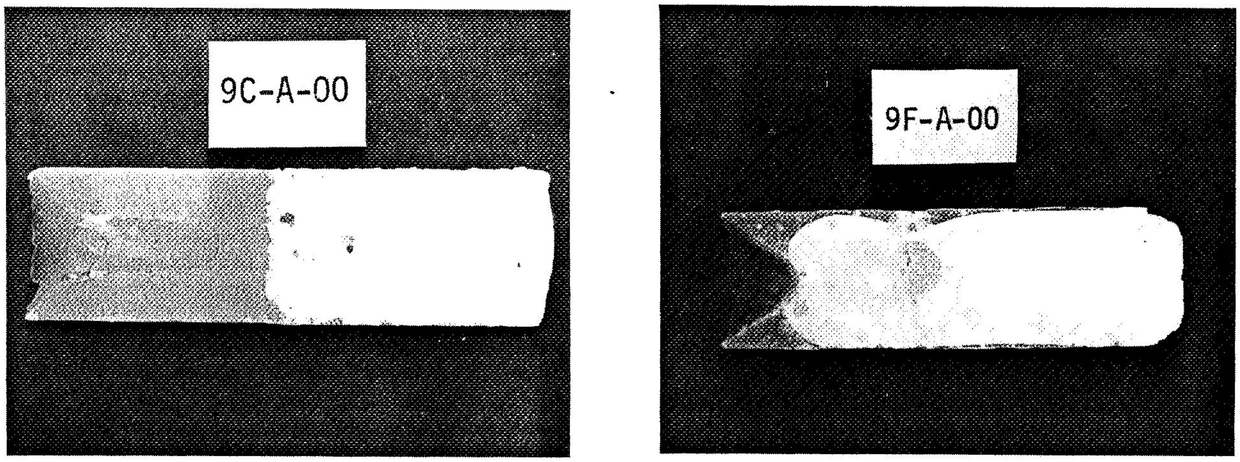

CONTROL FLIGHT

Figure 21. Sample 6, 1X magnification.

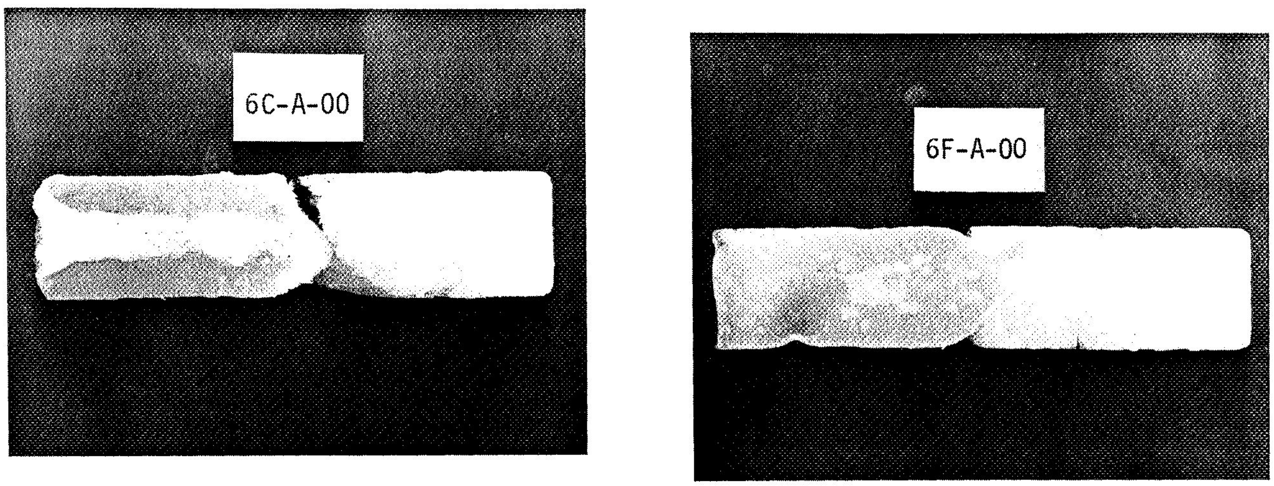

CONTROL FLIGHT

Figure 22. Sample 9, 1X magnification.

- Flight Specimen 9F-A-00 — The sodium acetate and paraffin are almost completely dispersed (Fig. 22). A thin layer of paraffin was located in the top of the capsule away from the heat sink, along with a small amount of sodium acetate (not shown). Thus, the shrinkage tube was actually a large gas pocket surrounded by paraffin. In addition, a thin layer of paraffin surrounds the entire dispersion. Interspersed in the paraffin shell are small spheres of sodium acetate and a few voids or gas pockets. The paraffin is primarily dispersed in the sodium acetate. A number of spheres consisting of a thin shell of paraffin enclosing a sphere of sodium acetate were observed in the sample (Fig. 23). This is known as the "grapeskin effect," or duplex dispersion, and has been observed in oil-water mixtures and in wet jet fuel being pumped through pipelines. In other areas a "double grapeskin effect," or a complex duplex dispersion, was observed. In this type dispersion paraffin

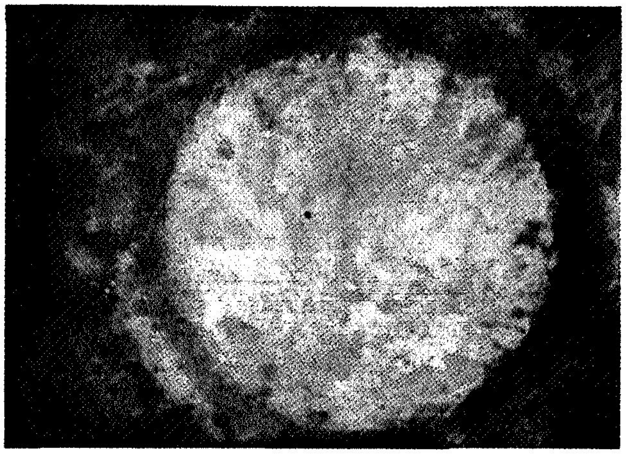

FLIGHT SPECIMEN 9F-A-00
DUPLEX DISPERSION OF PARAFFIN-SODIUM ACETATE
IN SODIUM ACETATE
50X MAGNIFICATION

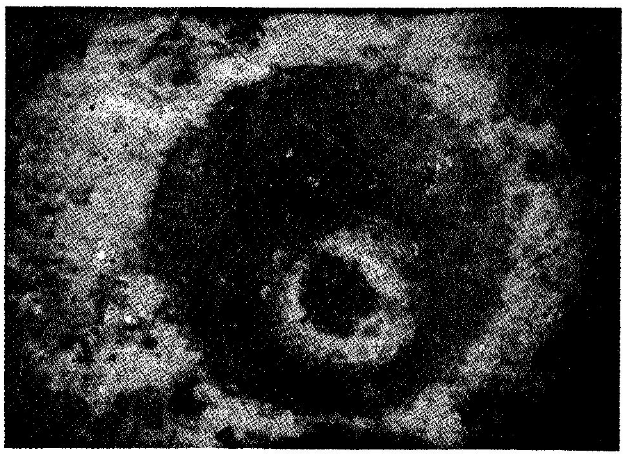

FLIGHT SPECIMEN 9F-A-00
COMPLEX DISPERSION OF PARAFFIN-SODIUM ACETATE-
PARAFFIN IN SODIUM ACETATE
50X MAGNIFICATION

Figure 23. Selected areas of specimen 9F-A-00.

surrounds sodium acetate which in turn surrounds paraffin, as seen in Figure 23.

Sample 12.

- Control Specimen 12C-A-00 — The paraffin, sodium acetate, and tungsten microspheres are segregated with the exception of a small cap of sodium acetate with a few tungsten microspheres over the top of the shrinkage tube (Fig. 24). The cap probably was formed in the same manner as mentioned for 6C-A-00.

The paraffin, sodium acetate interface is slightly rounded, but is not as smooth as that formed in the other two control samples. There are several droplets of paraffin embedded in the main body of the paraffin and a few tungsten microspheres present in the interface.

The sodium acetate, tungsten microsphere interface is partially graded. Microscopic examination of the interface indicates that as the sodium acetate crystallized, some of the tungsten microspheres were displaced into the predominantly sodium acetate phase.

- Flight Specimen 12F-A-00 — There appear to be three types of sodium acetate, paraffin, tungsten microsphere dispersions: a dispersion of paraffin (containing 90 percent of the tungsten microspheres) into the sodium acetate; paraffin with some sodium acetate dispersed into it; and a tungsten microsphere, paraffin blend with a dispersion of sodium acetate (Fig. 24). Since the tungsten microspheres are preferentially wetted by the paraffin, the continuous phase is predominantly paraffin with the sodium acetate as the dispersant over most of the length of the specimen.

- Surface Characterization, Sectioned Samples — All the control and flight specimens were axially sectioned at 0.63-cm (0.25-in.) intervals starting from the heat sink end, mounted in epoxy to prevent damage, and polished. The widely varying hardness of the specimen materials caused some damage to the polished surfaces of the samples, but satisfactory photomicrographs up to 1000X were taken and the morphological details of the samples could be observed easily. All the specimen samples were photographed at 1X and 10X, and selected area photomicrographs from 50X to 1000X were taken for study.

Sample 6.

- Control Samples 6C-A-01 through -12 — The crystal habit near the heat sink end for the control samples is random with dispersed 0.5- to 1.5-mm crystals in the axially cut plane. After approximately 1.4 cm, the crystals tend to become finer and randomly oriented up to the sodium acetate, paraffin interface. The interface area shows a relatively uniform transition from sodium acetate to paraffin, with a very small dispersion depth of approximately 0.5 mm maximum. The paraffin is free of sodium acetate except for the filled shrinkage tube. The distortion of the voids toward the interior of the samples indicates that

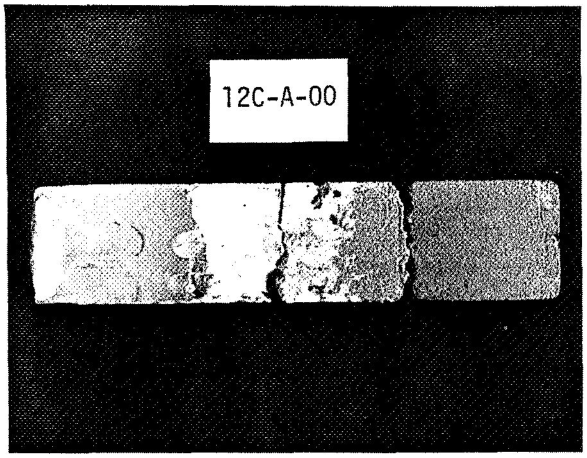

CONTROL

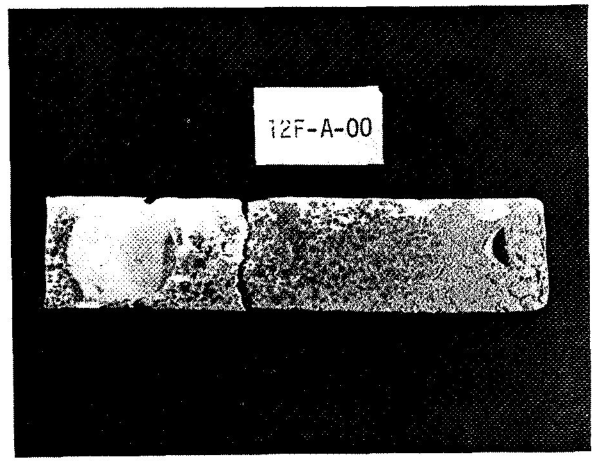

FLIGHT

Figure 24. Sample 12, 1X magnification.

the postulation of aspiration of the sodium acetate into the shrinkage tube is valid.

- Flight Samples 6F-A-01 through -13 — The crystal habit of the sodium acetate near the heat sink end consists primarily of fine crystals randomly dispersed. The crystal habit changes rather abruptly approximately 0.5 cm from the end, with the crystals becoming oriented toward the center of the specimen. The orientation angle changes gradually from approximately 45 deg to 90 deg (parallel to the axial plane) 2.5 cm from the heat sink end.

Numerous paraffin inclusions are dispersed throughout the sodium acetate-rich region. Most of the paraffin dispersions are spherical in shape, but a number of distorted spheres and elongated ellipsoids are present in the area where the sodium acetate is directionally oriented. This would indicate rather steep thermal gradients and concomitant directional solidification of the sodium acetate. Photomicrographs at 1000X (Fig. 25) show extremely fine, irregularly shaped dispersions of sodium acetate and paraffin (1 μm or less) in the grain boundaries of the sodium acetate crystals. It is not known if the solidification forced the dispersions to the grain boundaries or whether these dispersions were nucleation sites. In general, the spherical paraffin dispersions range from 4 mm to 1 μm in diameter.

The sodium acetate dispersions in the paraffin-rich region are relatively uniform spheres, the majority having diameters between 1 and 2 mm.

Sample 9.

- Control Samples 9C-A-01 through -10 — The sodium acetate near the heat sink end consists of small, random crystals for approximately 1 cm. Crystals having 2- to 4-mm lengths are randomly dispersed for approximately the next 1.5 cm and then tend to become finer up to the sodium acetate, paraffin interface.

The interface area shows a relatively uniform transition, with a dispersion depth of approximately 0.5 mm as in the case of control specimen 6, and the sodium acetate and paraffin are completely segregated.

- Flight Samples 9F-A-01 through -10 — Each sample surface of flight specimen 9 shows dispersions of sodium acetate in paraffin or paraffin in sodium acetate (Fig. 26). The majority also contain duplex dispersions and, in many instances, more complex dispersions of sodium acetate and paraffin.

The dispersions for the most part are spherical, although some of the sodium acetate dispersions in the duplex dispersions have irregular, crystalline shapes. Photomicrographs at 1000X show dispersions of 1 μm or less (Fig. 26). The dispersed phase in these cases is predominantly irregularly shaped sodium acetate crystals.

FLIGHT SPECIMEN 6F-A-05
1-μm DISPERSION
PRIMARILY SODIUM ACETATE IN PARAFFIN
1000X MAGNIFICATION

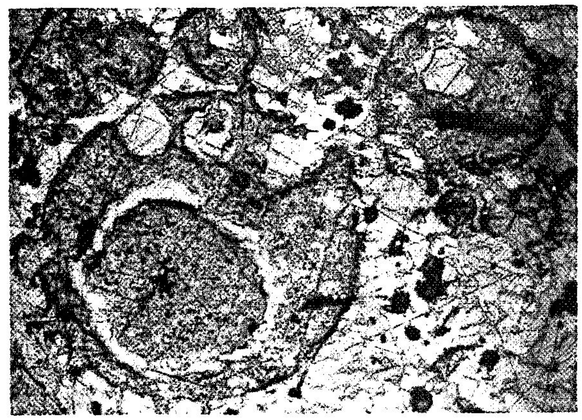

FLIGHT SPECIMEN 9F-A-07
COMPLEX DISPERSIONS OF PARAFFIN-SODIUM ACETATE-PARAFFIN IN SODIUM ACETATE; ALSO SODIUM ACETATE IN PARAFFIN IN SODIUM ACETATE
50X MAGNIFICATION

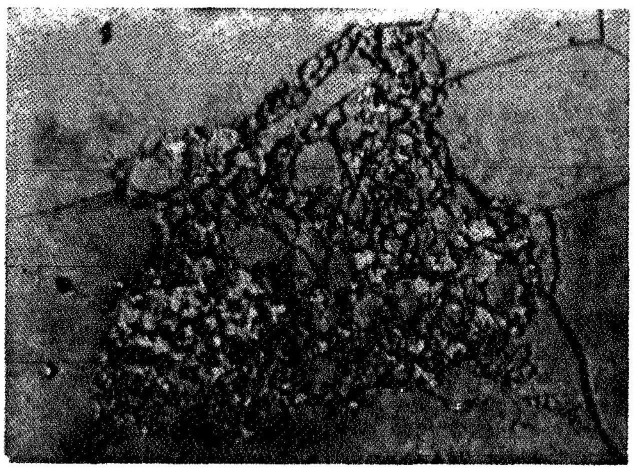

FLIGHT SPECIMEN 6F-A-02
1-μm DISPERSION OF SODIUM ACETATE IN PARAFFIN SURROUNDED BY SODIUM ACETATE
1000X MAGNIFICATION

Figure 25. Fine dispersions in specimen 6F.

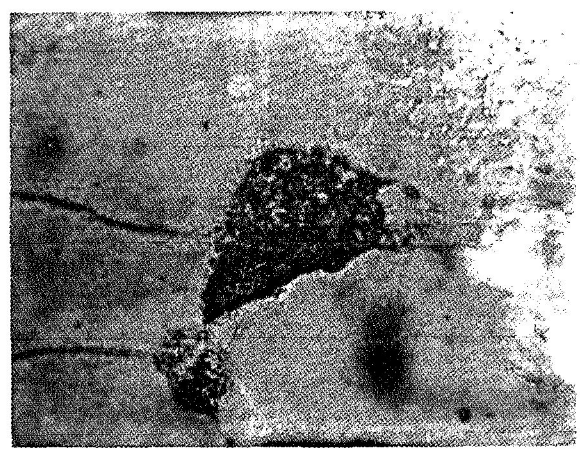

FLIGHT SPECIMEN 9F-A-01
1-μm DISPERSION OF SODIUM ACETATE IN PARAFFIN SURROUNDED BY SODIUM ACETATE, HEAT SINK END
1000X MAGNIFICATION

Figure 26. Fine dispersions in specimen 9F.

The spherical dispersions range in diameter from 8 mm to approximately 1 μm, although there may be smaller dispersions not optically resolvable.

Sample 12.

- Control Samples 12C-A-01 through -13 — The sectioned samples exhibited similar morphological details as were shown on the surface of the unsectioned specimen. The tungsten is primarily segregated in the first 2.5 cm from the heat sink end, and the tungsten, sodium acetate interface dispersion depth is approximately 8 mm. The sodium acetate region is predominantly crystallized in a fine, random orientation and exhibits a porous structure. There are a few moderately sized (0.5 mm) sodium acetate crystals near the sodium acetate, paraffin interface, which has a dispersion depth of approximately 5 mm. Some tungsten microspheres are randomly dispersed throughout the specimen samples, with a higher concentration located at

the top of the shrinkage tube along with some sodium acetate.

- Flight Samples 12F-A-01 through -14 — There are three primary types of dispersions present within flight specimen 12 as mentioned previously: (1) a tungsten microsphere, paraffin blend with a dispersion of sodium acetate; (2) a tungsten microsphere, paraffin blend dispersed in sodium acetate; and (3) sodium acetate dispersed in paraffin. These dispersions occur within various areas of the samples and are described below.

The dispersion of sodium acetate in the tungsten microsphere, paraffin blend is predominant in the first 4.5 cm of length from the heat sink end. The concentration of tungsten microspheres decreases away from the heat sink end, and the dispersion type changes to the tungsten microsphere, paraffin blend dispersed in sodium acetate for approximately 1 cm up to the shrinkage cavity and at the top of the specimen. The shrinkage cavity is surrounded by a paraffin sphere containing a dispersion of sodium acetate.

The sodium acetate dispersed in paraffin is spherical, but the majority of the other two types of dispersions are either distorted spheres or irregular in shape. This is in contrast to flight specimens 6 and 9, where the dispersions are predominantly spherical. Since the tungsten microspheres are preferentially wetted by the paraffin, this blend has the tendency to form a continuous phase and become a three-dimensional, nonspherical random network.

The size distribution of the spherical dispersions ranges from 0.01 to 1.3 mm in diameter. To date, only one dispersion area of 1 μm (Fig. 27) has been found, but this may be due to the influence of the tungsten microspheres. Several duplex dispersions of sodium acetate in paraffin surrounded by sodium acetate have been found (Fig. 27).

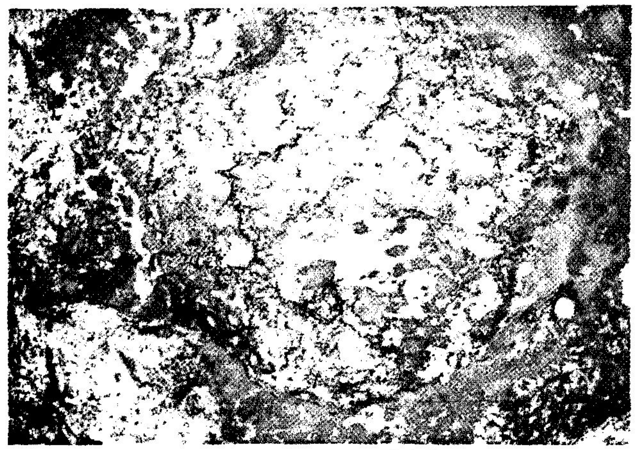

FLIGHT SPECIMEN 12F-A-09
DUPLEX DISPERSION, SODIUM ACETATE IN PARAFFIN
SURROUNDED BY SODIUM ACETATE
50X MAGNIFICATION

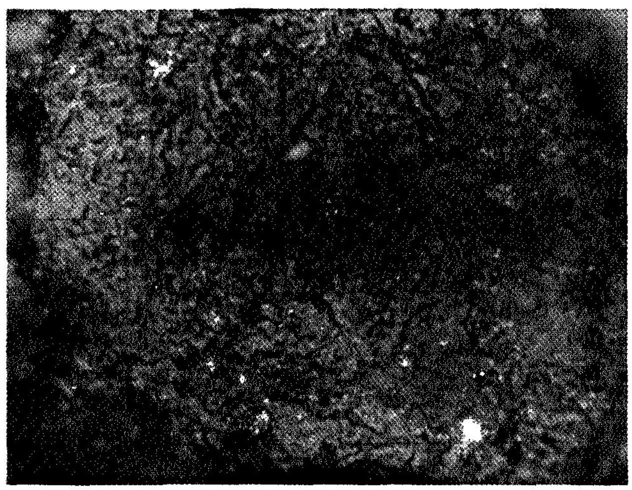

FLIGHT SPECIMEN 12F-A-04
1-μm DISPERSION OF SODIUM ACETATE IN PARAFFIN
SURROUNDED BY SODIUM ACETATE
1000X MAGNIFICATION

Figure 27. Fine dispersions in specimen 12F.

CONCLUSIONS

The Apollo 14 composite casting demonstrations have shown the potential for preparing unique metal-matrix composite materials and mixtures of immiscible systems by liquid phase processing in a weightless environment. By controlling gravity-induced forces to very low levels, stable mixtures of liquid, solid, or gaseous phases may be prepared and maintained through solidification. Under the influence of gravity on earth, the phases separate because of density differences and thermal convection. It was evident in the samples that as gravity forces diminish, molecular forces play an increasingly significant role in processing materials in space. The inflight samples showed the following advantages over ground-processed samples:

1. A more homogeneous and stable distribution of particles and fibers in a metal matrix in flight samples 1, 4, 5, 8, and 10 demonstrates the potential for producing reinforced metal-matrix composites.

2. A more homogeneous and stable distribution of gas bubbles in a fiber-reinforced metal matrix in flight sample 4 demonstrates the potential for producing reinforced foam composites.

3. Stable simple and duplex dispersions of immiscible materials in flight samples 6, 9, and 12 demonstrate the potential for producing homogenized mixtures of immiscible materials.

A number of subtle effects were observed in the flight samples, such as agglomeration of nonwetting particles at surfaces or interfaces, fiber alignment in surfaces, enhanced gas migration to surfaces in some samples, and differences in surface crystallography. These effects must be studied further, and additional tests must be run in order to determine if these were indeed space effects. Two of the samples were essentially free-floating during solidification, indicating the potential for further extended free-fall demonstrations using spherical nonwetting containers without elaborate electromagnetic positioning systems.

Much has been learned from this demonstration that will aid in planning future experiments in the Materials Science and Manufacturing in Space Program. Further research including extended free-fall testing is recommended.

N73-22922

EXPERIMENTAL STUDIES OF MANUFACTURING PROCESSES PERFORMED IN ZERO-G

By
Vaughn H. Yost

SUMMARY

Manufacturing in space conducted in support of the Skylab program and in anticipation of future programs is summarized in this review. Methods used to obtain short periods of near-zero-g are illustrated, and the advantages and disavantages of each are listed. Four experiments developed to investigate three manufacturing-in-space processes are illustrated, their operating sequence is described, and the results of each are presented.

INTRODUCTION

In the spring of 1966 Mr. Hans F. Wuenscher[1] conceived the idea of processing materials in the weightless environment of space. The principal objective of this idea was to obtain materials with improved or unique mechanical, electrical, and/or optical properties. Since 1968 studies have been completed that delineate a series of experiments that can be conducted during short periods of near-zero-g to verify expected results.

Three methods of obtaining near-zero-g — drop towers, research aircraft, and research rockets — have been used. Two techniques for forming and deploying liquid metals in zero-g were developed and proven successful with drop tower tests. A containerless processing system was developed and tested in both the drop tower and the KC-135 aircraft. The drop tower tests tended to show that the system will work. Lastly, research rockets were used to investigate the stability of metal gas dispersions in a liquid state under zero-g.

METHODS USED TO OBTAIN SHORT PERIODS OF NEAR-ZERO-G

Drop Towers

General Information. The drop tower used for this work is located at NASA's Marshall Space Flight Center. It is a part of the Saturn V Dynamic Test Stand, building 4650.

Technical Information. The drop tower consists of the following major assemblies: a drag shield, the package that contains the experiment, a power system, an instrumentation system, an operations room, a thruster system, a release system, guide rails, a catch tube, and a winch system (Fig. 1).

The following are the major steps in a test sequence (beginning with the drag shield at the top of the guide rails):

1. The door of the drag shield is opened, the package is placed on the drag shield floor, and the flat conductor cables are connected that transmit power and sequencing signals to the package and experiment (Fig. 2).

2. The motor-generator set is started, and the package and experiment are sequenced to verify that they will work during the drop.

3. Verification is made that the instrumentation system, which is up to six channels of data telemetered to the Block House, is operating.

1. Assistant Director for Advanced Projects, Process Engineering Laboratory, MSFC.

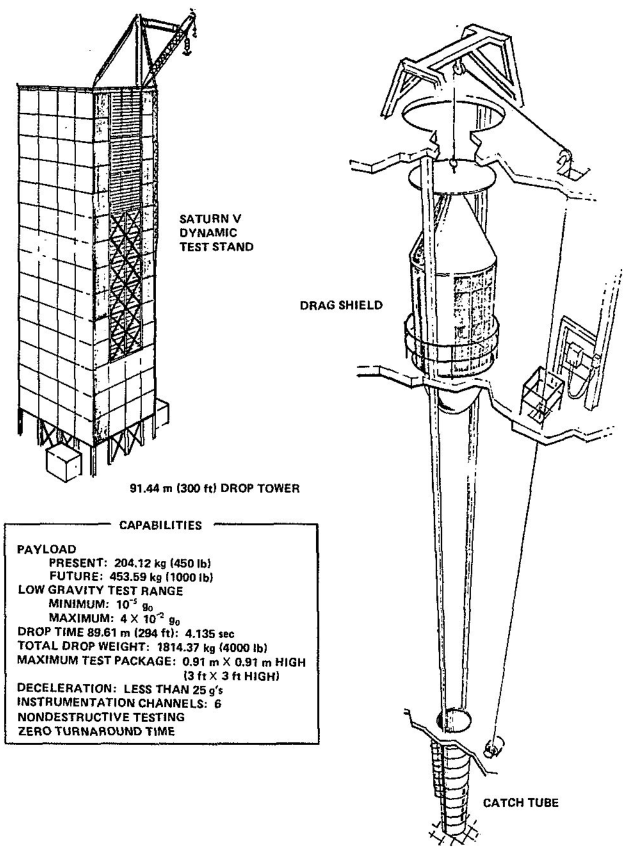

Figure 1. Schematic of MSFC 91.44-m (300-ft) drop tower.

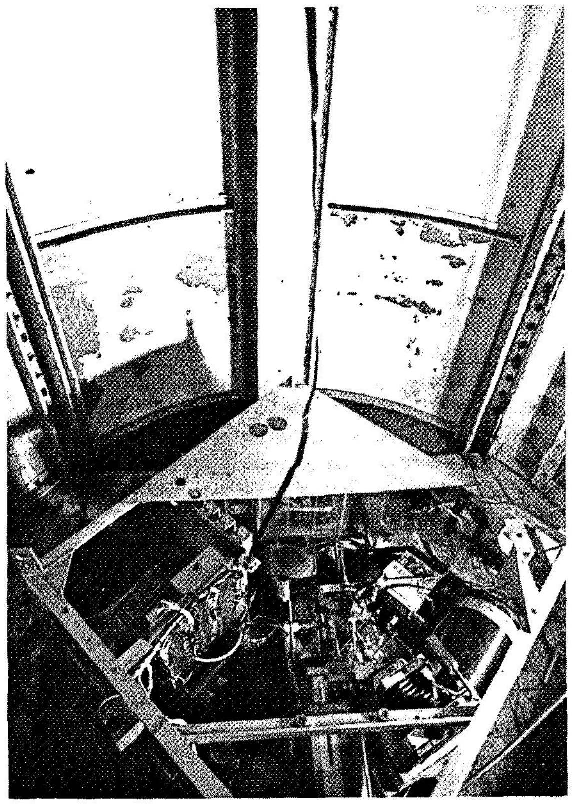

Figure 2. Top view of drop tower showing experiment loaded on drag shield floor and flat conductor cables connected.

4. The drag shield door is closed, and all personnel then move to the steel-covered operations room at the top of the tower.

5. The high pressure gas spheres in the top of the drag shield are filled with air to a pressure of approximately 1.21×10^7 N/m^2 (1750 psig), some air is then discharged through the thrusters on top of the drag shield to verify that the system is working, and the sphere is refilled to 1.21×10^7 N/m^2 (1750 psig).

6. The air trusters are then turned on; the drag shield is released; the thrusters accelerate the drag shield down the guide rails faster than free-fall [9.8 m/sec^2 (32.16 ft/sec^2)], the result of which is the drag shield floor is separated from the package; the package approaches free-fall (1×10^{-5} g) inside the drag shield for up to 4.135 sec or 89.61 m (294 ft) of the guide rails, at which time the deceleration produced by air and guide rail friction is greater than the acceleration produced by the thrusters; and the package comes to rest on the drag shield floor.

7. The drag shield then enters the top of the 12.19-m (40-ft) long catch tube, which it fits rather loosely; the air which is at 1 atm in the catch tube is compressed in the volume between the nose of the drag shield and the bottom of the catch tube; and this compressed air is permitted to escape around the drag shield and out holes in the side of the catch tube at such a rate as to decelerate the drag shield (maximum deceleration is less than 25 g's) in 12.19 m (40 ft) to zero velocity, where it comes to rest on a cushion of rubberized horse hair.

8. The cable on the winch is then lowered to the top of the drag shield in the catch tube and attached, and the drag shield is pulled to the top of the guide rails where it is secured.

Packages may be cubes as large as 0.91 m (3 ft) in diameter and 0.91 m (3 ft) high and are designed to withstand decelerations as high as 25 g's. The package including the experiment may weigh up to 204.12 kg (450 lb).

This method of obtaining near-zero-g is compared in Table 1 to the two others discussed in this paper.

KC-135 Research Aircraft

General Information. The KC-135 Research Aircraft used for this work are based at Wright Patterson Air Force Base (WPAFB), Ohio. The element responsible for scheduling flights is the Zero "G" Office at WPAFB.

Technical Information. Elevation and plan views of a KC-135 aircraft are shown in Figure 3. The interior of the aircraft is covered with foam.

To obtain near-zero-g, the aircraft is flown through a zero-gravity maneuver as shown in Figure 4. At the top of the parabola, up to 30 sec of near-zero-g can be obtained. However, as a general rule only 6 to 7 sec of $\pm 1 \times 10^{-1}$ g is obtained.

Research Rockets

General Information. The research rockets used for this work are prepared by the Sounding Rocket Division of NASA's Goddard Space Flight Center (GSFC), Greenbelt, Maryland, and are launched from either the U. S. Navy Ordnance and Missile

TABLE 1. COMPARISON OF METHODS OF OBTAINING SHORT PERIODS OF NEAR-ZERO-G

	Drop Tower	KC-135 Research Aircraft	Research Rocket
Advantages	• Steady near-zero-g, 1×10^{-5} g • Facility located at MSFC • Normal design and safety requirements • Simple test procedure	• Relatively easy to schedule test • Experimenter supplies package and test procedure. S&E-ASTN-SMS transports package to WPAFB, Ohio, performs test, and returns package and data to the experimenter	• 4 to 9 min near-zero-g time • Design and safety procedures for unmanned flight • Simple test procedure • Low cost for piggyback experiment
Disavatnages	• Short period of zero-g, 4 sec • Sometimes difficult to schedule because of limited manpower available to operate tower	• Yawing of aircraft during near-zero-g portion of parabola is unsatisfactory for most unmanned experiments • Location: aircraft are based at WPAFB, Ohio; hence, package and operator must be flown up and back • Flight design and safety requirements must be met • Detailed step-by-step test procedure required	• Payload spin and coning (precession) during near-zero-g introduces some accelerations, but these can be largely overcome by adding a control system • Location: launches from White Sands, New Mexico or Wallops Station, Virginia • Scheduling of piggyback experiments depends on dimensions and weight of experiment • High cost if experimenter purchases rocket

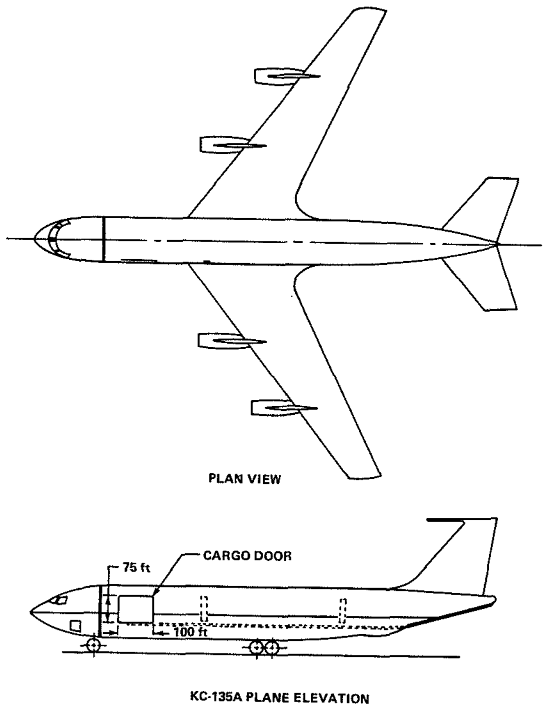

Figure 3. Elevation and plan views of a KC-135 Research Aircraft.

Test Facility, White Sands, New Mexico, or NASA's Wallops Station, Wallops Island, Virginia. The Sounding Rocket Division reviews the payloads of the rockets that they are preparing and the experiments that MSFC has available to see if the latter can be substituted for lead ballast which often makes up part of the payload. Once a favorable determination is made, MSFC provides the experiment and test procedure, assists in integrating the experiment into the rocket, and attends the rocket launch and recovery.

Two MSFC experiments had been integrated into two rockets by GSFC, an Aerobee 170 and a Black Brant VC, when this review was presented on September 28, 1971. The Aerobee was launched October 19, 1971, and the Black Brant VC on January 27, 1972.

Technical Information.

Aerobee 170A Research Rocket and the Flight of NASA 13.113. This vehicle (Fig. 5) is manufactured by the Space General Division of Aerojet General Corporation, El Monte, California. It can be launched from the Nike launcher (Fig. 5), the multiple-purpose launcher, or the adjustable Aerobee towers at NASA's facilities at Wallops Island, Virginia, and USNOMTF at White Sands, New Mexico.

Aerobee 170A NASA 13.113 was flown from Aerobee 150 tower B at the USNOMTF. This flight was launched at 11:30 a.m., MDT, on October 19, 1971. Although the vehicle carried some science and rocket engineering instrumentation, it was primarily a test round to aid in evaluating the dispersion characteristics of this three-finned version of the Aerobee 170. The meteorological report[2] on this launch revealed a theoretical apogee altitude of 155.00 km (96.4 mi) and a theoretical impact point 97.17 km (60.7 mi) north and 7.40 km (4.6 mi) west of the launcher. The actual apogee was 147.22 km (91.5 mi), and an impact point was 91.33 km (58.3 mi) north and 2.41 km (1.5 mi) west of the launcher (Fig. 6).

The Aerobee 170A is composed of a three-fin Aerobee 150A sustainer and the Nike booster system. The solid propellant booster and liquid propellant sustainer are fired simultaneously with the sustainer ignition controlled by the standard start valve and burst diaphragms. At booster ignition, the sustainer is pressurized and starts to thrust at 0.6 sec. The booster drag separates at 3.35 sec.

This rocket had an outside diameter of 0.38 m (15 in.) and a length of approximately 12.89 m (507.48 in.), of which 3.88 m (152.75 in.) was the sustainer and 4.05 m (159.31 in.) was the payload for Aerobee 170A NASA 13.113. The overall length of NASA 13.113 was 16.49 m (636.79 in.). The vehicle trajectory is dependent on the effective launch angle and the mass of the payload. The mass of NASA 13.113 was 422.92 kg (3137 lbm) at lift-off, of which 202.07 kg (445.5 lbm) was payload. After burnout, 51.27 sec into the flight, its total mass was 349.1 kg (748.1 lbm). A number of channels of telemetry are usually available for transmitting rocket and payload data to the ground.

Mr. Roy McIntosh, Jr.,[3] the other experimenter on Aerobee 170A NASA 13.113, had two Endevco Q-Flex low level accelerometers in his experiment area. One, on telemetry channel 13, was mounted in a plane parallel to the long axis of the rocket to measure thrust levels and the other, on telemetry channel 15, in a plane perpendicular to the long axis to measure angular accelerations. Both were mounted 0.127 ± 0.0127 m (5 ± 0.5 in.) from the long axis of the vehicle and 2.413 ± 0.0127 m

2. Prepared by the Atmospheric Sciences Laboratory, White Sands Missile Range.
3. Thermophysics Branch, Engineering Physics Division, Space Applications and Technology Directorate, GSFC.

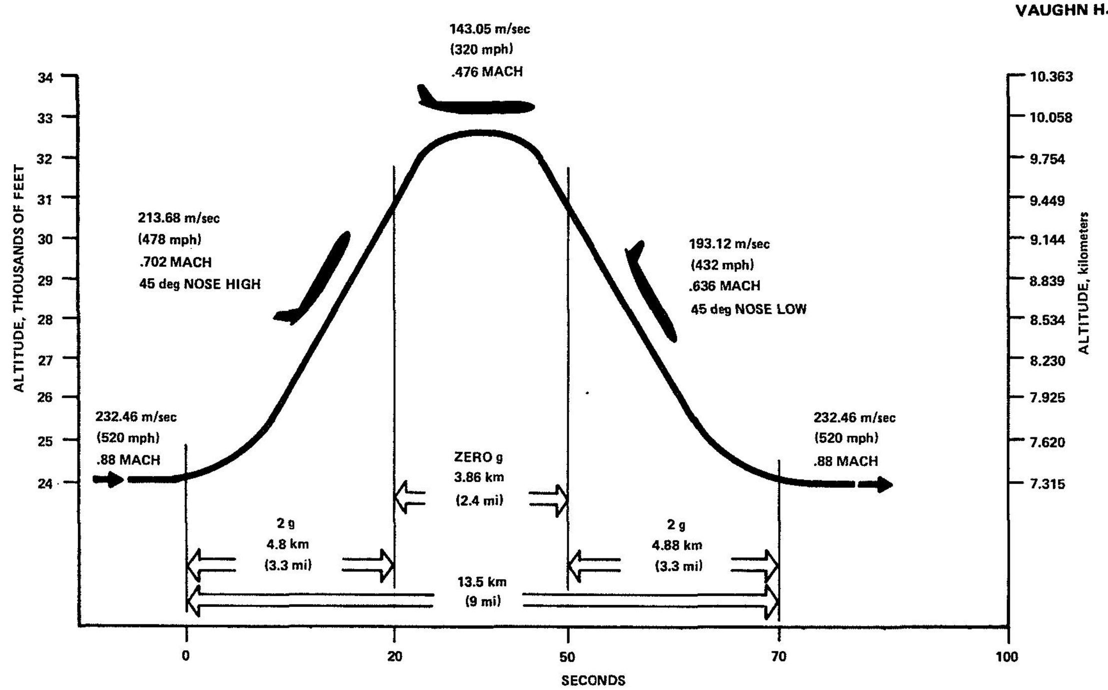

Figure 4. KC-135 Research Aircraft trajectory, zero-gravity maneuver.

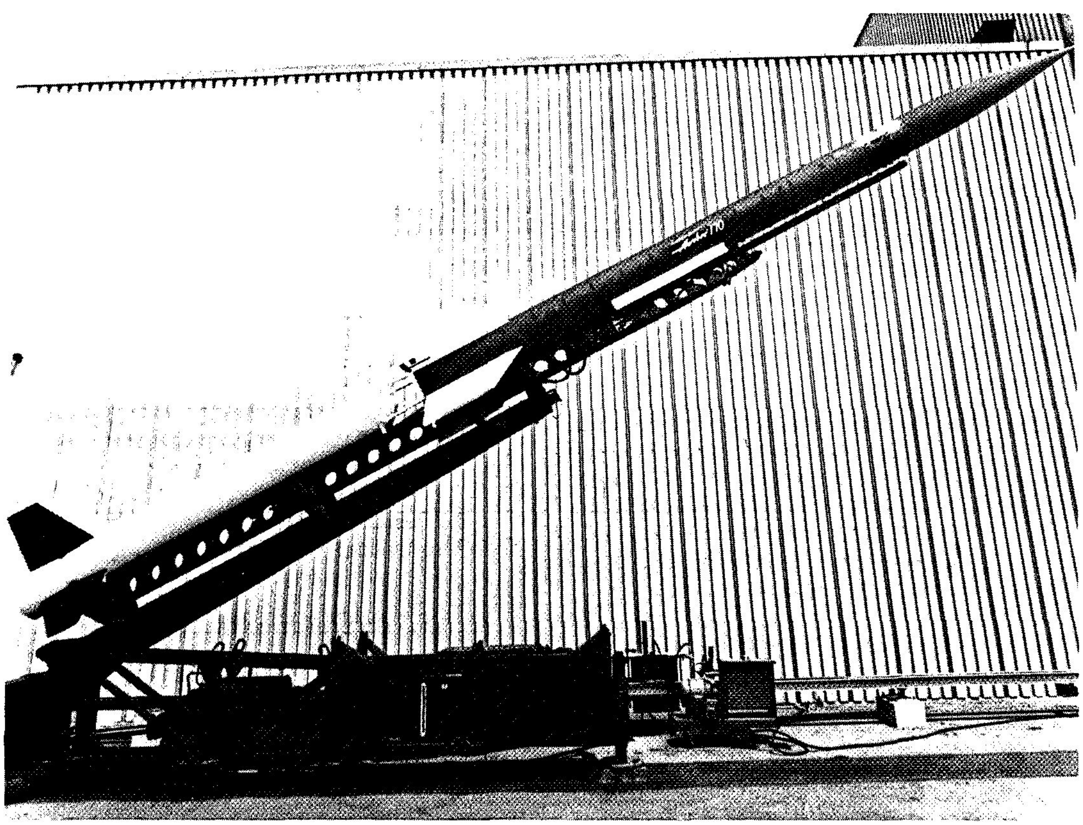

Figure 5. Aerobee 170A Research Rocket mounted on a Nike launcher.

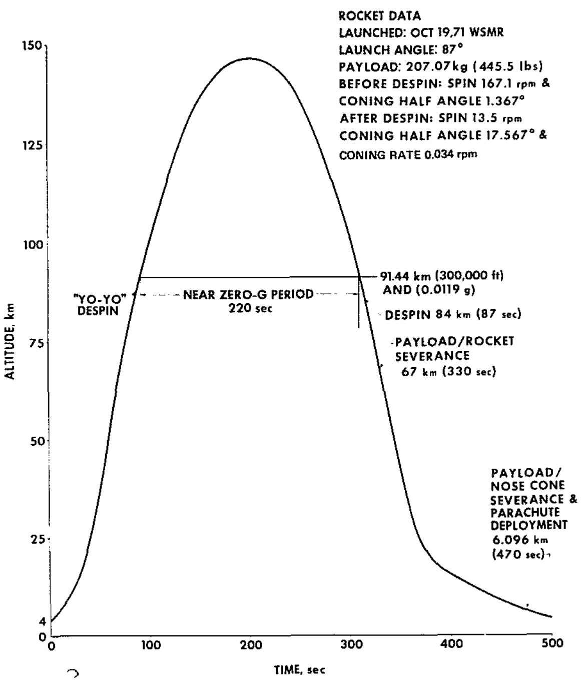

Figure 6. Altitude versus time for Aerobee 170A NASA 13.113.

(95 ± 0.5 in.) from its tip. After burnout, the center of gravity of the vehicle was 4.11 m (162.1 in.) from its tip or 1.711 m (67.1 in.) aft of the accelerometers (Fig. 7).

The vehicle can be despun with a "yo-yo" despin system. Yo-yo despin is accomplished by deploying weights on the ends of cables which are attached to the vehicle. Two cable and weight assemblies are used. The vehicle can be despun with this system to approximately any desired rate including zero by selecting appropriate cable lengths and weight masses.

The trajectory profile for NASA 13.113 is shown in Figure 6. Yo-yo despin occurred between 83.2661 and 83.3662 sec,[4] according to the spin accelerometer which showed a change in acceleration of -0.10 to -0.052 g. This is confirmed by the thrust accelerometer which showed a deceleration of +0.108 to +0.044 g between 83.3622 and 83.4668 sec.[5]

After 85.8780 sec, the spin accelerometer reached a mean acceleration of -0.026 g. From this, the final spin rate after despin was calculated to be approximately 13.52 rpm, as shown below

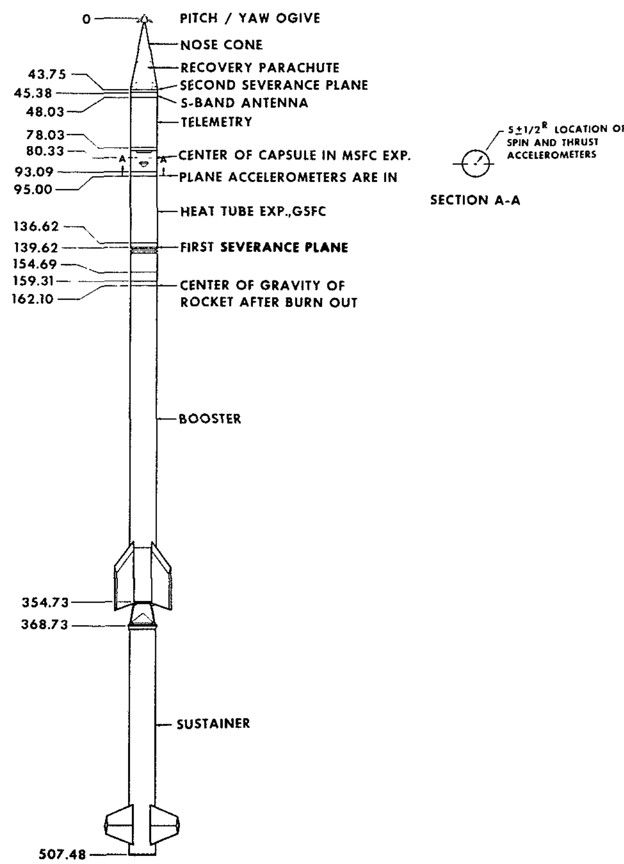

Figure 7. Aerobee 170A NASA 13.113 configuration.

$$a_R = r\omega'^2 \quad , \quad \omega'^2 = \frac{a_R}{r} \tag{1}$$

where

a_R is the radial component of acceleration, in m/sec² (ft/sec²),

r is the radius, here the distance of the spin accelerometer from the spin axis of the vehicle, in m (in.),

ω' is the angular velocity of the vehicle, in radians/sec,

$$\omega'^2 = \frac{(0.026\ g \times 9.81)\ m/sec^2}{0.127\ m} \quad ,$$

$$\omega'^2 = 2.08/sec^2 \quad ,$$

4. Spin accelerometer, Aerobee 170A NASA 13.113 telemetry channel 15 (2251.5 MHz) Time versus TM volts.
5. Thrust accelerometer, Aerobee 170A NASA 13.113 telemetry channel 13 (2251.5 MHz) Time versus TM volts.

$$\omega' = 1.417 \text{ rad/sec} \quad ,$$

and

$$n' = \frac{2\pi\omega}{60} \quad , \tag{2}$$

where

n' is the angular velocity, in revolutions per minute;

$$n' = 1.417 \text{ rad/sec} \times \frac{1 \text{ rev}}{2\pi \text{ rad}} \times \frac{60 \text{ sec}}{\text{min}}$$

$$= 13.52 \text{ rpm} \quad .$$

Generally, at low atmospheric pressures (3.7 μm Hg) at 84 m (52.21 mi) where despin occurs, as the spin rate decreases, precession about the center of gravity of the vehicle [called coning (Figs. 8a and 8b) in research vehicles] increases. With precession, an up and down oscillation of the vehicle axis [called nutation (Fig. 8c)] occurs. The latter is caused by things such as mass asymmetries, but is very small in amplitude and may be ignored. The angle ϵ is defined as the coning half-angle and, assuming no external forces act on the vehicle, this angle remains constant. The magnitude of this angle is defined by the ratio between the vehicle angular momentum in the pitch/yaw and the spin planes. If this relationship changes, the magnitude of the coning angle also changes. In the case of vehicle despin, the spin momentum is suddenly reduced and the coning angle is consequently increased. This situation is illustrated in Figure 8d.

The relationship between the spin and pitch/yaw angular momenta prior to despin is given by

$$H = \sqrt{H_s^2 + H_j^2} \quad ; \tag{3}$$

also

$$\tan \epsilon = \frac{H_j}{H_s} \quad , \tag{4}$$

where

H is the total momentum of the vehicle, in kg-m^2/sec (slug-ft^2/sec),

H_s is the spin angular momentum prior to despin, in kg-m^2/sec (slug-ft^2/sec),

H_j is the pitch/yaw angular momentum prior to despin, in kg-m^2/sec (slug-ft^2/sec),

and

ϵ is the coning half-angle prior to despin, in deg.

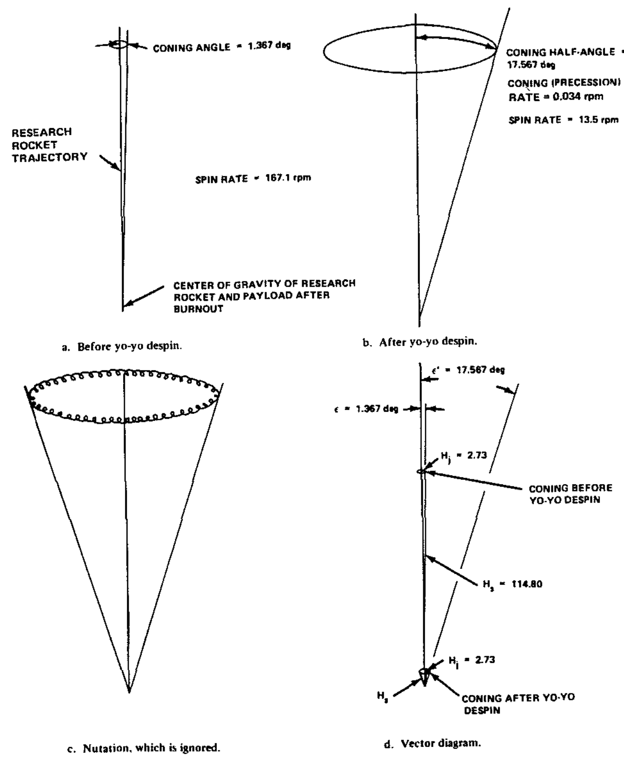

Figure 8. Relationships between spin rate, coning (precession) angle and rate, and nutation before and after yo-yo despin of Aerobee 170A NASA 13.113.

After despin, the spin momentum is reduced to H_s', but the pitch/yaw momentum remains unchanged. The new coning angle is given by

$$\tan \epsilon = \frac{H_j}{H_s'} \quad , \tag{5}$$

where

H_s is the spin angular momentum after despin, in kg-m²/sec (slug-ft²/sec),

and

ϵ' is the coning half-angle after despin, in deg.

Comparing equations (4) and (5) yields

$$H_s \tan \epsilon = H_s' \tan \epsilon'$$

$$\tan \epsilon' = \frac{H_s}{H_s'} \tan \epsilon \quad . \tag{6}$$

The spin angular momentum is also the spin moment of inertia times the spin rate. Hence,

$$H_s = I_s \omega \tag{7}$$

and

$$H_s' = I_s \omega' \quad , \tag{8}$$

where

I_s is the spin moment of inertia of the vehicle, in kg-m² (slug-ft²),

ω is the spin rate prior to despin, in rad/sec,

and

ω' is the spin rate after despin, in rad/sec.

Substituting equations (7) and (8) into equation (6) yields

$$\tan \epsilon' = \frac{\omega}{\omega'} \tan \epsilon \quad . \tag{9}$$

It is also noted that not only does the coning angle change, but the fixed line in space about which the vehicle cones also changes. This is seen in Figure 8c.[6]

The coning rate is the angular rate at which the vehicle describes the cone and is given by

$$\sigma = \omega' \frac{I_s}{I_j} \frac{\cos \alpha}{\cos \epsilon'} \quad , \tag{10}$$

where

σ is the coning rate, in rad/sec,

I_j is the pitch/yaw moment of inertia of the vehicle, in kg-m² (slug-ft²),

I_s is the spin moment of inertia of the vehicle, in kg-m² (slug-ft²),

ω' is the spin rate after despin, in rad/sec.

and

ϵ' is the coning half-angle after despin, in deg.[7]

From this, the coning half-angles before and after yo-yo despin, as well as the coning rate for NASA 13.113, were calculated to be approximately 1.367 deg, 17.567 deg, and 0.034 rpm, respectively.

Coning half-angle before yo-yo despin. Between 81 and 90 sec into the rocket's trajectory, its pitch/yaw angle, ω_j, changed from 8.01 to 8.58 deg, or

$$\frac{\frac{8.58 \text{ deg} - 8.01 \text{ deg}}{9 \text{ sec}}}{57.2958 \text{ deg/rad}} = \frac{0.0633 \text{ deg/sec}}{57.2958 \text{ deg/rad}}$$

$$= 0.0011 \text{ rad/sec}$$

6. Letter No. 600-002-2 dated November 8, 1971, from B. R. Payne, Design Engineer, Rocket and Space Division, Bristol Aerospace (1968) Limited, P.O. Box 874, Winnipeg, Canada.
7. S. W. Groesberg, Advanced Mechanics, John Wiley & Sons, Inc., New York, 1968, pp. 195-198.

$$\tan \epsilon = \frac{H_j}{H_s} = \frac{I_j \omega_j}{I_s \omega_s} = \frac{2484 \text{ slug-ft}^2 \times 0.0011 \text{ rad/sec}}{6.56 \text{ slug-ft}^2 \times 17.5 \text{ rad/sec}}$$

$$= \frac{2.7324}{114.80}$$

$$\tan \epsilon = 0.0238$$

$$\epsilon = \text{arc tan } 0.0238 = 1.367 \text{ deg} \quad .$$

Coning half-angle after yo-yo despin.

$$\tan \epsilon' = \frac{H_j}{H_s'} = \frac{2.7324}{6.56 \text{ slug-ft}^2 \times 1.38 \text{ rad/sec}} = \frac{2.7324}{9.05}$$

$$\tan \epsilon' = 0.3019$$

$$\tan \epsilon' = \text{arc tan } 0.3019 = 17.567 \text{ deg} \quad .$$

Coning rate.

$$\sigma = \omega \frac{I_s}{I_j} \frac{\cos \alpha}{\cos \epsilon'}$$

$$= \frac{1.417 \text{ rad/sec} \times 6.56 \text{ slug-ft}^2 \times \cos 17.567 \text{ deg}}{2484 \text{ slug-ft}^2 \times \cos 1.367 \text{ deg}}$$

$$\sigma = \frac{1.417 \times 6.56 \times 0.9532}{2484 \times 0.9997} = 0.00357 \text{ rad/sec}$$

$$\sigma = 0.00357 \text{ rad/sec} \times \frac{60 \text{ sec}}{\text{min}} \times \frac{\text{rev}}{2\pi} = 0.034 \text{ rpm} \quad .$$

Space General also makes the Mark II Attitude Control System which is a multiple-purpose system for exo-atmospheric attitude control of rocket payloads. It is inertially referenced and provides three-axis control of the payload by use of cold gas reaction jets. Preprogrammed guidance data sequences control the payload attitude. This was not used on NASA 13.113.

On payloads with experiments that are forward looking, e.g., photographing celestial bodies, the nose cone is severed from the rocket/payload on the upward leg of the flight. Generally, when the payload does not contain a forward-looking experiment, the nose cone is not severed until late in the flight. On NASA 13.113 both severances occurred on the downward leg of the flight because there were no forward-looking experiments on it. The first severance, payload from the rocket (Figs. 6 and 7), occurred at an altitude of approximately 67 km (41.63 mi) between 329.7740 and 331.9840 sec according to the spin accelerometer and between 329.7740 and 330.4768 sec according to the thrust accelerometer into the flight.

The second severance, nose cone from payload (Figs. 6 and 7), was actuated by an aneroid switch set for 6.096 km (3.79 mi). This severance occurred approximately 470 sec into the flight.

After the payload enters the atmosphere, it makes a difference whether or not the nose cone has been severed. If the payload has the nose cone off, the payload will come down a flat spin with the forward edge of the plane of spin tilted up 20 to 30 deg with respect to the surface of the impact area. If the nose cone is left on, as in the case of NASA 13.113, the payload/nose cone will tend to come down nose first.

The parachute may be attached to either the forward or aft end of the payload. Of course, with forward-looking experiments in the payload, it must be attached to the aft end. On NASA 13.113 it was attached to the forward end of the payload and the severed nose cone was used to pull its rip cord and pull the parachute from its canvas pack.

Black Brant VC Research and the Flight of NASA 21.006. The vehicle (Fig. 9) is manufactured by Bristol Aerospace (1968) Limited, Winnipeg, Canada. It can be launched from the adjustable Aerobee towers at Wallops Island and White Sands.

Black Brant VC NASA 21.006 was flown from the Aerobee tower on Wallops Island. This flight was launched at 11:30 a.m., EST, on January 27, 1972. Although this vehicle carried an MSFC experiment, it was, primarily, a test round to verify the Black Brant VC system.

The Black Brant V has a single stage solid propellant motor. The "C" model is fitted with

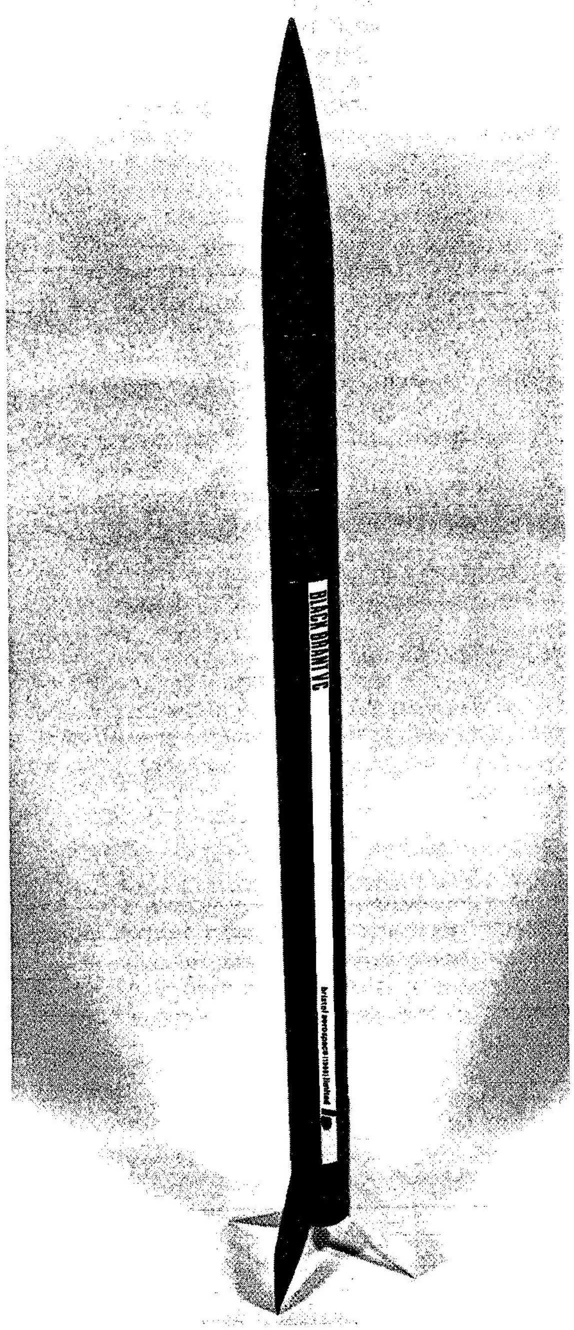

Figure 9. Black Brant VC Research Rocket.

four fins which can be set to produce the required spin (roll) rate. This rocket has an outside diameter of 0.43 m (17.2 in.) and a length of 5.27 m (207.61 in.) plus the payload, which was 3.50 m (134.87 in.) at launch for NASA 21.006. After the payload was severed from the rocket, the payload was 3.16 m (124.45 in.) long because severance occurred 0.25 m (10.42 in.) forward of the aft end of the payload. The overall length of NASA 21.006 was 8.71 m (342.48 in.).

The Black Brant VC trajectory is dependent on the effective launch angle and the mass of the payload. The angle of launch was 80 deg but, when the effect of the winds was taken into consideration, the effective angle of launch was 80.7 deg. The mass of NASA 21.006 was 1261.89 kg (2782 lbm) at lift-off, of which 256.73 kg (566 lbm) was payload. After burnout, the mass of the vehicle was 501.22 kg (1105 lbm), of which 244.49 kg (539 lbm) was the rocket. The trajectory was calculated to have an altitude of 240.32 km (149.33 mi) and a range of 192.50 km (119.62 mi). Radar used to track this vehicle indicated that actual altitude and range were 221.47 km (141.97 mi) and 251.46 km (156.25 mi), respectively.

Since this was a test round, the major events of the flight were monitored, and the data were telemetered to the ground. These data were recorded on strip charts. These charts indicated the despin occurred at 55 sec and the spin rates before and after despin were 4.10 rps and 1.95 rps, respectively. The desired rate after despin was 1.00 rps. Other charts indicated that the payload/nose cone was severed from the rocket at 60 sec and that the flight was a success up to the point where the heat shield was supposed to be severed from the aft end of the payload at 6.10 km (3.79 mi). According to this chart, severance did not occur. Radar tracking ceased at approximately 4.87 km (3.03 mi) above sea level because of the curvature of the earth and the fact that radar signals bend only slightly. However, between 4.87 km (3.03 mi) and 6.10 km (3.79 mi), there was no indication on the radar that the heat shield was severed from the payload or that the parachute was deployed.

A four-engine plane was flown to the point of impact but neither the dye marker nor the payload was found. For this reason and the fact that 241.15 km (150 mi) is about the maximum range of the helicopters, they were never sent out. The following day the weather was too bad to send out the airplane. However, the U. S. Navy sent one of its newest submarines to the impact area to search the area and bottom with sonar. The water was about 3.1 km (1700 fathoms) at the point of impact. The impact area was searched the next day with the airplane. The payload was not found and is

most likely lost because Wallops Station has never had a payload sighted or recovered by a passing ship.

EXPERIMENTS PREPARED FOR AND TESTED IN THE DROP TOWER AND KC-135 RESEARCH AIRCRAFT

General Information

The purpose of these experiments was to demonstrate that certain manufacturing processes are possible in a near-zero-g environment that are not possible on earth and to develop equipment for these processes. Two techniques for forming and deploying liquid metal were developed and tested by MSFC, and a containerless processing system for holding liquid metal through solidification and cooling to ambient temperature was developed under contract and tested by MSFC.

Technical Information

Techniques of Forming and Deploying Liquid Metals.

Tube and Reservoir Technique. The Tube and Reservoir (T&R) is located in the left half of the plexiglass box shown in Figure 10. The T&R is used to learn how to form and deploy a solid sphere of fluid approximately 5 cm (2 in.) in diameter with a minimum of internal fluid flow and surface oscillations. The purpose of the plexiglass box is to limit the movement of the sphere while in zero-g and to collect the fluid when the period of zero-g is complete. A hand-squeeze bubble pump is used to pump the fluid out the drain hole in the lower left hand corner of the plexiglass box and back into the reservoir; hence, it is a closed system. The bulb pump and tubing are not shown. An air bottle, regulator, and two solenoid-operated valves, one upstream and the other downstream from the regulator, to pressurize the reservoir are also not shown.

The sequence for preparing the T&R is as follows: (1) fill the reservoir to a level such that the fluid comes to the top of the tube, (2) fill the air bottle with air at 6.89×10^5 N/m^2 (100 psig), and (3) adjust the regulator in zero-g so that extremely low pressure air [less than 1.72×10^3 N/m^2 (0.25 psig)] pressurizes the reservoir for a period long

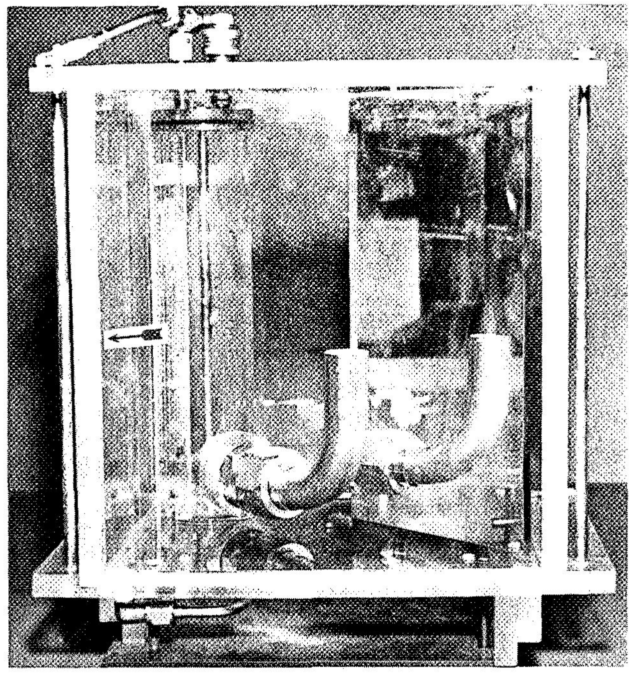

Figure 10. Tube and Reservoir technique of forming and deploying liquid metals.

enough (approximately 2 sec) to expel sufficient fluid to form a 5-cm (2-in.) diameter sphere. For mercury, this combination of pressure and time causes a sphere to form and be deployed (Fig. 11). Glycerin and glycerol (65-percent glycerin and 35-percent deionized water by weight) do not deploy.

A Milliken DBM 5 High Speed Motion Picture Camera taking pictures at the rate of 64 frames per second is used. The aluminized plexiglass behind and at 45 deg to the front of the box provides a second view of the sphere on the same motion picture film, thereby eliminating the problem of reading and interpreting two separate films.

Ejector Technique. The Ejector is located in the center of the plexiglass box shown in Figures 12 and 13. The Ejector is also used to learn how to form and deploy solid spheres of fluid approximately 5 cm (2 in.) in diameter in zero-g with a minimum of internal fluid flow and surface oscillations. The purpose of the plexiglass box is to limit the movement of the sphere while in zero-g and to collect the fluid when the period of zero-g is over. A hand-squeeze bulb pump is used to pump the fluid out the drain hole in the lower left hand corner of

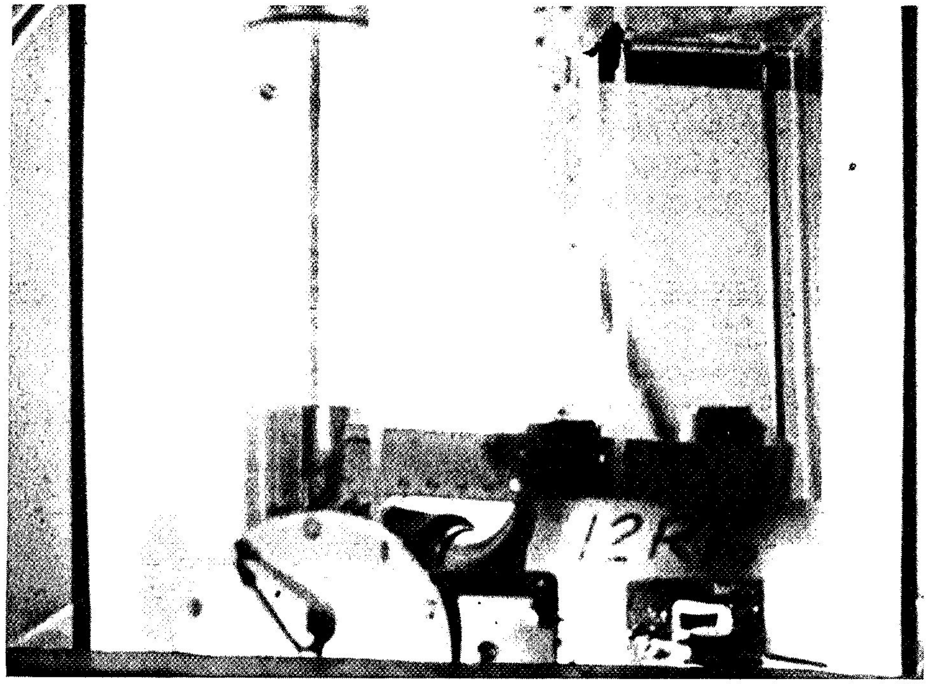

(a)

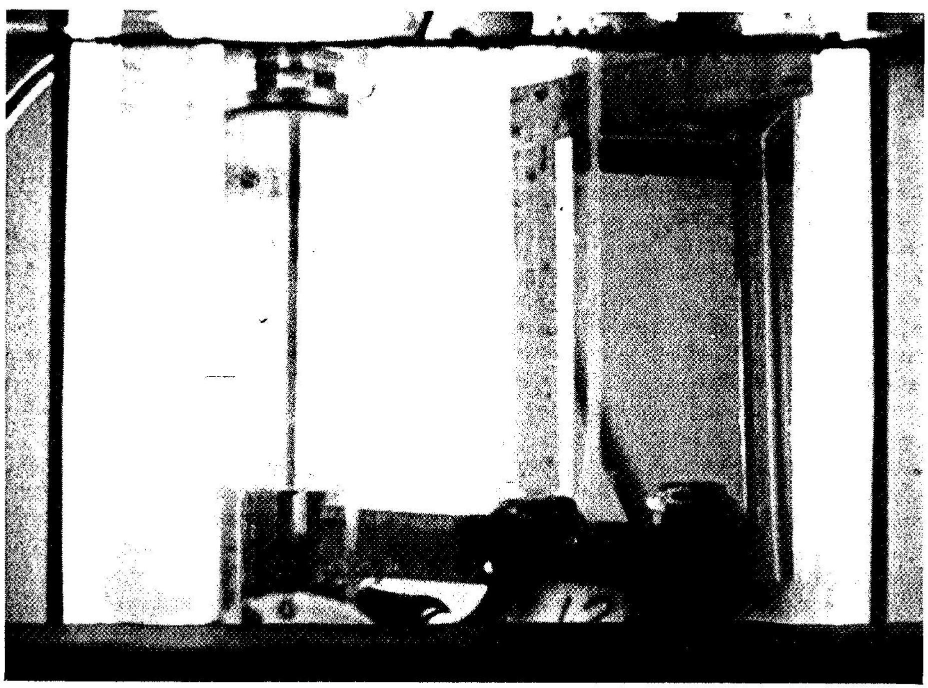

(b)

Figure 11. Drop tower test showing the forming and deploying mercury spheres using the Tube and Reservoir technique.

(c)

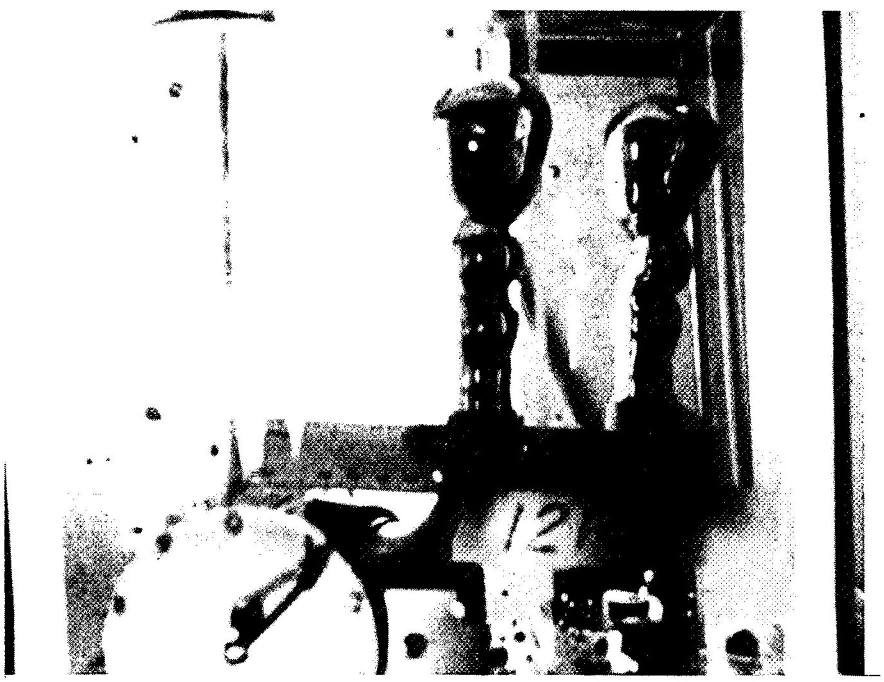

(d)

Figure 11. (Continued).

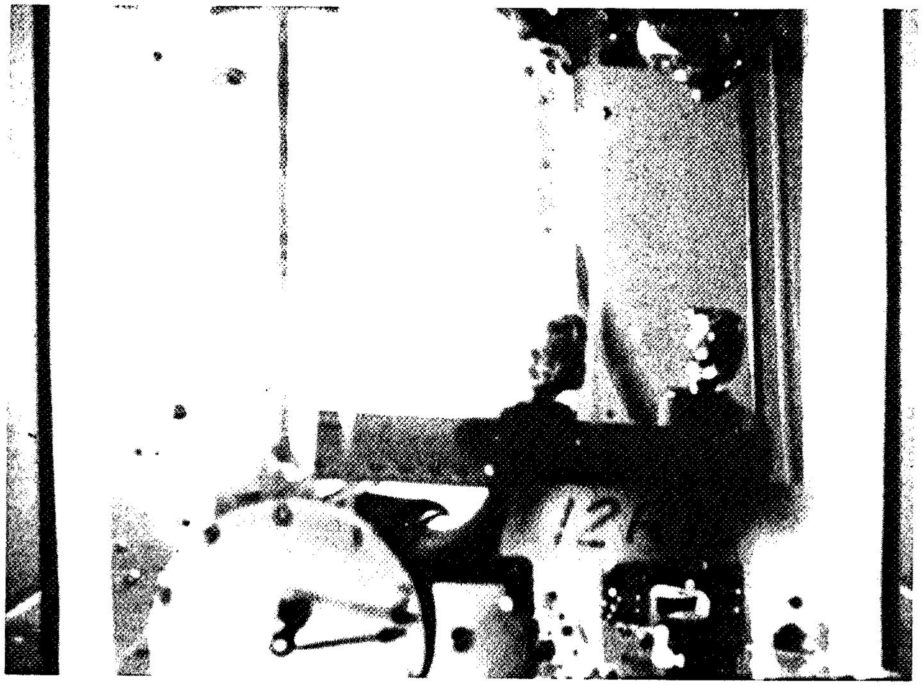

(e)

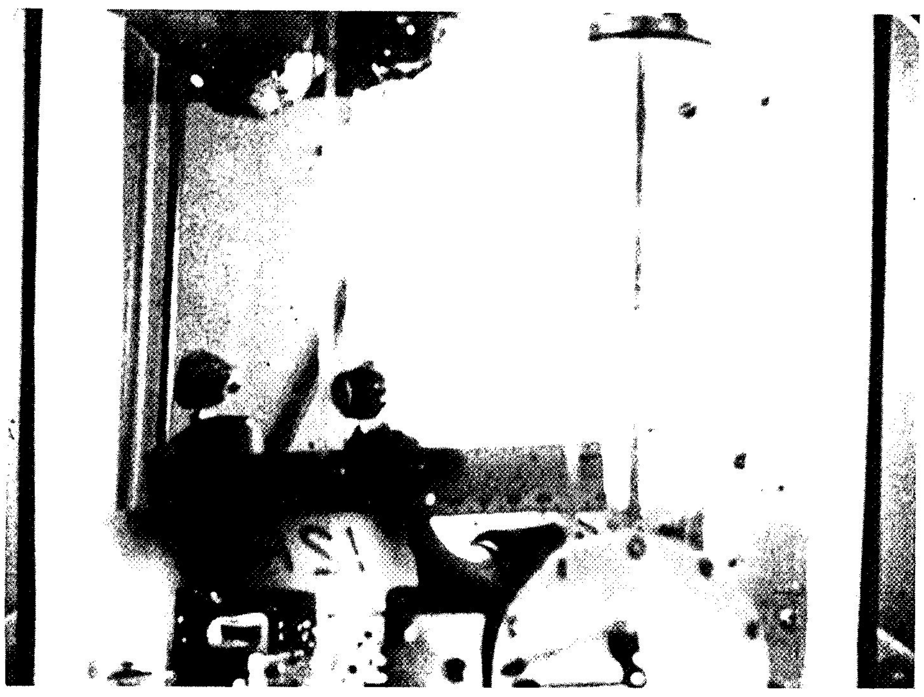

(f)

Figure 11. (Continued).

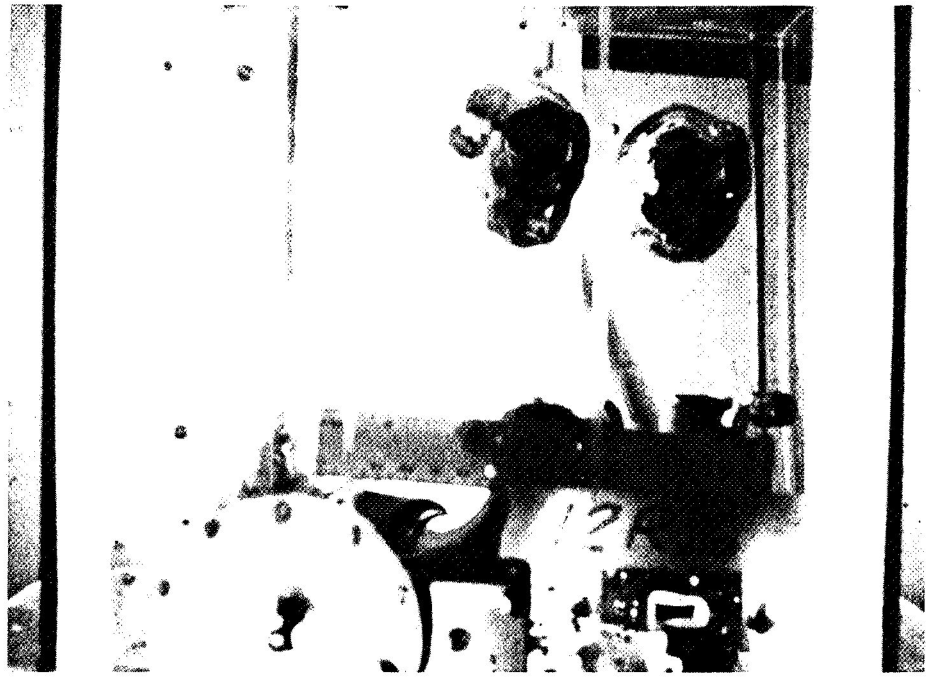

(g)

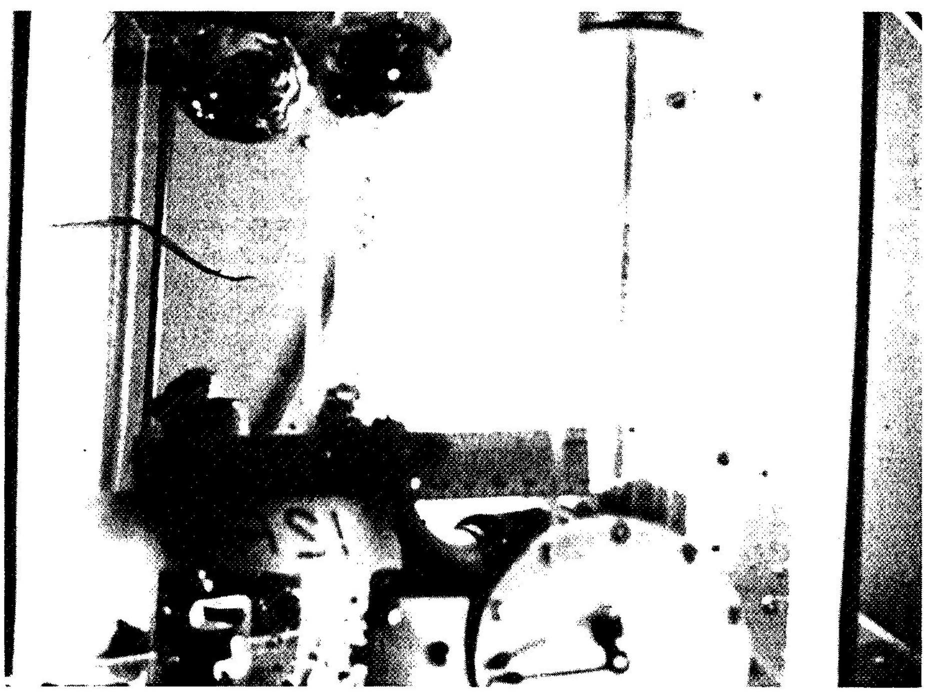

(h)

Figure 11. (Concluded).

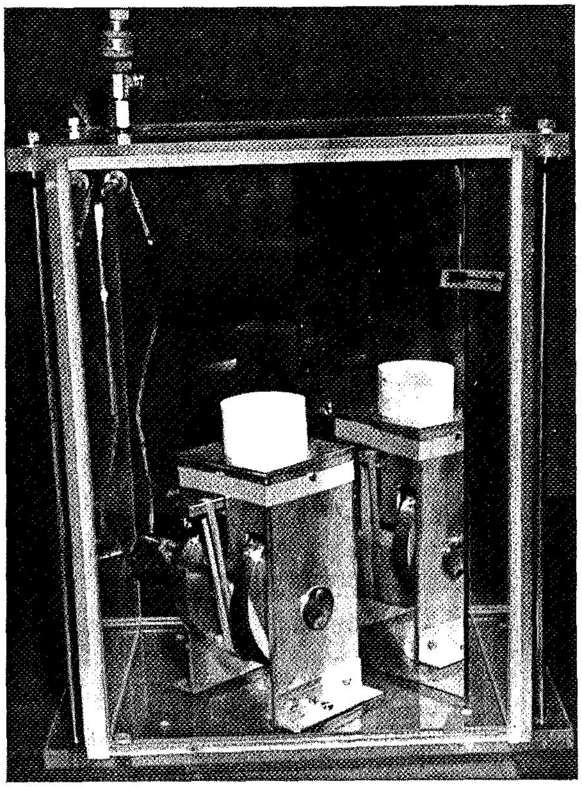

Figure 12. Ejector technique of forming and deploying liquid metals — cavity for liquid metal is formed when cylinder is at TDC and piston is at BDC.

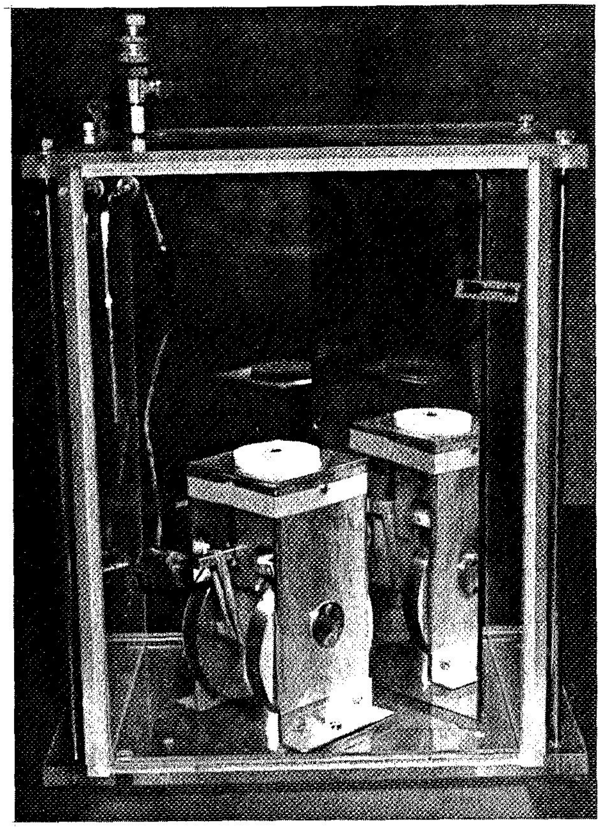

Figure 13. Ejector technique of forming and deploying liquid metals — cylinder at BDC and piston at TDC.

the plexiglass box to the Teflon cavity on the top of the Ejector; hence, it is a closed system. The bulb pump, fittings, and tubing are not shown.

The Ejector consists of a 28-Vdc gearmotor that has an output angular velocity of 30 rpm. The output shaft drives a camshaft that has three circular cams, two large cams with the smaller one in between them. The smaller cam cannot be seen because it is inside a Scotch yoke that is attached to the piston by a connecting rod. A flange on the bottom of the moveable cylinder is held against the two large cams with several rubber bands.

The sequence for preparing the Ejector is as follows: jog the gearmotor so the cylinder is at top dead center (TDC) and the piston is at bottom dead center (BDC) and fill the cavity with the fluid that the sphere is to be made from (Fig. 12). Once in zero-g, the gearmotor is run for 0.5 sec, which moves the cylinder to BDC and the piston to TDC with vertical displacements of 0.019 m (0.75 in.) down and 0.025 m (1 in.) up respectively (Fig. 13). This leaves the fluid unsupported and moving at a low velocity upward. The surface tension of the fluid causes it to form a sphere. For mercury, this combination of cylinder and piston movements causes the sphere to be deployed; i.e., separate from the top of the piston (Fig. 14). Glycerin and glycerol (65-percent glycerin and 35-percent deionized water by weight) do not deploy.

A Milliken DBM 5 High Speed Motion Picture Camera taking pictures at the rate of 64 frames per second is used. The aluminized plexiglass behind and at 45 deg to the front of the box provides a second view of the sphere on the same motion picture film, thereby eliminating the problem of reading and interpreting two separate films.

Containerless Processing System. Figures 15 and 16 show the components of this system mounted

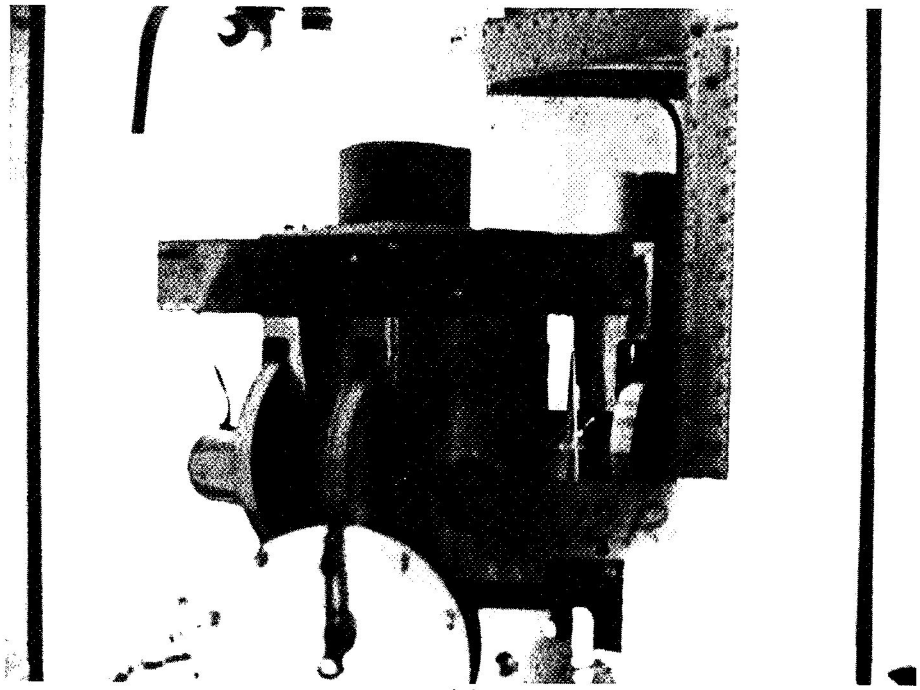

(a)

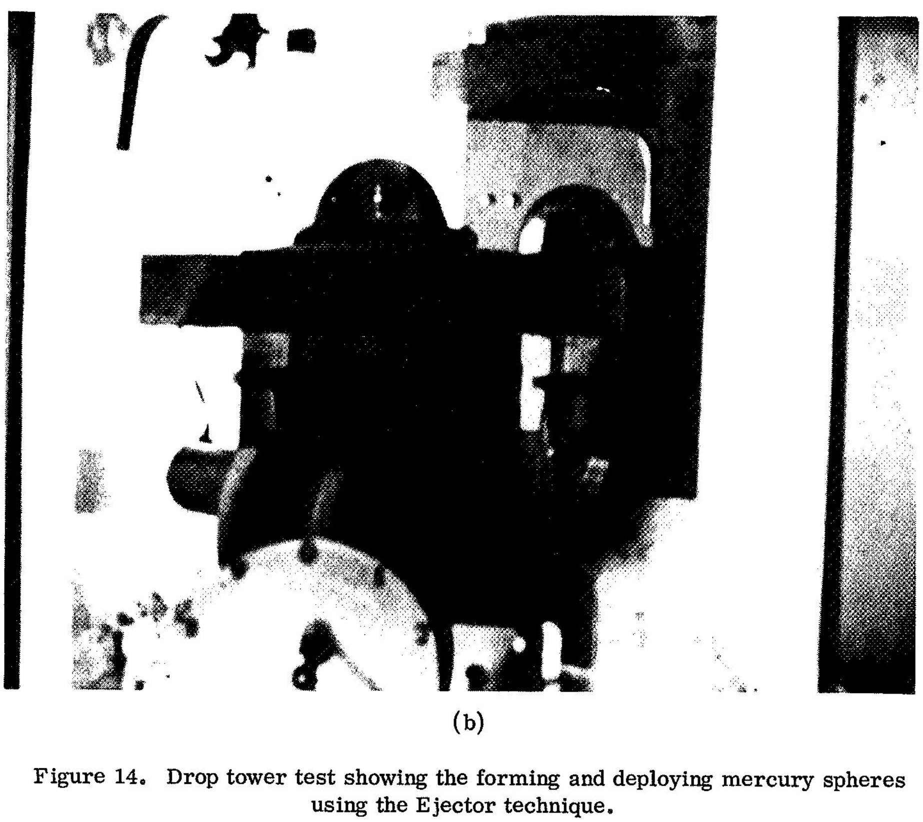

(b)

Figure 14. Drop tower test showing the forming and deploying mercury spheres using the Ejector technique.

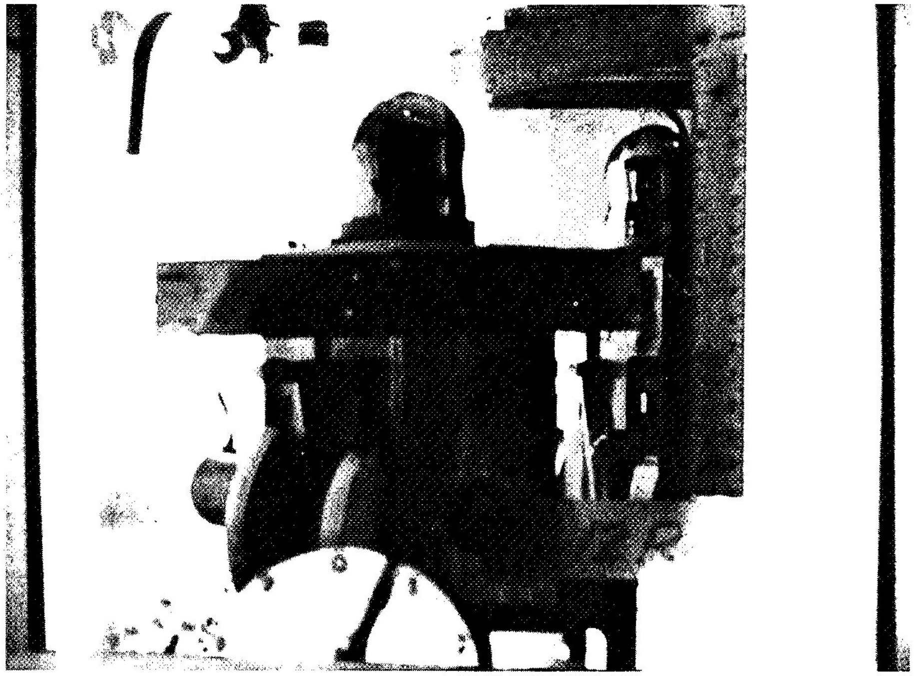

(c)

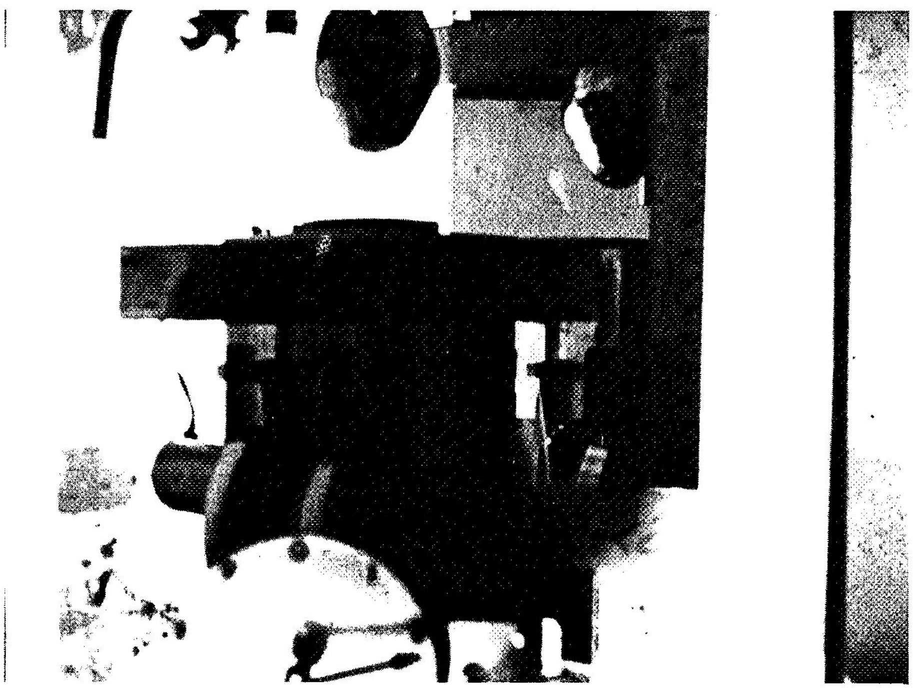

(d)

Figure 14. (Continued).

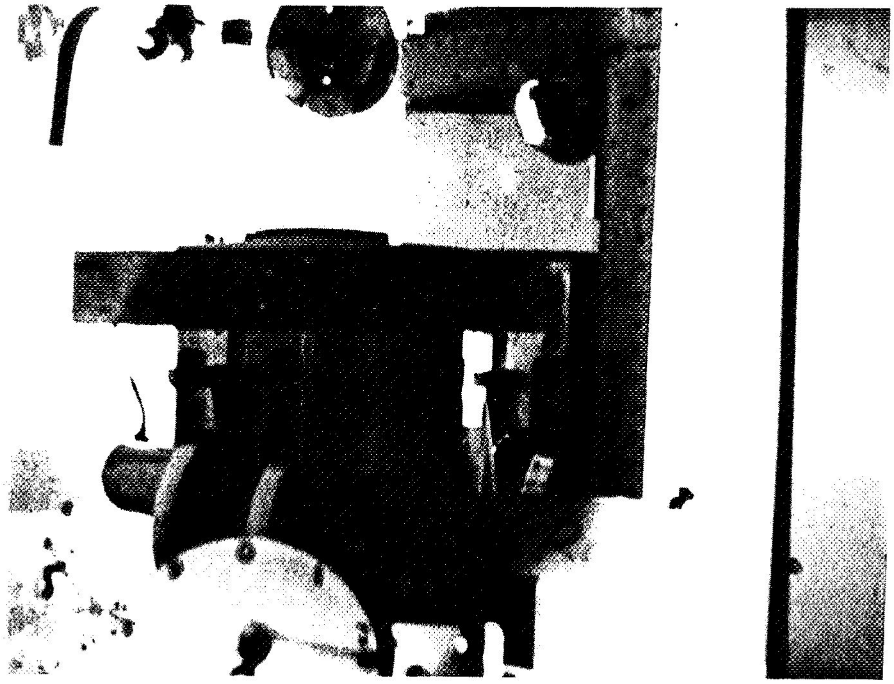

(e)

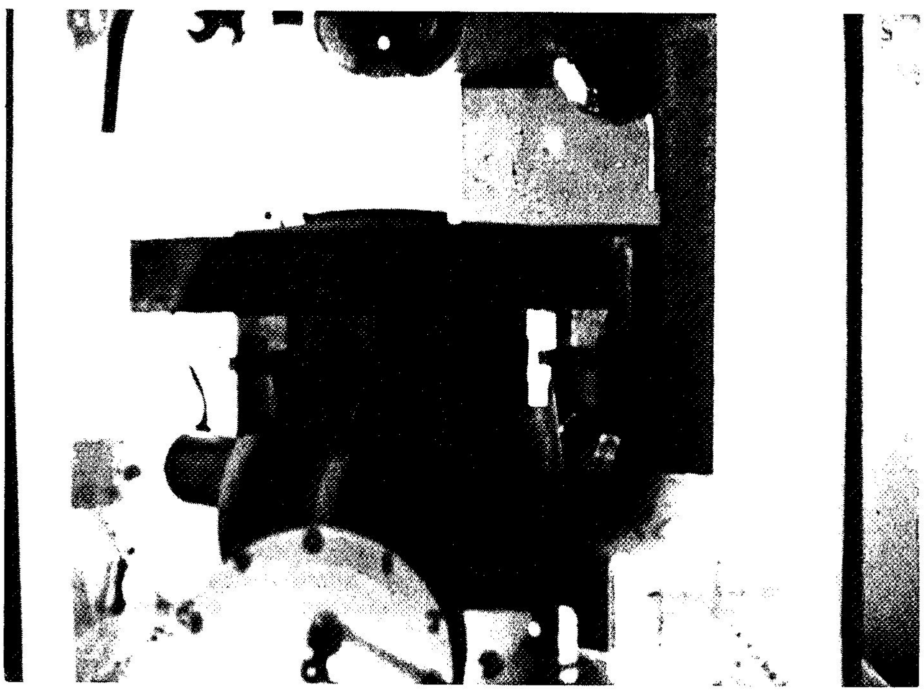

(f)

Figure 14. (Concluded).

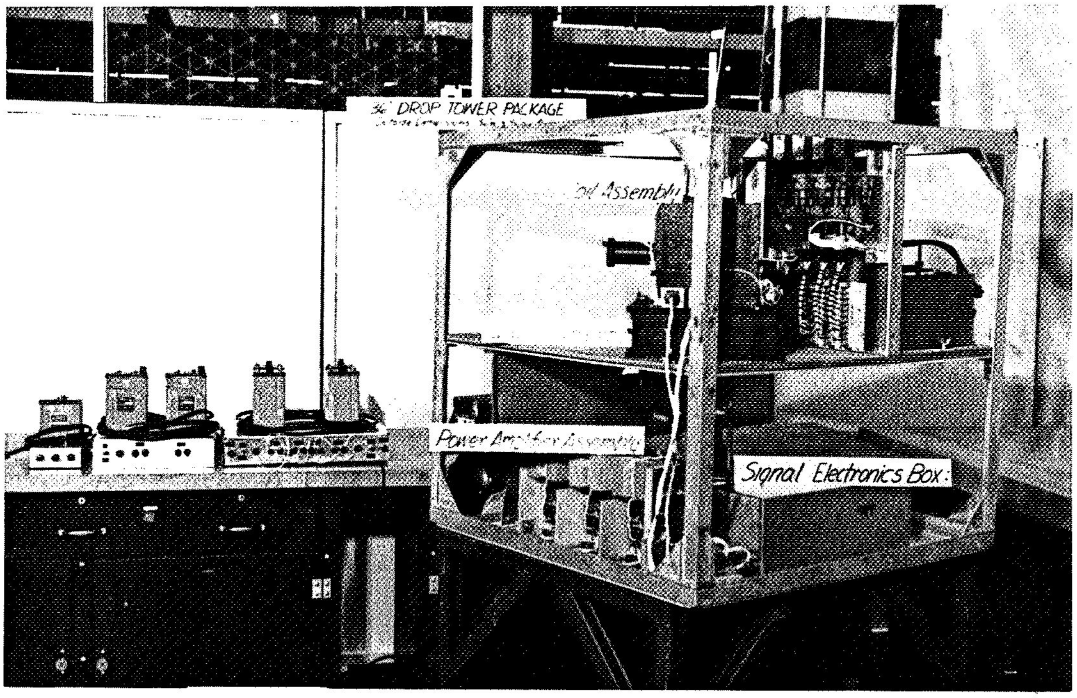

Figure 15. Containerless Processing System mounted in a 0.91-m (3-ft) high drop tower package — the major components of this system are labeled.

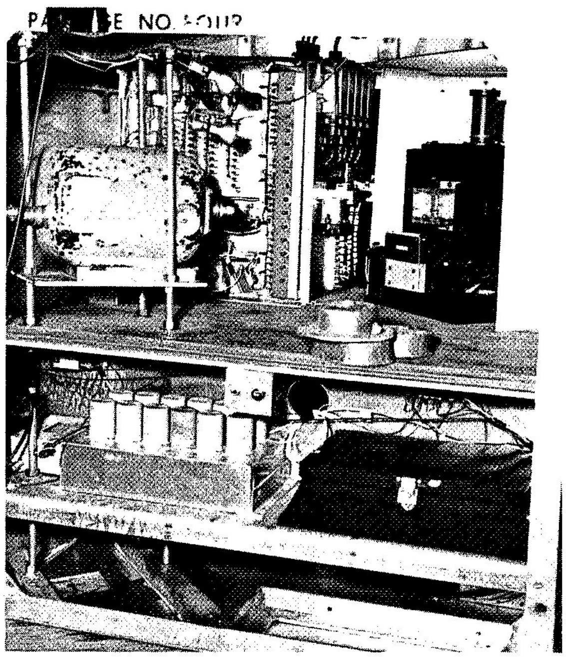

Figure 16. Containerless Processing System mounted in a 0.91-m (3-ft) high drop tower package — camera takes photographs of sphere in coil and spheres in plexiglass box for comparison.

in a 0.91-m (3-ft) high package which has been used both in MSFC's drop tower and a KC-135 aircraft. The purpose of this system is to demonstrate the feasibility of using controllable magnetic fields for positioning and processing free-suspended solid and liquid materials in a zero-gravity environment.

Containerless processing of materials reduces the possibility of contamination and eliminates chemical reaction with the container. Possible applications are the preparation of ultrapure materials and the solidification of materials well below their freezing temperatures (subcooling).

This system positions and processes levitating conducting materials by the influence of three pairs of centering coils, excited to produce oscillating magnetic fields. Attraction and repulsion forces, created by the oscillating fields on the levitating material, are controlled by light-sensitive devices that detect when the material is not in the center of the coils and cause restoring forces to be applied.

Figure 16 shows a plexiglass box mounted on the coil assembly just to the right of the coil toward which the camera is pointed. The box contains several spheres of different diameters and

densities. A hollow aluminum sphere 0.019 m (0.75 in.) in diameter is in the central area of the system coils. Figure 17 is a film sequence from a drop tower test that shows the system damping the oscillations of the sphere in its fields, as compared to the spheres in the plexiglass box.

EXPERIMENTS PREPARED FOR AND TESTED IN RESEARCH ROCKETS

General Information

The purpose of these experiments was to verify and complete some Apollo flyback composite casting demonstrations. These composite casting demonstrations were designed to survey phenomena that occur when a variety of metallic and nonmetallic compositions along with particles and/or gas are melted, mixed, and solidified in a weightless environment.

Technical Information

Temperature Control Units.

Temperature Control Unit, Zero-g Experiment, Aerobee Rocket, MIT 15473. This unit (Fig. 18) was developed to verify and complete the Apollo flyback composite casting demonstrations with research rockets such as the Aerobees and Black Brants. Briefly, this is accomplished by heating the contents of the capsules so the phase change from solid to liquid occurs in near-zero-g (above 91.44 km or 56.82 mi),[8] keeping the contents liquid to permit the occurrence of any changes, and then cooling the capsule to produce a change in phase from liquid to solid before leaving near-zero-g.

Integration of Units into Research Rockets. The major components are noted on the cross section of the unit shown in Figure 19.

Integration of a unit into a rocket includes the following: disassembling the unit sufficiently to insert the flight capsule into the heater and reassembling; filling the hemispherical dome with water; mechanically attaching the unit mounting plate to the bolt circle in the rocket section; charging the battery pack; installing the battery pack in the rocket section; electrically connecting heater and solenoid relays to the timers, battery pack, and unit; setting the timers; and verifying that the system is operational.

A unit is shown mounted in a 0.38-m (15-in.) long cylindrical section of an Aerobee 170A in Figures 20 and 21. Figure 22 shows another unit mounted in a section of a Black Brant VC. For both rockets, the unit is mounted so the centerlines of the vehicle and unit are coincidental to reduce the effect of centrifugal forces on the capsule contents produced by spinning and coning (precession).

To eliminate the possibility of the unit adversely affecting the rocket and/or other experiments on the rocket, a separate battery pack sized to operate the heater and solenoid valve is used. The battery pack used on NASA 21.006 is shown in Figure 22. It contains 24 Yardney HD-3 DC-2 Silvercels. The mass of this battery pack is 2.09 kg (4.6 lbm) and it is 0.188 m (7.4 in.) long by 0.087 m (3.44 in.) wide by 0.072 m (2.85 in.) high.

Each rocket is equipped with dual Haydon timers to provide a redundant means of sequencing both the rocket and payload events. These timers were used to close and open relays which started and stopped the flow of current to both the unit heater and solenoid valve.

Test setup. Figure 23 shows the test setup used to obtain the time-temperature curves. A wooden cradle was made to support the unit in such a way that the long axis of the capsule is in the horizontal plane and the air tube is on the top; this prevents the air tube from being filled with water before the heater housing is filled. The power supply in the foreground provided power for both the heater and solenoid valve. The combination switch and circuit breakers in the wire harness connecting the power supply to the unit were used to manually start and stop the heater and to open and close the solenoid valve during tests.

A time-temperature curve was made for each test. At first, a thermocouple was attached to the top of the capsule. However, this proved unsatisfactory because it did not indicate what was needed, the temperature at the center of the capsule where melting occurred last, and it indicated a much faster drop in temperature during water quench

8. U.S. Standard Atmosphere, 1962, Table II Geometric Altitude, Metric Units, p.80 for 91.5 km g = 9.530 m/sec^2 less acceleration of rocket, 9.414 m/sec^2 = 0.117 m/sec^2, 0.117 m/sec^2/9.80665 m/sec^2 = 0.0119 g.

C-2

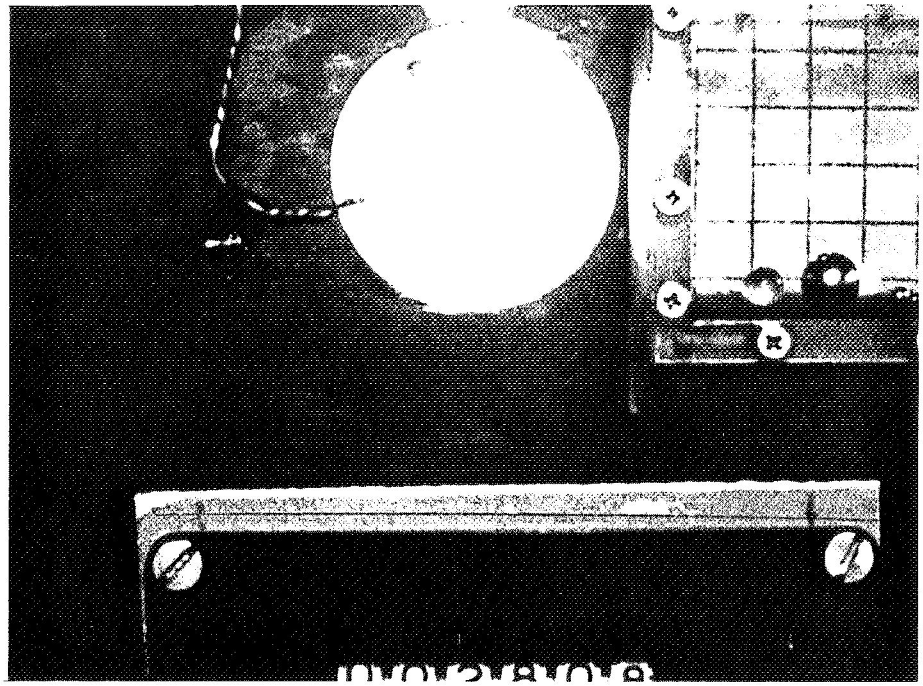

(a)

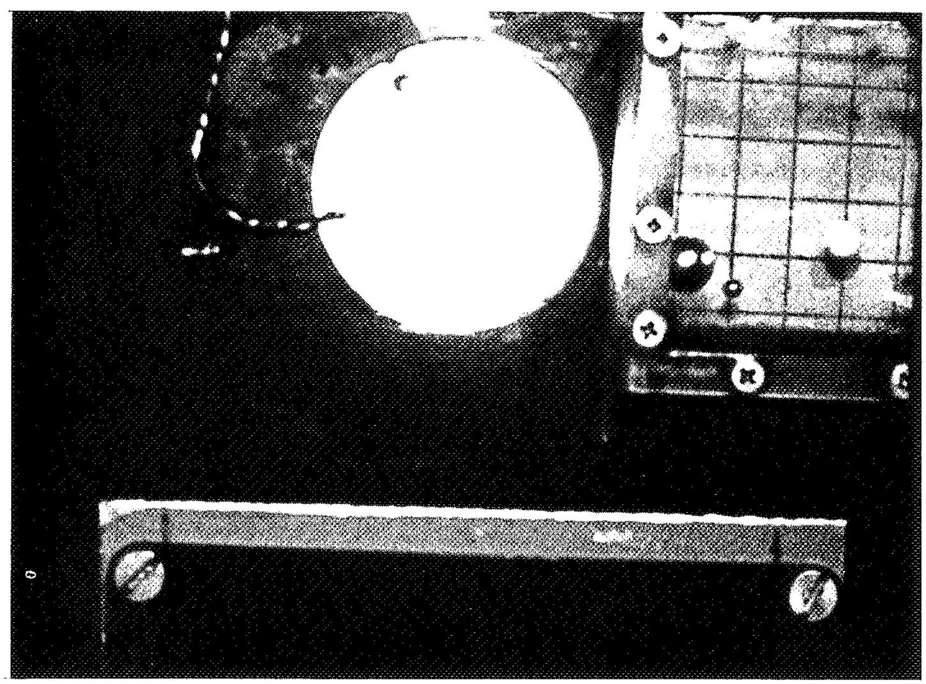

(b)

Figure 17. Drop tower test showing the Containerless Processing System starting to center (damping its oscillations) a hollow aluminum sphere.

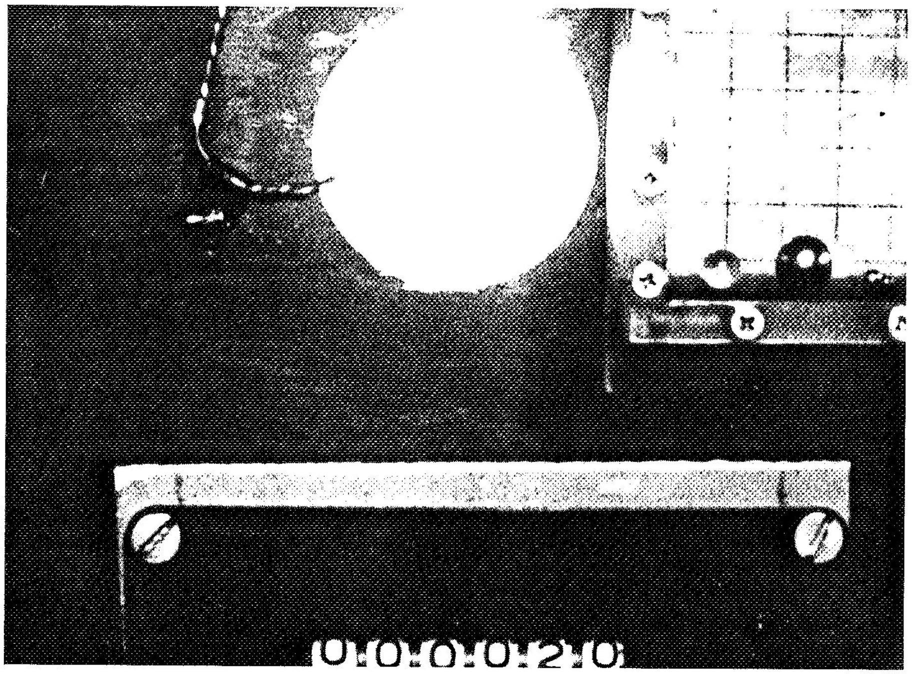

(c)

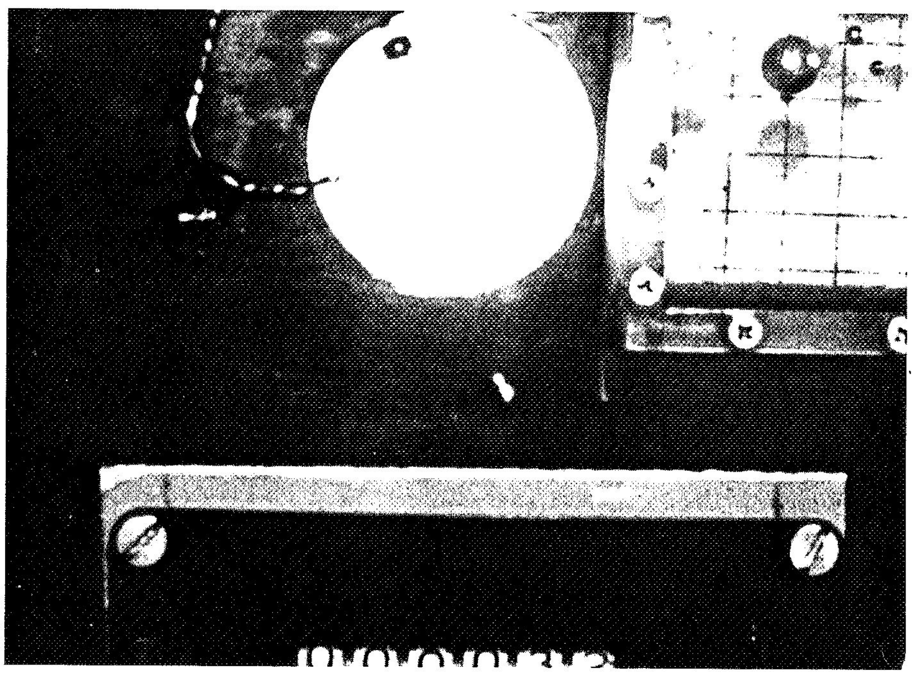

(d)

Figure 17. (Concluded).

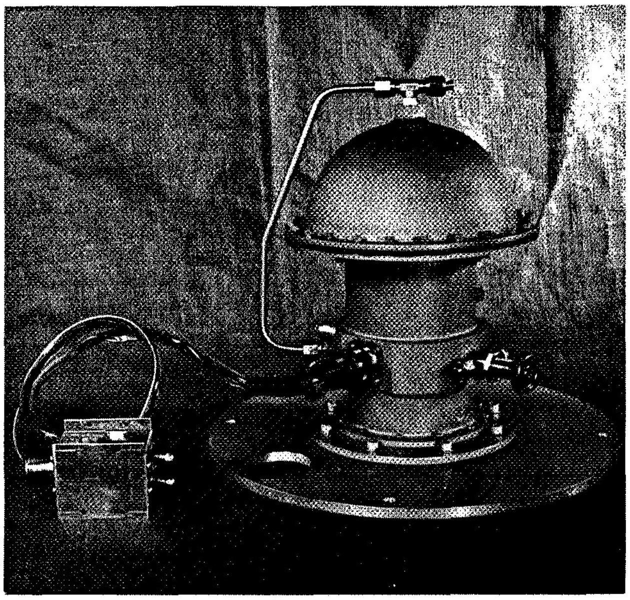

Figure 18. Temperature Control Unit, zero-g experiment, Aerobee rocket, MIT 15473.

than actually occurred. To remedy this, a hole was drilled in the large end of the test capsule and the thermocouple was inserted to such a depth that it was in the center of the capsule. This produced satisfactory time-temperature curves and gave an indication of the relationship between the internally and externally mounted thermocouples.

Time-temperature tests. The purpose of these tests was to develop heating and cooling cycles which permit both phase changes of the capsule constituents — solid to liquid and liquid to solid — during the time it was in near-zero-g, above 91.44 km (56.82 mi).

The time above 91.44 km was 220 sec for NASA 13.113 (Fig. 6) as compared to 347 sec for NASA 21.006. Figures 24 and 25 show the time-temperature relationships developed for NASA 13.113 and NASA 21.006, respectively.

To accomplish both phase changes for NASA 13.113, it was necessary to keep to a minimum the time to change from solid to liquid and the hold

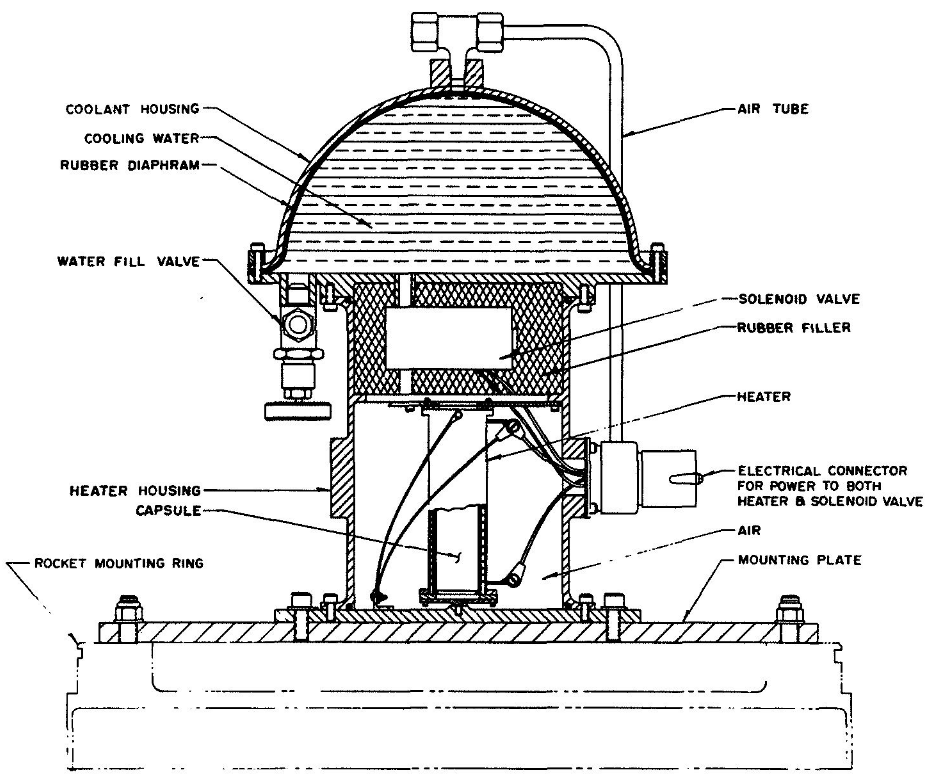

Figure 19. Cross section of Temperature Control Unit, zero-g experiment, Aerobee rocket, MIT 15473, with major components labeled.

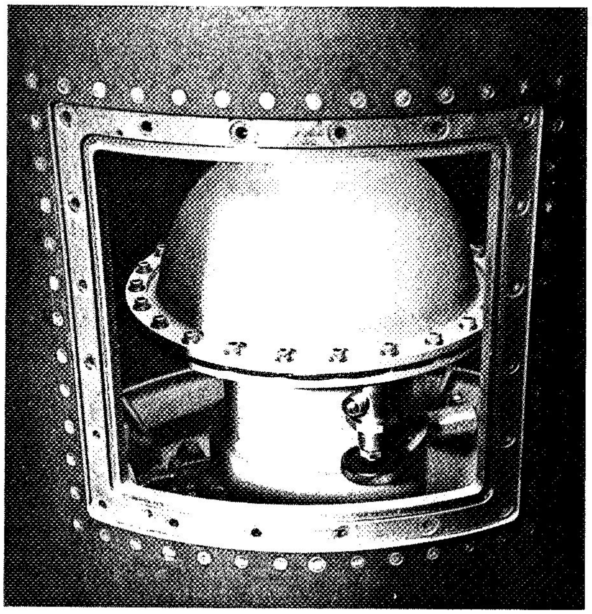

Figure 20. Oblique view of Temperature Control Unit mounted in 0.38-m (15-in.) long cylindrical section of an Aerobee 170A Research Rocket.

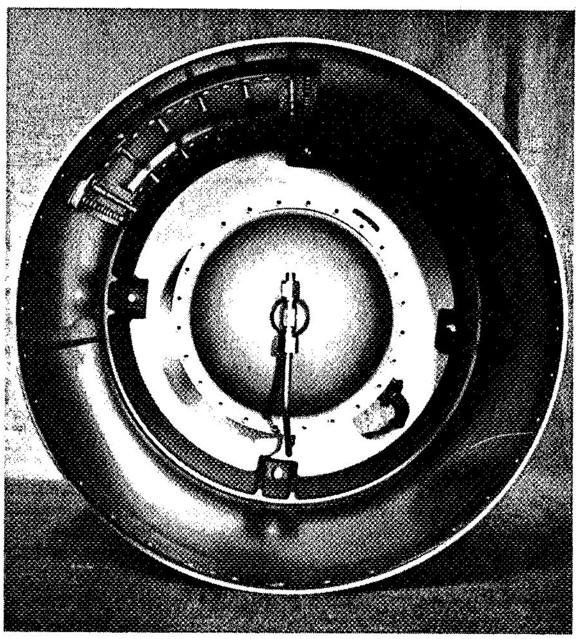

Figure 21. Top view of Temperature Control Unit mounted in 0.38-m (15-in.) diameter cylindrical section of an Aerobee 170A Research Rocket.

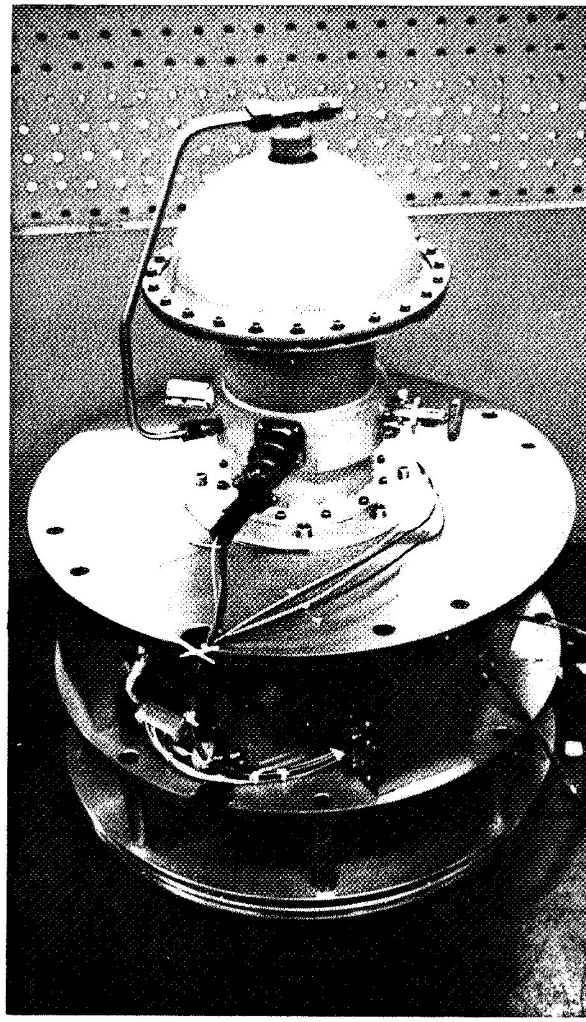

Figure 22. Temperature Control Unit mounted in a section of Black Brant VC Research Rocket NASA 21.006.

time in the liquid state. Several tests with various length heating times were conducted before 100 sec of heating for NASA 13.113 and 90 sec for NASA 21.006 were established. By increasing the heating time 10 sec, the time required for the solid-to-liquid phase change was reduced 60 sec, from 77 sec to 17 sec.

Flight Data.

Aerobee 170A Research Rocket and the Flight of NASA 13.113. In Figure 26, the relationships between altitude versus time for Aerobee 170A

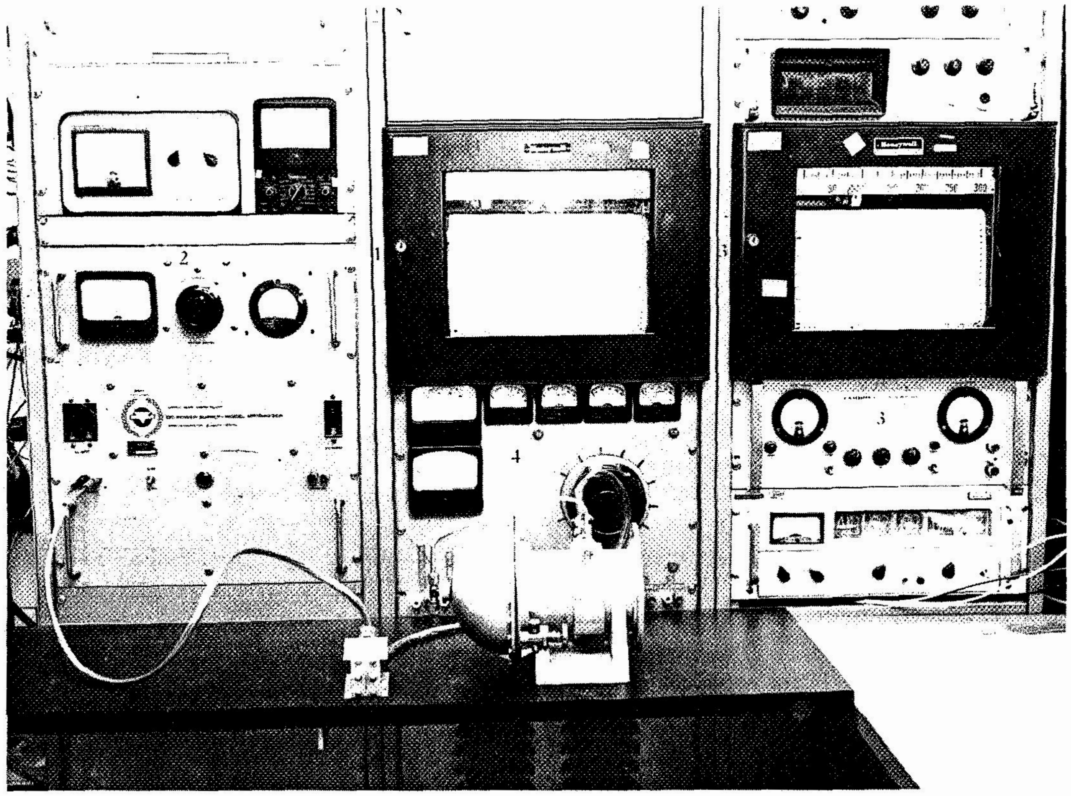

Figure 23. Test setup used to obtain time-temperature curves with capsule containing InBi and a thermocouple located at its center in the Temperature Control Unit.

NASA 13.113 and temperature versus time for the temperature control unit are shown.

MSFC did not request any holding time because early tests indicated the specimen could not be cooled rapidly enough to obtain the liquid-to-solid phase change above 91.44 km (56.82 mi). However, by the time of the launch, October 19, 1971, MSFC had worked out a procedure where approximately 70 sec of holding time would have been the maximum. At White Sands Missile Range, Mr. Wuenscher requested that the timers be changed to provide 30 sec of holding time. GSFC was able to adjust the timers to provide 9 sec of holding time (Fig. 26).

After yo-yo despin, from 167.1 to 13.5 rpm, there is an acceleration of approximately 0.0018 g at the inner wall of the capsule as shown below.

Acceleration at inner wall of capsule produced by spinning (Fig. 27).

$$a_s = r\omega^2 \quad ,$$

where

a_s is the acceleration produced by spinning at the inner wall of the capsule, in m/sec^2 (ft/sec^2),

r is the radius of the capsule, in m (in.),

and

ω' is the angular velocity of the vehicle after despin, in rad/sec.

$$a_s = \frac{0.690 \text{ in.}}{2} \times \frac{1 \text{ ft}}{12 \text{ in.}} \times (1.417 \text{ rad/sec})^2 \quad ,$$

$$a_s = 0.058 \text{ ft/sec}^2 \quad .$$

$$g_s = \frac{a_s}{32.16 \text{ ft/sec}^2} = \frac{0.058}{32.16} = 0.0018 \text{ g} \quad .$$

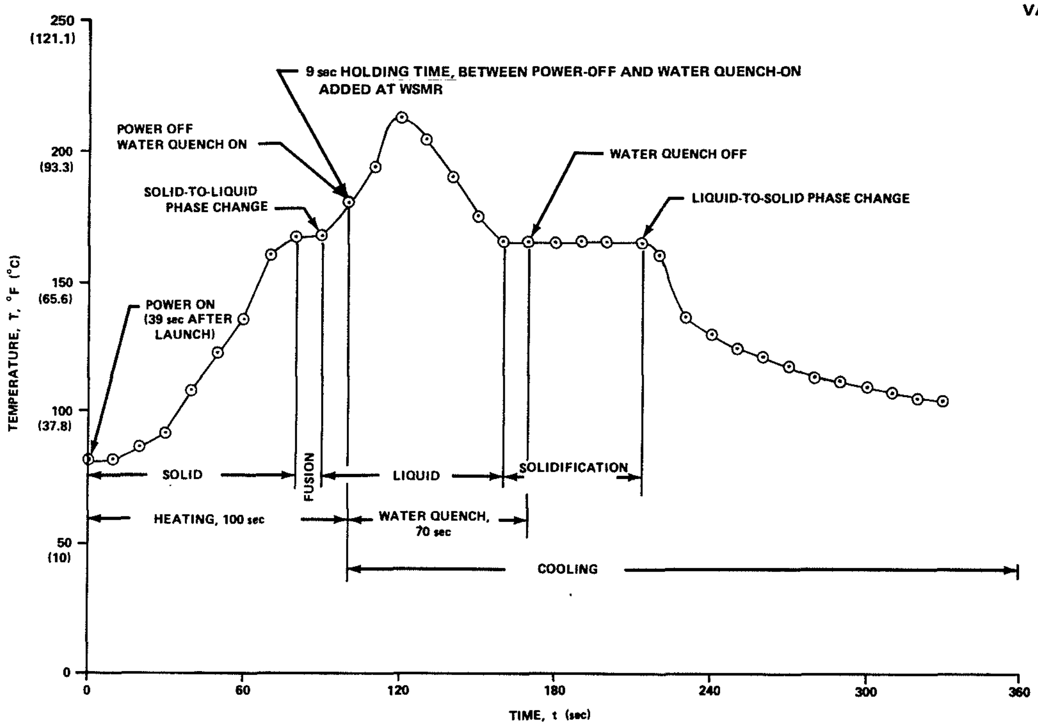

Figure 24. Time versus temperature relationship developed by MSFC for processing capsule on Aerobee 170A NASA 13.113.

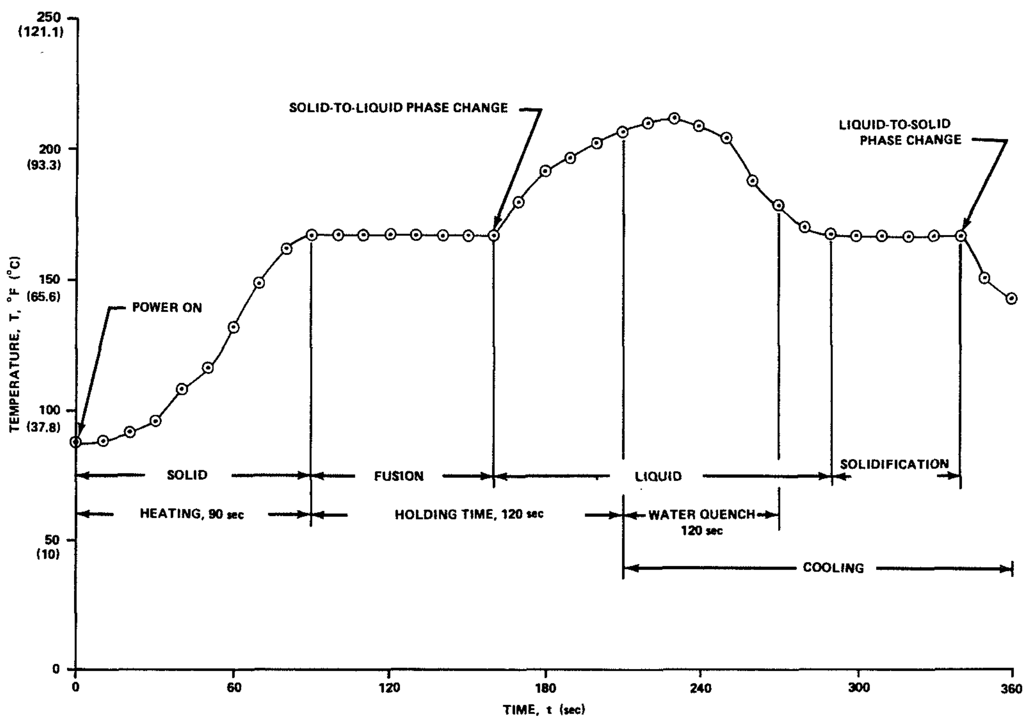

Figure 25. Time versus temperature relationship developed by MSFC for processing capsule on Black Brant VC NASA 21.006.

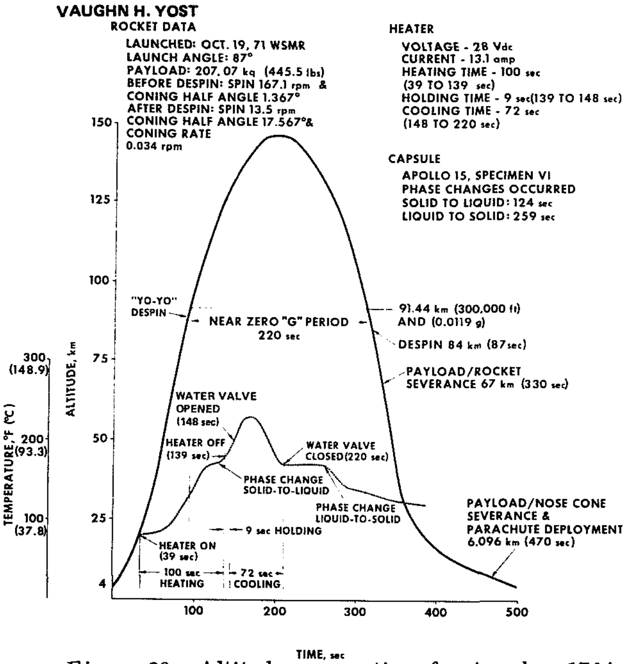

Figure 26. Altitude versus time for Aerobee 170A NASA 13.113 and temperature versus time for Temperature Control Unit.

Acceleration at inner wall of capsule produced by coning (Fig. 27).

$$a_c = r\omega^2 \quad ,$$

where

a_c is the acceleration produced by coning at the inner wall of the capsule, in in./sec^2 (ft/sec^2),

r is the distance from research rocket trajectory to inner wall of capsule,

and

ω' is the coning rate, in rad/sec.

$$a_c = \left(81.77 \text{ in.} \times \sin 17.567 \text{ deg} + \frac{0.690 \text{ in.}}{2}\right.$$

$$\left. \div \cos 17.567 \text{ deg}\right) \frac{1 \text{ ft}}{12 \text{ in.}} \times (0.00357 \text{ rad/sec})^2 ,$$

$$a_c = \frac{24.661 + 0.362}{12} \times 0.0000128 \quad ,$$

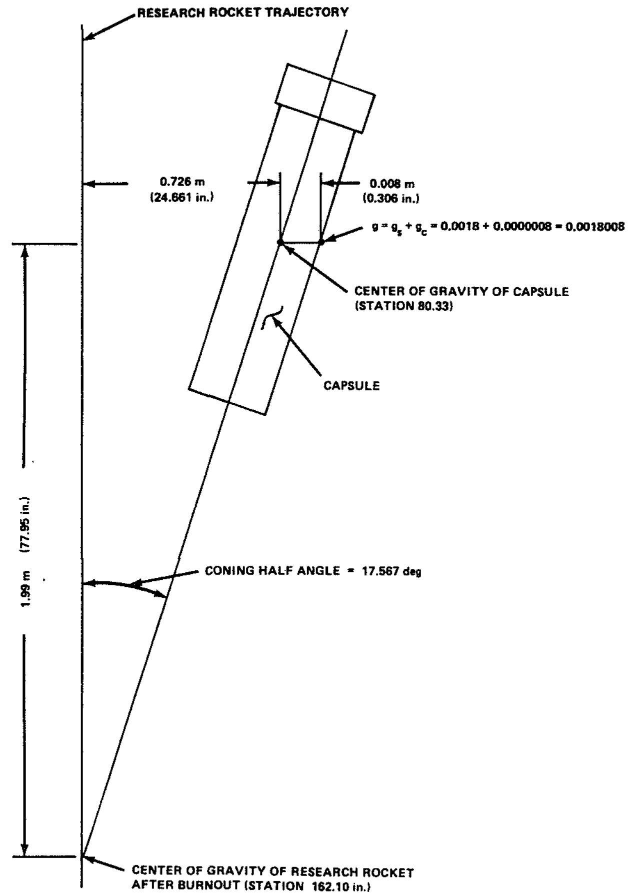

Figure 27. Acceleration at inner wall of capsule produced by spinning and coning of Aerobee 170A NASA 13.113.

$$a_c = 0.000025 \quad .$$

$$g_c = \frac{a_c}{32.16 \text{ ft/sec}^2} = 0.0000008 \text{ g} \quad ,$$

$$g = g_s + g_c \quad ,$$

$$g = 0.0018 + 0.0000008 = 0.0018008 \quad .$$

Capsule.

Objective. The objective of the experiment was to investigate the stability of gas bubbles in plain and fiber-reinforced metal melted and solidified in a near-zero-g environment.

Description of Sample. The sample originally designed and fabricated for the Apollo 15 composite casting demonstration by General Dynamics/Convair was made up of two material systems: interconnected gas cells in a fiber-reinforced metal matrix in the A-half of the sample and discrete gas bubbles in plain metal matrix in the B-half of the sample. The A-half was made up of 11 disks of InBi-coated copper wire layups which formed interconnected gas cells. The B-half was made up of 20 disks of InBi eutectic alloy which had been coined to form 27 half-spherical impressions in each side. When the disks were stacked, discrete uniformly distributed spheres were formed. The two halves, separated by an aluminum divider, were placed into an aluminum sample capsule as shown in Figure 28 and were capped in an argon chamber. The sample capsule was, subsequently, sealed by electron beam welding.

Preparation and Processing of Sample.

A-half, interconnected gas cells. Lengths of 0.0001-m (0.005-in.) beryllium copper wire were coated with the InBi eutectic alloy by placing four wires into a 0.001-m (0.045-in.) ID plastic tube and injecting molten InBi into the tube while it was immersed in a hot water bath as shown in Figure 29. After the tube was filled, it was removed from the hot water bath and straightened. The InBi solidified in a few minutes after removal from the bath. The plastic tubing was then stripped from the InBi-coated copper wires. The coated wires were straightened, cut to length, and layed up in a tool as shown in Figure 30. The layup was compressed in a platen press as shown in Figure 31 to a finished thickness of approximately 0.003 m (0.140 in.). Disks 0.017 m (0.687 in.) in diameter were then cut from the layup as shown in Figure 32. An enlarged view of the cells formed by the coated wires is shown in Figure 33. The sample half was then assembled in a chamber filled with argon by stacking 11 disks in an assembly fixture and compressing them to the final dimension of 0.037 m (1.440 in.).

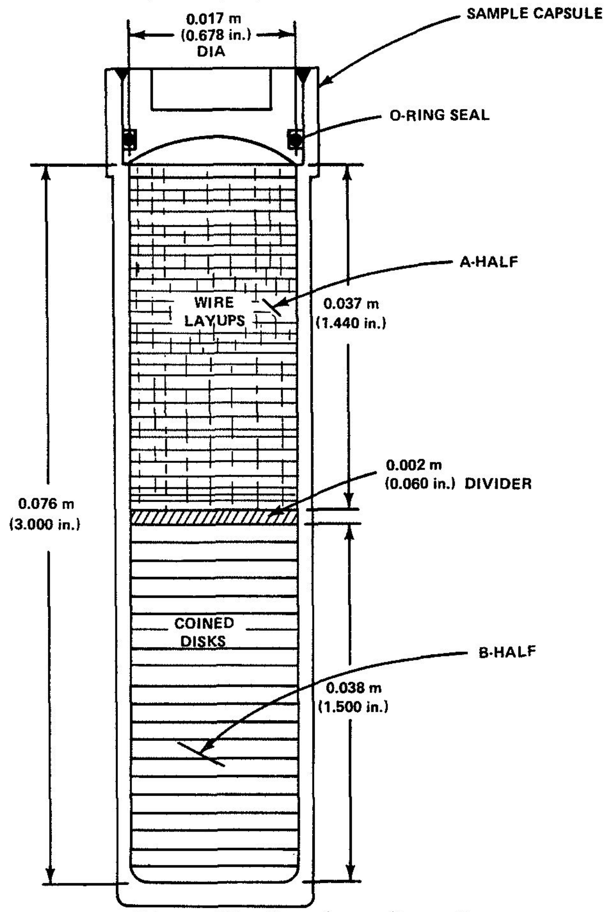

Figure 28. Sample configuration.

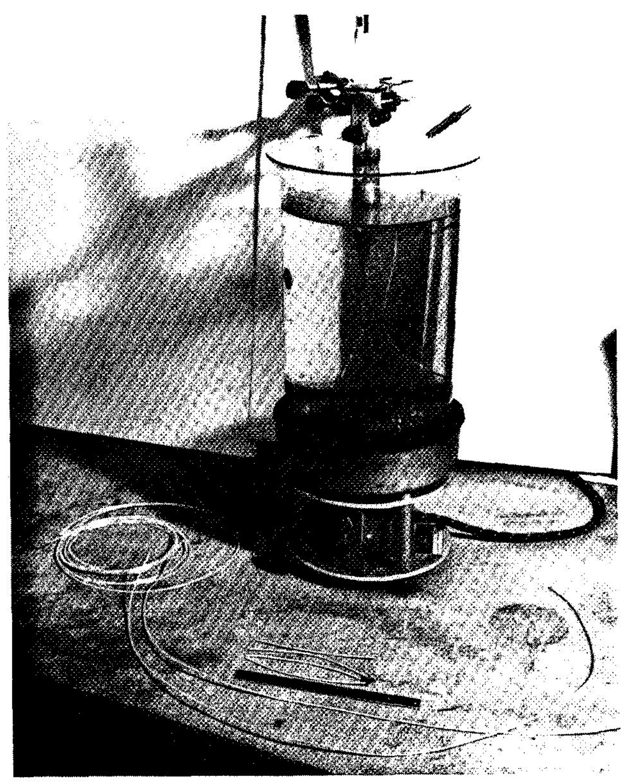

Figure 29. Casting of layup wires — molten InBi injected in 0.76-m (30-in.) long plastic tube 0.001 m (0.045 in.) in diameter containing four Cu-Be wires 0.001 m (0.005 in.) in diameter.

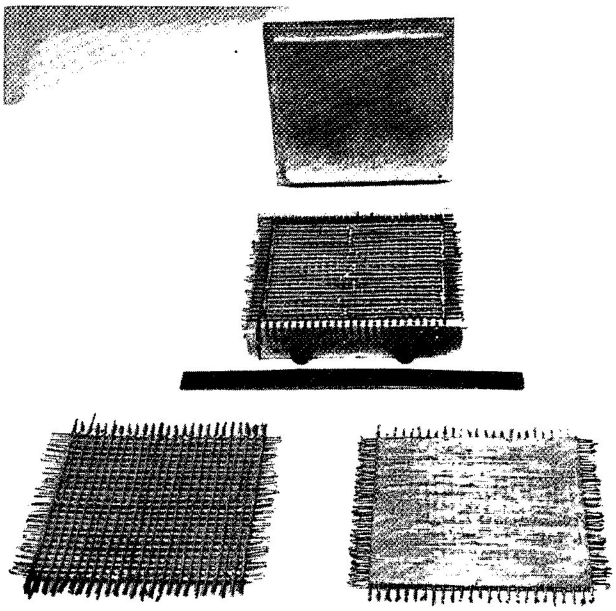

Figure 30. Layup at various stages of assembly and layup tooling.

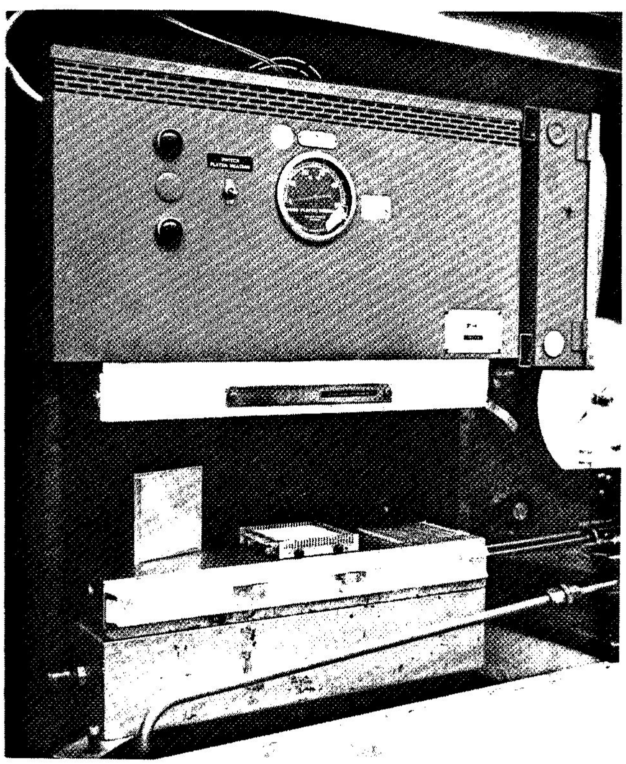

Figure 31. Layup in press for bonding.

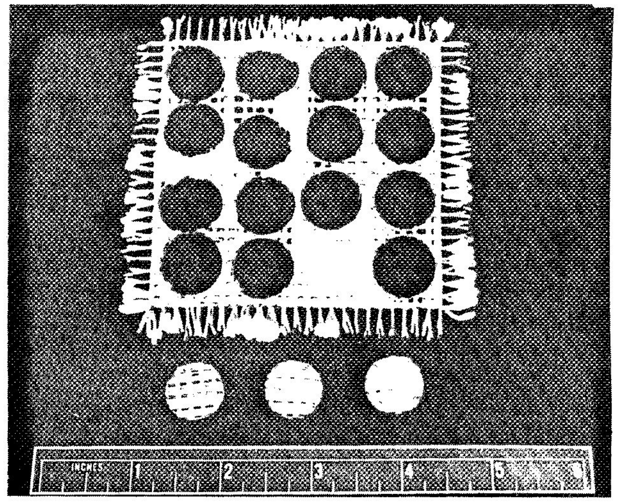

Figure 32. Cutting of layup disks — first layup (subsequent disks were more perfect).

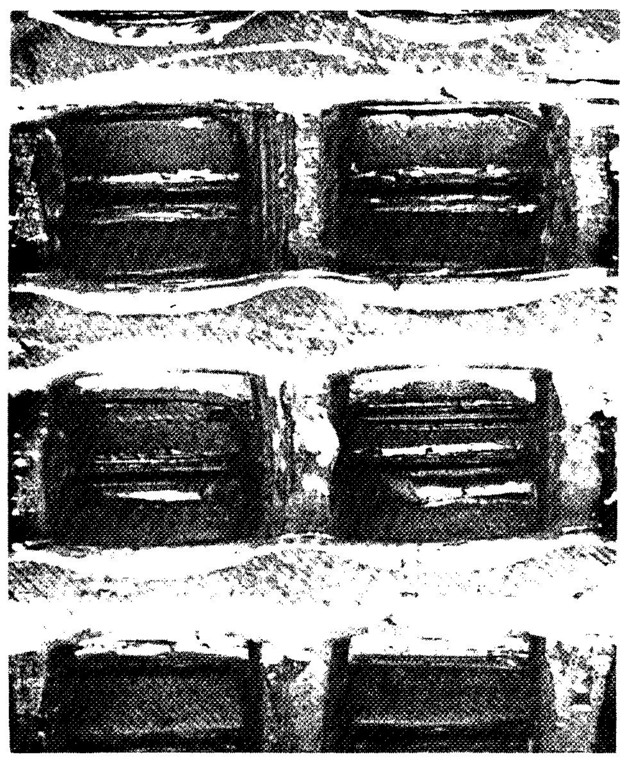

Figure 33. Layup cells (approximately 25X) [cell spacing between wired centerlines approximately 0.003 m (0.130 in.)].[9]

9. All figures in this paper that have magnifications shown have been reduced for printing purposes.

B-half, discrete gas bubbles. Cast rods of InBi eutectic alloy were cut into slices which were then coined using tooling shown in Figure 34 and the press shown in Figure 35. A finished coin is shown in Figure 36. The coins were cleaned and stacks of 20 disks were bonded together by compressing them at 60°C (140°F) to the finished length of 0.038 m (1.5 in.) in a chamber filled with argon (Fig. 37). The bonded stack was removed from the tool and turned to 0.017-m (0.687-in.) OD. A section cut from an assembled sample is shown in Figure 38.

Sample assembly. The A and B sample halves were inserted into an aluminum sample capsule and capped in a chamber filled with argon. Final sealing of the capsule was accomplished by electron beam welding the cap to the capsule.

Processing of sample. The flight sample was processed in the unit as shown in Figures 37, 38, 39, and 40.

An identical ground control sample was processed in the same equipment using the same procedures. The sample was in the horizontal position; therefore, gravity forces were acting perpendicular to the long axis.

Evaluation of Sample.

Removal from capsule and preliminary evaluation. Both the flight and ground control samples were sectioned longitudinally using the electrical discharge machining (EDM) technique. The samples were sectioned while in the aluminum capsule to simplify holding the sample. Unfortunately the flight sample had shrunk slightly and rotated during the cutting operation. Consequently, the finished cut was irregular and additional material was inadvertently removed from one end of the sample.

Examination of the flight sample revealed that the A-half of the sample had not been heated sufficiently to melt the InBi coating on the wires except in a small area as seen in Figure 39. Therefore, further evaluation of this sample half was not performed.

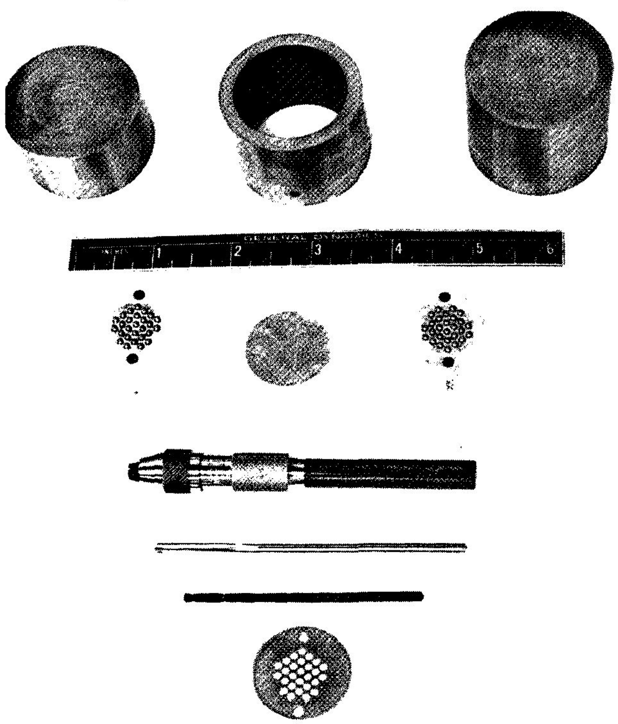

Figure 34. Coin tooling.

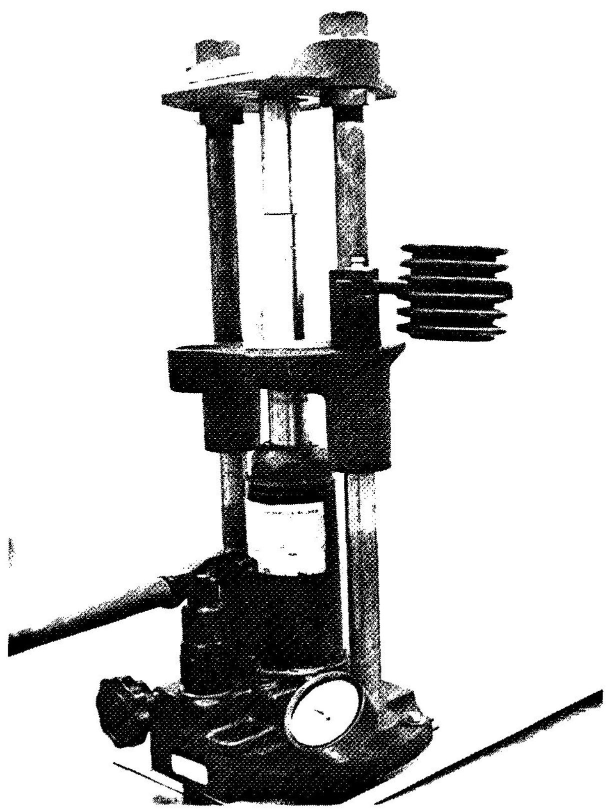

Figure 35. Tooling for coins in press (used for manufacture of coins and for bonding of stack).

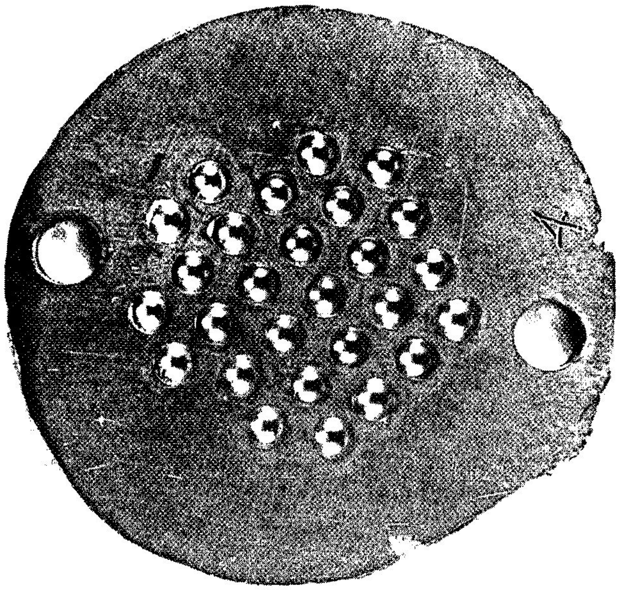

Figure 36. Finished coin (plain InBi).

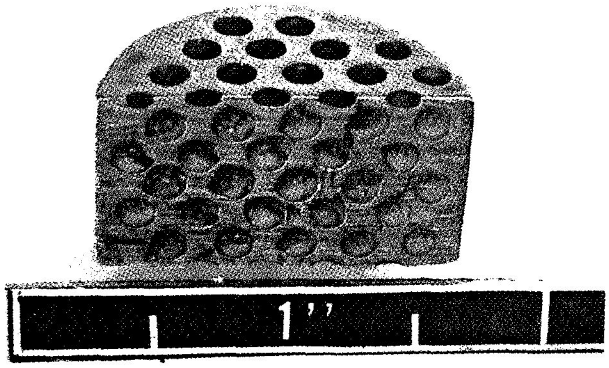

Figure 38. Section of B sample.

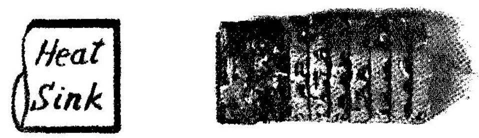

Specimen No. VI/2 F — Sample Configuration
as filled — X Complete
ground processed — Segment
X flight processed — Section
View: top bottom
Side (0)/90/180/270°
Enlargement: x
cm 2 3 4 5 6 7 8 9 10

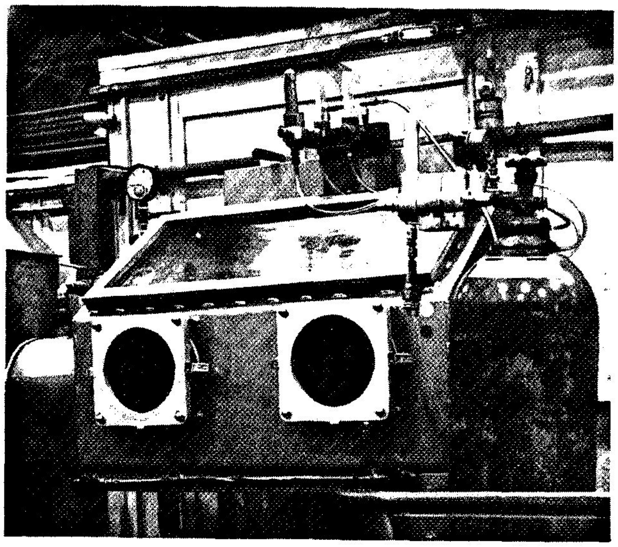

Figure 37. Argon-filled chamber used for sample assembly.

The B-half of the sample had melted considerably more as evidenced by the appearance of the external surfaces as seen in Figure 40 and the sectioned surfaces as seen in Figure 41. More melting obviously occurred in the end of the sample nearest the bottom of the capsule (heat sink) and in the half identified

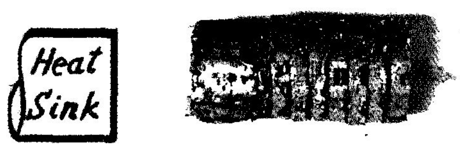

Specimen No. VI/2 F — Sample Configuration
as filled — X Complete
ground processed — Segment
X flight processed — Section
View: top bottom
Side 0/90/(180)/270°
Enlargement: x
cm 2 3 4 5 6 7 8 9 10

Figure 39. A sample half as removed from capsule.

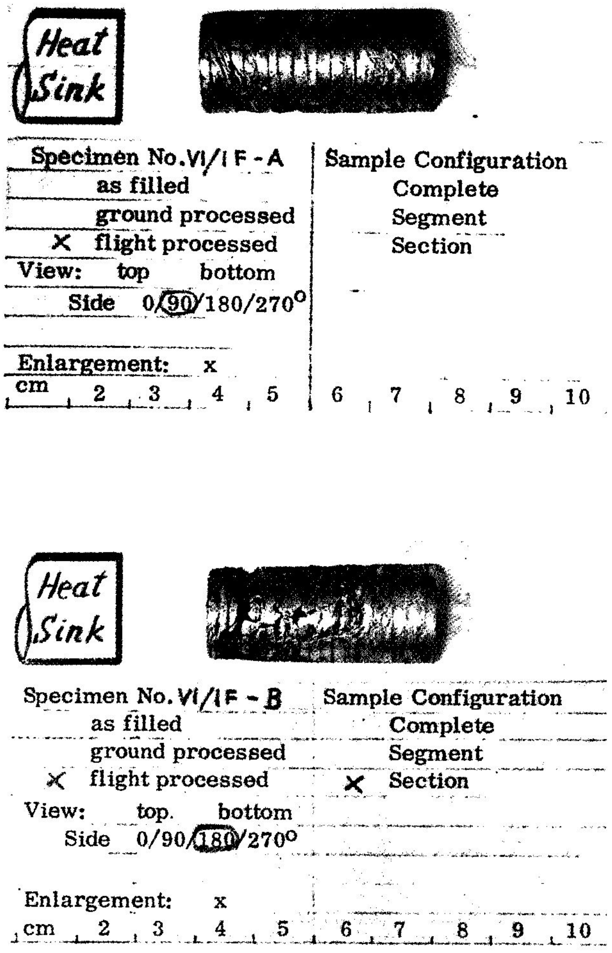

Figure 40. B sample half, external surface as removed from capsule.

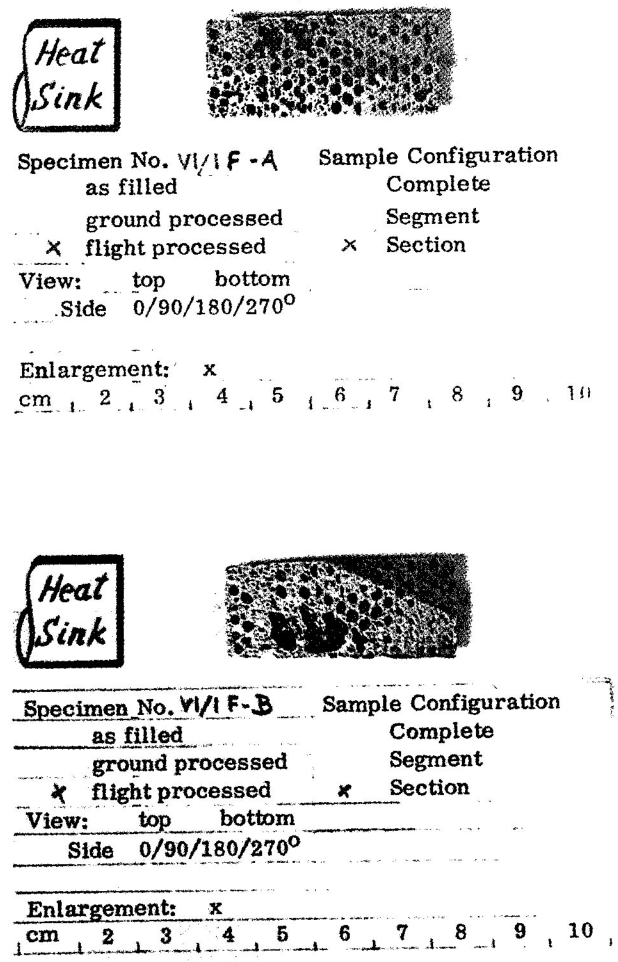

Figure 41. B sample, longitudinal sections as sectioned.

as VI/IF-B in Figures 40b and 41b. Some bubble coalescence did occur in this portion of the sample.

Detailed evaluation of B-half of sample. The sectioned sample halves, both flight and ground control, were mounted in plastic, polished, and etched for more detailed evaluation.

The ground control sample shown in Figures 42 and 43 appears to have melted throughout and most of the gas bubbles have been eliminated because of buoyancy forces.

Longitudinal sections of the flight sample are shown in Figures 44 and 45 after initial preparation. These photomacrographs show that only partial melting occurred in the sample. In the areas which appeared to have melted, three conditions were noted: some bubbles had disappeared, some bubbles had coalesced, and some bubbles remained in place.

At this point a decision was made to polish the sample sections further to expose other layers of bubbles. The section identified as VI/IF-A was remounted in plastic so that it could be polished in the transverse direction.

Further polishing and etching of the longitudinal section VI/IF-B shown in Figure 46 revealed two distinct zones. The lighter area with the variation in structure at the left and top of the

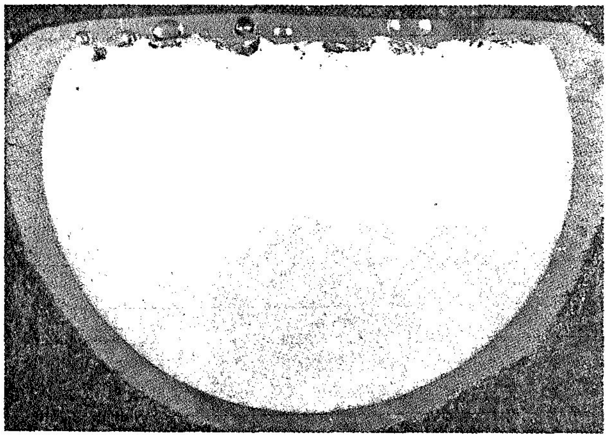

Figure 42. Transverse section of ground control sample (6X).

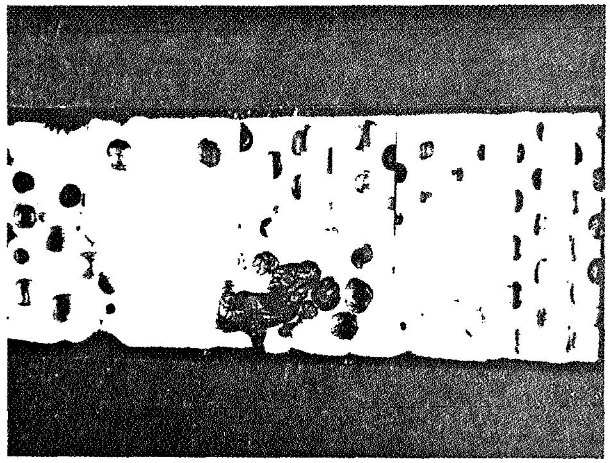

Figure 44. Longitudinal section of bottom of flight sample VI/IF-B (3X).

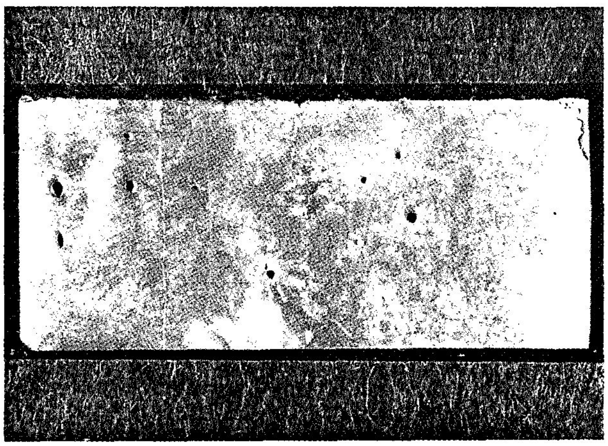

Figure 43. Longitudinal section of ground control sample (4X).

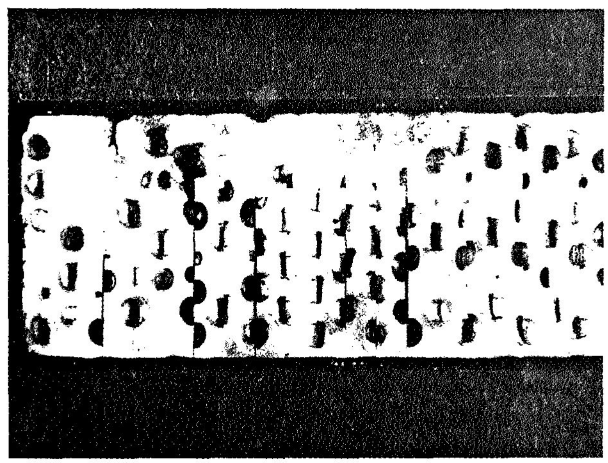

Figure 45. Longitudinal section of bottom of flight sample VI/IF-A (2.75X).

photomacrograph is the melted zone. The darker area at the bottom right is the unmelted, or unaffected, zone. Photomicrographs of the circled areas in Figure 46 are shown in Figures 47, 48, 49, and 50. These show the microstructure in the melted zone, at the transition, and in the unmelted zone. The microstructure of the unmelted area (Fig. 50) is comparable to that taken from an as-coined disk (Figs. 51, 52, and 53).

Further polishing and etching of section VI/IF-A in the transverse direction showed similar structure (Fig. 54). Photomicrographs of the areas in melted, transition, and unmelted zones are shown in Figures 55, 56, and 57.

Additional cuts made through each section of the sample show similar structures. The wide variations in structure throughout the flight sample are indicative of its complex thermal history. Obviously, the sample did not approach an equilibrium temperature.

CONCLUSIONS

1. The drop tower is the preferred method of obtaining short periods of near-zero-g — 1×10^{-5} g.

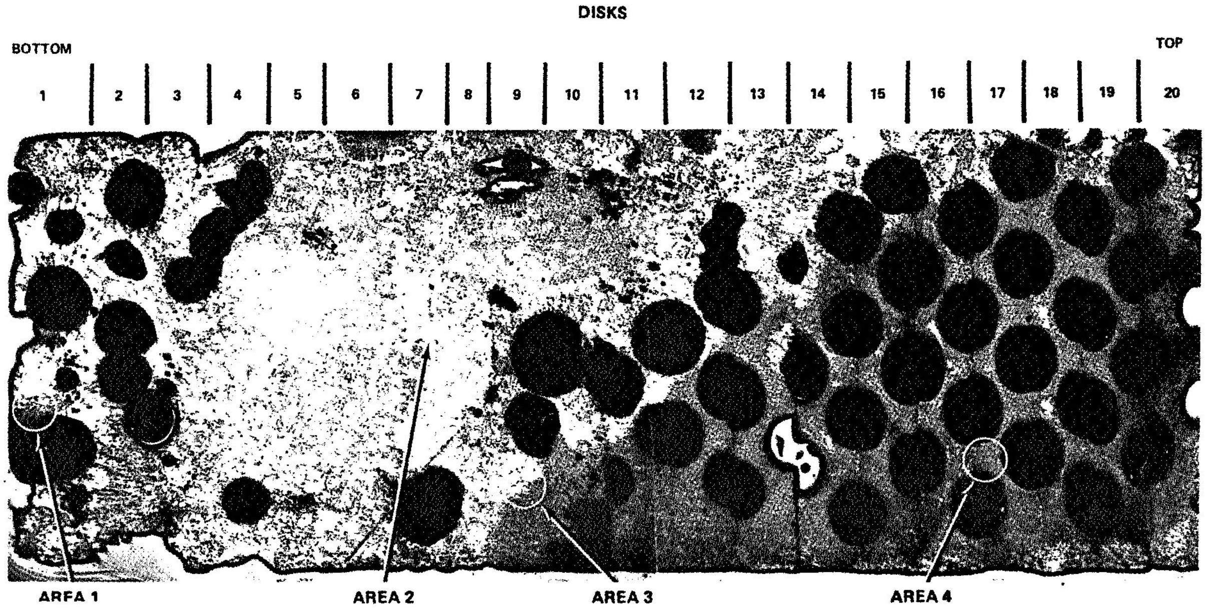

Figure 46. Longitudinal section VI/IF-B showing etched macrostructure of Aerobee wafer composite (areas 1 through 4 were documented to show recrystallized structure resulting from flight test, transition zone, and unaffected structure) (7X).

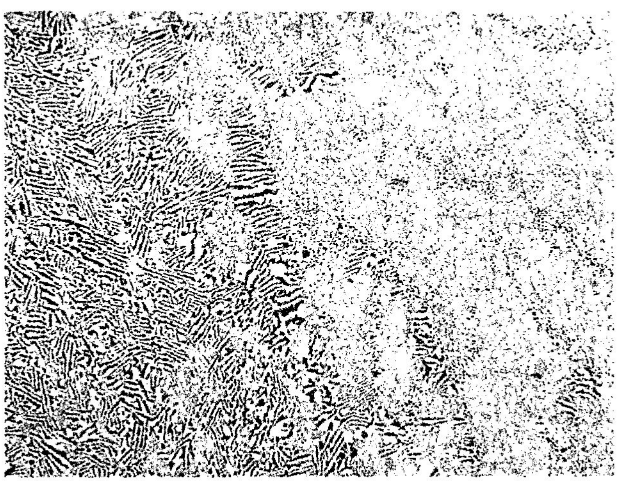

Figure 47. Microstructure at area 1, Figure 46 (100X).

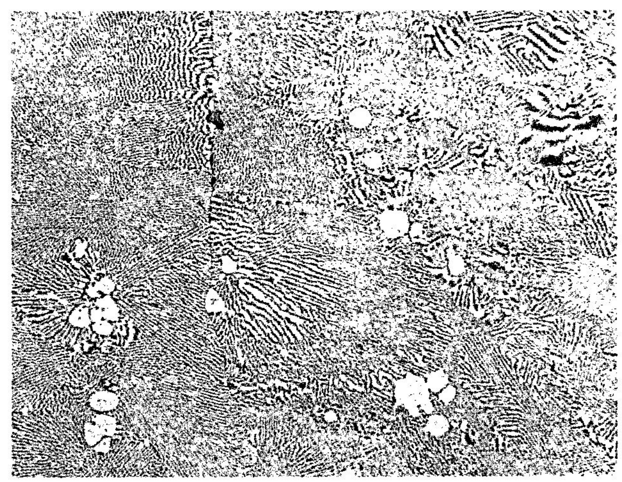

Figure 48. Microstructure in melted area at area 2, Figure 46 (100X).

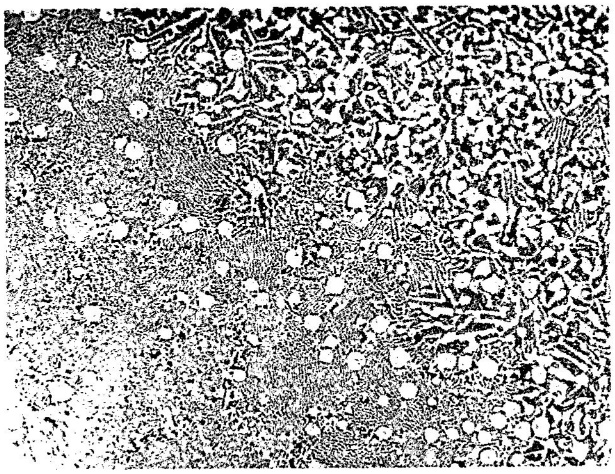

Figure 49. Duplex microstructure in transition zone at area 3, Figure 46 (100X).

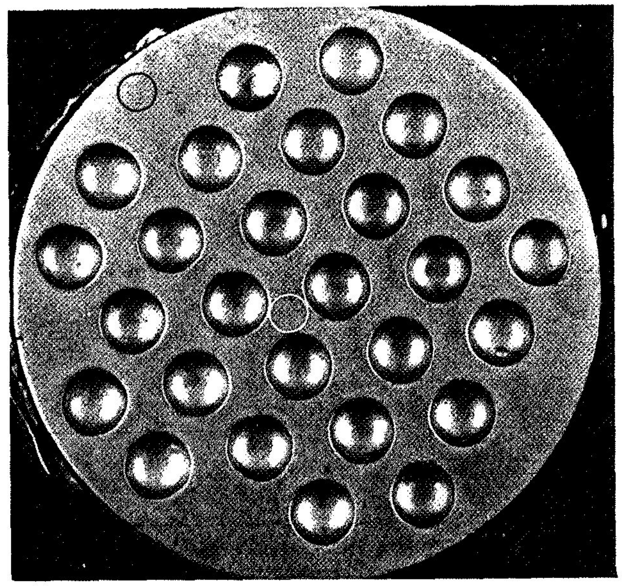

Figure 51. Surface view of as-received wafer showing macrostructure and configuration of bubbles (enlargement of areas shown at black and white circles are shown in Figures 52 and 53, respectively) (7X).

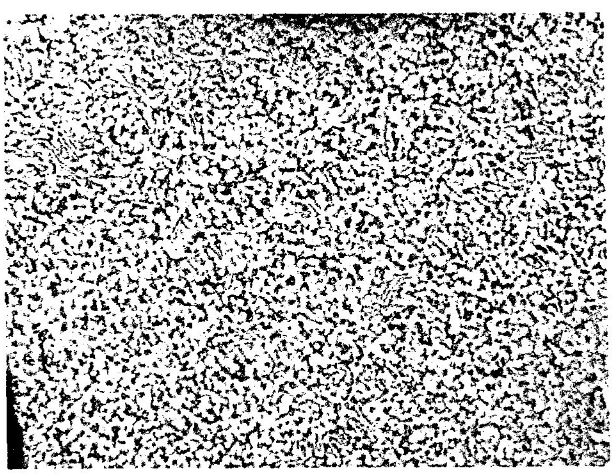

Figure 50. Unaffected microstructure at area 4, Figure 46 (100X).

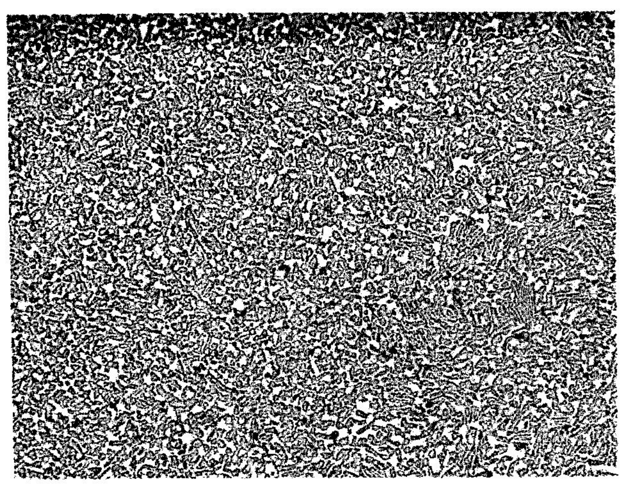

Figure 52. Surface at periphery of as-received wafer (black circle, Figure 51) (100X).

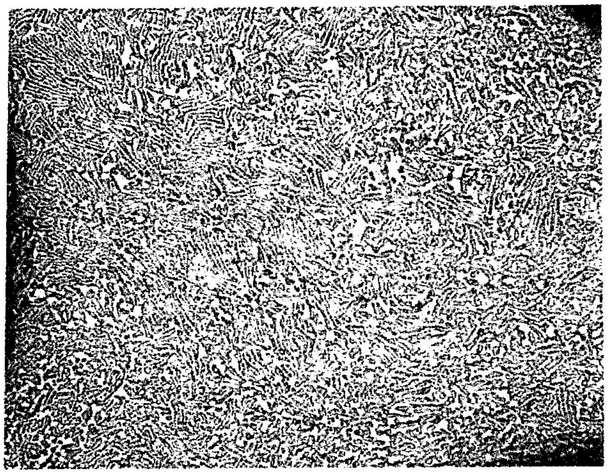

Figure 53. Surface microstructure between bubbles near center of as-received wafer (white circle, Figure 51) (100X).

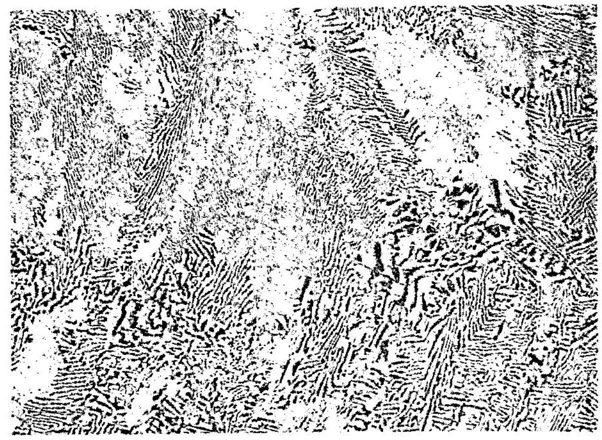

Figure 55. Enlargement of area at black circle showing recrystallized structure in melted areas (number 3 disk) (100X).

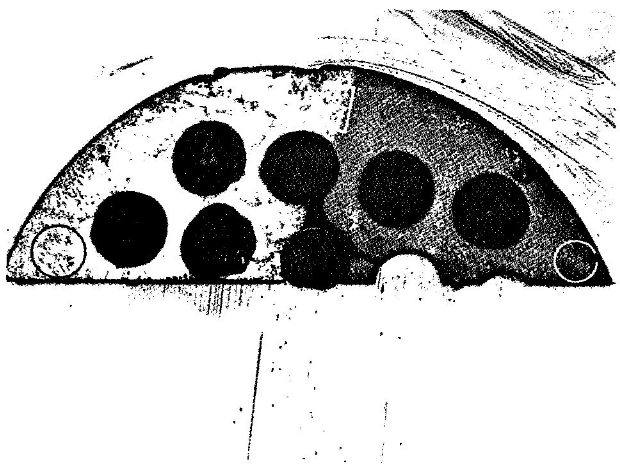

Figure 54. Transverse section exhibiting macrostructure of disk number 3 near bottom of composite (enlargements of melted structure, transition area, and unaffected structures are shown in Figures 55 through 57) (7X).

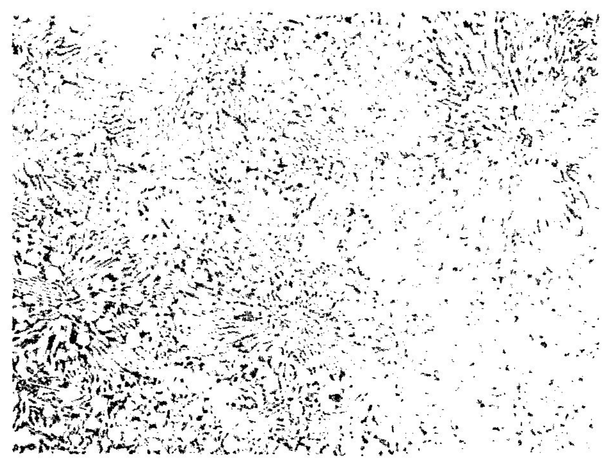

Figure 56. Enlargement of area at rectangle exhibiting microstructure of transition area between melted and unaffected structure (number 3 disk) (100X).

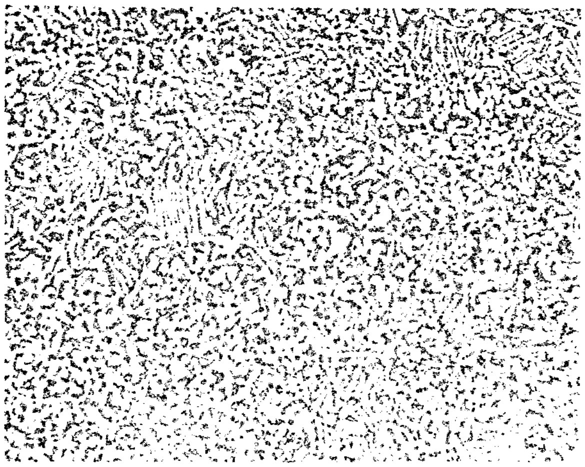

Figure 57. Enlargement of area at white circle depicting unaffected structure (number 3 disk) (100X).

2. Many manufacturing-in-space processes can be verified or trends of what will ultimately occur can be shown with drop tower tests.

3. KC-135 Research Aircraft flights offer little or no advantage over drop tower tests.

4. Research rockets are capable of providing periods of near-zero-g for processing materials which are 50 to 100 times longer than MSFC's 300-ft drop tower and 20 to 50 times longer than KC-135 Research Aircraft.

5. Centrifugal acceleration produced by coning (precession) after yo-yo despin of the Aerobee 170A NASA 13.113 was insignificant (8×10^{-7} g) compared to that produced by the final spin rate.

6. Research rockets equipped with altitude control systems and despun to zero provide a good environment for processing materials.

7. The best location for experiments on rockets which are not despun to zero and are not equipped with altitude control is at the center of gravity of the payload/nose cone, with the centerlines of the rocket and experiment coincidental.

8. Experiments should be designed to fit standard rocket section lengths and mounting bolt circles.

9. Experiments which can be mounted on either the forward or aft side of a mounting plate have a better chance of being selected as "piggyback" experiments.

10. Experiments which are essentially self-contained and require minimum effort to integrate are most likely to be selected as "piggyback" experiments.

11. Experiments should have a minimum number of mechanical, electrical, and telemetry connections to the research rocket.

12. Experiments should be preset and should require no last minute checks and calibrations, which interfere with launch operations.

13. Experiments flown on Aerobee 170's and Black Brant VC's must meet the Aerobee 170 Vibration Specification (Appendix).

14. The results of the vibration tests must be documented and a copy will most likely be required by the center responsible for the research rocket.

15. Since there are often delays during assembly and test of a research rocket, experiments should be designed and documented so that it is not necessary for anyone to accompany the experiment to the center where it is to be integrated.

16. The integration procedure should be concise.

17. The experiment should be designed so that it can be operated by the integrating center during assembly and checkout of the rocket (e.g., the unit was shipped with a dummy capsule to the integrating center and the flight capsule was exchanged for the dummy by the experimenter during final assembly of the rocket at the launch site).

18. The Ejector technique is better than the Tube and Reservoir technique of forming and deploying liquid metals in near-zero-g.

19. The Containerless Processing System began to damp the oscillations of the hollow aluminum sphere.

20. The capsule contents tended to pull away from the capsule wall as they melted, causing incomplete melting and decreasing the effectiveness of the water quench cooling system.

21. A longer holding time is needed.

22. In areas where melting occurred it was demonstrated that mixture stability in metal-gas composites processed in near-zero-g was much greater than that processed in one-g where all the gas bubbles escaped or were reduced in size because of the buoyancy forces acting on them.

RECOMMENDATIONS

1. The capsule interiors should be plated with some material that does not repel the capsule constituents.

2. A means of increasing the cooling capability of the unit should be devised.

3. A means of reducing or eliminating the accelerations produced by spin should be devised.

APPENDIX – AEROBEE 170 VIBRATION SPECIFICATION

PROTOTYPE — SINUSOIDAL

Axis	Frequency	Level	Sweep Rate
Thrust Z-Z	10 - 60 60 - 160 160 - 2000	3.5 g 6.8 g 11.3 g	2 octaves/min
Lateral X-X and Y-Y	5 - 60 60 - 250 250 - 2000	5.1 ips 0.0 g 11.2 g	2 octaves/min

PROTOTYPE — RANDOM

Axis	Frequency Range	PSD Level	Overall
Thrust Z-Z	20 - 2000	0.125	15.75 g rms
Lateral X-X and Y-Y	20 - 2000	0.228	22.5 g rms

Duration: 20 sec per axis

FLIGHT — SINUSOIDAL

Axis	Frequency	Level	Sweep Rate
Thrust Z-Z	10 - 60 60 - 160 160 - 2000	2.3 g 4.5 g 7.5 g	4 octaves/min
Lateral X-X and Y-Y	5 - 60 60 - 250 250 - 2000	5.4 ips 5.3 g 7.5 g	4 octaves/min

FLIGHT — RANDOM

Axis	Frequency Range	PSD Level	Overall
Thrust Z-Z	20 - 2000	0.056	10.5 g rms
Lateral X-X and Y-Y	20 - 2000	0.113	15 g rms

Duration: 10 sec per axis

N 73-22923

NEUTRAL BUOYANCY SPACE SIMULATION

By

James L. Splawn

ABSTRACT

The MSFC Neutral Buoyancy Simulator, which is used to duplicate the weightless condition experienced by astronauts, is described herein. The Simulator consists of a tank of water 22.9 m (75 ft) in diameter by 12.2 m (40 ft) deep, full scale mockup hardware, communication and recording instrumentation, and special subsystems to insure the safety of the test subjects. The principal advantages of this neutral buoyancy technique for hardware configuration definition and crew procedural training over other methods are validated.

DISCUSSION

The Neutral Buoyancy Simulator is a tool that is used to defy our normal 1-g environment to permit simulation of the weightless conditions of space. It was discussed a few years ago that an excellent simulation of the weightlessness of space could be obtained by going underwater; thus, this technique was developed to permit a test bed for MSFC's designs and techniques as well as to add another identity to the MSFC capability.

Figure 1 is an underwater photograph of actual test operations in the Simulator. Note that the two test subjects are wearing pressure suits and their attendant safety divers are dressed in scuba gear. Figure 2 is a front view of the Simulator. The tank is 12.2 m (40 ft) high and has viewports for multi-level viewing into the tank. Notice the skylight that has been placed in the roof of the building so that good underwater TV coverage as well as sufficient light levels for underwater photography can be obtained. There is a monorail hoist system which allows proper handling of the test articles while being placed in the tank. Figure 3 is a view across the top of the tank which is 22.9 m (75 ft) in diameter. Shown in the background is the main work area on the top level of the tank and the surface control console with its related instrumentation. The reflection of the test articles in the water itself can also be seen.

The primary principle of this form of simulation is to defy the normal laws of gravity existing on earth by going underwater. There are several ways in which tests can be conducted, and the mode used depends on the requirements for that particular test. The shirt-sleeve environment can also be simulated; this will be in response to a test required to be conducted internally in, for example, the Skylab cluster, or intra-vehicular activity (IVA) type situations. For a shirt-sleeve type environment, the test subject is equipped with standard scuba gear. This is the simplest mode of simulation wherein the man actually carries his breathing air supply on his back. Excellent mobility is attained while in this mode. There is, however, a limitation as far as communication is concerned. The test subject can be spoken to and given directions by means of an underwater speaker, but he can only talk back, at the present time, by using hand signals. If he needs to interface with some form of foot restraint while in this shirt-sleeve type environment, the normal flippers that are standard for scuba type simulation are eliminated and special boots are applied that will interface with the foot restraints.

A variation of this method of simulation for shirt-sleeve environments is to utilize a Kirby-Morgan type helmet. This is essentially a one-gas suit which envelops the head only. It is very similar to the pressure suit helmet, or maybe a more common similar item would be a football helmet, in that it simply seals around the lower portion of the head and around the neck to create an airtight environment inside. The mobility of the test subject is excellent and there is the added capability of having hard-wire communications to the subject so that he can comment on the design and operation of the hardware or give his personal sensations as he is actually conducting the test. The test subject breathes air from an umbilical

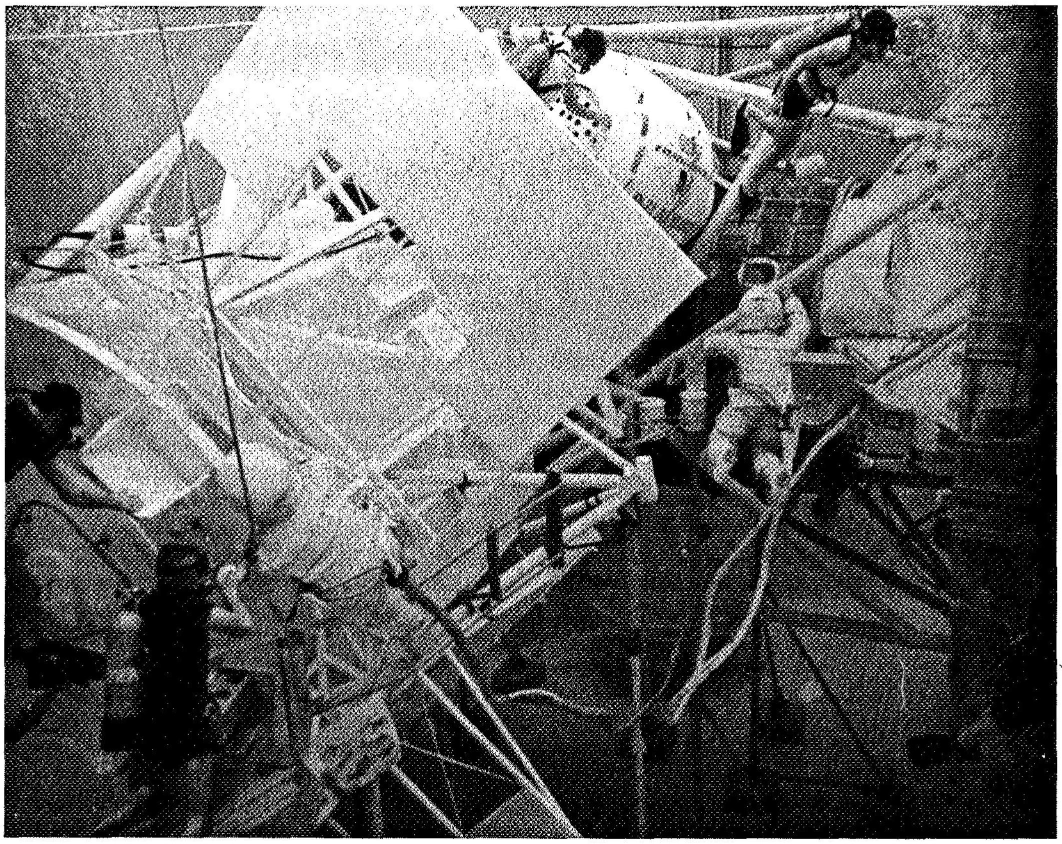

Figure 1. Test subjects at work on the Skylab Trainer.

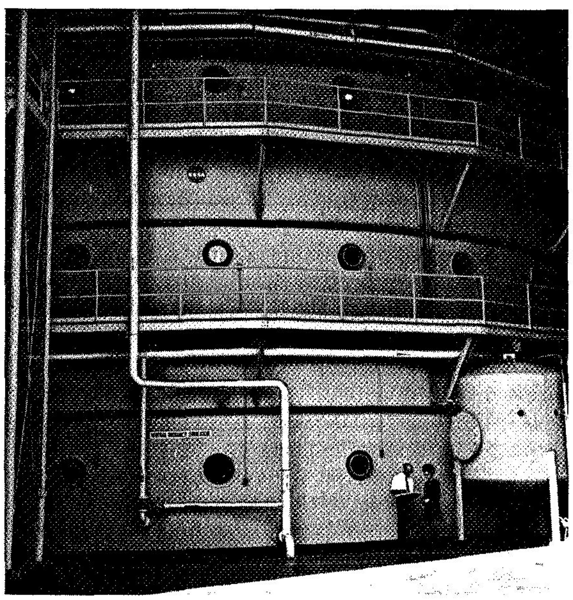

Figure 2. Neutral Buoyancy Simulator (front view).

air supply connected directly to the helmet. Those are the modes for basic shirt-sleeve type environments.

When simulations are performed for the extravehicular activity (EVA), the space-walk simulation, more is involved because this always requires the use of pressure suits. Two men dressed in pressure suits can be seen in Figure 1. These are standard Apollo type pressure suits that are located in the laboratory for use not only in this particular mode of simulation, but in all simulations at MSFC that require pressure suits. The pressure suit has minimum changes that are required for underwater use, but there are some related systems that required some rather unique developments to make the suit usable. Obviously, the suit must be pressurized, so a regulator had to be developed that would sense the changing head pressure of the water. As the subject translates vertically in the water, the regulator, which is mounted in the chest area of the pressure suit, will sense the changing head pressure through pressure transducers and

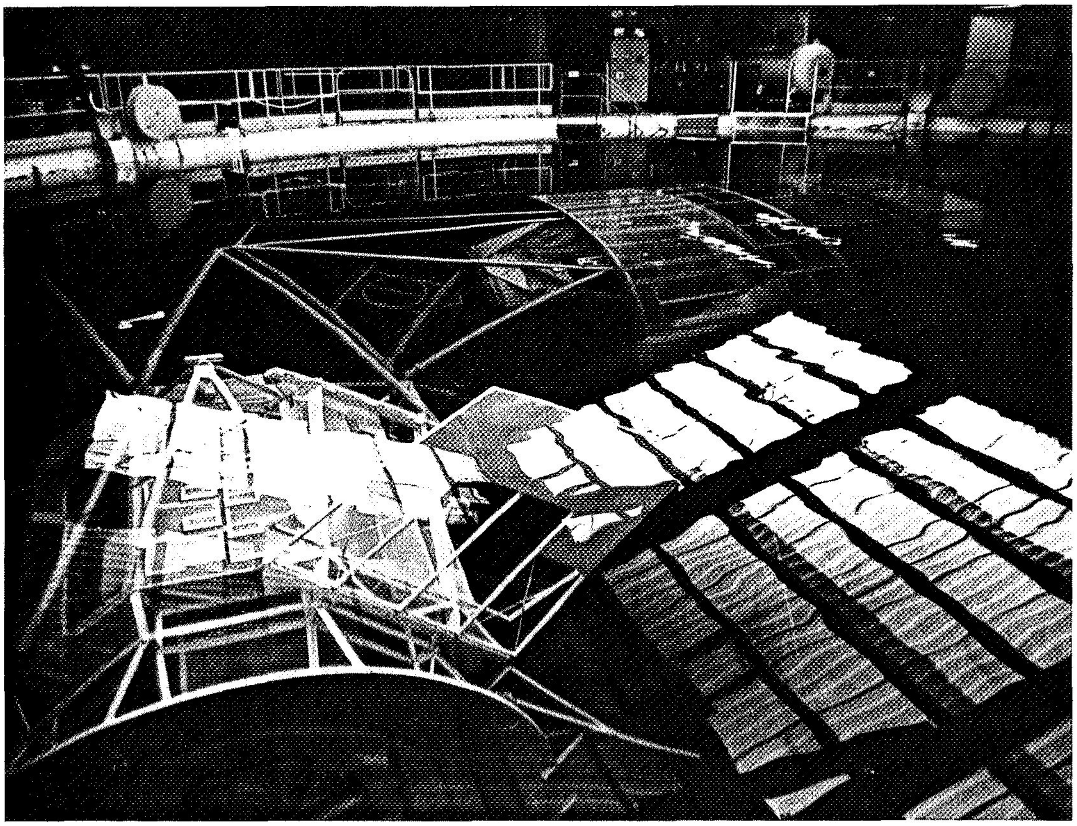

Figure 3. Neutral Buoyancy Simulator (top view).

will maintain a constant pressure of 25.5×10^3 N/m^2 (3.7 psi) in the pressure suit.

The pressure suit is umbilically fed, just as it will be in actual flight. This umbilical houses the primary air supply system, the return air system back to the surface of the tank, communications, and any biomedical measurements that are required for the particular test.

Another unique feature is the ballasting system. If a man is placed in the water in a pressure suit he will simply float on the surface of the water because of the trapped volume of air in the suit. Therefore, the buoyant force must be counterbalanced with a ballast system. In this case a harness was built in which lead weights can be placed. These harnesses are equipped with individual pockets so that small lead weights can be inserted as needed. This harness permits the distribution of these weights over the body so that a preferred attitude is not achieved in the water. It is required to maintain any attitude, just as in space.

The construction of the test articles themselves is somewhat out of the ordinary, in that open wire mesh type construction has been used where necessary. This permits internal and external observation of the mockups via the underwater TV system. This is a unique feature as far as construction is concerned. Of course corrosion problems exist that would normally be expected in the tank, but these have been solved by using special paints and by placing sacrificial anodes on the test articles.

The portable packages that the test subjects must handle while they are in the water are also made neutrally buoyant; that is, they do not float or sink, they simply maintain a constant attitude while in the water.

Figure 4 is a pictorial representation of the entire Simulator. The tank is 22.9 m (75 ft) in diameter by 12.2 m (40 ft) deep and holds approximately 5299 m^3 (1 400 000 gal) of water. The tank is equipped with its own water purification

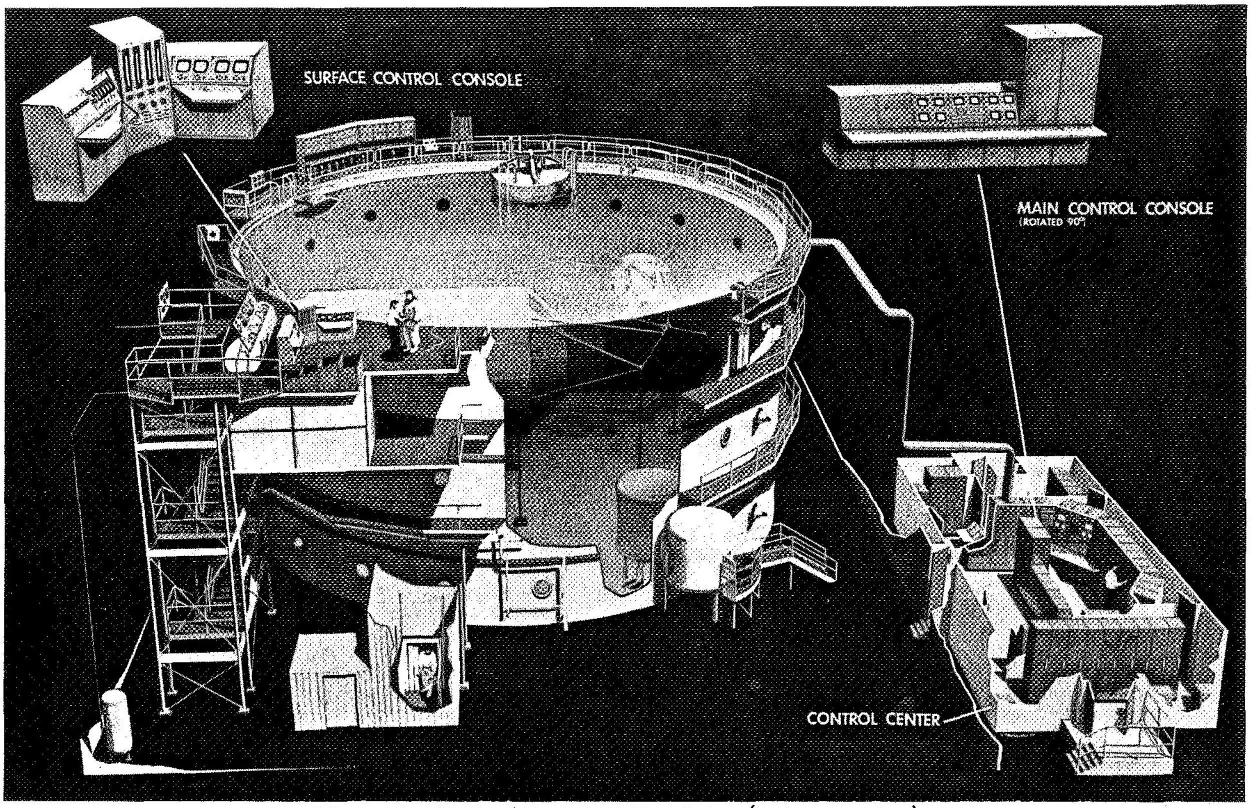

Figure 4. Neutral Buoyancy Simulator (cut-away view).

system. An elevator services the top level of the tank. On the top level of the tank is located the surface control console, the primary station for pressurizing the suited subject prior to his entry into the water. A hyperbaric chamber or a recompression chamber, also located on the top level, will be used by trained technicians in joint efforts with the Medical Center for treatment in the event of a diving accident in the water.

A very important aspect of the Simulator is the control center. All tests in the tank are conducted from the control center. The tests are recorded on video tape, which gives a video and audio record of what actually happened in the test sequence for later detailed analysis, if necessary. Approximately 200 channels of information are available from the tank area into the control center. Pertinent data relative to test subject status, Simulator subsystem status, or mockup status are available in the control center for monitoring and/or recording purposes. The underwater communication system and the underwater TV system provide the test director the information he must have to conduct a meaningful and safe test. Underwater photography, either still shots or movies, are provided when required. The biomedical monitoring system is under development at this time. This monitoring system will permit evaluation, simultaneously and instantaneously, of three different modes used in determining the work rate of the test subjects: thermal, gas analysis, and heart rate regression.

The Simulator was originally built as a tool to be used in support of research and development activities at MSFC. It is now being used in conjunction with the Skylab program. During the last 3 years considerable developmental simulations have been performed to assist designers in both the Astrionics and Astronautics laboratories in evaluating the designs of those components for which they were responsible. The astronauts will be interfacing with these components while they are actually in orbit.

In summary, the Neutral Buoyancy Simulator was an idea that was conceived at MSFC and has progressively developed to meet the requirements

of the program with which MSFC has been involved. Currently, modifications to the Simulator and its many subsystems are being completed in order to conduct approximately 2 years of crew training for the flight crews of the Skylab program. This training will be done simultaneously with the continuous research and development efforts in support of future programs such as the Shuttle, Sortie Lab, Large Space Telescope, Space Station, etc.

N73-22924

THE EKG ISOLATOR AND CARDIOTACHOMETER SYSTEM

By

Hubert E. Smith

INTRODUCTION

The electrocardiogram (EKG) isolator and cardiotachometer system are discussed herein. Although these items can be used together to form one complete system, they are discussed separately in this paper. The following list shows the advantages and features of each item:

- EKG Isolator
  - Light Beam Electrical Protection
  - Compact
  - Developed for MSFC Neutral Buoyancy Simulator
- Cardiotachometer System
  - Digital Electronics
  - Nixie Tube Readout in Heartbeats per Minute
  - Continuous Pulse-to-Pulse Readout
  - Compact and Portable

EKG ISOLATOR

The EKG isolator was developed to protect test subjects from the hazard of an electrical shock in the event there is an equipment failure. The possibility of electrocution because of an electrical breakdown in the system is a problem that has always been associated with EKG equipment. The estimate of the number of deaths caused by EKG and shock-induced equipment ranges from a low of 100 annually to more than 1200 annually, with many additional injury cases. The highest estimate of fatalities by electrocution from this type equipment was made by Ralph Nader, who claims there are more than 5000 deaths per year. However, there is no way of definitely knowing how many deaths are caused by electrical equipment in hospitals. Two of the more obvious reasons for this are: (1) the doctor may not recognize electrocution as the cause since there is very little tissue damage and (2) the medical profession would not publicize that a patient died by electrocution.

Figure 1 is a typical electrocardiogram system. Isolation is obtained with isolation transformers in the power supply system and in the output to the recorder or display unit. There is an ac or 60-Hz path to ground because of stray capacitance from the wiring and isolation transformers. If there is an electrical breakdown in a transformer, fatal currents can result because of the stray capacitance. Also, if there is a short circuit between the input and output of an isolation transformer, an attendant or any other person can complete a fatal current path by touching the patient. Additional protection can be obtained by placing isolation elements in the leads connected to the body. The isolation unit in the body leads can be a high resistor or a current limiter unit. If resistors are used, an electrical breakdown can cause excessive current to flow through the body. Using the current limiter unit, an electrical breakdown could cause a high voltage that could damage the unit, or the unit could be faulty; in either case there could be a dangerous shock if the patient came in contact with the building ground or power ground, which can be made through another person.

Using the EKG isolator unit (Fig. 2) the test subject is completely isolated from the electrical power system and from earth ground. The electronic pickup portion of the circuitry that is connected to the body is powered by small dc batteries, with this portion being electrically isolated from the power system by the photoisolator, which requires a potential greater than 5000 V before breaking down. The signal is transferred from the input circuit to the output circuit by the change in intensity of a

PRECEDING PAGE BLANK NOT FILMED

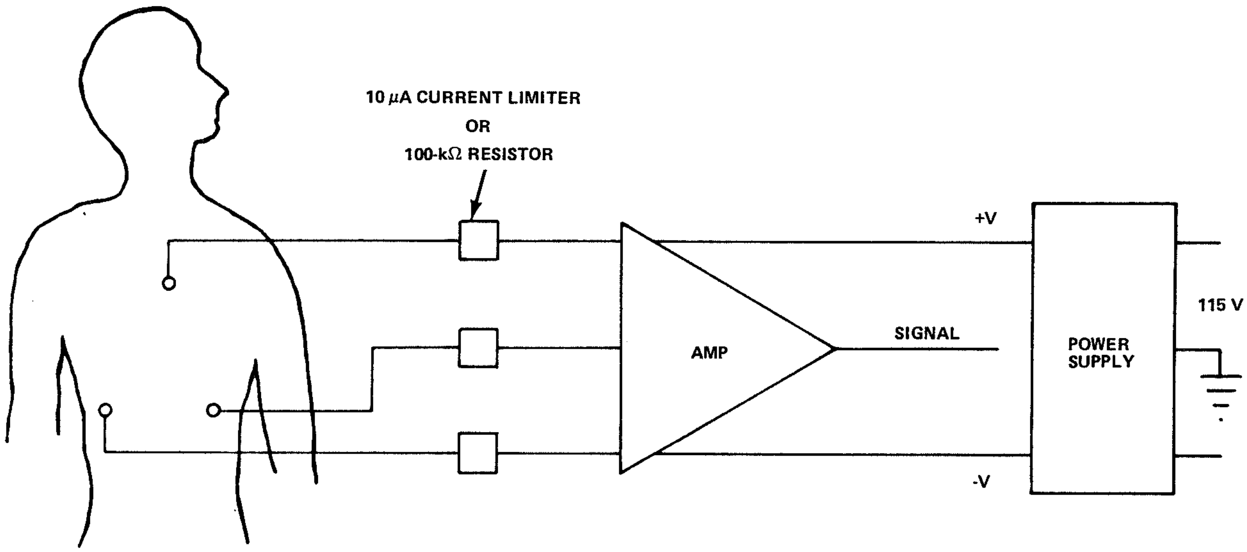

Figure 1. Schematic of typical EKG system.

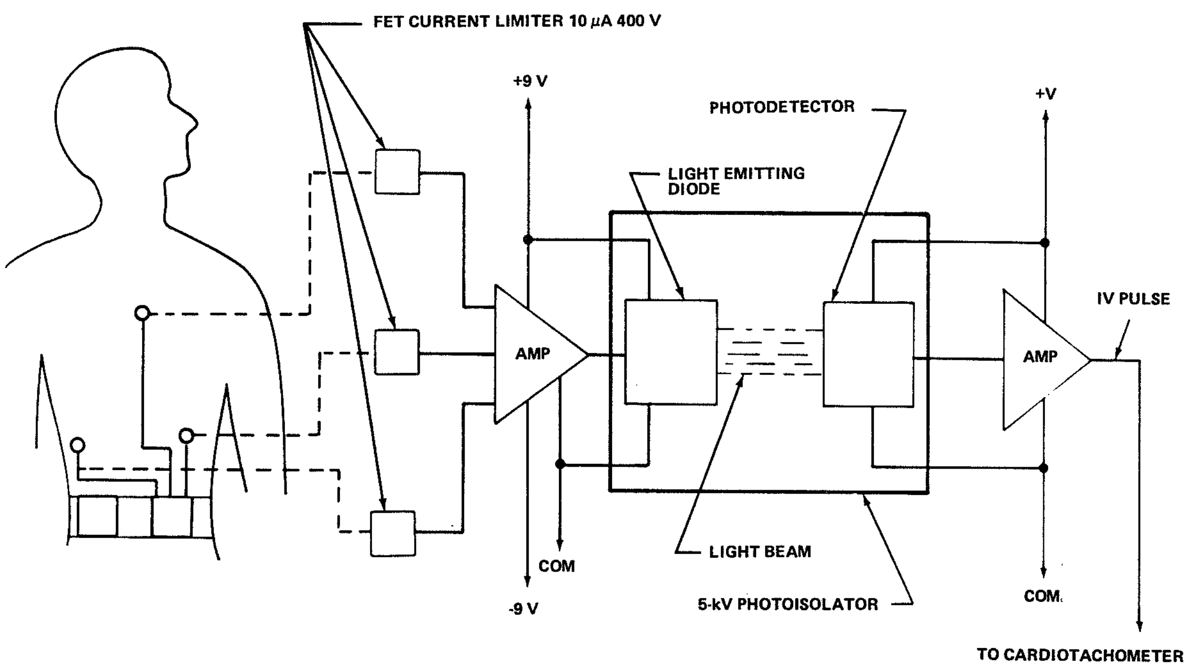

Figure 2. Schematic of EKG isolator unit.

light beam. The subject is isolated from the dc batteries by a field-effect transistor, 10-μA, 400-V current limiter unit. There is one of these units in each line. This will limit the current going through the body to 10 μA even though one of the units fails, because the current must go through two of the units since there is no other path.

On the input of the isolator there is a light-emitting diode and on the output of the unit there is a transistor photodetector. As the electrical pulse from the heartbeat increases in amplitude, the diode increases its light emission causing the light intensity to increase. This in turn causes the transistor to increase the output signal (in a negative

direction), which drives the output amplifier. The output signal from this amplifier can be used to drive a recorder, an oscilloscope, the cardiotachometer unit, or some other display device. Also, since this amplifier has a low impedance output and a large signal output, long transmission wires can be used. The transmission wires used in the Neutral Buoyancy Space Simulation Facility are over 381 cm (150 ft) long.

Figure 3 shows a prototype EKG isolator unit that has been fabricated and tested. This figure shows the prototype, the electrodes that connect to the body, and the batteries. The photoisolator is approximately 6 mm (0.25 in.) in diameter and 7 mm (0.3125 in.) long. The complete printed circuit board of the EKG isolator unit is approximately 3.82 cm by 7.62 cm. The printed circuit board unit can be conformal-coated to avoid the possibility of breakdown or short circuit as a result of coming in contact with a metallic substance or particle.

CARDIOTACHOMETER SYSTEM

The cardiotachometer system can be used in conjunction with the EKG isolator to visually display the heart rate. Past methods used to monitor heart rate include recording the electrical pulses, displaying the pulses on an oscilloscope, or counting the pulses for 20 or 30 sec to obtain an average. For space simulation activities, it was desired to have a continuous heart-rate monitoring system on a beat-to-beat basis. The cardiotachometer system is a digital system and utilizes the time between two consecutive pulses to calculate and display the heart rate in beats per minute.

As shown in Figure 4, the first heartbeat pulse starts the timing circuit. The second pulse stops the timer and starts the calculator. The rate in beats per minute is calculated, and the rate is displayed 0.3 sec after the second pulse. The

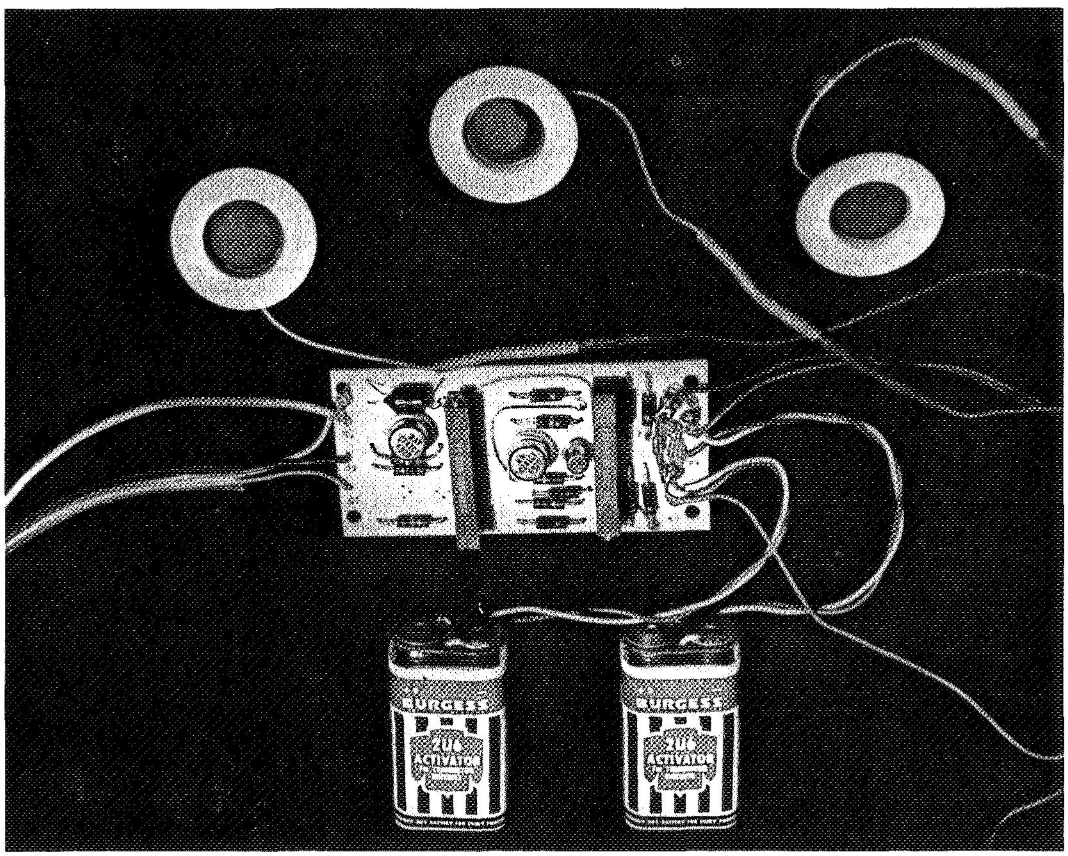

Figure 3. Prototype EKG isolator unit.

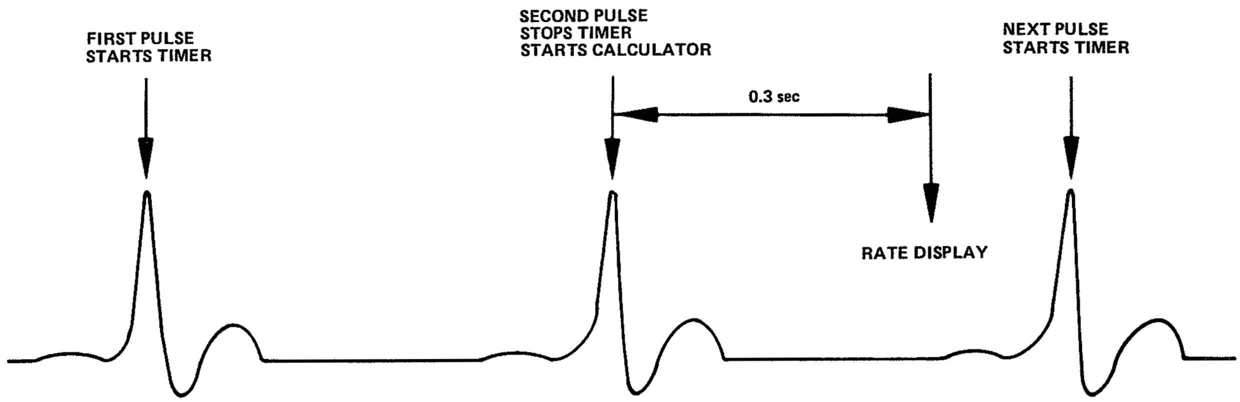

Figure 4. Heart pulse wave shape.

display changes only if the heartbeat rate changes. At a heart rate above 100 beats per minute, the time between the electrical pulses is fairly constant and the display is steady. When a person is relaxed, the heartbeat is erratic because of muscle movements; therefore, the time between each pulse differs causing an erratic display. For this reason four pulses may be averaged and the rate calculated and displayed. This is accomplished by changing a switch position.

Several methods were available to accomplish the computation. The one selected seemed to be the simplest and required the least number of components (Fig. 5). This unit has only four printed circuit boards of integrated circuit components and was designed to rack-mount two units in a standard 48-cm (19-in.) panel. The pulse signal from the heartbeat, which can be from the EKG isolator or any other EKG signal pickup system, is fed into the

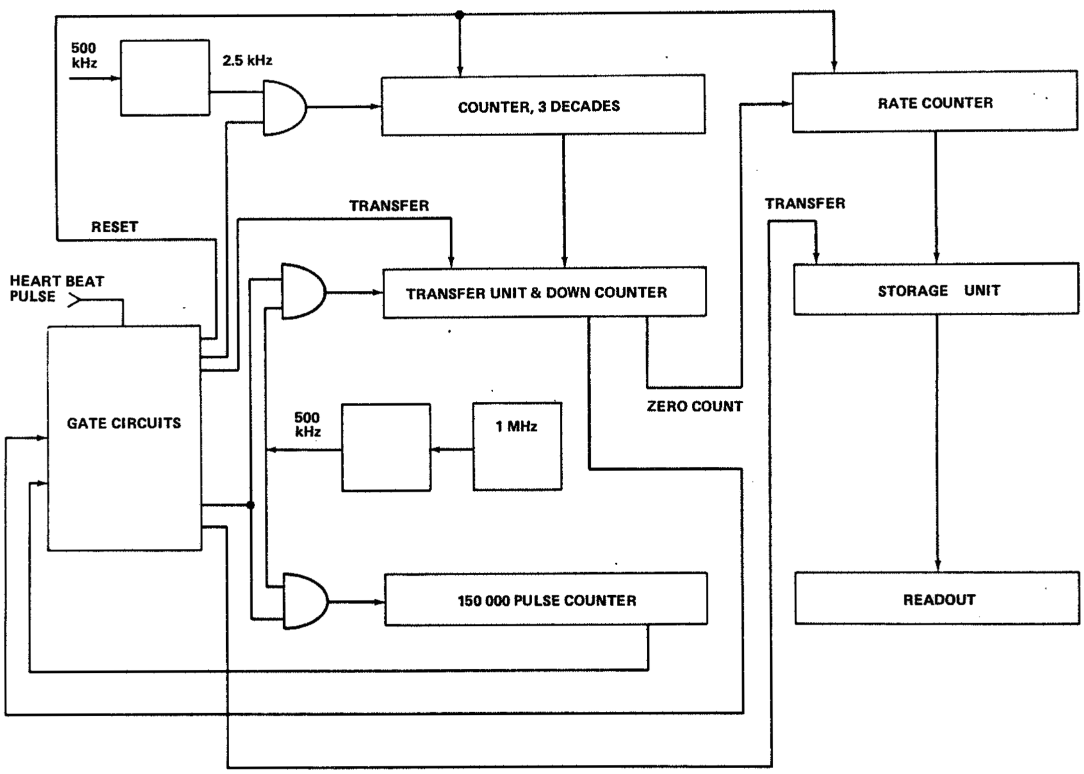

Figure 5. Block diagram of cardiotachometer system.

system. Initially all elements are set to zero. The first pulse entering the system opens the gate allowing a string of pulses at a 2500-Hz rate to enter the three-decade counter. This 2500 Hz is generated by an accurate oscillator (0.001 percent) at 1 MHz (1 Mc) (one pulse per thousand). The second pulse closes the gate and at the same time transfers the contents of the three-decade counter into the down counter. Another gate is then opened allowing pulses at a 500-Hz rate to be fed into the down counter and into the 150 000 counter. When the down counter reaches zero, a pulse is fed into the rate counter and the contents of the three-decade counter are again transferred. The 500-kHz gates are again opened. This process continues until 150 000 pulses are loaded into the 150 000 counter, at which time the computation stops. The contents of the rate counter are then transferred into the storage counter and displayed on the nixie tubes. All units are again reset, and are now ready for the next pulse to enter.

Figure 6 shows the cardiotachometer with a heartbeat rate of 73 beats per minute, the EKG isolator with the electrodes, and the batteries. The unit is approximately 25.40 by 17.75 by 12.70 cm. The cardiotachometer system is portable and may be remotely located for monitoring purposes.

CONCLUSION

Although the EKG isolator unit and the cardiotachometer system were developed for space simulation, they can be used in the medical profession. A cardiotachometer system has been in use at the Veterans' Administration Hospital and University Hospital complex in Birmingham, Alabama, for approximately 1 year. One has also been in operation at the NASA Medical Center for well over 1 year. Both of these units are located in the treadmill room so that a heart patient exercising on the treadmill can monitor his heart rate and maintain the rate desired. These units have been very well received in both installations and it is felt that the cardiotachometer system and the EKG isolator unit can be used in other sections of hospitals, such as surgery, and also in the offices of medical doctors.

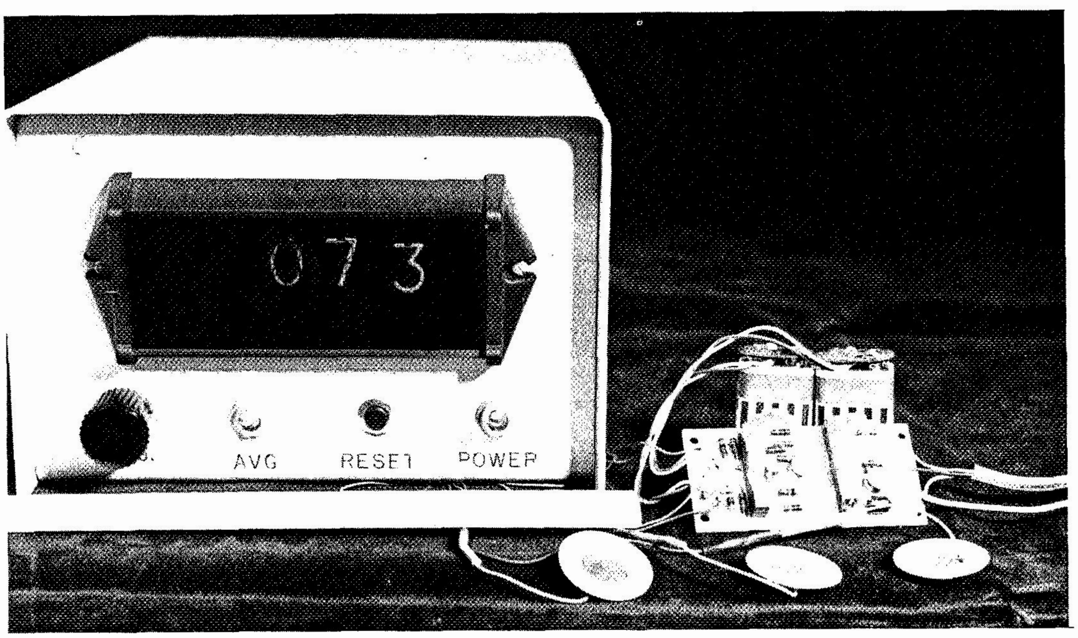

Figure 6. Cardiotachometer system with EKG isolator unit and batteries.

N 73-22925

FREE FLYING TELEOPERATOR

By

Herman T. Blaise

SUMMARY

Free Flying Teleoperators (FFT) are being tested extensively at the Process Engineering Laboratory of Marshall Space Flight Center. FFT's are the culmination of several years of research and development in space-orbital simulation studies. FFT's include a wide spectrum of manipulator and maneuvering devices ranging from those that are directly controlled by human operator, through supervisory control, to relatively autonomous control.

FFT systems presently being tested in an air-bearing (ground-effect machine) environment will evolve into more sophisticated systems and be tested in the neutral buoyancy water environment, which closely simulates space-orbital situations.

Influencing factors for space teleoperator development are as follows:

- Terrestrial experience of operating mechanical/electrical devices in a hostile environment.
- A need to extend man's capability in space.
- Reduce space and planetary exploration costs.
- Astronaut safety.

Space-rated teleoperator systems may be similar to the General Electric Company's concept in Figure 1 or may resemble the Aerojet General Corporation's modular concept shown in Figure 2.

INTRODUCTION

For many years, man has been able to work in terrestrial hostile environments because of his use of remotely operated manipulators and various forms of mobile devices. Therefore, with the oncoming extended stay and planned semiautomated missions for planet explorations, it is apparent that a requirement exists for investigation and development of manipulators and maneuvering devices to operate in this new environment. Since it is not always economically feasible to develop experimental flight items, simulation devices and facilities are being developed that will provide scientists and engineers candidate working systems for their evaluation.

Consequently, a great deal of effort has been and is being expended in the development of hardware systems for space-orbital situations. FFT's are being tested extensively as a simulation system. The system consists of two main divisions, manipulators and maneuvering devices. The term manipulators (teleoperators) is used to cover a spectrum that ranges from direct control by human operator, through supervisory control, to a relatively autonomous control system with human involvement for verification only. Maneuvering devices are used to simulate on earth the dynamics that man and equipment have in space. The air-bearing machines, able to float several hundred pounds with less than an ounce of frictional force, satisfy this requirement. The combination of manipulators and maneuvering devices into various configurations and applied in simulation is represented by the FFT systems.

Various subsystems have been developed to operate FFT's including a semiexoskeletal master control unit, a joystick-analog unit, and a three-dimensional television system for remote operation. These systems are tested in the simulator facility of the Process Engineering Laboratory where there is a 303-m^2 (3264-ft^2) air-bearing table (flat working surface).

The next step in simulation is the transistion from air-bearing machines to experiments in neutral buoyancy. FFT subsystems have been developed in such a manner that they can be exposed to a water environment of neutral buoyancy simulation experiments with little modification.

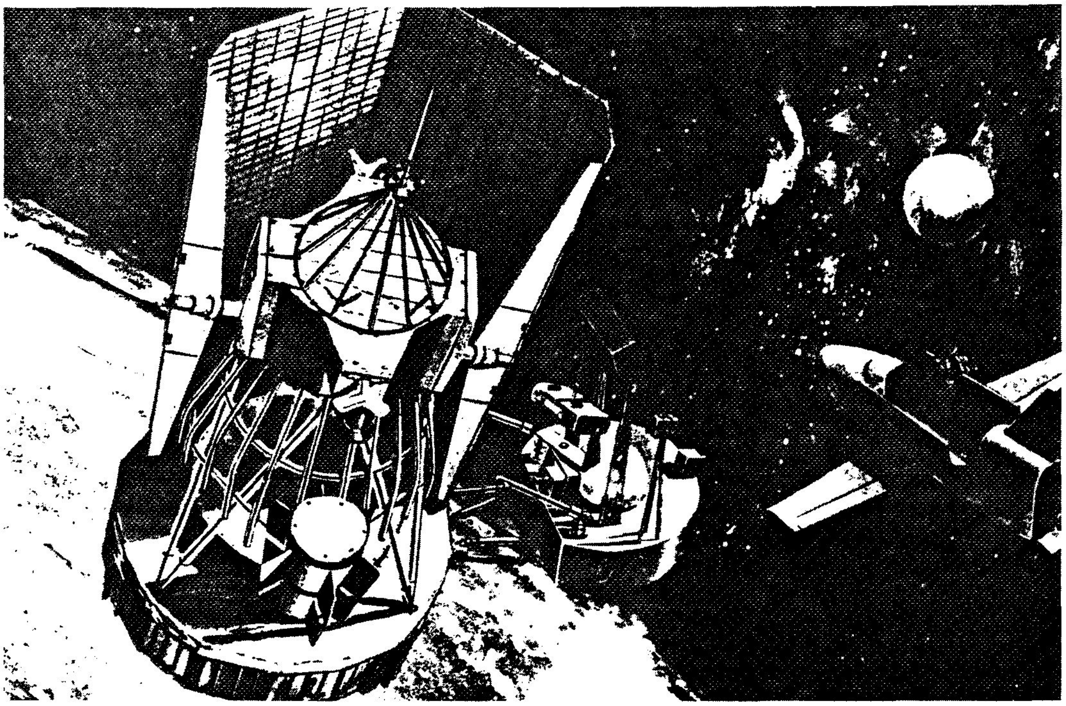

Figure 1. Free Flying Teleoperator.

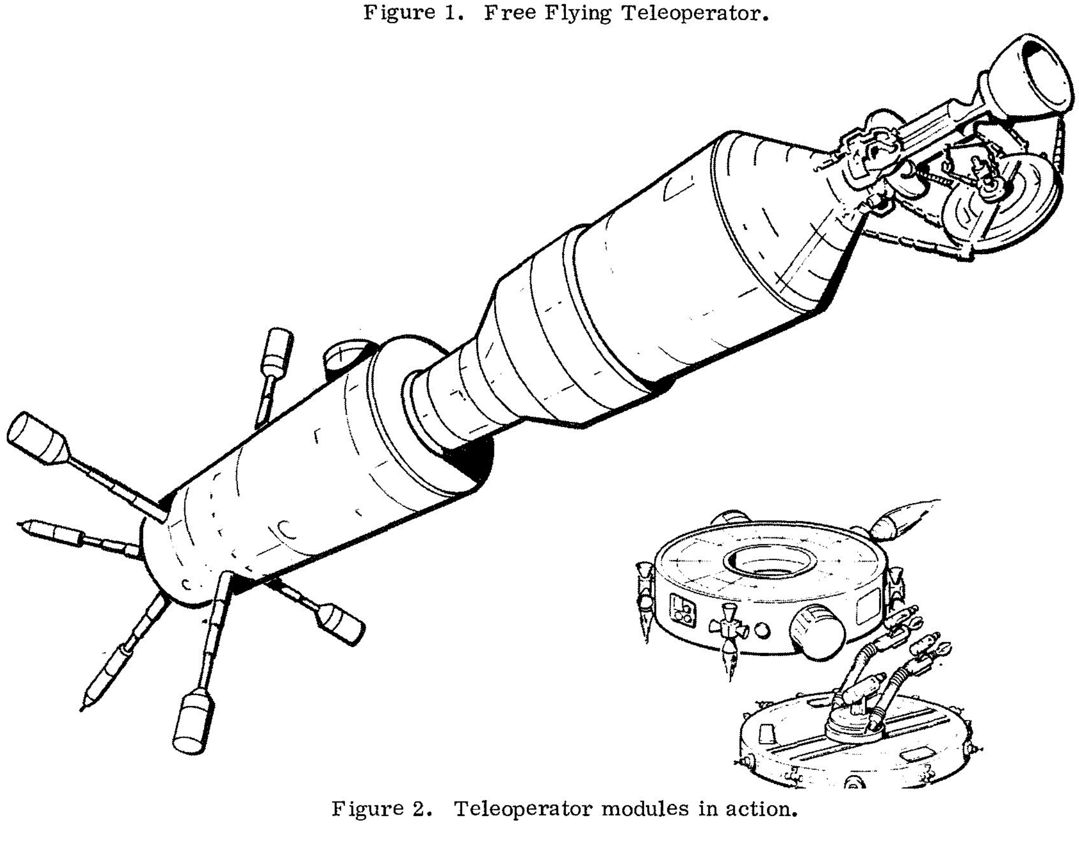

Figure 2. Teleoperator modules in action.

FREE FLYING TELEOPERATOR SIMULATION SYSTEMS

FFT simulation systems, as shown in Figure 3, may consist of a propulsion module, manipulator/ maneuvering module, crew module, base control console, and stereo (three-dimensional) television. The modular concepts may be considered as parts of a kit joined together for various applications and missions. The following descriptions present these systems and subsystems and their purposes. Figure 2 shows teleoperators as they may be used in space.

Manipulators

Joystick Directional Controller. The joystick directional controller (Fig. 4) is an analog, hand-held, proportional, rate controller that is fixed-mounted and contains various switches to signal, through electronics, motor rotation or braking. Certain types allow directional movement by an operator and are linked mechanically to an analog unit that provides electrical signals to the slave motor for movement. Figure 5 shows the MSFC-developed joystick/analog controller.

Exoskeleton Control. The exoskeleton control (Fig. 6) is a brace-type master control structure normally fitted to an operator's shoulder, arms, and hands.

Terminal Tools. Terminal tools or end effectors are jaw-like hands, shown in Figure 7 in the open position affixed to the slave arm end. Two types of devices are included: the mechanically actuated triggered hand and the alternate hand for advanced action manipulator.

Mechanically Actuated Triggered Hand (MATH). The mechanically actuated triggered hand with touch control (Fig. 8) is a prototype unit that extends the usefulness of manipulator units by providing a self-contained unit that can be attached to any manipulator

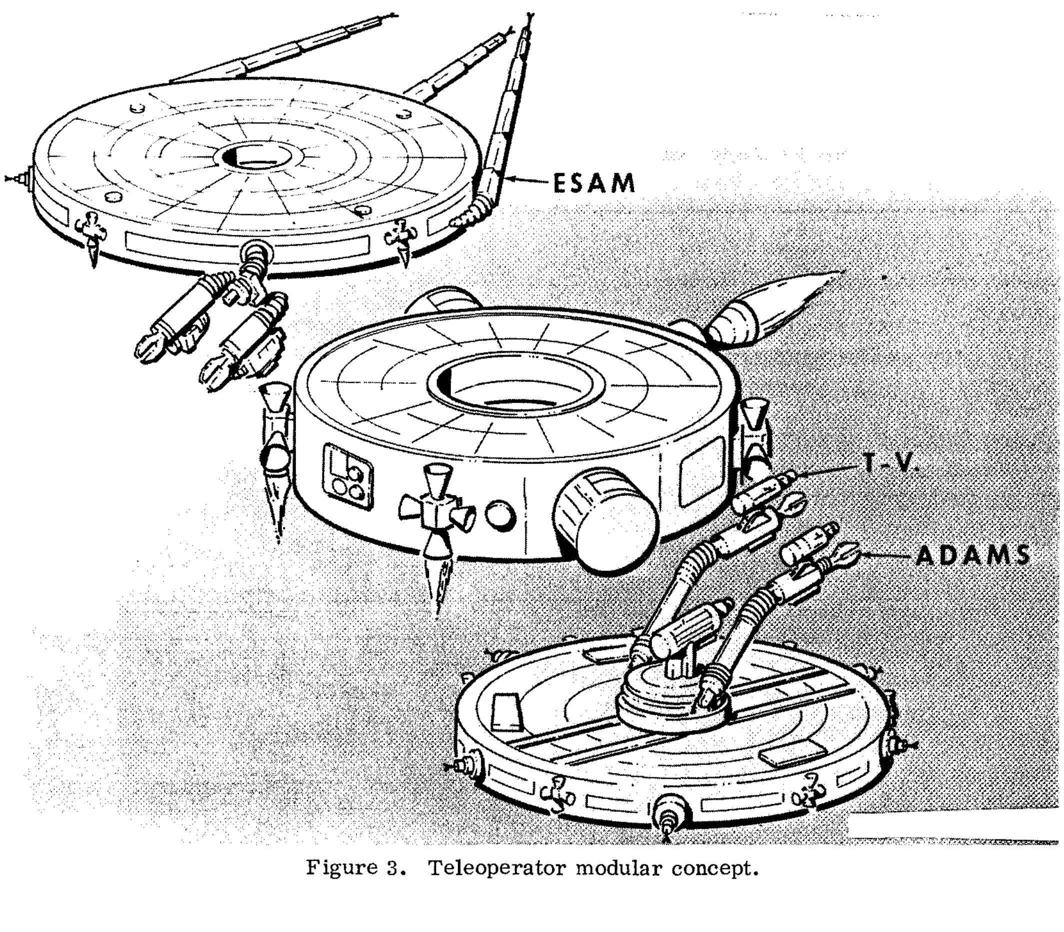

Figure 3. Teleoperator modular concept.

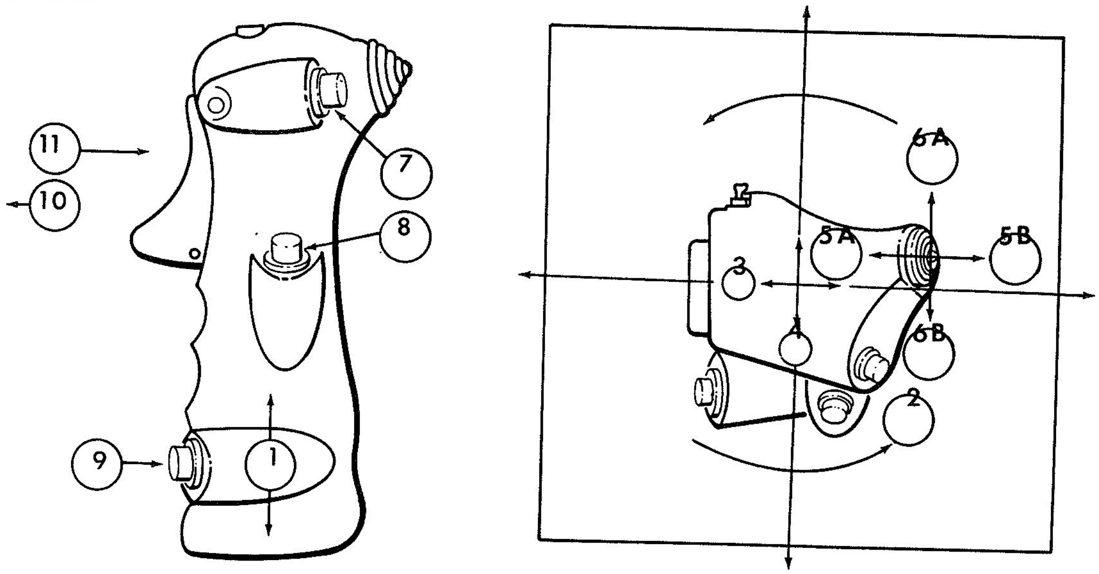

1 SHOULDER PITCH
2 HUMERAL ROLL
3 ELBOW EXTEND/RETRACT
4 SHOULDER ROLL
5 WRIST ROLL
6 WRIST PITCH
7 JAW OPEN
8 JAW CLOSE
9 STEPPER SWITCH
10 BRAKES
11 RATE CONTROL (ALL MOTORS)

Figure 4. Directional controls switch designation.

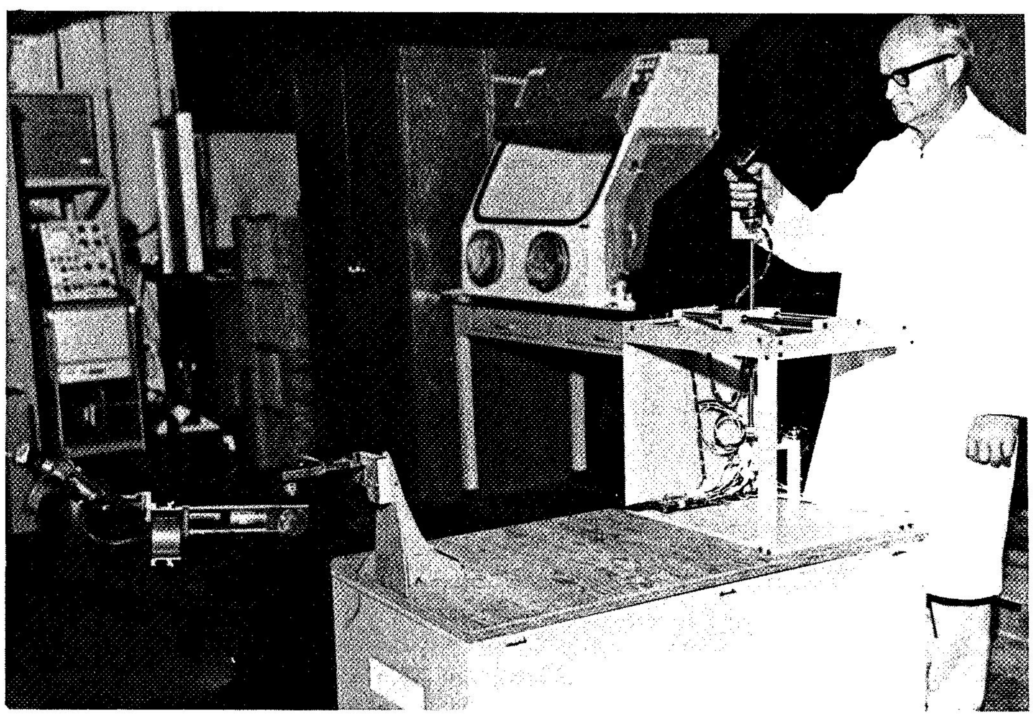

Figure 5. Joystick/analog manipulator controller.

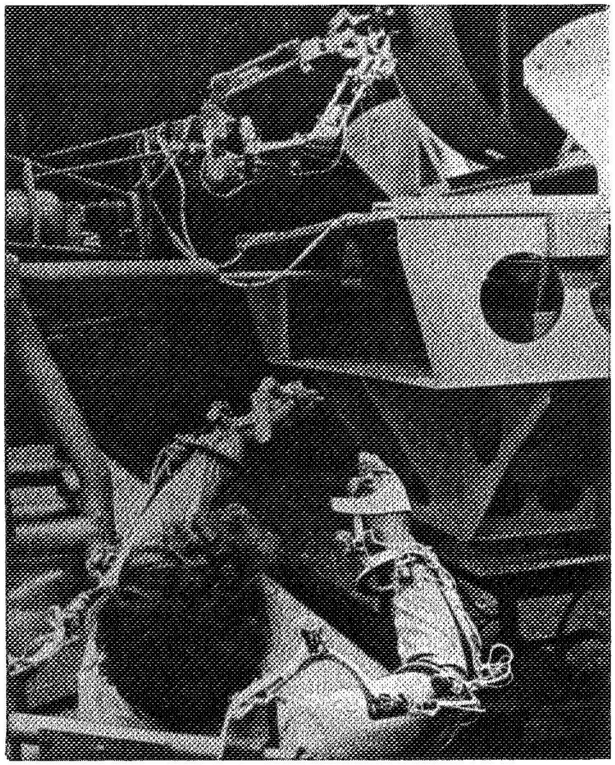

Figure 6. Exoskeleton master manipulator controller.

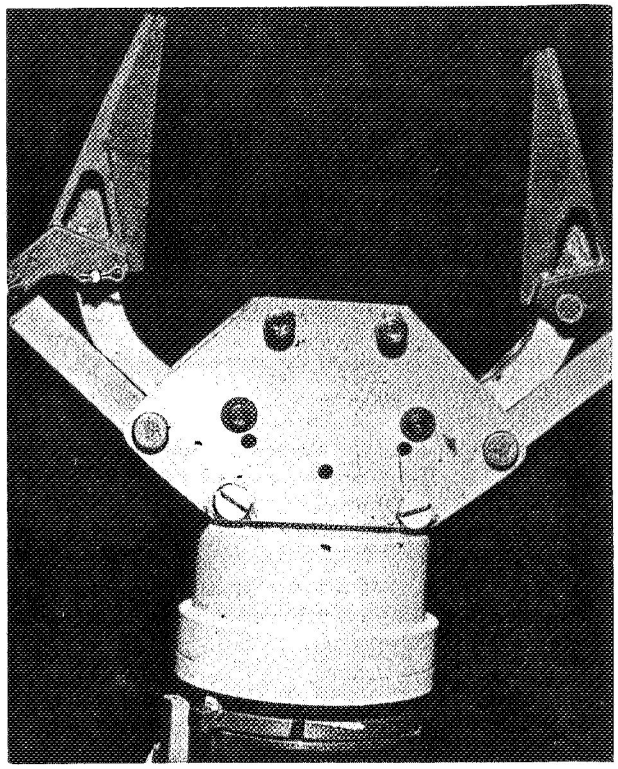

Figure 7. End effector (open position).

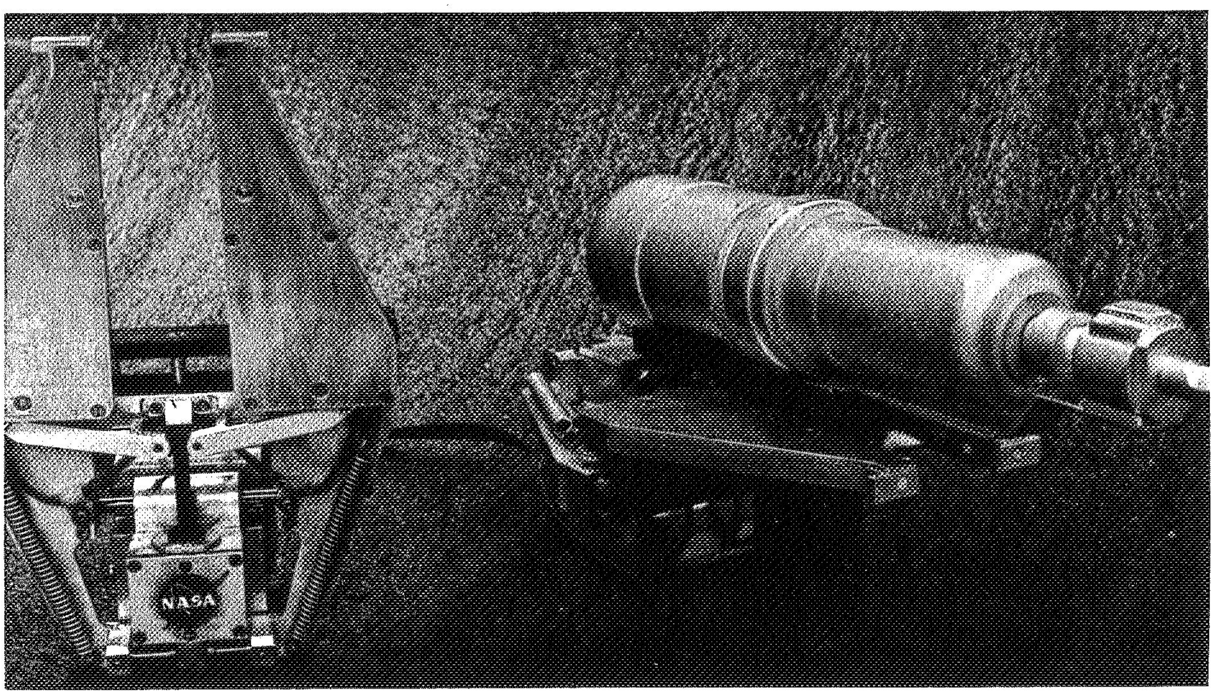

Figure 8. Mechanically actuated triggered hand.

system without modification to that system. Special features of this hand are as follows:

1. Can hold tools.

2. Can actuate triggers on tools.

3. Can work on flat surfaces.

4. Has automatic centering jaws.

5. Can hold in both directions.

This hand has overcome many of the restrictions that existed with earlier hands.

Alternate Hand for Advanced Action Manipulator (ADAM II). The alternate hand for advanced action manipulator is a lightweight hand that is highly efficient for the advanced action manipulator, is self-locking, and requires no power to hold its grip on an object. The system is for use in remote handling of cargo as well as assembly and/or repair of structures in space (Fig. 9).

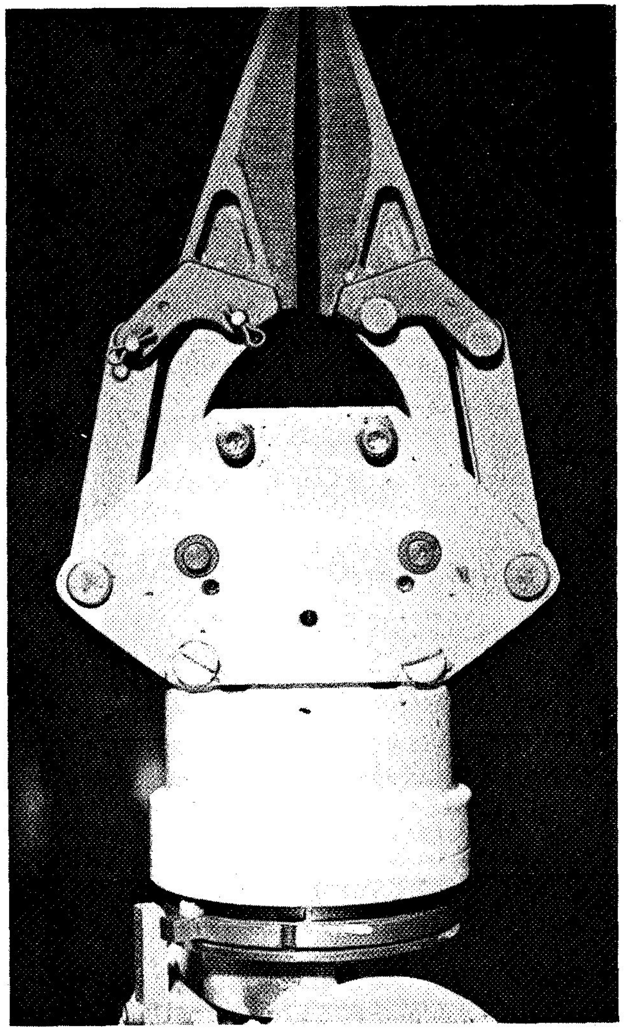

Figure 9. ADAM II hand.

Rancho Manipulator. Figure 10 illustrates a rancho bilateral remote manipulator mounted on a material handling boom. It demonstrates the feasibility of a manipulator doing work after the material handling device captures and despins an orbiting satellite.

Material Handling Device. Figure 10 also illustrates a material handling device assembled to the thrusted air-bearing scooter assembly with a simulation crew station added. An air-bearing lift pad is provided with a counterbalance assembly support mockup satellite.

Advanced Action Manipulator System (ADAMS). This device is a semiexoskeletion master/slave teleoperator system (Fig. 11) employing lightweight and compact components including a solid-state proportional rate control adjustable over discrete steps to provide a range of master/slave control gains. A semiexoskeleton master control unit with optional switch controls is provided. The master unit is handheld and externally worn. The system consists of two 106.7-cm (42-in.) arms.

Extendible Stiff Arm Manipulators (ESAM). This is a manipulator designed for grappling and moving an item or vehicle into position, and holding it in place and allowing other devices to perform work (Fig. 12).

Experimental Material Handling Device. This device (Fig. 13) consists of a rigid arm assembly 3.35 m (11 ft) long that is mounted at the end of a pincer-type grappler. The grappler can spin independently of the arm to synchronize with a spinning satellite for a despin mission. Maximum spin is ± 36 rpm.

The grappler unit as shown in Figure 14 was developed in the early phases of the Process Engineering Laboratory's space-simulation endeavor. The unit's primary novel features are infinite wrist rotation and telescoping forearm, and share type controls that will operate a mobility unit by trigger switching, such as the air-bearing thrusted vehicle. In addition to being used

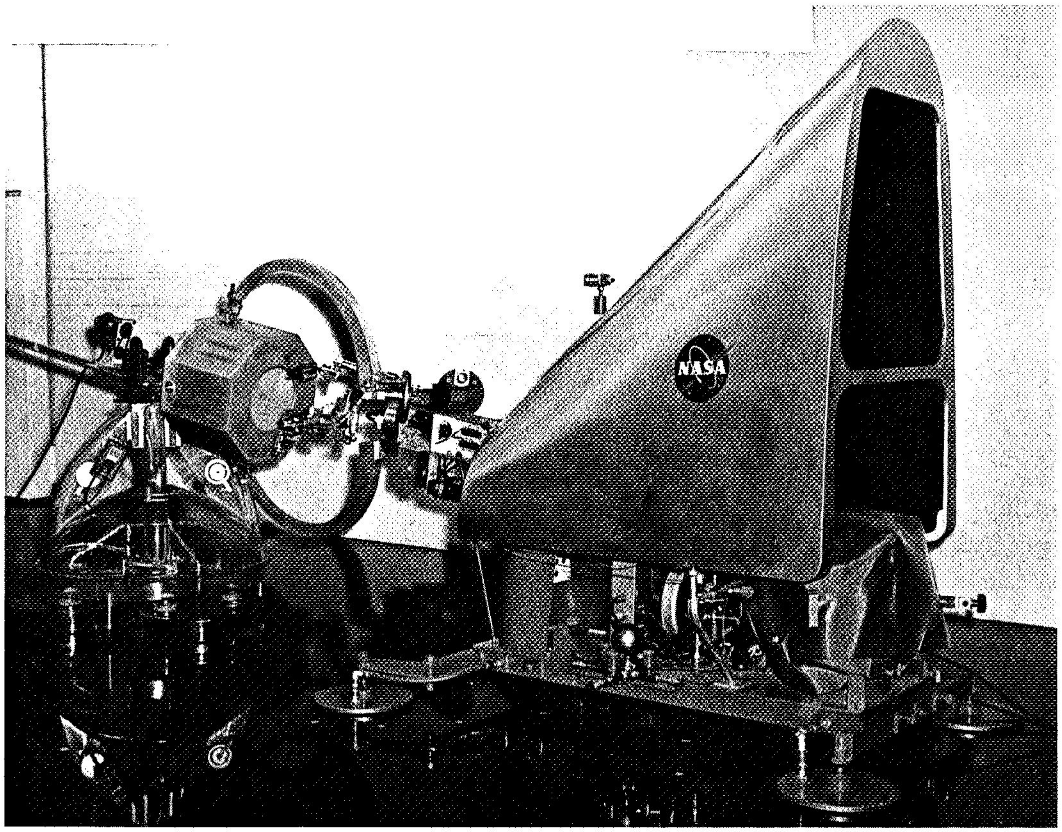

Figure 10. Rancho manipulator mounted on material handling device.

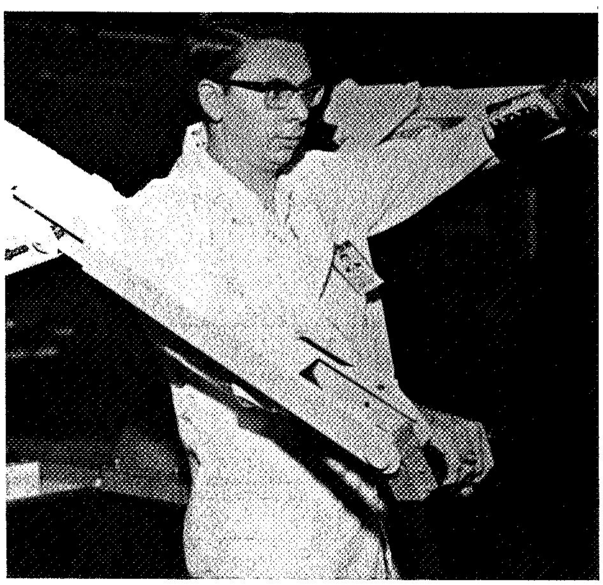

Figure 11. Advanced action manipulator master arms (semiexoskeleton).

for grappling, the unit is being used as a general purpose "cherry-picker" type manipulator, where items being handled are not too fragile, and to serve as a vise while performing work with other manipulators.

Serpentuator Development. Various versions of the serpentuator actuator concept have been tested, improved, and demonstrated over the past 3 years. The first concept was the five-link mechanical simulation model having links that actuate 20 deg in one direction. This model (Fig. 15) was statically and dynamically tested in support of evaluation of a software mathematical model. The information gained provided the means for the development of improved models such as the 12.19-m (40-ft) and the ± 180-deg actuated hermetically sealed models. The serpentuator concept is constantly mentioned as a candidate system for various actuator teleoperator proposed systems.

Orthotic Arm Joint. Figure 16 illustrates an improved design of an orthotic arm joint that

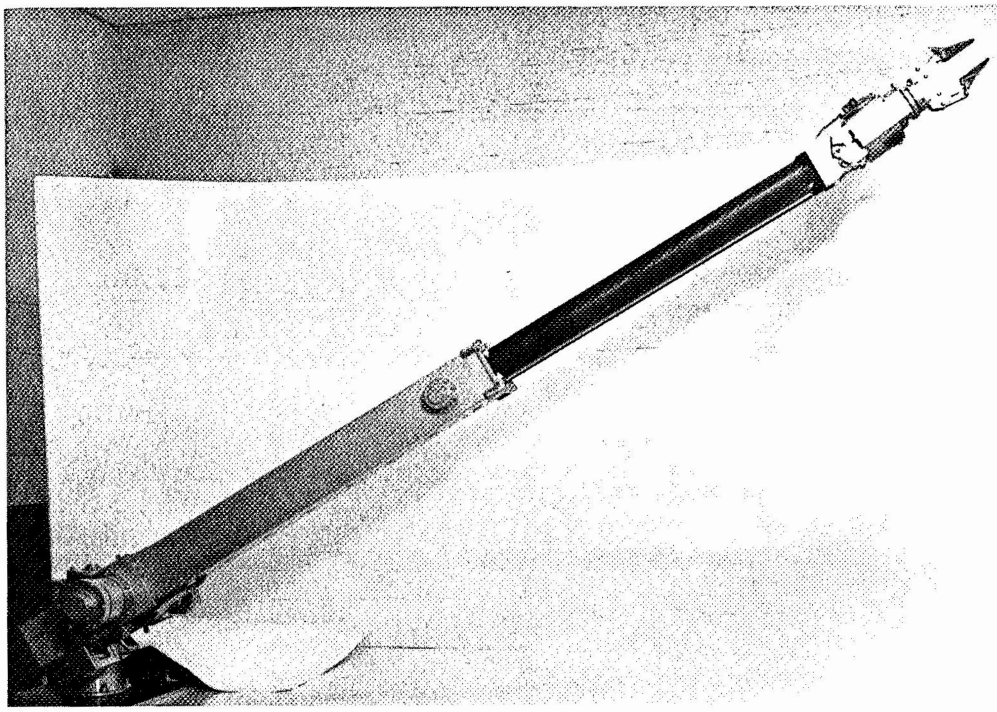

Figure 12. Extendible stiff arm manipulator (ESAM).

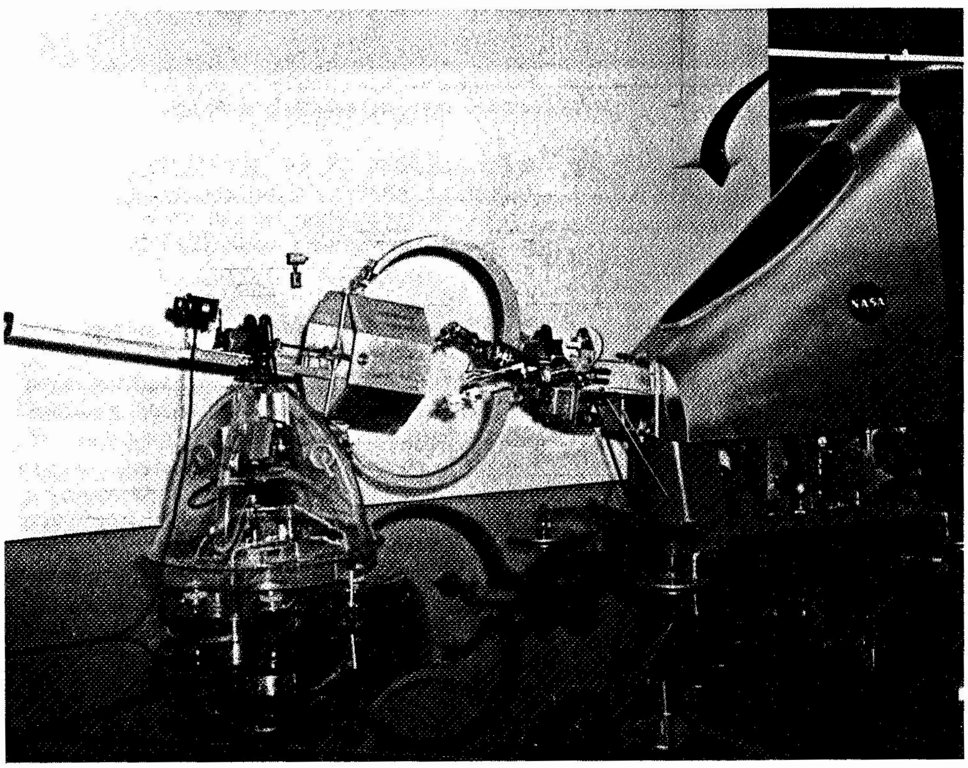

Figure 13. Experimental material handling device.

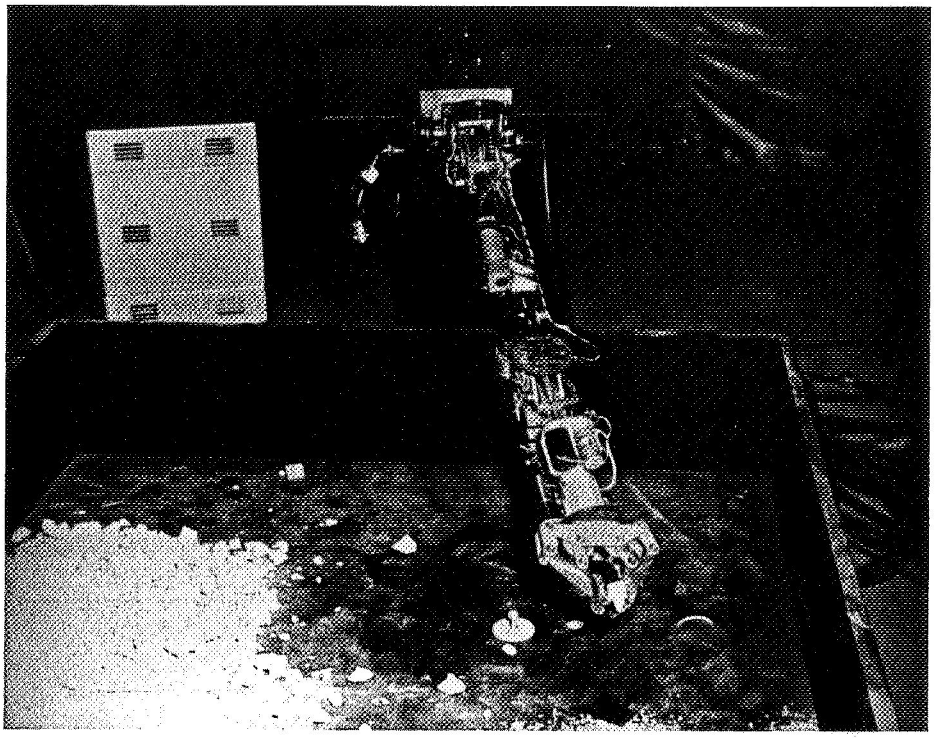

Figure 14. Grappler manipulator ("cherry-picker type").

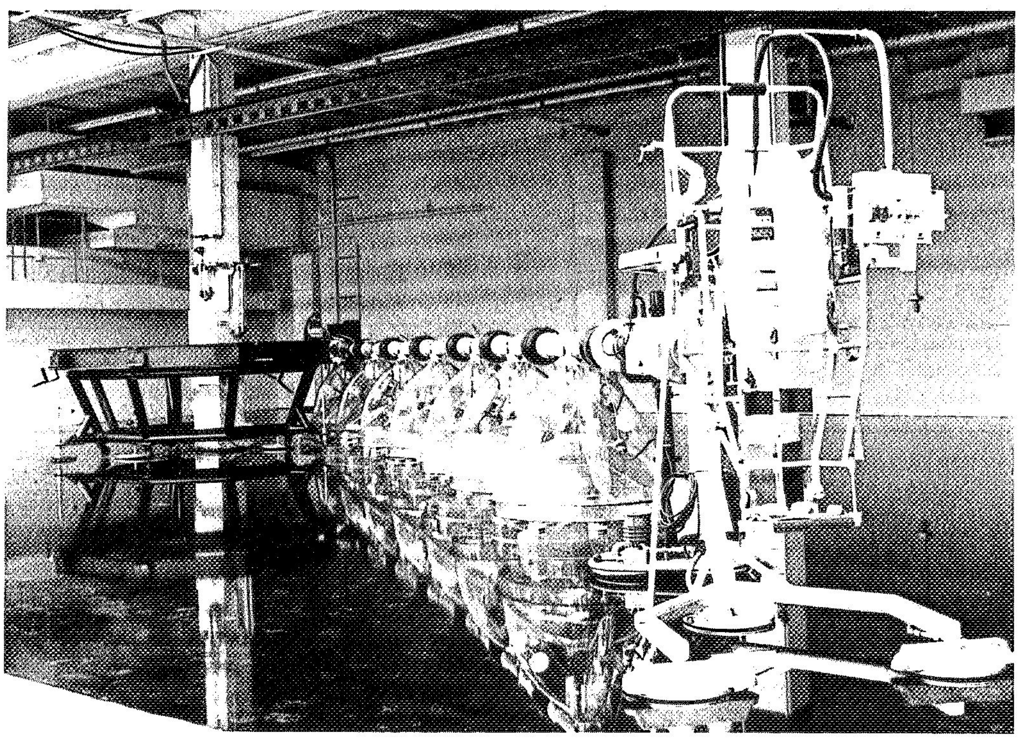

Figure 15. 40-ft serpentuator.

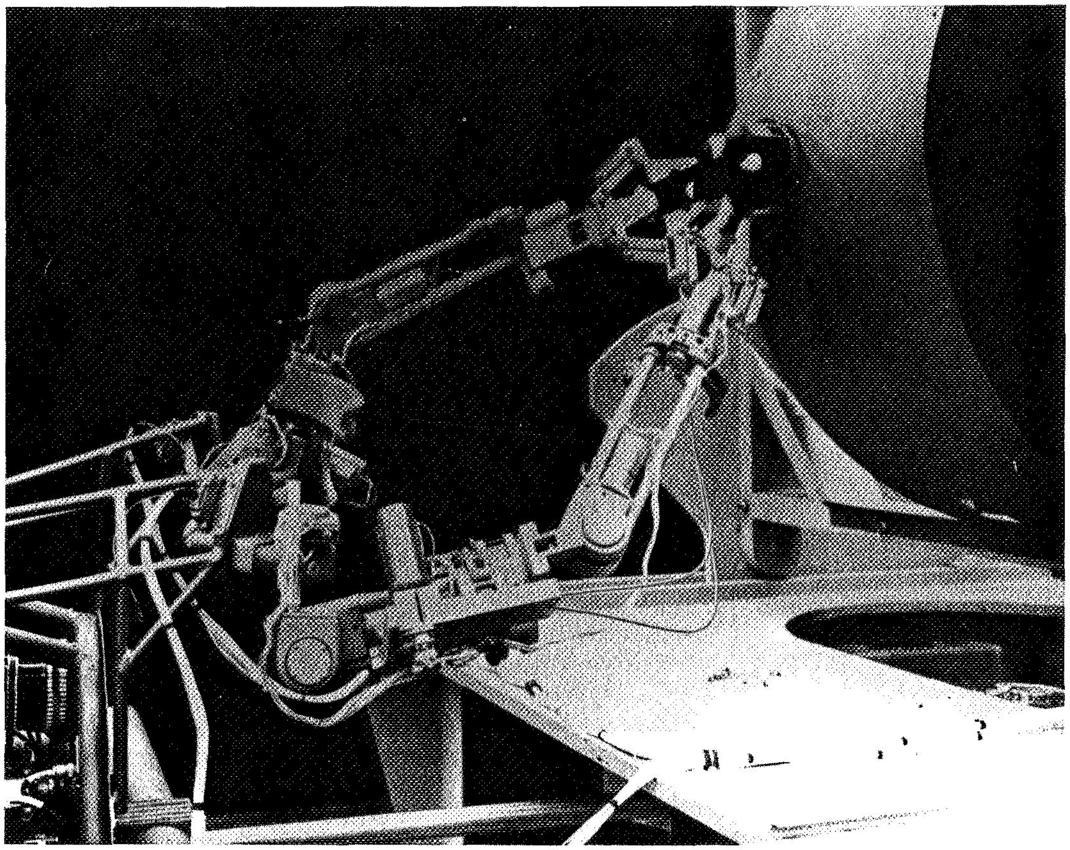

Figure 16. Orthotic arm joint (MSFC rancho manipulator).

permits smoother and easier movement of the arm. The joint is smaller and lighter than previous designs. All components are mounted internally, which eliminates protruding potentiometers but provides for external adjustment of the potentiometer. The new design incorporates a friction clutch for protection of the gears and motors and provides maximum use of off-the-shelf hardware; e.g., bearings and potentiometers. The joint is interchangeable and may be used on either arm at the shoulder or at the elbow. Manufacturing cost of the new joint is approximately the same or less than other joints now in use.

Maneuvering Devices

Air-Bearing Table. A 14.63 by 20.73 m (48 by 68 ft) floor area is currently being used to develop design concepts for cargo transfer systems and to store the serpentuator. The floor surface is good for simulation of FFT mobility where high accuracy of positioning is not required (rendezvous and precontact docking). Because of irregularities in the floor, it should not be used for docking or satellite despin tasks unless the simulation is directed toward gross system design characteristics, or until the floor surface is improved.

Bladder-Type Air Bearing. The first free flying platform that was developed was a bladder-type air bearing, as previously shown in Figure 12, with high velocity onboard thrusters that provided near frictionless translation. With the constant testing and application of the air-bearing platform, it became evident that practical free flying experiments were not feasible because unlevel work surfaces created an excessive drift. After extensive studies had been conducted, a proposal was submitted to and approved by management to provide a 316-m^2 (3400-ft^2) area of flat working surface. The combination of frictionless translation and near drift-free characteristics of the improved working surface provided a means for practical free flying experiments.

Air-Bearing Lift Pad. The second type of free flying platform developed was the air-bearing lift pad (Fig. 17), an innovation of the ground-effect-type machine. These free flyers are discussed in more detail later in this report.

Thrusted Air-Bearing Scooter (TABS). TABS, as shown previously in Figure 9, is a platform mounted on bladder-type air bearings and has six high pressure thruster nozzles that are remotely operated by a controller system.

Air-Bearing Lift Pad Maneuvering Platform (ABLP). This unit (Fig. 18) consists of a box-type platform serving as the low pressure, high volume, air chamber mounted on air-bearing lift pads (a patented hybrid air-bearing/ground effects device). Thrusting of approximately 11.12 N (2.5 lb) is obtained by use of remote controllers which tilt the pads about the platform's center. Figure 19 shows the actual working model.

Control Systems

Stereo (Three-Dimensional) TV. One 30.5-cm (12-in.) TV monitor black and white camera delivers individual views to each eye. An attachment to the camera lens has two openings which form a picture for each eye. As the monitor, the transparent safety shield is replaced with a polarizing shield. The viewer uses stereo glasses with polarizing material suitably oriented.

Teleoperator Remote Control Station. The control station (Fig. 20) is equipped with remotely controlled, closed-circuit, three-dimensional TV, controls for the soil sampler, a grappler and a rancho bilateral remote manipulator, and an adjustable positioning pilot seat. The test subject is completely enclosed by a curtain to provide the effects of remoteness. Testing is in progress in support of soil sampling, remote work tasks, etc.

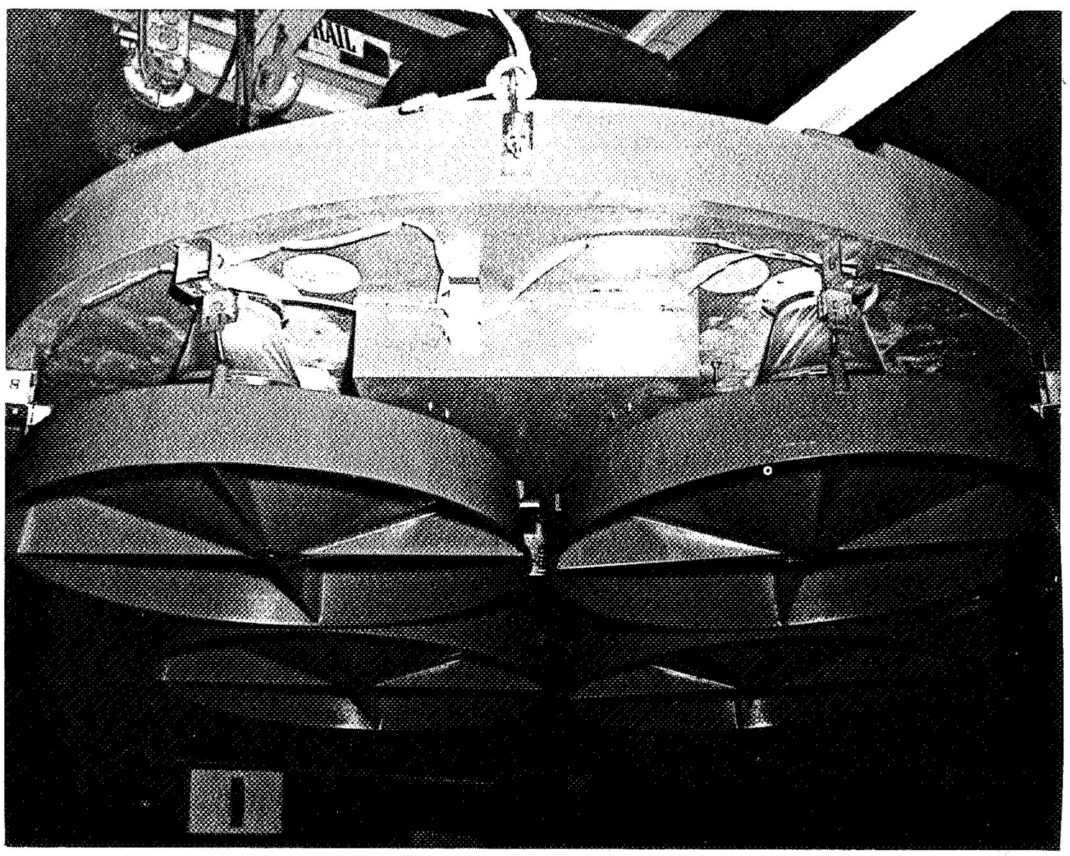

Figure 17. Air-bearing lift pad with thrust chambers shown.

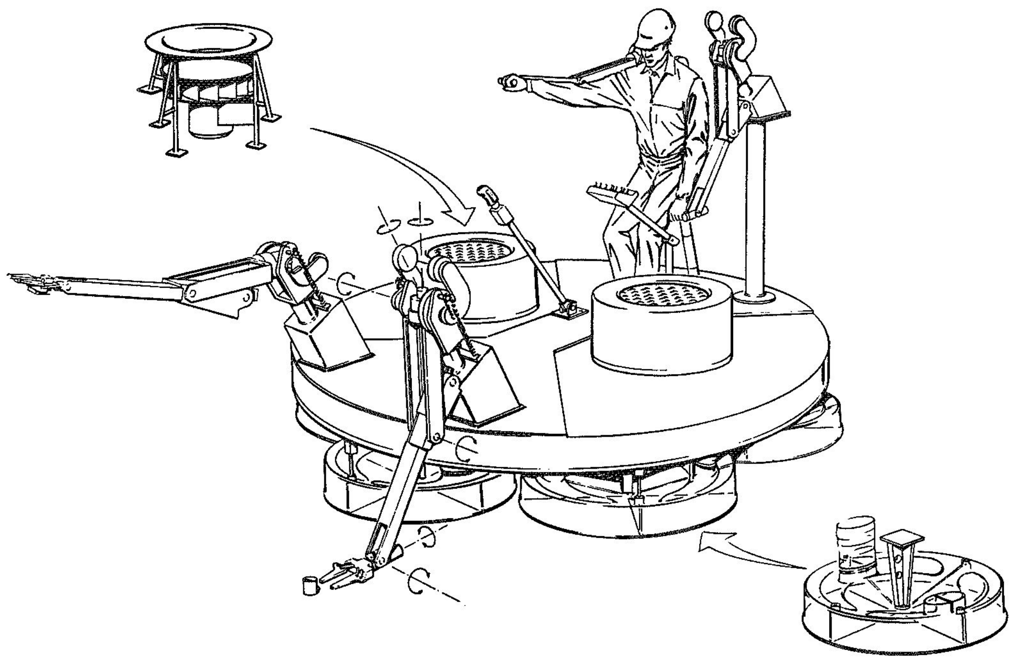

Figure 18. Air-bearing lift pad maneuvering platform (ABLP).

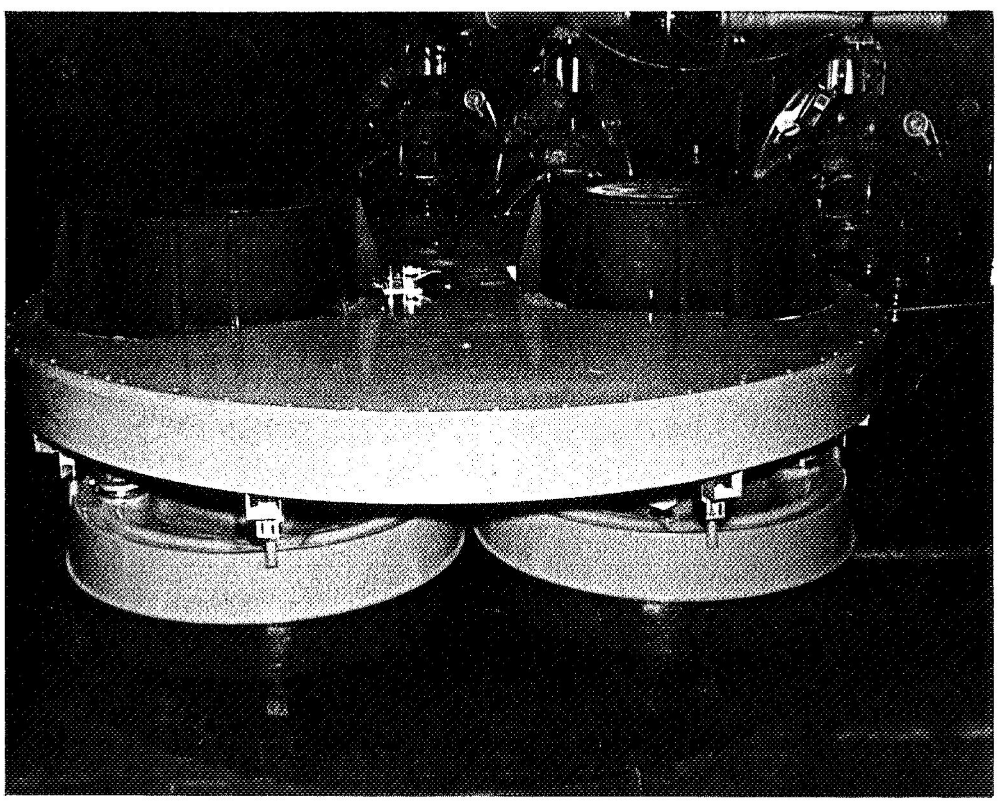

Figure 19. ABLP working model.

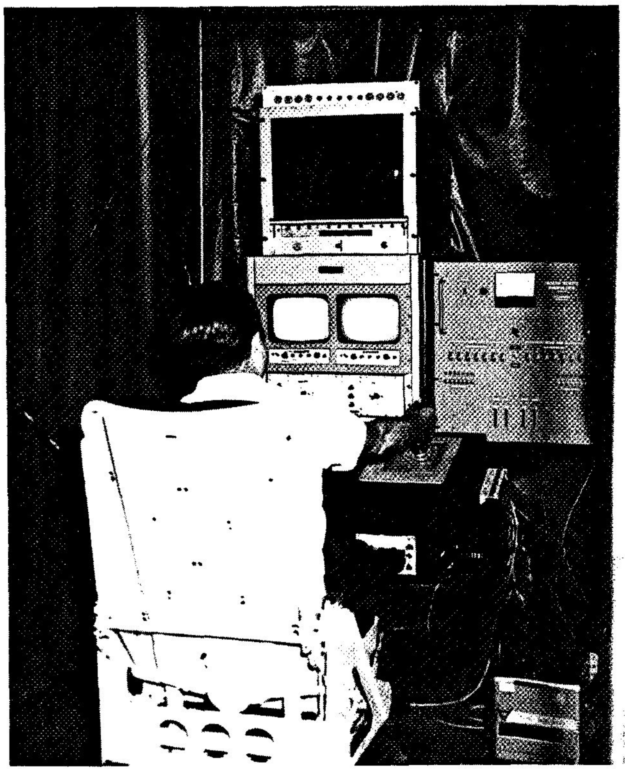

Figure 20. Teleoperator remote control station.

A time-delay system is being developed to support future lunar and Mars tasks. The work area is blacked out to provide a means for lighting effects.

Neutral Buoyancy Facility

The Neutral Buoyancy Facility consists of a 12.19-m (40-ft) tank (Fig. 21) with full provisions for conducting zero-g tests, monitored by closed-circuit TV, for acquisition and storage of performance data.

Underwater Model Capture and Maintenance Pilot (U-CAMP). The U-CAMP (Fig. 22) system has the following capabilities:

1. To nondestructively capture, despin, hold, position, and do work to various noncooperative and/or cooperative objects in orbit.

2. To transport the capture object to and from orbit to the position desired and to impart the proper dynamics to the object before it is released.

3. To perform assembly, modification, repair, or refurbishment and to assist in space manufacturing of various objects being held and positioned by remotely operated manipulators with the aid of remote viewing TV.

4. To aid in space manufacturing where remote operations are mandatory or desirable.

Rancho Manipulator Technology Spinoff

The rancho manipulator is a NASA development that offers considerable spinoff of technology to the medical field. This technology spinoff has resulted in the evolution of a multichannel proportional rate control system to operate direct current motors. NASA's chronological development of this system has produced two 14-channel null balance systems that are used to operate remote manipulators at the NASA facilities in Jackass Flats, Nevada, and Huntsville, Alabama. The first two prototype devices had the desirable feature of very accurately controlling the shaft positions of the motors that drive the remote manipulators. The devices, however, had the undesirable features of being quite bulky [on the order of 0.227 m^3 (8 ft^3)] and did not have velocity proportionality (only position proportionality).

A second generation device included the desirable feature of velocity proportionality; the bulk also was reduced to approximately 0.057 m^3 (2 ft^3). These improved units were used to operate a bilateral, powered, remote manipulator (14 degrees-of-freedom). At Goddard Space Flight Center and at Marshall Space Flight Center, the quality of the control achieved by this system was so good that it was decided to further reduce the volume of the controls to make them applicable for possible FFT applications.

An additional effort resulted in these units being reduced to a 0.001-m^3 (0.04-ft^3) volume. This miniature component was completed at Rancho Los Amigos Hospital where the design engineers working on the project felt that the amplifiers were small enough to be used for operation of externally powered orthotic arm braces. Consequently they tried these units on a near totally paralyzed patient. The results attained in the restoration of arm function via an electrical arm brace and the miniature proportional control were remarkable. The patient after some training could perform tasks

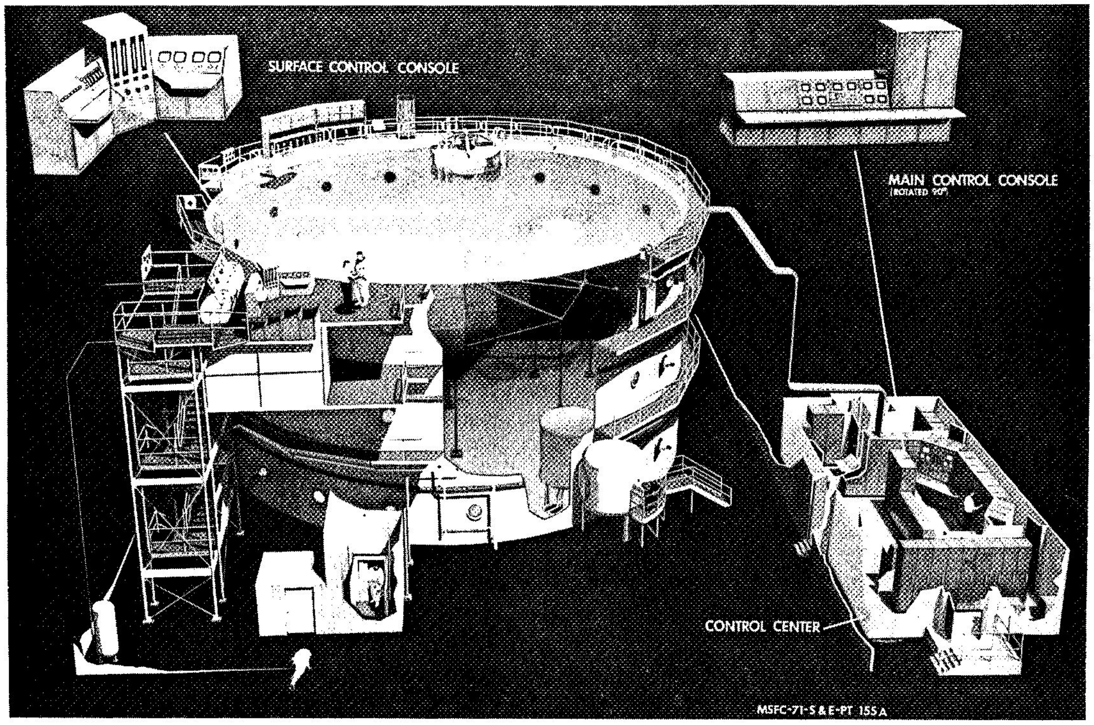

Figure 21. Neutral Buoyancy Space Simulator.

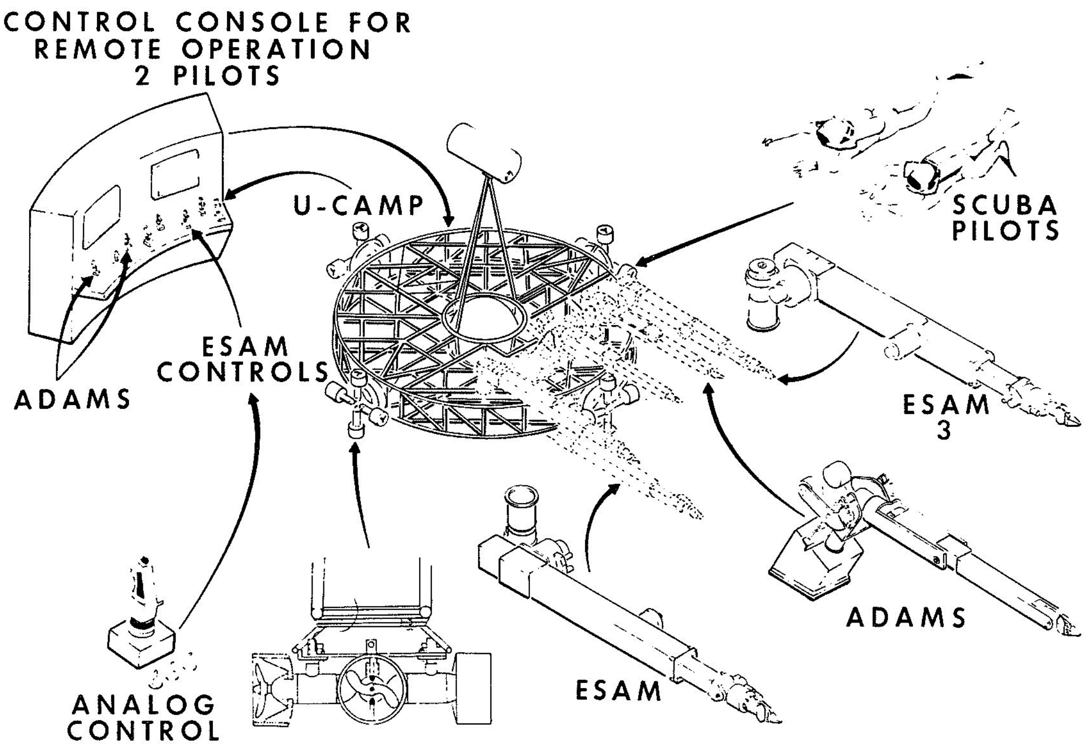

Figure 22. Underwater capture and maintenance pilot (U-CAMP).

requiring accuracy and dexterity that would tax some normal individuals; e.g., stacking blocks to a "nervous" height.

These control systems provided sufficiently "fine" control that the patient could do many routine tasks of daily living, such as self-feeding, drinking hot coffee without the benefit of a special container, turning pages, dialing a telephone, etc. A particularly amazing accomplishment was that the patient was able to write legible script of a normal size. Although the penmanship left something to be desired, it was completely legible. The first thing that the patient wrote was a letter to her daughter in which she stated that it was the first letter that she had been able to handwrite in 18 years. With the use of this control system, paralyzed patients can be fitted with proportionally controlled arm braces throughout the United States. The possibilities for achieving independence in many activities of daily living appear limited only by the person's individual motivation, since the controls offer the potential for functionally useful restoration of arm function to any patient with upper extremity paralysis.

CONCLUSIONS

Requirements resulting from the development of Skylab and similar programs have resulted in an increased need for space-orbital situation simulation capabilities. This need is being met by experiments that have been in progress in the Process Engineering Laboratory for several years. Research facilities have been greatly expanded to develop newer, more advanced manipulators and maneuvering devices. The development of semiautomatic manipulators, advanced air-bearing maneuvering devices, and complex control systems have resulted in Free Flying Teleoperator systems. These sophisticated systems are designed to serve in the air-bearing environment with ultimate evolution to the neutral buoyancy water environment where simulation situations more nearly depict those experienced in space-orbital situations.

Remotely operated mechanical and electrical teleoperator devices offer the following advantages:

- Extend man's capability in space.
- Permit earlier space and planetary exploration.
- Reduce costs of selected missions.
- Provide increased safety to astronauts.

February 1973 APPROVAL NASA TM X-64723

RESEARCH ACHIEVEMENTS REVIEW
VOLUME IV REPORT NO. 7

The information in these reports has been reviewed for security classification. Review of any information concerning Department of Defense or Atomic Energy Commission programs has been made by the MSFC Security Classification Officer. These reports, in their entirety, have been determined to be unclassified.

These reports have also been reviewed and approved for technical accuracy.

3/6/73

M. P. L. SIEBEL
Director, Process Engineering Laboratory

☆ U. S. GOVERNMENT PRINTING OFFICE: 1973—746829/4791